# Physico-chemistry, high pressure rheology and film-forming capacity of polymer-base oil solutions in EHL

Charlotte Mary

N° d'ordre : 2014ISAL0013 Année 2014

Thèse

# Physico-chemistry, high pressure rheology and film-forming capacity of polymer-base oil solutions in EHL

Présentée devant
L'Institut National des Sciences Appliquées de Lyon

Pour obtenir
Le grade de Docteur

Formation doctorale : Mécanique
École doctorale : Mécanique, Energétique, Génie civil, Acoustique (MEGA)

Par
Charlotte MARY
(Ingénieur ENSIACET)

Soutenue le 3 février 2014 devant la Commission d'examen

**Jury**

| | | |
|---|---|---|
| Président | P. Cassagnau | Professeur (Université Claude Bernard Lyon 1) |
| Rapporteur | M. Priest | Professeur (University of Leeds, U.K.) |
| Rapporteur | J.-F. Tassin | Professeur (Université du Maine) |
| Directeur | P. Vergne | Directeur de recherche (CNRS) (INSA de Lyon) |
| Co-directeur | D. Philippon | Maître de conférence (INSA de Lyon) |
| Invité | S. Bair | Docteur (Georgia Institute of Technology, U.S.A.) |
| Invité | D. Laurent | Ingénieur de recherche (Total, Solaize) |
| Invité | F. Rondelez | Directeur de recherche émérite (CNRS, Institut Curie) |

*Laboratoire de recherche : Laboratoire de Mécanique des Contacts et des Structures*
(Université de Lyon, INSA-Lyon, LaMCoS, CNRS, UMR5259, F-69621, France)

# INSA Direction de la Recherche - Ecoles Doctorales - Quinquennal 2011-2015

| SIGLE | ECOLE DOCTORALE | NOM ET COORDONNEES DU RESPONSABLE |
|---|---|---|
| **CHIMIE** | **CHIMIE DE LYON**<br>**http://www.edchimie-lyon.fr**<br><br>Insa : R. GOURDON | M. Jean Marc LANCELIN<br>Université de Lyon – Collège Doctoral<br>Bât ESCPE<br>43 bd du 11 novembre 1918<br>69622 VILLEURBANNE Cedex<br>Tél : 04.72.43 13 95<br>directeur@edchimie-lyon.fr |
| **E.E.A.** | **ELECTRONIQUE, ELECTROTECHNIQUE, AUTOMATIQUE**<br>**http://edeea.ec-lyon.fr**<br><br>Secrétariat : M.C. HAVGOUDOUKIAN<br>eea@ec-lyon.fr | M. Gérard SCORLETTI<br>Ecole Centrale de Lyon<br>36 avenue Guy de Collongue<br>69134 ECULLY<br>Tél : 04.72.18 60 97 Fax : 04 78 43 37 17<br>Gerard.scorletti@ec-lyon.fr |
| **E2M2** | **EVOLUTION, ECOSYSTEME, MICROBIOLOGIE, MODELISATION**<br>**http://e2m2.universite-lyon.fr**<br><br>Insa : H. CHARLES | Mme Gudrun BORNETTE<br>CNRS UMR 5023 LEHNA Université Claude Bernard Lyon 1<br>Bât Forel<br>43 bd du 11 novembre 1918<br>69622 VILLEURBANNE Cédex<br>Tél : 04.72.43.12.94<br>e2m2@biomserv.univ-lyon1.fr |
| **EDISS** | **INTERDISCIPLINAIRE SCIENCES-SANTE**<br>**http://ww2.ibcp.fr/ediss**<br><br>Sec : Safia AIT CHALAL<br>Insa : M. LAGARDE | M. Didier REVEL<br>Hôpital Louis Pradel<br>Bâtiment Central<br>28 Avenue Doyen Lépine<br>69677 BRON<br>Tél : 04.72.68 49 09 Fax :04 72 35 49 16<br>Didier.revel@creatis.uni-lyon1.fr |
| **INFOMATHS** | **INFORMATIQUE ET MATHEMATIQUES**<br>http://infomaths.univ-lyon1.fr | M. Johannes KELLENDONK<br>Université Claude Bernard Lyon 1<br>INFOMATHS<br>Bâtiment Braconnier<br>43 bd du 11 novembre 1918<br>69622 VILLEURBANNE Cedex<br>Tél : 04.72. 44.82.94 Fax 04 72 43 16 87<br>infomaths@univ-lyon1.fr |
| **Matériaux** | **MATERIAUX DE LYON**<br><br>Secrétariat : M. LABOUNE PM<br>: 71.70 –Fax : 87.12<br>Bat. Saint Exupéry<br>Ed.materiaux@insa-lyon.fr | M. Jean-Yves BUFFIERE<br>INSA de Lyon<br>MATEIS<br>Bâtiment Saint Exupéry<br>7 avenue Jean Capelle<br>69621 VILLEURBANNE Cédex<br>Tél : 04.72.43 83 18 Fax 04 72 43 85 28<br>Jean-yves.buffiere@insa-lyon.fr |
| **MEGA** | **MECANIQUE, ENERGETIQUE, GENIE CIVIL, ACOUSTIQUE**<br><br>Secrétariat : M. LABOUNE PM<br>: 71.70 –Fax : 87.12<br>Bat. Saint Exupéry<br>mega@insa-lyon.fr | M. Philippe BOISSE<br>INSA de Lyon<br>Laboratoire LAMCOS<br>Bâtiment Jacquard<br>25 bis avenue Jean Capelle<br>69621 VILLEURBANNE Cedex<br>Tél :04.72.43.71.70 Fax : 04 72 43 72 37<br>Philippe.boisse@insa-lyon.fr |
| **ScSo** | **ScSo***<br><br>M. OBADIA Lionel<br><br>Sec : Viviane POLSINELLI Insa<br>: J.Y. TOUSSAINT | M. OBADIA Lionel<br>Université Lyon 2<br>86 rue Pasteur<br>69365 LYON Cedex 07<br>Tél : 04.78.69.72.76 Fax : 04.37.28.04.48<br>Lionel.Obadia@univ-lyon2.fr |

*ScSo : Histoire, Geographie, Aménagement, Urbanisme, Archéologie, Science politique, Sociologie, Anthropologie

## Physico-chemistry, high pressure rheology and film-forming capacity of polymer-base oil solutions in EHL

Abstract

The development of high value-added lubricants overcoming more and more drastic operating conditions, fuel-efficient and providing excellent performance during a long time remains a huge challenge for oil makers. This thesis is dedicated to the study of the role and the actions of Viscosity Index Improvers (VII) in engine lubricants.

The first objective targeted in this work is the characterization of the rheological behaviors and the modeling of viscosity in function of realistic conditions of temperature, pressure and shear stress for polymer-thickened base oil solutions without functional additives. Several polymers (PAMA, OCP and PISH) with different molecular weights and conformations (comb, linear and star) are used with a concentration of 1.2% (w/w) in a hydrocracked mineral base oil. The originality of the thesis lies in the use of non-commercial rheometers under high pressure (up to 800 MPa).

A second challenge is the understanding of the relationship between the rheological response of simplified engine lubricants and the mechanisms occurring at the molecular scale by exploring the notions of conformation, solubility and hydrodynamic radius by the extension of the Einstein's law at high pressure.

Finally, the study focuses on the link between rheology and tribology and by extrapolation, between the chemical composition of the lubricant and tribology. The film thickness is measured and compared with the Hamrock-Dowson analytical predictions and with the numerical simulations based on the generalized Reynolds' equation including the rheological models. Both experimental and numerical data are in good agreement.

**Keywords**: rheology, non-Newtonian behavior, elastohydrodynamic lubrication, hydrodynamic radius, polymer, lubricant, rheological models, pressure, tribology

## Physico-chimie, rhéologie haute pression et capacité à former des films de solutions huile de base-polymère en EHL

Résumé

Le développement de lubrifiants à haute valeur ajoutée subissant des conditions opératoires de plus en plus draconiennes, économes en carburant et performants pendant une longue durée reste un défi considérable pour les fabricants d'huiles. Cette thèse concerne l'étude du rôle et des actions des améliorants d'indice de viscosité (ou Viscosity Index Improvers (VII)) dans les lubrifiants moteurs.

Le premier objectif visé dans ce travail est la caractérisation des comportements rhéologiques et la modélisation de la viscosité en fonction de conditions réelles de température, pression et contrainte de cisaillement pour des solutions d'huile de base et de polymère sans additifs fonctionnels. Plusieurs polymères (PAMA, OCP et PISH) de masses moléculaires et conformations (peigne, linéaire et étoile) différentes sont utilisés à 1,2% en masse dans une huile de base minérale hydrocraquée. L'originalité de la thèse réside dans l'utilisation de rhéomètres non-commerciaux à haute pression (jusqu'à 800 MPa).

Un deuxième défi réside dans la compréhension de la relation entre la réponse rhéologique des lubrifiants automobiles simplifiés et les mécanismes présents à l'échelle moléculaire en explorant les notions de conformation, de solubilité et de rayon hydrodynamique grâce à l'extension de la loi d'Einstein à haute pression.

Enfin, l'étude se concentre sur le lien entre rhéologie et tribologie et par extension, entre la composition chimique du lubrifiant et la tribologie. Les épaisseurs de film sont mesurées et comparées avec les prédictions analytiques de Hamrock-Dowson et avec les simulations numériques basées sur l'équation de Reynolds généralisée en incluant les modèles rhéologiques. Les données expérimentales et numériques sont en adéquation.

**Mots-Clés**: rhéologie, comportement non-Newtonien, lubrification élastohydrodynamique, rayon hydrodynamique, polymère, lubrifiant, modèles rhéologiques, pression, tribologie

# Acknowledgment

Cette thèse s'est déroulée au Laboratoire de Mécanique des Contacts et des Structures (LaMCoS) à l'INSA de Lyon et au Centre de Recherche de Solaize (CReS, TOTAL) avec un séjour de 3 mois au Georgia Institute of Technology à Atlanta. Je remercie donc les directeurs de chacune de ces entités pour leur accueil.

Je souhaite remercier tous les membres du jury pour l'intérêt qu'ils ont porté à ce travail, pour leur lecture attentive du manuscrit et pour la pertinence de leurs remarques.

Je tiens à remercier Philippe Vergne et David Philippon, mes directeurs de thèse, qui ont encadré ce projet de main de maître à la fois scientifiquement et humainement. Merci pour votre disponibilité, vos précieux conseils et votre appui dans les moments de doute et d'inquiétude qui ont fait progresser cette étude dans un climat serein et productif.

Mes remerciements sincères vont également à Olivier Lerasle et Delphine Laurent, mes encadrants industriels, pour leur soutien avec une mention spéciale pour Francis Rondelez qui a offert à ce travail des orientations innovantes et passionnantes.

Je remercie Scott Bair de m'avoir accueillie dans le « désordre organisé » de son laboratoire au Center for High Pressure Rheology (George W. Woodruff School of Mechanical Engineering) à GA Tech et d'avoir partagé avec moi une partie de son grand savoir sur la rhéologie des lubrifiants.

Dr. J. Eckelt, Prof. B.A. Wolf de WEE-Solve (Auf der Burg 6, D-55130 Mainz, Germany), Prof. C. Chassenieux, Prof. J.-F. Tassin et D. Chaveroux du laboratoire Polymères, Colloïdes, Interfaces (Université du Maine, Le Mans) ont contribué à la réalisation d'expérimentations nécessaires pour la compréhension de certains phénomènes et je les en remercie.

Ce travail est le fruit d'une collaboration entre plusieurs membres du LaMCoS. Je pense notamment à Nicolas Fillot, Nathalie Bouscharain, Lionel Lafarge et Nicolas Devaux pour leur aide scientifique et leur soutien moral dans les périodes de remise en question. Je dis un grand merci à toutes les personnes du labo qui ont participé de près ou de loin au projet (Marie-Hélène, Michel, Laetitia, Sylvie, Sayed, Hamza, Thomas, Vincent B., Daniele, Jonathan, Vincent S., Jean-David, Nicolas, Arnaud, Pierre, Marion, Jérôme, Matthieu, Rudy, Guillaume, + tous les autres…).

Au sein de Total, de nombreuses personnes ont été impliquées à qui je tiens à exprimer ma gratitude pour leur contribution: Éric Lacroix, Thomas Roussel, Pierre Daverat, Dominique Faure, Frédéric Jarnias, Raphaèle Iovine, Séverine Thévenet, Marc Chardonnet, Grégory Descroix, Sophie Opilliart, Christelle Vatry, Eric Tinguy, Nico, Vincent, Jérôme, Bernadette, Mickaël (son bavardage, sa capacité à me déconcentrer et ses montages photos), Catherine, Lauriane…

Merci à la team du Leeds-Lyon 2012 et à l'équipe du RU qui sont devenues au fil du temps un peu plus que des collègues grâce à nos longues discussions, nos séjours au ski, nos soirées au Dikkenek ou au BeRThoM (bon sas de décompression, ou pas… hein JB ?).

Merci à tous les présents à ma soutenance et notamment à Nathalie et Guillaume qui m'ont initiée au goût pour la recherche il y a bien longtemps, rue de Charenton.

Encore merci à tous mes amis qui me remplissent de bonheur jour après jour : Cécile, Sandrine, Hélène, Alicia, Krijou, Poutrelle, + tous les A7iens de la mailing list, Nolwenn, Margaux, Julia, Agnès, Delphine, Audrey, Sandrine, Chloé, Aline, Jess', Virginie, Eve-Marie, Camille, Orane, Céline, Mich, Fred, … Vous êtes géniaux !

Evidemment, une pensée particulière se dirige vers ma famille qui m'a soutenue tout au long de mon parcours et qui a toujours eu confiance en moi. Votre fierté a amplifié mon sentiment de réussite. Je vous aime.

# Table of contents

# List of tables



# List of figures

# Nomenclature

**Latin letters:**

| | |
|---|---|
| $A$ | Doolittle parameter |
| $a$ | parameter for the Carreau-Yasuda model |
| $a_H$ | radius of the Hertzian contact (m) |
| $a_{HD}$ | power of the parameter $U_{HD}$ in the Hamrock-Dowson equation |
| $a_v$ | thermal expansion defined for volume linear with temperature in the Tait equation ($K^{-1}$) |
| $B$ | Doolittle parameter |
| $b_{HD}$ | power of the parameter $W_{HD}$ in the Hamrock-Dowson equation |
| $C_1$, $C_2$, $A_1$, $A_2$, $B_1$, $B_2$ | WLF constants |
| $C$ | calibration constant for the falling body viscometer (Pa) |
| $C_\infty$ | characteristic ratio |
| $c$ | concentration in weight of active polymer ($g.cm^{-3}$) |
| $c^*$ | critical concentration ($g.cm^{-3}$) |
| $c_m$ | specific heat capacity ($J.kg^{-1}.K^{-1}$) |
| $c_{HD}$ | power of the parameter $G_{HD}$ in the Hamrock-Dowson equation |
| $D_F$ | fragility parameter in the VTF equation |
| $E$ | Young modulus (GPa) |
| $E_1$, $E_2$ | Young moduli of solids 1 and 2 respectively (GPa) |
| $E_{eq}$ | reduced Young elastic modulus of the contacting bodies (GPa) |
| $E_a$ | thermal activation energy ($J.mol^{-1}$) |
| $F$ | dimensionless relative thermal expansion of the free volume |
| $F_m$ | modified dimensionless relative thermal expansion of the free volume |
| $G$ | effective shear modulus (kPa) |
| $G'$ | elastic modulus (or storage modulus) (kPa) |
| $G''$ | viscous modulus (or loss modulus) (kPa) |
| $G_{HD}$ | Hamrock-Dowson dimensionless material properties parameter |
| $g$ | gravitational constant (9.80665 $m.s^{-2}$) |
| $H$ | height of the inner cylinder (m) |
| $H_{HD}$ | Hamrock-Dowson dimensionless film thickness |
| $H_{Moes}$ | Moes dimensionless film thickness |
| $h$ | film thickness (nm) |
| $h(p)$ | film thickness at the pressure $p$ |
| $h_0$ | film thickness at atmospheric pressure |
| $h_c$ | central film thickness (nm) |
| $h_{min}$ | minimal film thickness (nm) |
| $I$ | intensity captured by the detector |
| $I_0$ | intensity of the incident light beams |
| $I_1$ to $I_n$ | intensity of the reflected light beams |
| $k$ | thermal conductivity ($W.m^{-1}.K^{-1}$) |
| $K$, $a$ | Mark-Houwink-Sakurada empirical constants |
| $K_c$ | calibration constant in the Poiseuille equation ($mm^2.s^{-2}$) |
| $K_0$ | isothermal bulk modulus at $p$=0 (Pa) in the Tait equation |

| | |
|---|---|
| $K_{00}$ | $K_0$ at zero absolute temperature (Pa) in the Tait equation |
| $K_0'$ | pressure rate of change of isothermal bulk modulus at $p$=0 in the Tait equation |
| $K_{HD}$ | Hamrock-Dowson parameter |
| $k$ | liquid thermal conductivity ($W.m^{-1}.K^{-1}$) |
| $k_H$, $k_K$, $k_M$ | Huggins, Kraemer, Martin constants |
| $L_{Moes}$ | Moes dimensionless material properties parameter |
| $L$ | characteristic length of the flow (m) |
| $l$ | mean monomer size (cm) |
| $M_t$ | torque applied to the inner cylinder (N.m) |
| $M$ | mass of one molecule (g) |
| $M_{Moes}$ | Moes dimensionless load parameter |
| $M_n$ | number average molecular mass ($g.mol^{-1}$) |
| $M_w$ | weight average molecular mass ($g.mol^{-1}$) |
| $m_0$ | molecular mass of one monomer ($g.mol^{-1}$) |
| $m_i$ | mass of one atom (g) |
| $N$ | number of monomers ($N=M_w/m_0$) |
| $N_a$ | Avogadro number ($mol^{-1}$) |
| $Na$ | Nahme-Griffith number |
| $N_\gamma$ | number of studied shear rates |
| $N_{parameters}$ | number of parameters in the model |
| $n$ | power law exponent |
| $n_0$ | index of refraction at atmospheric pressure |
| $n(p)$ | index of refraction the pressure $p$ |
| $PDI$ | polydispersity index |
| $p$ | pressure (Pa) |
| $p_P$ | pole pressure in the Roelands model |
| $p_H$ | maximum Hertzian pressure (Pa) |
| $R_{coil}$ | radius of a polymer coil (nm) |
| $R$ | gas constant ($8.314\ J.mol^{-1}.K^{-1}$)) |
| $R_1$, $R_2$ | curvature radii (m) |
| $R_{ball}$ | curvature radii of the ball (m) |
| $R_{eq}$ | reduced radius of curvature (m) |
| $R_x$, $R_y$ | curvature radii in the $x$-direction and $y$-direction respectively (m) |
| $R_e$, $R_i$ | radius of the inner and outer cylinders in a Couette rheometer (m) |
| $R_g$ | radius of gyration (nm) |
| $R_h$ | hydrodynamic radius (nm) |
| $R_0$ | occupied volume fraction ($Vo/V$) at the reference state and at $p$=0 |
| $R_c$ | radius of the capillary (m) |
| $R_a$ | arithmetic average roughness (m) |
| $Rq_1$, $Rq_2$ | root mean square (RMS) roughness of materials 1 and 2 respectively (nm) |
| $Re$ | Reynolds number |
| $r$ | distance from the contact center (m) |
| $r_i$ | distance of an atom from the center of mass of a macromolecule (nm) |
| $S$ | Roelands slope index |
| $SRR$ | slide-to-roll ratio |
| $T$ | temperature (°C) |

| | |
|---|---|
| $T_\infty$ | Vogel (and Roelands) temperature at which the viscosity diverges (°C) |
| $T_g(0)$ | glass transition temperature at atmospheric pressure (°C) |
| $T_g(p)$ | glass transition temperature depending on pressure (°C) |
| $T_R$ | reference temperature (°C) |
| $t$ | falling time of the sinker in the falling body viscometer (s) |
| $t_c$ | flow time of the liquid in a capillary (s) |
| $U_{ball}$ | ball speed ($m.s^{-1}$) |
| $U_{disc}$ | disc speed ($m.s^{-1}$) |
| $U_e$ | entrainment speed ($m.s^{-1}$) |
| $\Delta U$ | sliding velocity ($m.s^{-1}$) |
| $U_{HD}$ | Hamrock-Dowson dimensionless speed |
| $u$ | velocity of the flow ($m.s^{-1}$) |
| $V_{coil}$ | volume of a polymer coil ($m^3$) |
| $V_{(T,p)}$ | total volume ($m^3$) |
| $V_{(T,p=0)}$ | total volume at atmospheric pressure ($m^3$) |
| $V_R$ | total volume at the reference state ($m^3$) |
| $V_o$ | occupied volume ($m^3$) |
| $V_f$ | free volume ($m^3$) |
| $V_c$ | volume of liquid flowing in the capillary viscometer ($m^3$) |
| $v$ | total volume ($m^3$) |
| $v_o$ | occupied volume ($m^3$) |
| $v_f$ | free volume ($m^3$) |
| $W$ | external normal applied load (N) |
| $W_{HD}$ | Hamrock-Dowson dimensionless load parameter |
| $W_i$ | Weissenberg number |
| $Z$ | Roelands pressure-viscosity index |

**Greek letters:**

| | |
|---|---|
| $\alpha$ | local pressure-viscosity coefficient ($GPa^{-1}$) |
| $\alpha^*$ | reciprocal asymptotic isoviscous pressure coefficient ($GPa^{-1}$) |
| $\beta$ | temperature-viscosity coefficient ($K^{-1}$) |
| $\beta_K$ | temperature coefficient of $K_0$ ($°C^{-1}$) in the Tait equation |
| $\varepsilon$ | occupied volume thermal expansion ($K^{-1}$) |
| $\varepsilon_{HD}$ | Hamrock-Dowson parameter |
| $\lambda$ | relaxation time (s) |
| $\lambda_l$ | light wavelength (m) |
| $\gamma$ | strain |
| $\dot{\gamma}$ | shear rate ($s^{-1}$) |
| $[\eta]$ | intrinsic viscosity ($cm^3.g^{-1}$) |
| $\eta$ | dynamic viscosity (Pa.s) |
| $\eta_{red}$ | reduced viscosity ($cm^3.g^{-1}$) |
| $\eta_r$ | relative viscosity |
| $\eta_{sp}$ | specific viscosity |
| $\eta_{solution}$ | viscosity of the solution (Pa.s) |

| | |
|---|---|
| $\eta_{solvent}$ | viscosity of the solvent (Pa.s) |
| $\eta_{\infty}$ | viscosity extrapolated to infinite temperature (Pa.s) |
| $\eta_g$ | viscosity at the glass transition (Pa.s) |
| $\eta_0$ | viscosity at low shear stress (Pa.s) |
| $\eta_{0(WLF)}$ | viscosity at low shear stress from the modified WLF-Yasutomi model (Pa.s) |
| $\eta_2$ | viscosity on the second Newtonian plateau (Pa.s) |
| $\eta_P$ | pole viscosity in the Roelands model (Pa.s) |
| $\eta_R$ | viscosity in the Roelands model at the reference temperature (Pa.s) |
| $\eta_{experiment}$ | experimental viscosity (Pa.s) |
| $\eta_{model}$ | viscosity calculated from the model (Pa.s) |
| $\nu$ | kinematic viscosity (cSt or $mm^2.s^{-1}$) |
| $\nu_p$ | Poisson's coefficient |
| $\nu_1, \nu_2$ | Poisson's coefficients of solids 1 and 2 respectively |
| $\rho$ | mass density ($g.cm^{-3}$) |
| $\rho_0$ | mass density at atmospheric pressure ($g.cm^{-3}$) |
| $\rho(p)$ | mass density at the pressure $p$ ($g.cm^{-3}$) |
| $\rho_R$ | mass density at the reference state ($g.cm^{-3}$) |
| $\rho_s$ | mass density of the sinker in the falling body viscometer ($g.cm^{-3}$) |
| $\sigma$ | composite RMS roughness of a couple of materials (nm) |
| $\tau$ | shear stress (kPa) |
| $\tau_c$ | characteristic shear stress (kPa) |
| $\Phi$ | volume fraction |
| $\Phi_0$ | universal Flory constant ($mol^{-1}$) |
| $\varphi_1$ | phase shift |
| $\Omega$ | applied angular speed |

# Résumé étendu

# Introduction et objectifs

Au cours du siècle passé, avec le nombre croissant de pays industrialisés et de pays en voie de développement, les activités humaines ont rejeté dans l'atmosphère d'énormes quantités de dioxyde de carbone et autres gaz à effet de serre. Le diagramme circulaire ci-dessous (Figure 1) représente la répartition mondiale des émissions de gaz à effet de serre pour différents domaines industriels et différentes sources d'émissions. La majeure partie (les deux tiers) des gaz rejetés proviennent des combustibles fossiles brûlés pour la chaleur et l'énergie, de la déforestation, de l'agriculture et d'autres procédés industriels. Un tiers des émissions de gaz nocifs provient du marché du pétrole et du gaz parmi lesquels le transport, la construction, l'industrie et les procédés de raffinage sont comptabilisés. La plus grande participation (13%) est attribuée au transport qui représente environ 40% des émissions liées au pétrole et au gaz.

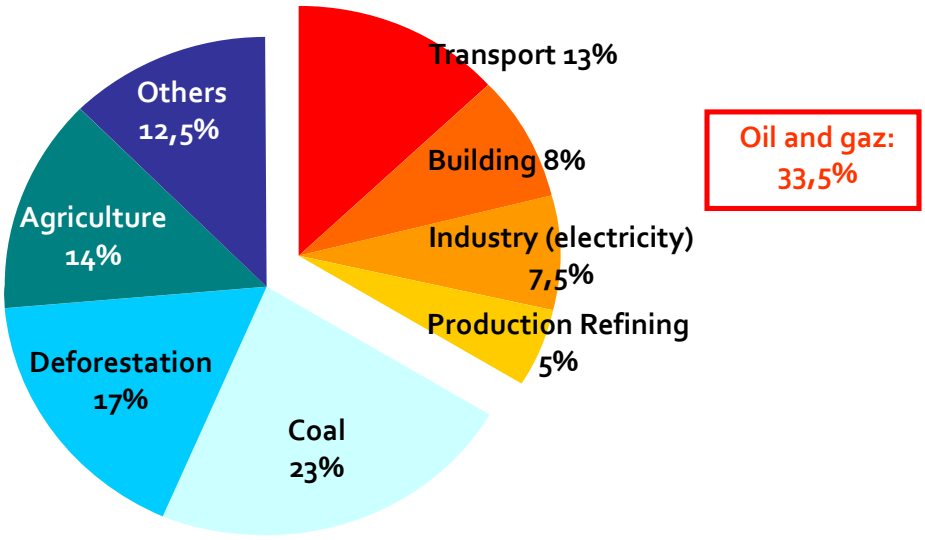


*Figure 1: Distribution mondiale des émissions de gaz à effet de serre, sources GIEC et AIE*

Le réchauffement climatique induit par les émissions de gaz à effet de serre, notamment dans le secteur automobile, est un problème de société et de santé publique. De plus, Taylor [1] souligne la dimension économique de ce phénomène. En effet, les prix élevés des carburants - dus à l'épuisement des ressources - doivent être pris en compte ainsi que les pénalités financières sévères encourues lorsque les objectifs de consommation ne sont pas atteints. L'Union Européenne vise à limiter les émissions de dioxyde de carbone par les voitures à moins de 130 $gCO_2.km^{-1}$ en 2015 et à moins de 95 $gCO_2.km^{-1}$ en 2020. Dans ce contexte de développement durable, diminuer la consommation de carburant et augmenter l'efficacité énergétique sont des aspirations de la plus haute importance.

## *Motivations industrielles et défis scientifiques*

Plusieurs pistes d'action peuvent être envisagées pour diminuer la consommation de carburant, notamment l'utilisation des énergies renouvelables. Bien que ces solutions promettent un avenir brillant, le travail de thèse est centré sur la réduction du frottement dans les moteurs automobiles, tout en maintenant et même en améliorant leur puissance.

Selon Holmberg *et al.* [2], dans une voiture particulière, 33% du carburant est dissipé dans les gaz d'échappement, 29% vont dans les systèmes de refroidissements et 38% sont convertis en énergie mécanique pour surmonter la résistance de l'air (5%) et les pertes par frottement (33%). Ces dernières sont attribuées aux frottements dans le moteur (11.5%), au système de transmission (5%), au contact pneu-route (11.5%) et aux freins (5%) (cf. Figure 2). Finalement, seulement 21.5% du carburant sont utilisés pour déplacer la voiture.

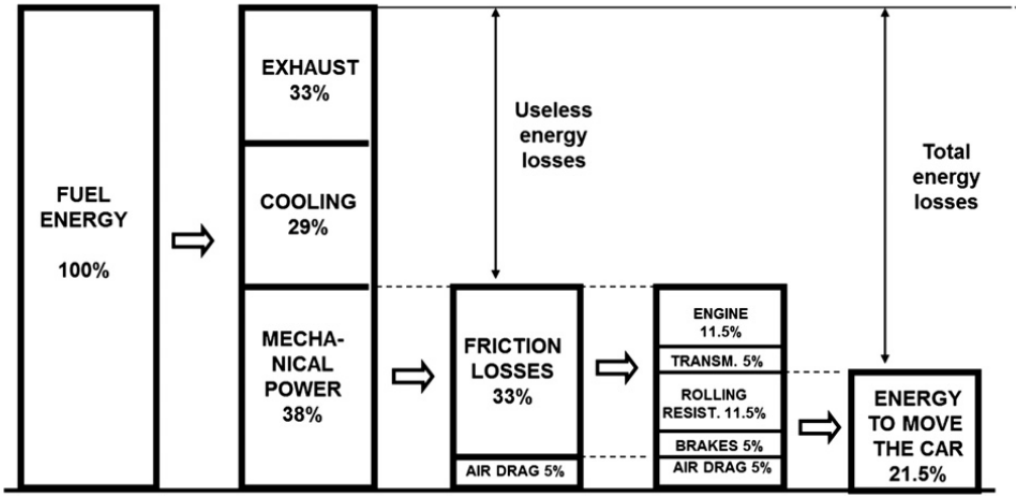


Figure 2: Pertes d'énergie dans une voiture particulière, selon [2]

En réponse aux problématiques environnementales et économiques, les constructeurs automobiles et les fournisseurs de lubrifiants développent ensemble de nouvelles technologies pour lutter contre le frottement et par conséquent, contre la pollution. Plusieurs avancées scientifiques ont été mises au point pour répondre à ces exigences drastiques : des revêtements de faible frottement et de faible usure ont été développés - tels que les revêtements Diamond-Like-Carbon (DLC) [3] - la topographie de surface et la texturation ont été améliorées et les lubrifiants revalorisés [2]. Holmberg *et al.* [2] mettent en évidence qu'une réduction de 10% des pertes par frottement entraîne une diminution de la consommation de carburant de 1.5%.

Une des options proposées pour minimiser les pertes d'énergie provenant du frottement dans les moteurs est de séparer le mieux possible les surfaces glissantes en contact par un film lubrifiant. Pour contrôler l'épaisseur de film entre ces surfaces, le facteur principal en jeu est la viscosité et de façon plus générale, le comportement rhéologique du lubrifiant. La viscosité peut être définie comme la capacité d'un fluide à résister au mouvement auquel il est soumis. Une viscosité élevée implique un film de lubrifiant plus épais et qui peut donc supporter des charges importantes. La clé pour ajuster la viscosité des huiles lubrifiantes est l'ajout de polymères, également appelés améliorants d'indice de viscosité (ou Viscosity Index Improvers (VII)). Ces derniers ont pour rôle d'augmenter la viscosité à haute température pour contrer la diminution de viscosité de l'huile de base sans l'augmenter significativement à basse température. En effet, à haute température, la viscosité doit être suffisamment importante pour maintenir une lubrification hydrodynamique acceptable et ainsi éviter le contact et l'usure des surfaces mais ne doit pas être trop élevée à faible température pour ne pas imposer un frottement visqueux trop important pendant la phase de démarrage du moteur. Holmberg *et al.* [2] affirment que la réduction de 25% de la viscosité du lubrifiant moteur à 100 °C équivaut à une économie de carburant de 0.6 à 5.5%, avec un coefficient de frottement minimum de 0.04.

Dans un moteur, le lubrifiant doit être multifonctionnel puisqu'il est seul à lubrifier les divers éléments mécaniques. Il subit des conditions sévères de température (de -70 °C à 290 °C), pression (supérieure à 1 GPa) et contrainte de cisaillement (supérieure à 1 MPa), entraînant des modifications de la viscosité. Si la température a tendance à diminuer la viscosité du lubrifiant, la pression, au contraire l'augmente considérablement. Les pressions subies par le fluide sont tellement grandes que les surfaces solides du moteur peuvent être déformées élastiquement. Il s'agit du régime de lubrification élastohydrodynamique (EHD) étudié depuis plus de 60 ans [4], [5], [6].

Développer des lubrifiants à haute valeur ajoutée subissant des conditions opératoires de plus en plus draconiennes et performants pendant une longue durée reste un défi considérable pour les fabricants d'huiles. Dans cette optique, de nombreuses études ont été menées pour optimiser la formulation des lubrifiants afin de minimiser le frottement et donc les émissions de gaz à effet de serre. Plusieurs étapes sont indispensables et notamment, le choix de l'huile de base, des polymères et des additifs fonctionnels, suivi de l'étude complète en laboratoire de la rhéologie à pression atmosphérique et autres propriétés physiques et chimiques. Ensuite, des tests tribologiques moteurs puis des essais dans une voiture en conditions réelles sont mis en place avant de commercialiser le produit fini. Il est évident que pour améliorer le processus de validation d'un lubrifiant, il faut établir des modèles rhéologiques précis pour prédire et contrôler la viscosité et guider le formulateur dans le choix de la composition des lubrifiants selon le cahier des charges du moteur. Les corrélations rhéologiques peuvent également être implémentées dans les modèles numériques hydrodynamiques et élastohydrodynamiques pour prévoir l'épaisseur de film et le frottement. Le but des recherches est de perfectionner le procédé de formulation en diminuant son temps, et donc son coût, en adaptant les caractéristiques des polymères et des huiles de base à la demande des concepteurs automobiles.

Les défis industriels présentés font partie d'un contexte multi-échelle : depuis l'échelle moléculaire à l'environnement, en passant par les contacts locaux, les pièces du moteur, la voiture et l'utilisateur qui veut augmenter les intervalles de vidange tout en diminuant sa consommation de carburant dans un souci d'économie budgétaire.

## *Objectifs et problématique de l'étude*

Parmi tous les challenges industriels développés ci-dessus, les différents objectifs de la thèse portent sur les premières étapes du procédé de formulation d'un lubrifiant : la sélection des composés chimiques et la caractérisation physico-chimique du fluide.

La première cible visée dans ce travail est l'observation des comportements rhéologiques et la prédiction de la viscosité en fonction de conditions réelles de température, pression et contrainte de cisaillement pour des solutions d'huile de base et polymère sans additifs fonctionnels. Plusieurs polymères de différentes masses moléculaires et conformations (peigne, linéaire et étoile) sont choisis.

Un deuxième défi réside dans la compréhension de la relation entre les mécanismes agissant à l'échelle moléculaire et la réponse rhéologique des lubrifiants automobiles.

Ensuite, l'étude se concentre sur l'analyse tribologique et la comparaison avec les modèles numériques.

Le but final est de relier les aspects moléculaires à l'efficacité énergétique.

La Figure 3 montre les différentes étapes de la démarche scientifique suivie au cours de la thèse.

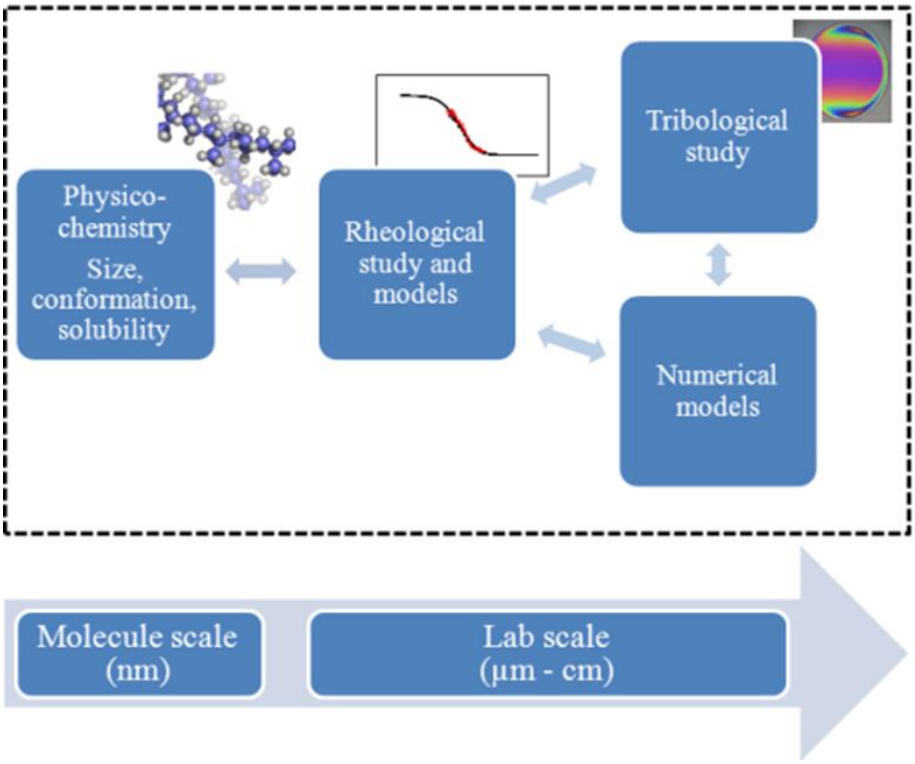


*Figure 3: Démarche multi-échelle de l'étude*

Une fois le contexte et les limites de l'étude fixés dans le chapitre introductif, le deuxième chapitre présente les notions nécessaires à la compréhension du rôle et des actions des améliorants d'indice de viscosité (ou Viscosity Index Improvers (VII)). Les différents régimes de lubrification, la rhéologie et la composition des lubrifiants, les bases théoriques de la physico-chimie des polymères en solution ainsi que les matériaux étudiés sont décrits. Le chapitre 0 fournit une étude détaillée du comportement rhéologique des mélanges d'huile de base et de polymère. Des modèles décrivant la variation de la viscosité en fonction de la température, de la pression et de la contrainte de cisaillement sont ajustés sur les résultats expérimentaux. L'originalité de la thèse réside dans l'utilisation de rhéomètres non-commerciaux à haute pression. La partie IV a pour but de connecter la rhéologie aux mécanismes présents à l'échelle moléculaire en explorant la notion de conformation et de rayon hydrodynamique par l'utilisation de la loi d'Einstein à haute pression. La relation structure-propriétés est mise en exergue dans ce chapitre. Le dernier chapitre démontre le lien entre rhéologie et tribologie et par extension, entre la composition chimique du lubrifiant et la tribologie. Les épaisseurs de film et coefficients de frottement sont mesurés et comparés avec les prédictions analytiques de Hamrock-Dowson [7] et avec les simulations numériques basées sur l'équation de Reynolds généralisée.

# Etat de l'art : lubrification, rhéologie et physico-chimie des polymères

Ce chapitre permet de rappeler quelques bases sur la lubrification - notamment sur les régimes de lubrification, la composition et le rôle d'un lubrifiant moteur - sur les modèles rhéologiques communément utilisés en lubrification moteur et enfin, sur la physico-chimie des solutions de polymères. Le chapitre II livre des éléments pour comprendre et prévoir le comportement des polymères et des solutions de polymères sous conditions de fonctionnement réel.

## *Lubrification moteur*

La diversité des pièces mécaniques et de leurs conditions d'utilisation implique une grande variété de lubrifiants : ils peuvent être solides (graphite, disulfure de molybdène, nitrure de bore…), liquides (eau, huiles végétales, émulsions…), pâteux (graisses, suspensions…) ou gazeux (air). Pour les moteurs, la lubrification est principalement assurée par un film fluide. Elle implique aussi la pluralité des régimes de lubrification. En effet, lorsque la vitesse de glissement entre deux surfaces est faible, la charge est principalement portée par le contact direct entre les aspérités de surface, ce qui entraîne des coefficients de frottement élevés : il s'agit du régime limite. La transition vers la lubrification mixte induit une séparation partielle entre les surfaces par un film de liquide très mince et une réduction du coefficient de frottement. Le minimum de ce dernier est atteint pour le régime élastohydrodynamique - pendant lequel les charges élevées supportées par le lubrifiant causent la déformation élastique des surfaces - avant d'atteindre la zone hydrodynamique à plus hautes vitesses et/ou plus faibles charges.

Les lubrifiants doivent répondre à plusieurs rôles critiques. Tout d'abord, ils doivent réduire les pertes d'énergie par frottement et empêcher l'usure des surfaces en contact en les séparant par un film fluide. Ils assurent l'équilibre thermique des moteurs ce qui limite aussi les phénomènes de corrosion. Ils nettoient les surfaces et enlèvent les contaminants tels que l'eau, les débris de métal issus de l'usure, les boues, la poussière… Les lubrifiants contribuent également à l'étanchéité, notamment dans la partie segment-piston-chemise.

La première fonction du lubrifiant est assurée par l'huile de base qui crée une couche de fluide séparant ainsi les surfaces en contact. Les huiles de base peuvent être minérales, synthétiques ou d'origine végétale. Les lubrifiants sont des fluides complexes constitués de 70 à 80% d'huile de base et de 20 à 30% d'additifs. Les additifs sont multiples : agents anti-usure, extrême pression, réducteur de frottement, détergents, dispersants, antioxydants, antirouille/anticorrosion, antimousse, abaisseur de point d'écoulement et améliorants d'indice de viscosité. Ces derniers se situent au cœur de la thèse. Leur utilisation dans les lubrifiants moteurs a pour but de réduire la dépendance en température de la viscosité, permettant un démarrage à froid satisfaisant et facilitant le fonctionnement du moteur à haute température. En effet, lorsque la température augmente, l'agitation moléculaire est amplifiée ainsi que la solubilité ; de fortes interactions sont créées entre le solvant et les chaînes de polymère et ces dernières gonflent. Le frottement intermoléculaire entre le solvant et le soluté entraîne l'augmentation de la viscosité du mélange. A basse température, la solubilité est moindre, les polymères se contractent et ressemblent à des globules. La viscosité de l'huile de base n'est que faiblement augmentée à basse température par l'ajout de VII.

## *Rhéologie des lubrifiants*

Comme évoqué précédemment, une des propriétés physiques principales d'un lubrifiant est sa viscosité. La rhéologie fait référence à l'étude de la déformation et de l'écoulement de matériaux. La viscosité mesure la résistance d'un gaz, d'un liquide ou d'un solide à la déformation par cisaillement. La rhéologie des lubrifiants concerne la relation entre la viscosité, le taux de cisaillement ou contrainte de cisaillement, la température et la pression et leurs influences combinées.

Dans le cas où la contrainte de cisaillement ($\tau$) est proportionnelle au taux de cisaillement ($\dot{\gamma}$) avec la viscosité comme coefficient de proportionnalité ($\eta$), le matériau est dit Newtonien et répond à l'équation suivante :

$$\tau = \eta\dot{\gamma} \qquad (1)$$

Cependant, les lubrifiants sont connus pour être des fluides rhéo-fluidifiants. Barnes *et al.* [8], Macosko [9] et Glass *et al.* [10] signalent que la contrainte de cisaillement induit une distorsion et un alignement des macromolécules, ce qui diminue la viscosité du fluide comme présenté sur la Figure 4. Lorsque la contrainte de cisaillement est nulle ou faible, les chaînes de polymère restent dans leur état initial, la viscosité n'est pas affectée et elle est appelée « 1$^{er}$ plateau Newtonien ». L'étirement des polymères dans l'écoulement conduit à une chute de viscosité. Si la contrainte de cisaillement n'est pas trop élevée et les molécules flexibles, ce phénomène est temporaire et les chaînes retrouvent la forme qu'elles avaient à contrainte nulle. Au contraire, si la contrainte de cisaillement est suffisamment élevée et les molécules de polymères peu résistantes, la déformation des macromolécules peut entraîner leur dégradation. A cause de cette rupture, la viscosité diminue de façon irréversible et ne retrouve plus sa valeur initiale. Dans les deux cas, à forte contrainte de cisaillement, la viscosité atteint une valeur stable et cet état est nommé « second plateau Newtonien ».

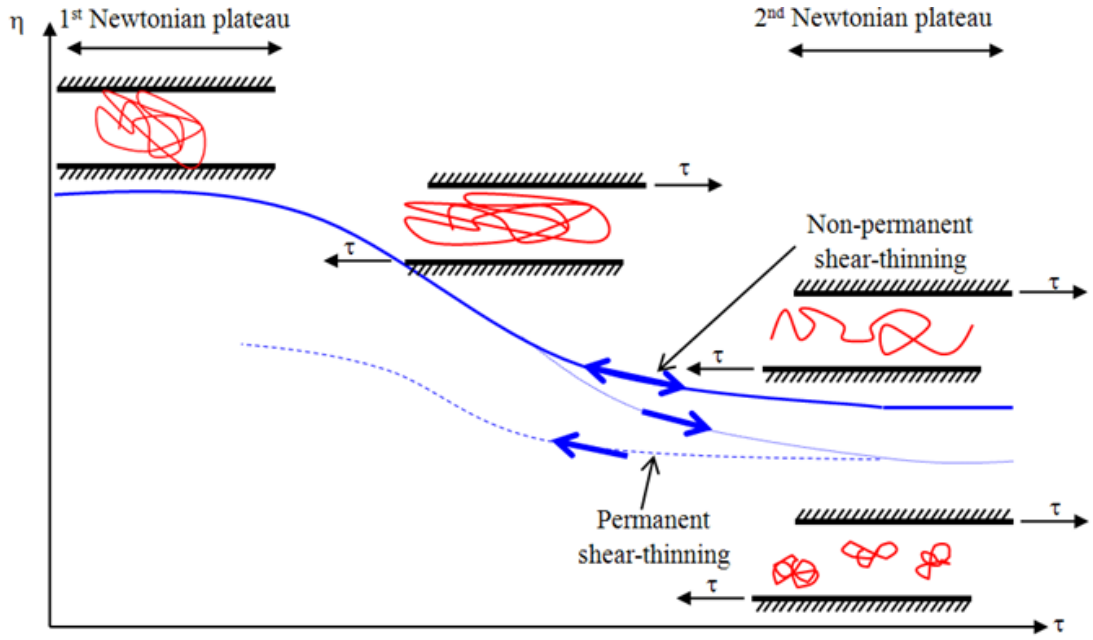


*Figure 4: Comportement rhéo-fluidifiant des lubrifiants*

La viscosité des lubrifiants dépend non seulement de la contrainte de cisaillement mais aussi fortement de la température et de la pression. De nombreux modèles rhéologiques sont utilisés pour décrire ces dépendances individuellement ou simultanément. Ne sont présentés dans le résumé étendu que les modèles utilisés dans le chapitre 0.

La loi de Vogel, Tammann et Fulcher (VTF) [11] décrit la dépendance en température de la viscosité:

$$\text{VTF} \qquad \eta_0\ T\ = \eta_\infty \exp\left[\frac{D_F T_\infty}{T - T_\infty}\right] \qquad (2)$$

où $D_F$ est le paramètre de fragilité, $\eta_\infty$ est la viscosité extrapolée à la température infinie et $T_\infty$, la température de Vogel pour laquelle la viscosité diverge.

La dépendance de la viscosité en température et pression suit l'équation suivante [**12**] :

$$\text{WLF-Yasutomi modifié} \qquad \eta_0(T,p) = \eta_g.\exp\left[\ln(10)\frac{-C_1(T - T_g(p))F(p)}{C_2 + (T - T_g(p))F(p)}\right] \qquad (3)$$
$$T_g(p) = T_g(0) + A_1 \ln(1 + A_2 p)$$
$$F(p) = (1 + B_1 p)^{B_2}$$

où $T_g(p)$ est la température de transition vitreuse à la pression $p$, $F$ est l'expansion thermique relative du volume libre, adimensionnée, $\eta_g$ est la viscosité à la transition vitreuse et $C_1$, $C_2$, $A_1$, $A_2$, $B_1$, $B_2$ sont les constantes numériques du modèle pour un fluide donné.

Enfin, Bair [13] a écrit l'équation généralisée issue de Carreau-Yasuda [14] décrivant la relation entre la viscosité et la contrainte de cisaillement :

$$\eta\ \tau\ = \eta_2 + \frac{\eta_0 - \eta_2}{\left(1 + \left(\frac{\tau}{G}\right)^a\right)^{\frac{\frac{1}{n}-1}{a}}} \qquad (4)$$

où $\eta_0$ est la viscosité du premier plateau Newtonien, $\eta_2$ celle du deuxième plateau newtonien, $G$ le module de cisaillement apparent, $n$ l'exposant de la loi puissance et $a$ un paramètre influant principalement sur la pente du comportement rhéo-fluidifiant.

Plusieurs rhéomètres ont été utilisés pour étudier le comportement des fluides sous différentes sollicitations, en particulier, un viscosimètre haute pression à chute de corps (noté HP-Visco) et un rhéomètre de Couette développés par Dr. Scott Bair du Georgia Institute of Technology. Leur spécificité réside dans leur fonctionnement à haute pression : 800 MPa pour le premier et 500 MPa pour le second.

## *Physico-chimie des polymères et des solutions de polymères*

Cette partie explique certaines notions nécessaires pour la compréhension des phénomènes décrits dans les chapitres IV et V. Divers propriétés physico-chimiques caractérisent les polymères et solutions de polymères, notamment leur masse moléculaire, leur conformation, leur taille, leur concentration, leur solubilité dans l'huile de base… Une des notions les plus étudiées dans la thèse reste la taille des macromolécules. Leur rayon hydrodynamique est déterminé à partir des mesures de viscosité à haute pression grâce, entre autres, à la loi d'Einstein appliquée pour un milieu dilué avec des polymères considérés comme des sphères dures [15] :

$$\eta_{solution} = \eta_{solvant}(1+2,5\phi) \qquad (5)$$

et $$\phi = \frac{c}{M}\frac{4}{3}\pi R_h^3 \qquad (6)$$

où $\Phi$ est la fraction de volume occupée par les sphères, $c$ la concentration and $M$ la masse moléculaire d'une molécule ($M=M_w/N_a$).

Toute l'investigation expérimentale décrite précédemment et l'exploration à l'échelle moléculaire sont effectuées sur plusieurs fluides décrits dans la section suivante.

## *Lubrifiants simplifiés*

Dans cette étude, des mélanges d'huile et de polymères (de concentration 1.2% en masse) sont considérés pour simplifier la réflexion sur les lubrifiants automobiles complexes. L'huile de base est une huile minérale hydrocraquée de groupe III (selon la classification API). Trois polymères de conformation, chimie et structure différentes sont choisis : un poly (alkylméthacrylate) de type peigne (PAMA), un copolymère d'oléfine linéaire (OCP) et un poly(isoprène-styrène-hydrogéné) étoile (PISH) avec un cœur styrène. Un quatrième polymère - polyisobutylène (PIB) - a été utilisé dans l'huile de base en tant que mélange modèle pour étudier l'effet de la LCST (Lower Critical Solution Temperature) sur la rhéologie. Les caractéristiques des polymères sont réunies dans le Tableau 1.

| | **PAMA** | **OCP** | **PISH** | **PIB** |
|---|---|---|---|---|
| **Formule chimique** | 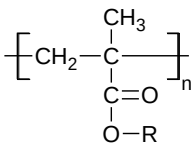 R=$C_{12}$ à $C_{17}$ Polaire | 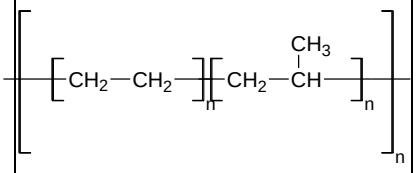 40% éthylène-60% propylène (en masse) | 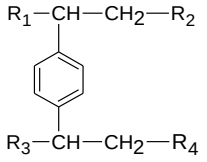 $R_1$,$R_2$,$R_3$,$R_4$= copolymères diène/styrène/diène (hydrogéné) | 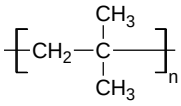 |
| **Structure moléculaire** |  Peigne |  Linéaire | 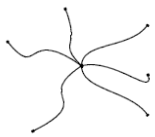 Etoile | |
| **$M_w$ (g/mol)** | 400 000 | 88 420 | 413 500 | 62 300 |
| **PDI** | ≈ 2 | 1.6 | 1.1 | 1.4 |

*Tableau 1: Caractéristiques des polymères*

## Expérimentations et modèles rhéologiques

L'établissement de modèles rhéologiques complets pour des mélanges huile de base-polymère à haute température, haute pression et haute contrainte de cisaillement est de la plus haute importance pour guider les fabricants de lubrifiants dans le choix des améliorants d'indice de viscosité correspondant aux exigences des constructeurs automobiles.

Ce chapitre est dédié à l'étude expérimentale et à la modélisation du comportement rhéologique des solutions diluées de polymères dans l'huile de base pour une large gamme de conditions expérimentales représentatives de celles rencontrées dans les moteurs.

### *Comportement rhéologique à pression atmosphérique*

La dépendance de la viscosité à basse contrainte de cisaillement et à pression atmosphérique en fonction de la température est obtenue à partir du rhéomètre de Couette Anton-Paar et est tracée sur la Figure 5 pour l'huile de base et la solution de PAMA. La viscosité diminue considérablement en fonction de la température. En effet, à mesure que la température augmente, le volume de la solution augmente (d'environ 7%), principalement à cause de l'expansion du solvant et par conséquent, le nombre de collisions potentielles entre les molécules de polymère diminue. Le transfert de moment d'une couche de fluide à l'autre chute et la viscosité s'affaisse [16]. La viscosité de la solution de PAMA diminue moins que celle de l'huile de base en fonction de la température. Le PAMA remplit donc bien son rôle d'améliorant d'indice de viscosité.

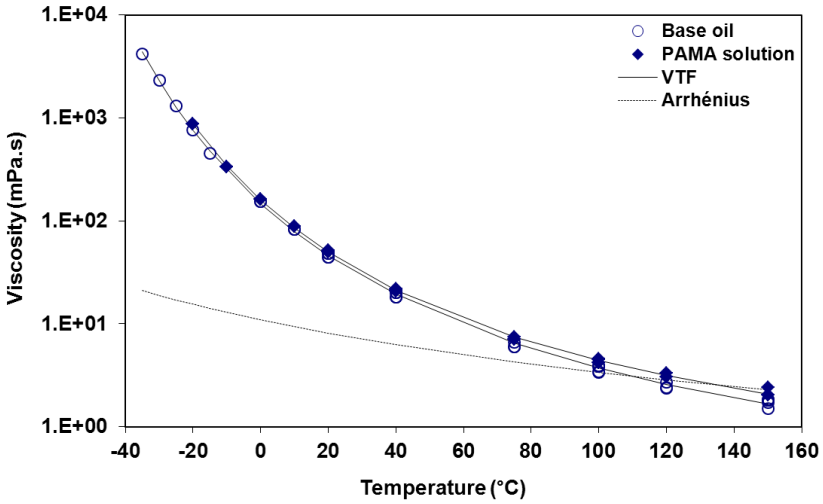


*Figure 5: Viscosité de l'huile de base et de la solution de PAMA à différentes températures modélisée par l'équation VTF*

La viscosité est modélisée par la loi de Vogel-Tamman et Fulcher (VTF) [11] (Equation (2), p. 24) décrite au chapitre précédent. Ce modèle est tout à fait adapté car il représente très bien le comportement visqueux de l'huile de base et des 3 mélanges de polymère. Cette première étape permet d'extraire la température de transition vitreuse à pression atmosphérique $T_g(0)$ nécessaire dans le modèle WLF-Yasutomi modifié utilisé dans le paragraphe suivant. Cette température est déterminée en considérant qu'il s'agit de la température lorsque la viscosité du fluide vaut $\eta_g=10^{12}$ mPa.s, viscosité des lubrifiants à la température de transition vitreuse, par convention [13].

### *Réponse rhéologique à haute pression*

Une série de tests a été effectuée avec le viscosimètre à chute de corps haute pression à cinq isothermes, de 40 à 150 °C et à plusieurs pressions. La courbe pour la solution de PAMA est tracée en Figure 6, l'allure des courbes pour les autres mélanges sont très proches. De 0.1 MPa à 800 MPa, la viscosité augmente de 2 à 3 ordres de grandeur. Des considérations sur la compressibilité peuvent expliquer qualitativement cette observation. En effet, lorsque la pression augmente, le volume du fluide diminue (d'environ 25-30%), ce qui entraîne un rapprochement entre les molécules de solvant et de polymères. Si le fluide est en mouvement, les forces de frottement entre les couches laminaires augmentent et ainsi la viscosité également.

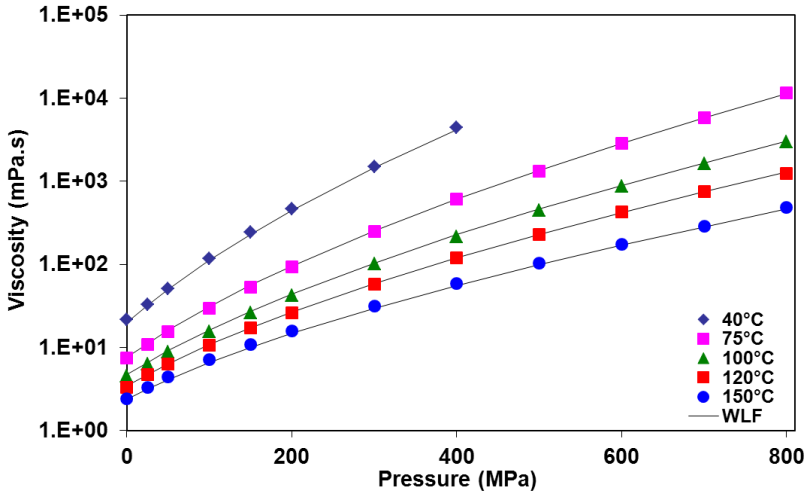


*Figure 6: Comportement piézo-visqueux de la solution de PAMA à plusieurs températures*

Les points expérimentaux sont corrélés avec l'équation WLF-Yasutomi modifié (Equation (3), p. 24). Le modèle est en bon accord avec l'expérience et est vérifié pour les autres mélanges.

L'effet de la contrainte de cisaillement sur les différentes solutions est étudié à pression élevée (200 à 400 MPa) grâce au rhéomètre de Couette haute pression à 25.9 et 40.5 °C. Les comportements rhéologiques de l'huile de base et des trois mélanges de polymères sont présentés sur la Figure 7 et modélisés par un modèle Newtonien ou par la relation de Carreau-Yasuda généralisée par Bair [13] (Equation (4), p. 24).

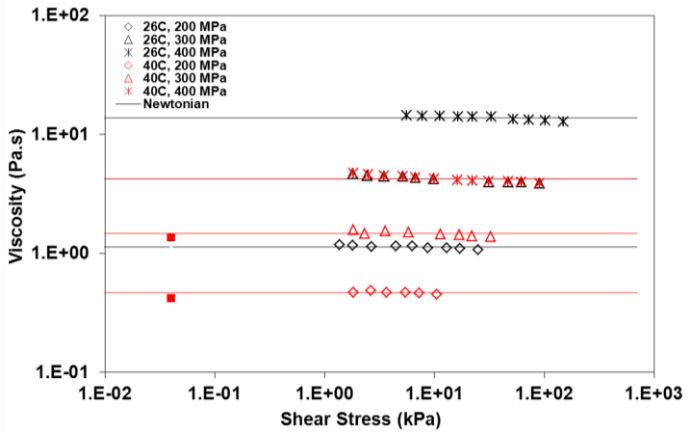


Huile de base

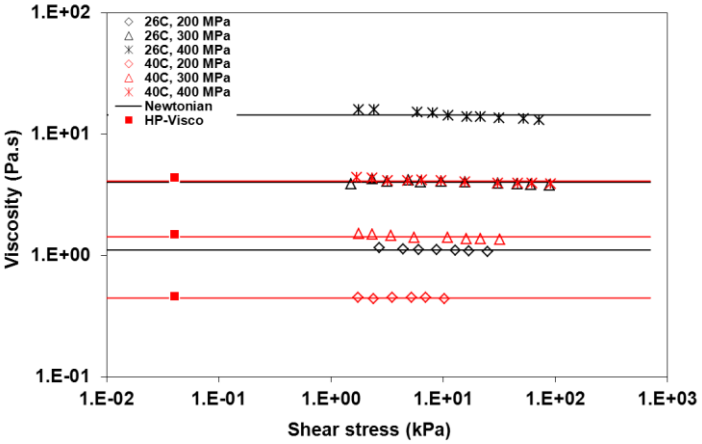


Solution de PAMA

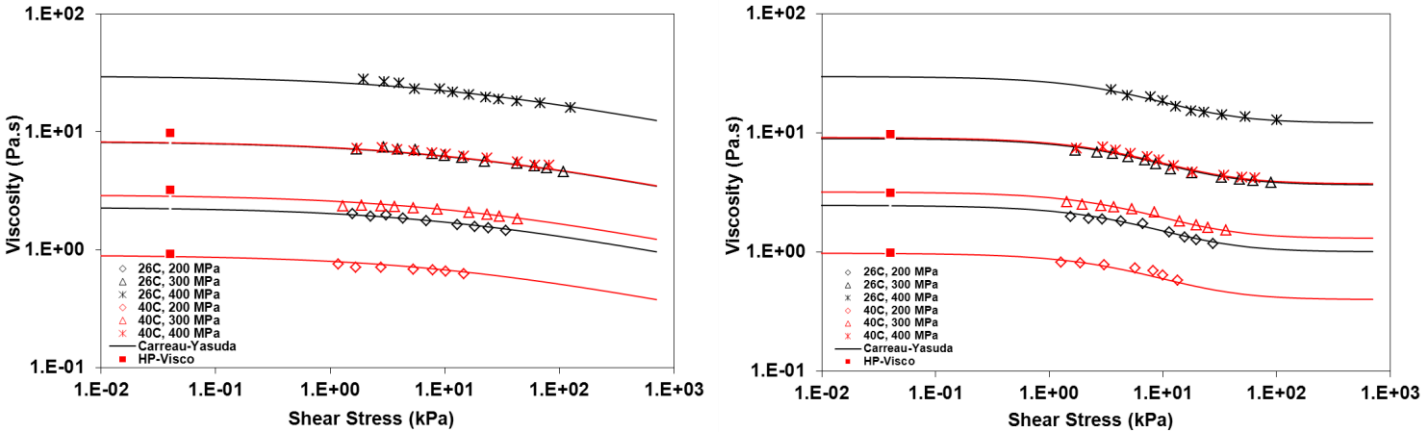


Solution d'OCP Solution de PISH

*Figure 7: Comportement rhéologique de l'huile de base et des solutions de polymère à plusieurs températures et pressions*

Les points correspondants aux viscosités à basse contrainte de cisaillement mesurées sur le viscosimètre haute pression (HP-Visco) sont reportés sur les courbes d'écoulement. Ces points montrent la cohérence des mesures entre les deux appareils et entre les deux modèles.

L'huile de base et la solution de PAMA se comportent comme des fluides Newtoniens alors que le mélange d'OCP et de PISH sont rhéo-fluidifiants, le PISH l'étant plus fortement. La chute de viscosité dans le cas de l'OCP est de 20 à 45% alors que celle correspondant à la solution de PISH est comprise entre 30 et 50%.

Pour conclure, la dépendance de la viscosité avec la température et la pression est précisément caractérisée pour tous les fluides. Ensuite, l'effet de la contrainte de cisaillement sur leur viscosité est étudié et modélisé avec un ou deux plateaux Newtoniens.

Pour chaque fluide, il est maintenant possible de prédire précisément son comportement rhéologique dans un contact en connaissant la température, la pression et la contrainte de cisaillement. Ceci est utile pour orienter les formulateurs dans le choix des composants d'un lubrifiant en fonction des applications et des conditions fixées par les constructeurs automobiles.

La partie suivante vise à comprendre les différents comportements rhéologiques en considérant l'échelle microscopique.

## Relation entre la rhéologie et l'échelle moléculaire

Afin de comprendre pleinement la réponse rhéologique des solutions de polymère sous conditions de fonctionnement telles que celles rencontrées dans un moteur, il est nécessaire d'explorer les mécanismes survenant à l'échelle moléculaire. En outre, la relation entre la physico-chimie des molécules et la rhéologie est importante pour interpréter le comportement du PAMA, dont la réponse Newtonienne est inattendue comparée aux lubrifiants automobiles ([8], [9] et [10]).

Ce quatrième chapitre discute le possible rôle joué par la concentration des polymères, l'ajout d'additifs fonctionnels, la LCST (Lower Critical Solution Temperature) et finalement, par la conformation et la taille des polymères dans l'huile de base minérale.

### *Concentration*

Tout d'abord, le pourcentage de polymère dans l'huile de base peut être mis en question pour expliquer le comportement rhéologique des solutions étudiées. En effet, si la concentration de la solution est au-dessus d'un certain seuil, les concepts physiques qui gouvernent l'écoulement sont différents de ceux appliqués en dessous de cette concentration. Au-dessus de la concentration critique $c^*$, les polymères commencent à se chevaucher et à s'enchevêtrer ce qui modifie l'écoulement. La concentration critique de chaque polymère est déterminée dans les deux cas extrêmes de « thêta solvant » et « bon solvant ». Pour chaque fluide, la concentration de polymère choisie de 1.2% en masse - représentative de la concentration dans les lubrifiants automobiles - est en dessous de la concentration critique $c^*$. L'étude a donc bien lieu en milieu dilué et l'hypothèse de concentration peut être exclue pour expliquer les différences de comportements rhéologiques.

### *Rôle éventuel des additifs*

En second lieu, le possible rôle des additifs (autres que les VII) doit être analysé puisque les lubrifiants entièrement formulés sont supposés montrer un comportement non-Newtonien alors que la solution de PAMA n'en montre pas. L'absence de paquet d'additif peut être mise en cause dans le comportement Newtonien observé dans le cas du PAMA. Des expériences supplémentaires ont été effectuées sur le rhéomètre de Couette haute pression avec un paquet d'additifs ajouté aux solutions de polymère. D'une part, le paquet d'additifs augmente la viscosité des solutions d'un facteur 1.4. D'autre part, les additifs n'affectent pas l'amplitude de la chute de viscosité en fonction de la contrainte de cisaillement. Par conséquent, le comportement rhéo-fluidifiant attendu pour les lubrifiants commercialisés ne peut pas être attribué, dans ce travail, aux additifs fonctionnalisant mais seulement aux améliorants d'indice de viscosité.

### *LCST*

La LCST est suspectée de jouer un rôle dans l'absence de comportement non-Newtonien pour la solution de PAMA. En effet, en approchant la LCST ou au-dessus de cette température, les chaînes de polymère ne sont plus solubles dans le solvant, le polymère ne peut plus épaissir l'huile de base et les propriétés rhéologiques peuvent être altérées. Deux mélanges modèles dont les LCST sont bien connues dans la littérature ont été retenus pour étudier la présence ou non de LCST dans les conditions de température et de pression étudiées. Finalement, que la LCST soit dans le domaine expérimental ou en dehors, aucune preuve de variation ou de discontinuité n'est détectée. La LCST n'a donc pas d'influence directe sur la rhéologie des solutions. Comme aucune discontinuité n'est observée sur les courbes obtenues avec solutions de polymères qui font l'objet de ce travail, nous pouvons en conclure que l'hypothèse de la LCST est écartée.

## *Conformation et taille*

Enfin, la chimie des polymères, leur conformation, leur masse moléculaire et leur solubilité doivent être étudiées pour appréhender les réponses rhéologiques précédemment examinées.

La loi d'Einstein - reliant la viscosité de la solution de polymère, la viscosité du solvant et le rayon hydrodynamique du polymère - est utilisée à différentes températures et à haute pression pour déterminer les rayons hydrodynamiques, $R_h$, à partir des mesures issues du viscosimètre à chute de corps. Les variations des $R_h$ en fonction de la température et de la pression sont tracées sur la Figure 8. Ils sont compris entre 7 et 14 nm, 10 et 12 nm et 17 et 20 nm dans la fenêtre expérimentale pour le PAMA, l'OCP et le PISH respectivement.

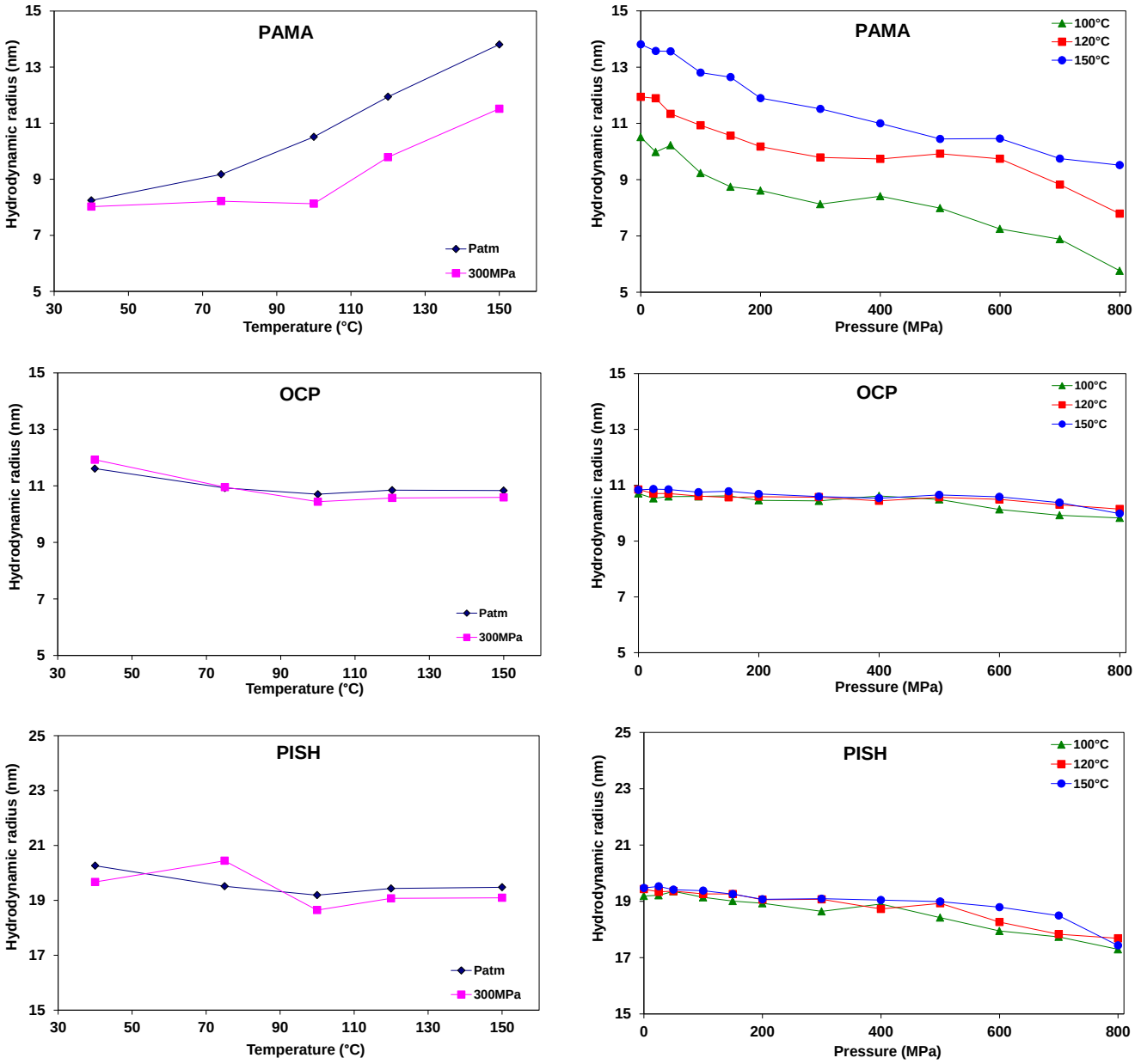


*Figure 8: Variation du rayon hydrodynamique $R_h$ (déduit de la loi d'Einstein) en fonction de la température (gauche) et de la pression (droite) pour les 3 solutions de polymère*

Le rayon hydrodynamique du PAMA augmente de 65% en fonction de la température. En effet, lorsque la température augmente, l'agitation thermique aussi et le volume libre des molécules de solvant accroît. Ainsi, les interactions entre les chaînes de polymère et le solvant augmentent et par conséquent, le polymère gonfle. La température agit sur la solubilité entre l'huile de base et le polymère. Au contraire, pour l'OCP et le PISH, le $R_h$ reste quasi-constant (avec une légère diminution) en fonction de la température. Puisque l'OCP est apolaire dans un solvant apolaire, il se trouve déjà en configuration de bon solvant, les pelotes sont déjà déployées et donc la température a très peu d'effet sur son $R_h$. Pour le PISH, l'encombrement stérique lié aux longues branches de l'étoile empêche les molécules de solvant de solubiliser la molécule.

En ce qui concerne l'influence de la pression, le $R_h$ du PAMA diminue de 30 à 45% alors que celui de l'OCP et du PISH reste quasiment constant (avec une légère chute). Dans le cas du PAMA, l'élévation de pression implique l'augmentation de la densité du solvant, il est donc plus difficile pour le polymère de s'entourer de molécules de solvant ce qui explique la contraction du PAMA avec la pression. La pression a également un effet sur la solubilité entre l'huile de base et le polymère. La pression n'agit pas sur l'OCP et le PISH car l'OCP est plutôt en configuration de bon solvant et les interactions sont trop nombreuses pour être altérées par l'influence de la pression. De plus, l'encombrement stérique du PISH est si important que les branches de l'étoile ne peuvent s'affaisser.

Le rayon hydrodynamique a été déterminé à pression atmosphérique par deux méthodes complémentaires - la viscosité intrinsèque et des mesures directes (chromatographie d'exclusion stérique triple détection et diffusion dynamique de la lumière) - pour confirmer les résultats obtenus avec la loi d'Einstein. Le Tableau 2 reporte les rayons hydrodynamiques des quatre polymères établis par les différentes méthodologies.

| | $R_h$ (nm) | PAMA | OCP | PISH | PIB* |
|---|---|---|---|---|---|
| Déduit | **Loi d'Einstein**<br>(huile de base, heptane pour PIB)<br>100 - 150 °C | 10.5 - 13.8 | 10.7 - 10.8 | 19.2 - 19.5 | 6.9 - 7.0<br>(A 25 MPa) |
| | **Viscosité intrinsèque**<br>(huile de base)<br>40 - 150 °C | 9.7 - 14.7 | 12.3 - 11.3 | 21.1 - 19.6 | - |
| | Equations de **Flory**<br>($R_h$=$R_g$ / 0.77)<br>solvant thêta<br>bon solvant | <br><br>13.7<br>(30.6) | <br><br>7.5<br>17.8 | <br><br>18.1<br>(46.6) | <br><br>7.1<br>15.4 |
| Measure<br>Direct e | **SEC triple détection**<br>(THF)<br>20 °C | - | 14.5 | 21 | 9 |
| | **Diffusion dynamique de la lumière**<br>(heptane)<br>20 °C | - | 12.3* | 22.5* | 7 |

*Tableau 2: Rayon hydrodynamique à partir de plusieurs méthodologies à pression atmosphérique*
** Polymère solide, non préalablement dilué*
*( ) hypothèse de bon solvant non validée a posteriori*

Lorsque les considérations moléculaires sont mises en parallèle des observations rhéologiques, plusieurs phénomènes peuvent être déduits.

Pour des tailles de polymères comparables (proches de 10 nm), le PAMA et l'OCP présentent des comportements rhéologiques très différents. Le comportement quasi-Newtonien du PAMA peut être attribué à sa conformation liée à sa solubilité. En effet, de nombreuses interactions (hydrogène et Van der Waals) existent entre les branches du peigne, impliquant une flexibilité moindre que celle de l'OCP linéaire. Les chaînes de PAMA s'étirent donc moins que celles de l'OCP sous contrainte de cisaillement. En termes de rhéologie, la viscosité de la solution contenant du PAMA diminue donc moins que celle de l'OCP.

En comparant deux polymères d'encombrement stérique proche - le PAMA et le PISH - on remarque qu'ils ont des $R_h$ (10 et 20 nm respectivement) et des comportements rhéologiques bien différents. Dans ce cas, la chute de viscosité peut être assignée à la taille du polymère. A conformation similaire, plus le $R_h$ du polymère est élevé, plus le cisaillement aura d'effet sur l'alignement des chaînes de polymère et donc sur la chute de viscosité.

Même si la conformation étoile est moins déformable que la conformation linéaire, la rhéo-fluidification est plus importante pour le PISH que pour l'OCP. En effet, le PISH est deux fois plus gros que l'OCP. L'effet de taille l'emporte donc sur la conformation dans ce cas.

En conclusion, ce chapitre montre l'étroite relation entre la rhéologie et la physico-chimie des polymères. Plusieurs comportements rhéologiques ont été mis en évidence selon la chimie et la conformation des polymères.

Plusieurs hypothèses telles que la concentration, l'effet des additifs fonctionnels et la LCST ont été réfutées pour justifier la réponse Newtonienne inattendue de la solution de PAMA.

La notion de rayon hydrodynamique reste la raison avancée la plus plausible pour expliquer les différentes rhéologies des solutions. Il a été déterminé grâce à la loi d'Einstein à haute pression et a été comparé avec d'autres méthodes à pression atmosphérique. Toutes les méthodes convergent vers des valeurs cohérentes. Le $R_h$ du PAMA augmente en fonction de la température et diminue en fonction de la pression alors que la température et la pression n'ont presqu'aucune influence sur le $R_h$ de l'OCP et du PISH.

L'effet de la contrainte de cisaillement sur le $R_h$ a été étudié. A $R_h$ équivalent, l'OCP linéaire s'étire plus facilement que le PAMA peigne à cause de leur différence de conformation. De plus, à conformation similaire, la taille du polymère devient le paramètre déterminant dans l'alignement des chaînes de polymères. A conformation et taille différentes, l'effet de taille prévaut sur l'effet de conformation.

Cette section montre comment le comportement rhéologique des solutions de polymère, important dans l'industrie automobile, peut être rationnalisé sur une base de taille hydrodynamique et de conformation moléculaire dans le cas de trois polymères particuliers.

## De la rhéologie à la tribologie

Un moteur est un organe complexe avec des éléments tribologiques subissant l'ensemble des régimes de lubrification. Une étude multi-échelle vise à optimiser le procédé de formulation et à prévoir le comportement tribologique sous conditions de fonctionnement extrêmes une fois que la composition physico-chimique est connue. L'objectif de ce chapitre concerne l'exploration tribologique complète des solutions de polymère. Les épaisseurs de film ainsi que les coefficients de frottement sont mesurés et comparés avec des modèles analytiques et numériques. Cette section présente aussi la relation entre la rhéologie et la tribologie et, par extension, entre la tribologie et la physico-chimie des polymères.

### *Epaisseur de film*

Le régime élastohydrodynamique est reproduit sur l'appareil JEROTRIB (cf. Appendix G) avec la configuration bille/disque. Le contact EHD est créé entre la bille en acier 100C6 et le disque en verre BK7 revêtu d'une couche de chrome semi-réfléchissante. Le principe de la mesure d'épaisseur de film, développé par Molimard [17], [18] et récemment plus détaillé par Doki-Thonon [19], est basé sur l'interférométrie optique en lumière blanche. Un exemple d'interférogramme est présenté sur la Figure 9 pour l'huile de base, à 25 °C, à la vitesse d'entraînement de 1.72 m/s et en roulement pur (où le ratio glissement-roulement *SRR* est nul). L'épaisseur centrale $h_c$ et minimale $h_{min}$ sont issues du traitement de ces images.

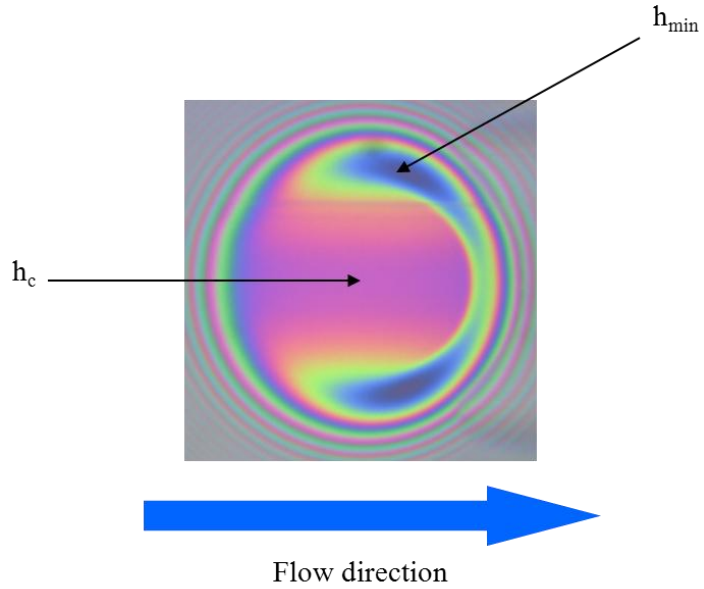


*Figure 9: Interférogramme en lumière banche (Huile de base, 25 °C, 27 N, $U_e$=1.72 m/s, SRR=0)*

Les interférogrammes sont obtenus pour l'huile de base et les trois solutions de polymère pour différentes conditions de température et vitesse. Les courbes d'épaisseur de film peuvent donc être tracées en fonction de la vitesse d'entraînement et comparées aux modèles analytiques de Hamrock-Dowson [7], Moes [20] et Moes Chevalier [21]. A 25 et 75 °C, les courbes obtenues pour l'huile de base et le PAMA sont très proches des modèles, ce qui confirme le comportement Newtonien observé en rhéologie. Au contraire, dans les cas de l'OCP et du PISH, les points expérimentaux sont éloignés

des modèles analytiques tout en restant parallèles, ce qui signifie que les fluides seraient rhéo-fluidifiants et qu'aucun phénomène d'échauffement visqueux n'interviendrait.

Les épaisseurs de films ont également été comparées à des modèles numériques. Le modèle développé par Habchi [22] et Doki-Thonon [19] est basé sur une approche par éléments finis et résout des problèmes de lubrification élastohydrodynamique. Cette méthode s'applique pour des contacts circulaires EHD tridimensionnels, non-Newtoniens, stationnaires et thermiques. Elle est fondée sur la résolution simultanée d'équations parmi lesquelles on trouve l'équation de Reynolds généralisée, la compressibilité et la piézo-viscosité du lubrifiant, les équations de déformation sur un solide équivalent, l'équation d'épaisseur de film et la relation d'équilibre de la charge. Des équations supplémentaires peuvent être introduites pour simuler les effets liés à la température.

Les épaisseurs centrale et minimale sont très bien prédites par ce modèle numérique pour tous les fluides. Un modèle isotherme Newtonien est utilisé pour décrire le comportement de l'huile de base et de la solution de PAMA alors que pour les deux autres fluides, un modèle isotherme non-Newtonien (issu des résultats du chapitre 0) est implémenté. La comparaison entre les cas Newtonien et non-Newtonien est présentée sur la Figure 10 dans le cas de la solution de PISH à 25 °C.

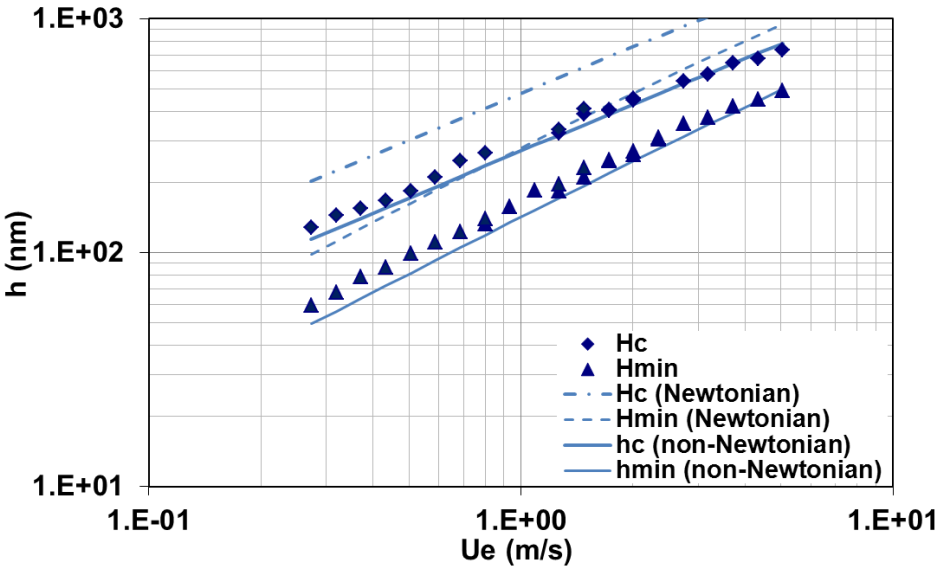


*Figure 10: Epaisseur de film centrale et minimale, expérimentale et numérique pour la solution de PISH à 25 °C, 27 N, SRR=0 dans le cas d'un fluide Newtonien et non-Newtonien*

Ce graphique montre le très bon accord entre l'expérimental et le modèle non-Newtonien dans le cas du PISH. Il montre aussi l'intérêt et la nécessité de connaître précisément le comportement rhéologique des fluides pour une meilleure prédiction des épaisseurs de film. Les simulations pour les autres fluides sont également en bon accord avec l'expérience.

## *Coefficient de frottement*

Pour une étude tribologique complète, l'exploration des coefficients de frottement (ou de traction) est indispensable. Les coefficients de traction sont mesurés sur l'appareil JEROTRIB avec un disque en acier. Différentes charges, vitesses et taux de glissement-roulement (*SRR*) ont été testés. La Figure 11 montre la comparaison entre les coefficients de traction de l'huile de base et des solutions de polymère.

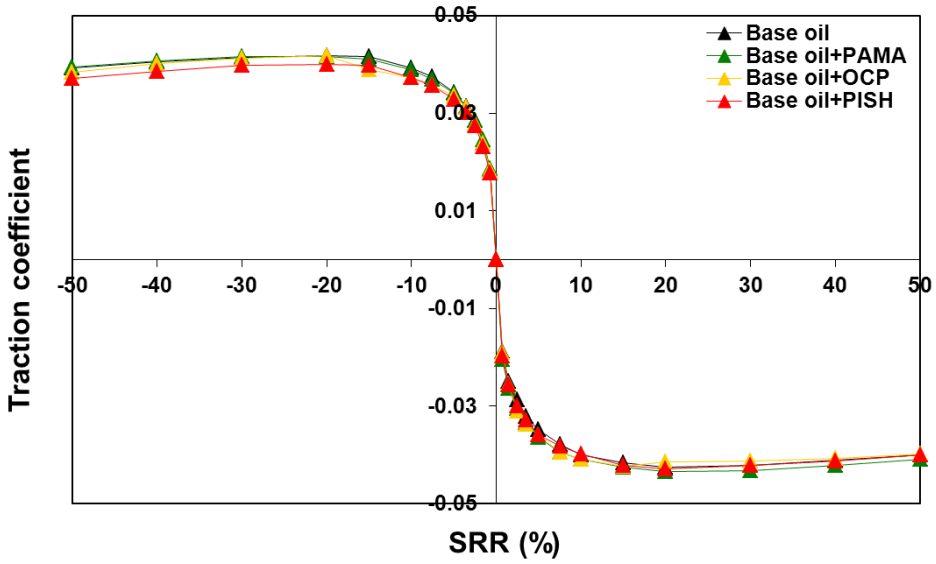


*Figure 11: Coefficients de traction pour toutes les solutions à 25 °C, 2.5 m/s et 64 N (1 GPa)*

Il n'y a pas de discrimination claire entre les fluides pour le frottement. D'autres conditions ont été examinées, conduisant à la même observation. Il est donc difficile de tirer des conclusions sur le rôle des polymères sur le coefficient de frottement. Nous pouvons simplement affirmer que ce dernier est totalement gouverné par les propriétés de l'huile de base.

Dans ce chapitre, les comportements tribologiques de l'huile de base et des mélanges de polymère dans un contact EHD circulaire en roulement-glissement ont été étudiés.

Les résultats issus de modèles numériques avancés ont montré un excellent accord avec les épaisseurs de film expérimentales. La nécessité de bien connaître les modèles rhéologiques pour la prédiction des épaisseurs de film a été soulignée. La rhéologie est donc très intimement liée à la tribologie. Par extension, la tribologie est corrélée aux propriétés physico-chimiques des lubrifiants. Cette conclusion est importante pour les formulateurs car ils peuvent ainsi sélectionner les composés chimiques du lubrifiant en fonction de la performance tribologique désirée.

Les coefficients de traction ont été fournis mais ne montrent pas de discrimination claire entre les différentes solutions. Dans les conditions de l'étude, le frottement est régi par l'huile de base. Des modèles numériques ont été utilisés pour prédire le coefficient de traction dans les conditions expérimentales de l'étude, en prenant en compte les effets non-Newtonien et thermique, mais la contrainte est trop forte dans le contact pour obtenir un bon accord avec l'expérience.

## Conclusion générale et recommandations

Cette thèse vise à comprendre les rôles et fonctions joués par les améliorants d'indice de viscosité dans la formulation des lubrifiants moteurs. Une étude multi-échelle a été adoptée : depuis la physico-chimie à la tribologie, en passant par la rhéologie.

Tout d'abord, la revue bibliographique initiale de l'impact du frottement sur l'environnement nous a fait prendre conscience de l'importance d'une réflexion sur la lubrification. A cause des pressions législatives sur la limitation des rejets de gaz à effet de serre et à cause d'une volonté de vivre sur une planète plus saine, l'étude des lubrifiants est devenue un sujet de première importance. Une des motivations industrielles est l'optimisation du procédé de formulation, conduisant à un gain de temps et d'argent pour le formulateur. La bonne connaissance de la relation entre la physico-chimie, la rhéologie et la tribologie permet l'amélioration du procédé en évitant les tests moteurs systématiques. Le principal objectif de la thèse était de comparer les réponses rhéologiques et tribologiques d'une huile de base minérale hydrocraquée et de solutions de polymères de différentes natures.

L'utilisation d'une formulation complexe pour un lubrifiant est nécessaire pour surmonter les dégradations subies dans les différentes parties du moteur et pour maintenir un niveau de performance élevé. Le chapitre II décrit largement la composition et les rôles des lubrifiants moteurs. Les notions de frottement, de régimes de lubrification ainsi que la rhéologie sont présentées. Les modèles utilisés classiquement pour décrire les variations de la viscosité avec la température, la pression et la contrainte de cisaillement ont été établis. Enfin, des généralités sur la physico-chimie des polymères et des solutions de polymères ont été expliquées. La conformation, le rayon hydrodynamique, le rayon de giration, la concentration critique et les considérations de solubilité sont les concepts approchés pour nourrir la discussion du chapitre IV.

Dans la partie III, plusieurs modèles rhéologiques ont été combinés pour estimer la viscosité des solutions aux températures, pression, cisaillement considérés. Un modèle VTF a été choisi pour décrire la dépendance de la viscosité avec la température et fournir la température de transition vitreuse à pression atmosphérique. Une équation WLF-Yasutomi modifié utilisée pour modéliser la réponse de la viscosité en température-pression jusqu'à 800 MPa a été implémentée dans la loi de Carreau-Yasuda, fiable pour la dépendance en contrainte de cisaillement. Ces modèles ont montré un très bon accord avec les points expérimentaux pour toutes les solutions étudiées. Plusieurs comportements rhéologiques ont été mis en évidence : l'huile de base et la solution de PAMA ont plutôt un comportement Newtonien alors que les solutions d'OCP et de PISH ont une réponse rhéo-fluidifiante. Le comportement rhéologique inattendu du PAMA - par rapport à son utilisation dans les lubrifiants économes en carburant - a été l'objet des réflexions apportées au chapitre suivant.

Le chapitre IV a témoigné de la forte connexion entre la rhéologie et la physico-chimie des composants des lubrifiants. Les comportements rhéologiques différents identifiés au chapitre précédent ont été observés en parallèle des caractéristiques des polymères tels que leur concentration, leur composition, leur conformation, leur rayon hydrodynamique, leur élasticité et leur solubilité dans l'huile de base.

Plusieurs hypothèses ont été avancées pour expliquer le comportement Newtonien inattendu de la solution de PAMA. La concentration choisie pour les polymères est représentative de la concentration dans les lubrifiants moteurs et n'implique pas d'interactions entre les macromolécules.

De plus, la présence d'additifs ne conduit pas à une augmentation du comportement rhéo-fluidifiant. Enfin, la LCST est hors de cause dans les conditions de fonctionnement de l'étude.

Le cœur de la thèse repose sur la notion de rayon hydrodynamique ($R_h$). Son originalité provient de la déduction des rayons hydrodynamiques à partir des mesures de viscosité par extension de la loi d'Einstein à haute pression.

Le $R_h$ du PAMA augmente en fonction de la température et diminue en fonction de la pression alors que la température et la pression n'ont quasiment aucun effet sur les $R_h$ de l'OCP et du PISH.

Plusieurs tendances rhéologiques peuvent être expliquées à partir de considérations de taille et de conformation. A taille égale, l'effet de la conformation l'emporte. Le PAMA et l'OCP ont des $R_h$ proches mais le PAMA a plus d'interactions intramoléculaires liées à sa conformation peigne impliquant une plus grande résistance à l'étirement sous cisaillement, ce qui explique le comportement Newtonien observé pour le PAMA. A conformations proches (PAMA et PISH), l'effet de taille gouverne. En effet, le PISH a un $R_h$ deux fois plus gros que celui du PAMA et est beaucoup plus rhéo-fluidifiant. Les plus grosses molécules s'alignent plus sous cisaillement. A conformation et taille différentes (OCP et PISH), l'effet de taille prévaut sur la conformation : la solution de PISH est plus rhéo-fluidifiante que celle d'OCP. De plus, le PAMA ne s'étire pas peut-être parce qu'il est plus élastique que les deux autres. Son temps de relaxation est environ 100 fois plus petit que ceux de l'OCP et du PISH.

Finalement, cette section a montré que la connaissance de la nature et des propriétés des polymères peut apporter plusieurs pistes dans la prédiction de la réponse rhéologique. Cette analyse est essentielle pour les formulateurs et peut orienter les fabricants d'huiles dans la découverte de nouveaux axes d'amélioration pour les lubrifiants « fuel-economy ».

Le dernier chapitre a abordé le dernier volet de l'étude multi-échelle de ce travail de thèse. Cette partie a mis en lumière la réponse tribologique d'un contact EHD circulaire de roulement-glissement. Tout d'abord, les épaisseurs de film ont été mesurées par interférométrie optique en lumière blanche. Des modèles analytiques et numériques ont été comparés aux mesures expérimentales. Les modèles analytiques sont cohérents pour l'huile de base et la solution de PAMA Newtoniennes alors que l'écart est important pour les fluides rhéo-fluidifiants. Les modèles numériques prenant en compte la rhéologie des solutions décrivent très bien les comportements des solutions ce qui montre la nécessité d'implémenter les modèles rhéologiques dans les modèles numériques.

Les coefficients de traction ont été mesurés sous conditions de ratio glissement-roulement variables. Les courbes pour les différentes solutions et à différentes conditions se superposent. Ainsi, l'effet du polymère sur le coefficient de frottement est très faible sous les conditions opératoires spécifiques à l'étude. Les modèles numériques ne permettent pas une bonne prédiction des coefficients de traction.

Enfin, le chapitre précédent a prouvé la forte relation entre la physico-chimie et la rhéologie. Le chapitre V a démontré que la rhéologie est fortement corrélée à la tribologie. Par extrapolation, nous pouvons déduire que la tribologie est liée à la physico-chimie des lubrifiants. La sélection des composants chimiques par les formulateurs est orientée par la compréhension de ces relations couplées.

En dépit du travail accompli au cours de la thèse, en termes de physico-chimie, rhéologie et tribologie, à la fois expérimentalement et numériquement, il reste plusieurs domaines à explorer et des questions supplémentaires en suspens. Cette section traite des directions possibles à considérer pour

approfondir la compréhension des relations structure-propriétés-performances des améliorants d'indice de viscosité (VII) dans les lubrifiants moteurs sous conditions de fonctionnement réelles.

En premier lieu, la concentration pourrait être modifiée pour connaître son influence sur les propriétés des VII. De plus, la présence d'un paquet d'additifs mérite d'être étudiée de façon plus approfondie.

La dégradation et le vieillissement des lubrifiants après quelques cycles sont aussi à prendre en considération dans le rhéomètre haute pression pour représenter les conditions réelles d'un moteur. Le cisaillement permanent serait alors considéré.

Ensuite, les perspectives d'étude pourraient consister en l'utilisation de polymères de chimie, masse moléculaire, conformation… différentes et d'autres huiles de base telles qu'une huile polaire.

La notion de temps de relaxation a été évoquée au chapitre IV pour expliquer que le PAMA retrouverait son état initial plus rapidement que les deux autres sous contrainte de cisaillement. Ce paramètre peut être directement déterminé par rhéologie dynamique en mesurant le module élastique ($G'$) et le module visqueux ($G''$).

La comparaison des résultats avec des simulations de dynamique moléculaire pourrait être très intéressante pour la compréhension des mécanismes moléculaires.

Dans le chapitre V, nous avons révélé l'intérêt de la connaissance de l'équation de compressibilité sous haute pression pour fournir un modèle numérique puissant et des prédictions d'épaisseur de film dans un contact circulaire chargé précises. L'utilisation de la formule de Tait pourrait être améliorée par la détermination expérimentale des variations exactes de la densité pour chaque lubrifiant.

Finalement, une caractérisation expérimentale de la contrainte limite de cisaillement permettrait une modélisation numérique précise des coefficients de frottement dans un contact.

# I Introduction and objectives

Over the past century, with an increasing number of industrialized and developing countries, human activities have released large amounts of carbon dioxide and other greenhouse gases into the atmosphere. Even if the greenhouse effect is essential to support life on Earth, its growth causes climate changes which jeopardize human health and ecosystems. The majority of greenhouse gases come from burning fossil fuels for heat and energy, although deforestation, industrial processes, and some agricultural practices also emit gases into the atmosphere. The following circular diagram (Figure 12) shows the distribution of the global emissions of greenhouse gases for different industrial areas and different sources of emission. Based on oil and gas consumption, transport, building, industry and production refining account for one third of the total gases emissions. Among those, the main participation is attributed to transportation (13%) which represents almost 40% of the oil and gas emissions.

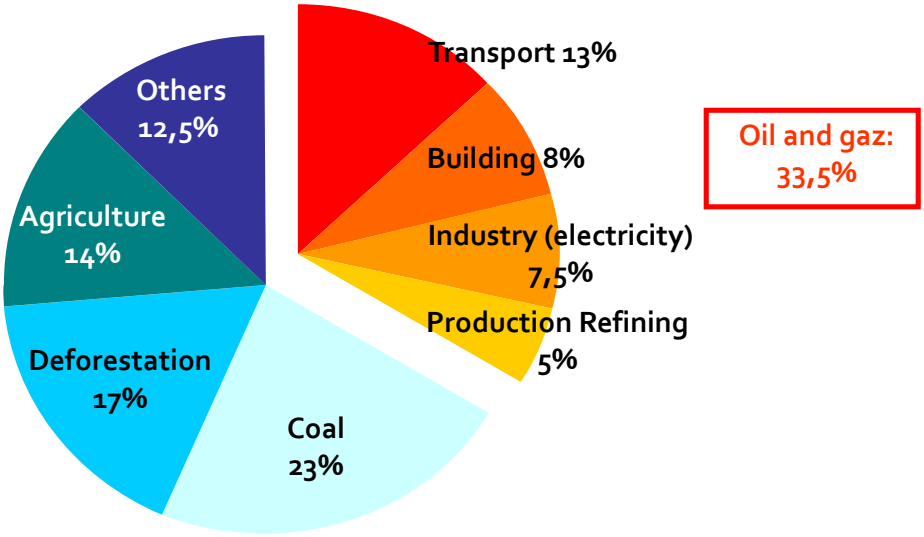


*Figure 12: Distribution of the global emissions of greenhouse gases, GIEC and AIE sources*

Global warming due to greenhouse gas emissions is a central societal and public health issue. In addition, Taylor [1] has outlined the economic dimension of the problem. Indeed, high fuel prices - due to exhaustible resources - have to be taken into account and stiff financial penalties are incurred when fuel consumption targets are not reached. The aim of the European Union is to limit carbon dioxide emission by cars to less than 130 $gCO_2.km^{-1}$ in 2015 and less than 95 $gCO_2.km^{-1}$ in 2020. In this sustainable development context, decreasing fuel consumption and increasing energy efficiency have become major issues.

The protection of the environment, the use of the energy resources and the satisfaction of users are at the heart of our daily concerns, especially in the domain of transportation. As explained in [23], Stefan Korcek (Ford) and Masami Nakada (Toyota) consider that all these problems can be solved by engine and fuel technologies, in the one hand and by tribology, in the other hand (see Figure 13).

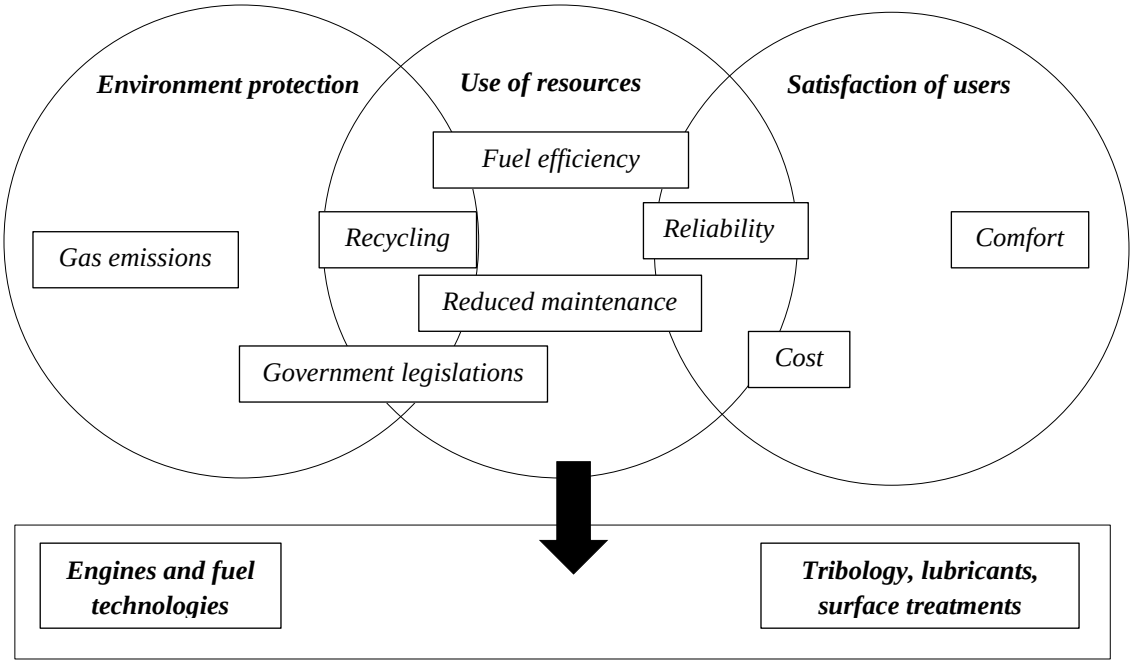


*Figure 13: Expectations for engines, according to Korcek and Nakada [23]*

Consequently, since our society is more and more demanding on environmental subjects and because fossil energy sources are declining, reducing fuel consumption in transportation is a main goal of the industry.

# *I.1 Industrial motivations and scientific challenges*

One way to decrease fuel consumption could be to explore the renewable energy sources including wind power, solar power, hydroelectric power, tidal power, geothermal energy or biomass. Even though these solutions promise a bright future, the present work will focus on the reduction of friction in car engines, while maintaining or even improving their efficiency.

According to Leonardo Da Vinci (1452-1519), friction is the resistance to motion of one body in contact with another and is proportional to the applied load but independent of the sliding surface area [24]. These laws were then re-discovered by Amontons [25] in 1699. In 1781, Coulomb [26] distinguished static friction, the force required to start sliding, from kinetic friction, the force required to maintain motion. He evidenced that kinetic friction is lower than static friction and is nearly always independent of the speed of sliding [27].

In a passenger car, 33% of the fuel energy is heat dissipated in the exhaust gases, 29% goes to the cooling systems and 38% is converted into mechanical power to overcome air drag (5%) and friction losses (33%). The latter are attributed to the friction in the engine (11.5%), the transmission system (5%), the tire-road contact (11.5%) and the brakes (5%) (cf. Figure 14). Finally, only 21.5% of the fuel energy is used to actually move the car [2].

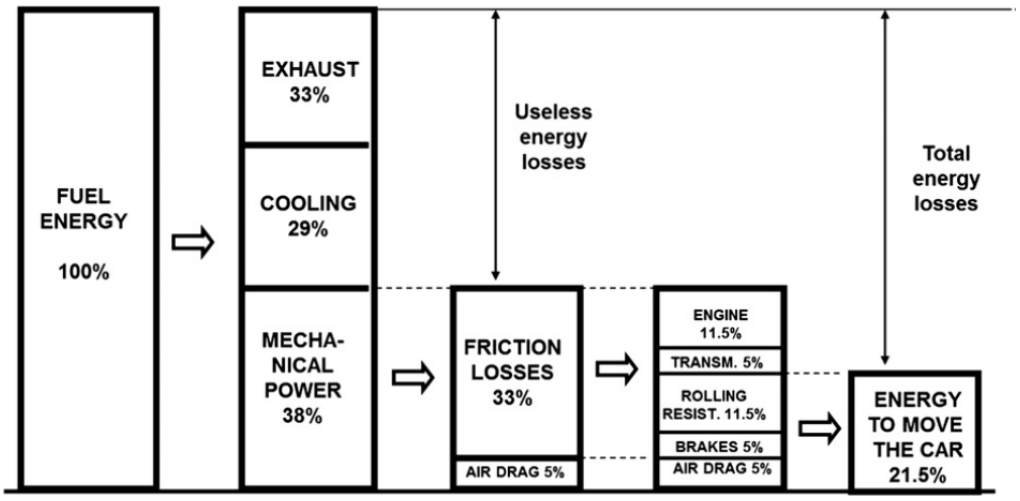


*Figure 14: Energy losses in a passenger car, according to [2]*

In response to this environmental and economic issue, automobile and lubricants manufacturers work together to develop new technologies to fight against friction and consequently, pollution. Many technological breakthroughs have been made to respond to these drastic requirements: low friction and low wear coatings have been developed - such as Diamond-Like-Carbon (DLC) coatings [3] - surface topography and texturing have been upgraded and lubricants have been improved [2]. Holmberg *et al.* [2] highlight that 10% of mechanical loss reduction involves a decrease of 1.5% in fuel consumption.

Leonardo Da Vinci wrote that "all things and everything whatsoever, however thin it be, which is interposed in the middle between objects that rub together, lighten the difficulty of this friction" [27]. Thus, another option to minimize power losses coming from friction in engines is to separate the sliding contact surfaces as far as possible by a lubricating film. The physical benefits of having a lubricant film between surfaces in relative motion have been known for several millennia. Dowson [24] found an Egyptian hieroglyph of a large stone block hauled by many slaves. Close inspection showed fluid, presumably water, being poured into the path of the block. Moderately refined vegetable oils and fats were increasingly used to lubricate machines and wagon bearings. The benefits of reducing the force needed to operate them were a widely received wisdom up to the end of the Middle Ages [27].

To control the film thickness between the sliding surfaces, the main factor appears to be the viscosity of the lubricant and more generally its rheological behavior. Viscosity can be defined as the ability of the fluid to resist to motion. A high viscosity means that a fluid does not flow easily. A higher viscosity fluid will typically make a thicker film between the moving surfaces and support greater loads. The key is to adjust the viscosity of lubricants for engine applications by adding polymers, also called Viscosity Index Improvers (VII), to base oils. The relationship between the viscosity of polymer solutions and temperature is expressed as the Viscosity Index (VI) scale (cf. Appendix A). The VI is calculated from the kinematic viscosity of the polymer solution at 40 °C and 100 °C. The smaller the difference in viscosity at low (40 °C) and high temperatures (100 °C), the higher the VI obtained [28]. The role fulfilled by polymers is to increase the viscosity at high temperature to counteract the lowering of the base oil viscosity without greatly enhancing it at low temperature. The motivation is thus to minimize the viscosity drop with temperature and to offer an acceptable hydrodynamic lubrication at high temperatures, without incurring excessive frictional

losses at low temperatures [8]. Indeed, the engine starts at ambient temperature which can reach really low temperatures according to the localization. These considerations are of primary interest to control the reduction of friction over the complete engine operating temperature domain. To meet the engine specifications, the lubricant must not be too viscous at low temperature which would increase viscous friction during the starting phase, and not too fluid at high temperature which would lead to very thin film and can cause direct contacts between the moving parts of the engine and thereby surface damage. Holmberg *et al.* affirm [2] that a reduction of the engine oil viscosity by approximately 25% at 100 °C is equivalent to fuel savings of 0.6 to 5.5%, with a minimum friction coefficient around 0.04.

In an engine, the lubricant must be multifunctional because it is unique to lubricate a broad variety of mechanical elements. It overcomes severe conditions of temperature, pressure and shear stress (Figure 15) which have strong influence on its viscosity. The temperature in the piston-liner-segment zone can reach 290 °C due to the combustion of fuel. Moreover, in case of cold weather, the lubricant can undergo really low temperatures (down to -70 °C in Russia, for example). The distribution, mainly composed by the camshafts and the valve system, displays pressures up to 800 MPa. In specific contacts, the pressure can even reach 1 GPa or more.

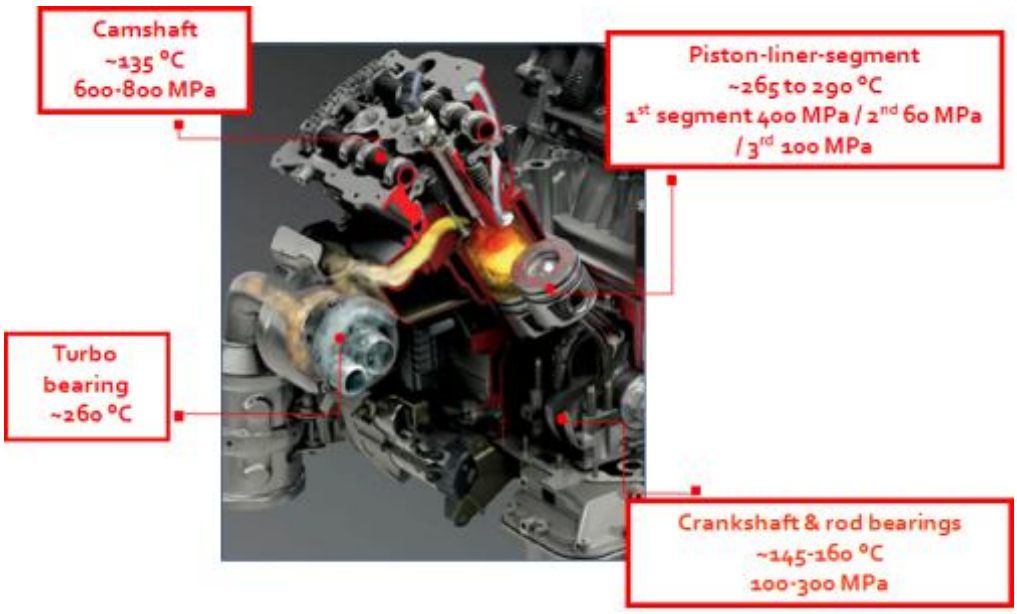


*Figure 15: Severe conditions of temperature and pressure in a combustion engine*

The pressures overcome by the lubricant are so high that the sliding solid surfaces in an engine can be elastically deformed. Pressure also causes a substantial increase of viscosity.

High pressure lubrication - called elastohydrodynamic lubrication (EHL) - has been extensively studied for more than 60 years [4], [5], [6]. Actually, the history of EHL began one century earlier. In the mid-19$^{th}$, the first investigations to understand lubrication were led by Hirn [29] (1854). Experimental works performed by Tower [30] (1883) in England and Petrov [31] in Russia emphasized that the full-film of lubricant exerted a supporting force on the rigid surfaces of a hydrodynamic journal bearing. In 1886, Reynolds published the famous Reynolds' equation which provides the physical explanation of the previous observations and sets the basis of all actual lubrication theories. He established the differential equation describing the pressure distribution (in

function of the geometry and the kinematics of the moving parts) and load-carrying capacity for journal bearings [32]. At the beginning of the 20th century, Martin [33] and Gümbel [34] applied the Reynolds' equation to the case of rigid gears and found film thicknesses unexpectedly too small to confirm the full-film lubrication observed. In 1941, elastic deformations - based on the Hertz theory of the deformation of semi-infinite elastic bodies under dry contact conditions - caused by the pressure were included by Meldahl [35] in the predictions which were unfortunately still too low. Finally, in 1945, Ertel [36] (published by Grubin in 1949 [37], see Cameron [38]) added a pressure-viscosity law (Barus [39]) and previous experimental film thicknesses were thus confirmed. Thereby, the fundamental features of *elastohydrodynamic lubrication* were revealed. The second half of the 20th century was the witness of a growing interest in both the experimental technology - based on optical interferometry techniques [40], [41], [42], [43] - and the numerical resolution of lubrication problems. Line contacts predictions were numerically developed by Petrusevich [44] and Dowson and Higginson [45] and the circular problem was solved in 1976 by Hamrock and Dowson [46]. Mulitlevel techniques were introduced by Lubrecht *et al.* [47] and improved by Venner [48]. Further improvements were developed by Nijenbanning *et al.* [20] in 1994. Many others focused on thermal EHL, starved EHL and mixed lubrication.

When designing a new product, the lubricant supplier is always thinking about how to meet customer needs. As the need grows to have lubricants functionning under more and more stressful operating conditions, the challenge persists to develop a value-added product that can provide excellent performance over a long operating time [28]. For many years, a lot of studies have been run to optimize the formulation of lubricants in order to minimize the friction and thereby the gas emissions. The current development process of a new lubricant follows many steps described in Figure 16.

The classical formulation of a lubricant includes the selection of the base oil, the polymers and the functional additives, followed by a complete study, in the laboratory, at atmospheric pressure of its viscosity and other chemical and physical properties. Empirical adjustments are made to meet the engine requirements imposed by the car manufacturer. Once the first candidates are selected, engine tests are run and further settings are made or the formulation is directly validated. The lubricant is then tested in a real car used under realistic conditions and finally marketed.

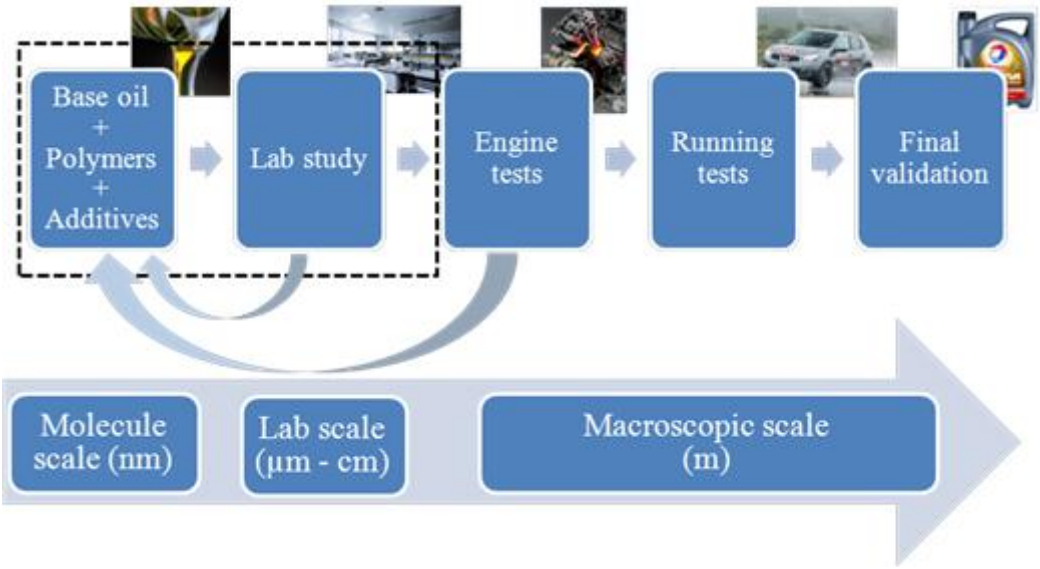


*Figure 16: Steps of the formulation process of a lubricant at various scales*

Moreover, it is of main interest to explore the rheological behavior of the lubricant, i.e. the evolution of its viscosity over temperature, pressure and shear stress. Establishing accurate rheological models for a lubricant is of primary importance to predict and control the viscosity and to guide oil manufacturers in choosing the composition of the lubricants according to the engine specifications. Then, the rheological properties can be included in hydrodynamic and elastohydrodynamic (EHD) numerical lubrication models to foresee film thickness and friction [49], based on laboratory data independently obtained from the application. Even if a global validation of a lubricant is possible using full-scale engine tests, their operation remains too costly to be systematically used during the lubricants formulation process. The determination of complete and reliable rheological models of lubricants is a more efficient alternative in terms of duration and cost for oil makers. The aim is to improve the formulation process diminishing its time and thus its cost, adapting the characteristics of polymers and base oils to the demand of the car manufacturers. The final goal is to more easily obtain bespoke lubricants.

To sum up, the general industrial problematic is part of a multi-scale context. Figure 17 describes the scope of the scientific challenges from the molecular scale to the environmental concern via local contacts, engine parts, a whole engine, a car and users who want to increase the drain intervals while decreasing the fuel consumption to save money.

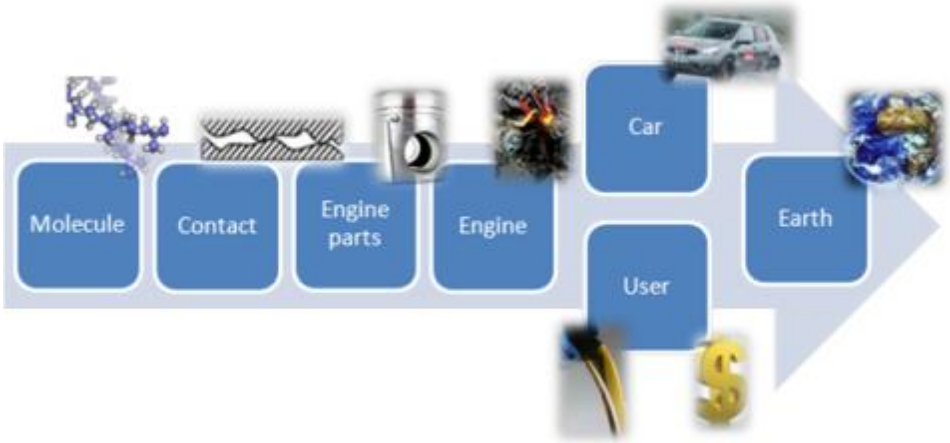


*Figure 17: Scope of the general industrial challenges*

# *I.2 Objectives of the study*

Among all the previous targeted industrial challenges, the objectives of the thesis fit in the first steps of the formulation process of a lubricant (in the black dotted square in Figure 16): the selection of chemicals, the laboratory scale analysis and the relationship between the latter and the molecular scale.

The first objective of this work is to obtain a complete rheological behavior in function of realistic temperature, pressure and shear stress conditions for typical polymer-thickened base oil solutions without functional additives. Indeed it is of main interest to foresee the viscosity of a lubricant under specific operating conditions in an engine so as to predict the film thickness in a contact and thus, know if the thickness of lubricant is enough to avoid wear.

A second challenge aims at quantifying the relationship between the molecular scale and the rheological response of simplified engine lubricants. It is of main importance to understand the role played by the VII and the parameters influencing their viscosity and impacting their action within the

lubricant. As a matter of fact, once the link is established, the choice of polymers in function of the targeted application is easier for the oil makers.

Then, the work focuses on tribological explorations. One can guess that the viscosity has direct impact on the film thickness and the friction of lubricants. The aim here is to establish how rheology impacts tribology.

The final goal is to bridge the gap between molecular aspects and tribological efficiency. If the physico-chemistry impacts the rheology which influences itself the tribology, by extension, the relationship between the molecular scale and the tribology will be thereby evidenced.

Figure 18 shows the different steps of the scientific approach followed in this work.

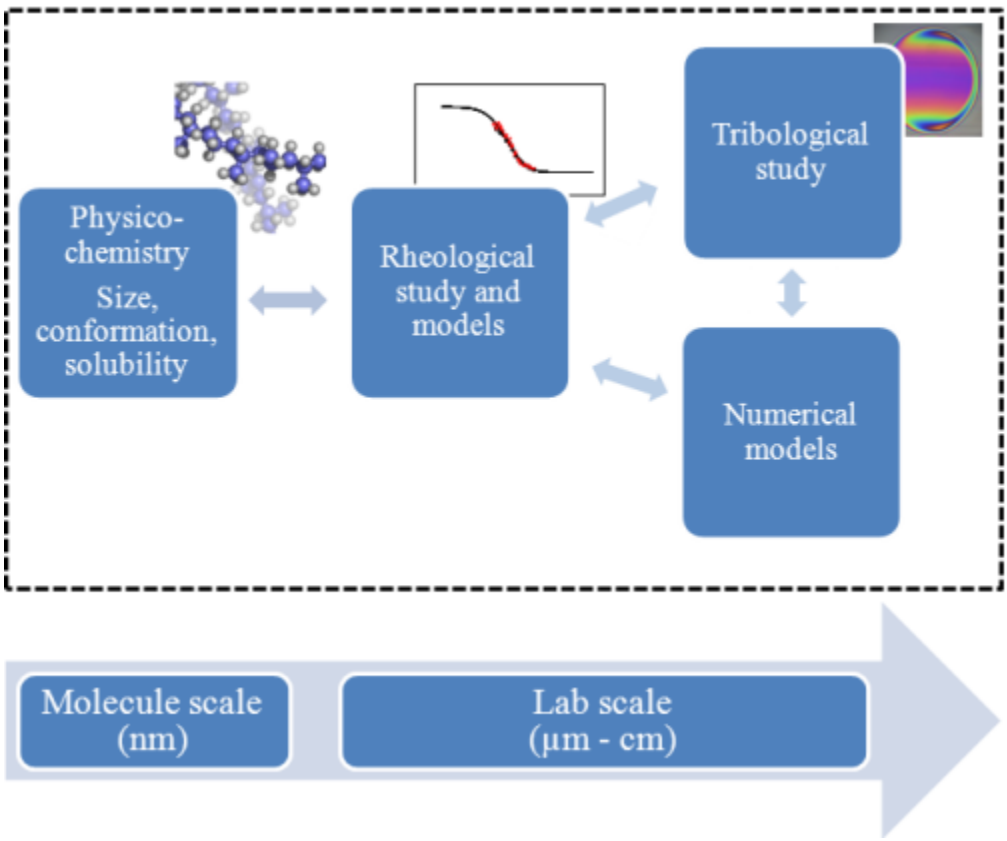


*Figure 18: Approach of the study at different scales*

The following section describes the means used to answer the previous objectives.

## *I.3 Outline of the thesis*

This brief introduction sets the context, the limits and the objectives of the study. Restricting the full-scale engine tests to optimize the formulation process involves savings of time and money. The development of high technology lubricants aims at improving the economy, the environment and the comfort of the users. The main industrial motivations of this work are to reduce the fuel consumption to decrease the emission of greenhouse gases and to extend the drain intervals. The

properties of the lubricant have to meet the car manufacturers' requirements for all parts of the engine operating under various lubrication regimes. In this context, the scientific objective of this work is to link the molecular scale - by the choice of the base oils and the polymers - to the lab scale, by a rheological and tribological investigation.

The second chapter presents the state of the art on the role and action of Viscosity Index Improvers. The friction coefficient and the film thickness (few nanometers to several hundreds of nanometers) in a contact are described according to the lubrication regimes of the engine parts. Then, the rheology of lubricants is approached. Rheological models over temperature, pressure and shear stress are detailed and instruments are depicted. The composition and the role of a lubricant are highlighted. Physico-chemistry basis are provided, especially on conformation, size, concentration, specific temperature and solubility of polymers. Finally, the studied materials are specified.

Section III provides a full study of the rheological behavior of polymer-thickened base stock solutions, both with experiments and models. The explored operating conditions are realistic for the intended application (car engines). First, temperature and shear stress dependences are examined at atmospheric pressure. Next, the viscosity dependence on temperature, pressure up to 800 MPa and shear stress is investigated. The originality of the approach lies in the specific use of non-commercial rheometers in a domain of elevated pressures. Temperature and pressure dependences are simultaneously predicted and models of viscosity over shear stress are fitted to experimental data in specific cases.

Part IV aims at connecting rheology to molecular scale mechanisms. Indeed, according to the chosen polymer, the rheological behavior is different and the goal of this section is to understand the origins of those dissimilarities. The concentration of polymers, the possible effect of the presence of additives, the occurrence of a Lower Critical Solution Temperature (LCST), the conformation and the size (hydrodynamic radius) of the polymers in solution are suspected. The size is investigated extending the Einstein's law to high pressures in the dilute regime. The calculated and the directly measured hydrodynamic radii are compared. Finally, the conformation and the size of polymers in solution allow an explanation of their rheological behaviors. The structure-properties relationship is highlighted here.

The last chapter focuses on the relationship between rheology and tribology. Film thickness and friction coefficient measurements are carried out and compared with analytical predictions and with numerical results based on the generalized Reynolds' equation and on the rheological models obtained in chapter III. Lastly, the tribological behavior is directly related to the rheology and thus, the tribological behavior is linked to the physico-chemical properties of polymers and solvent.

Finally, a general conclusion is drawn from the various aspects discussed in this thesis. Despite the extensive work achieved, in terms of physico-chemistry, rheology and tribology, some points deserve to be deeper investigated and some questions remain unanswered. This document ends with a review of some possible directions for future research.

# II State of the art on lubrication, rheology and physico-chemistry of polymers

The introductory chapter set the industrial and scientific context of the thesis. The objectives and the approach of the study were then defined. The main idea involved in this work is the lubrication, in terms of rheology and physico-chemistry of lubricants. The following chapter aims at recalling some basics on engine lubrication - especially on the lubrication regimes and the composition and the role of an engine lubricant - on the rheological models commonly used in this area and finally, on physico-chemistry of polymers and polymer solutions. It provides the scientific background to understand the role of lubricants and the action of polymers in an engine, and to predict their behavior under the realistic conditions encountered in an automotive engine.

# *II.1 Engine lubrication*

Lubricants are necessary to separate surfaces in relative motion of any mechanical system. The diversity of lubricated parts and of their operating conditions implies a wide diversity of lubricants. They can be solid (graphite, molybdenum disulfide, boron nitride…), liquid (water, vegetable oils, emulsions…), pasty (greases, suspensions…) or gaseous (air). For car engines, most lubrication is ensured by a fluid film.

## II.1.1 Friction and lubrication regimes

Due to the variety of mechanical parts in an engine, several lubrication regimes can be distinguished: hydrodynamic (HD), elastohydrodynamic (EHD), mixed and boundary. The Stribeck curve (Figure 19) describes the variation of the friction coefficient - defined as the ratio of the tangential force to the normal force - in function of the lubricating parameter - defined as the ratio of the viscosity times the speed by the load.

The lubrication regimes and the friction coefficient are modified as the speed changes. When the speed of the surfaces is low, the direct contact between the asperities is the cause of the high friction characterizing the **boundary regime**. The transition to **mixed lubrication** results in a partial separation of the sliding surfaces by a thin film of liquid and in the reduction of the friction coefficient. The latter reaches a minimum in the **elastohydrodynamic regime** before rising in the **hydrodynamic zone**.

It is assumed that a minimum pressure of about 300 MPa (3000 bars) is necessary to significantly deform the solid surfaces in a loaded contact. Pressures under this threshold are typically called “low pressures”. Nowadays, in mechanisms sustaining more and more stresses, the maximal pressure in a lubricated contact can exceed 1 GPa and even reach 3 to 4 GPa.

Considering film thickness in descending order, the lubrication regimes are sorted as follow. The two first regimes concern full-films unlike the two latter. Usually, the thickness of the fluid film in a lubricated contact ranges from a few nanometers to several hundreds of nanometers. The in-plane contact dimension is approximately 0.5 mm.

In the **hydrodynamic regime (HD)**, the thickness of the full film of lubricant is large compared to the average roughness of the surfaces. The direct contact between the two surfaces cannot occur. The lubricant bears the whole load and maintains the surfaces separated. It happens when the pressure generated within the contact is relatively low. This is typically the case in conformal contacts which are characterized by large contact surfaces and therefore low pressures. Journal bearings are representative of this type of lubrication [22].

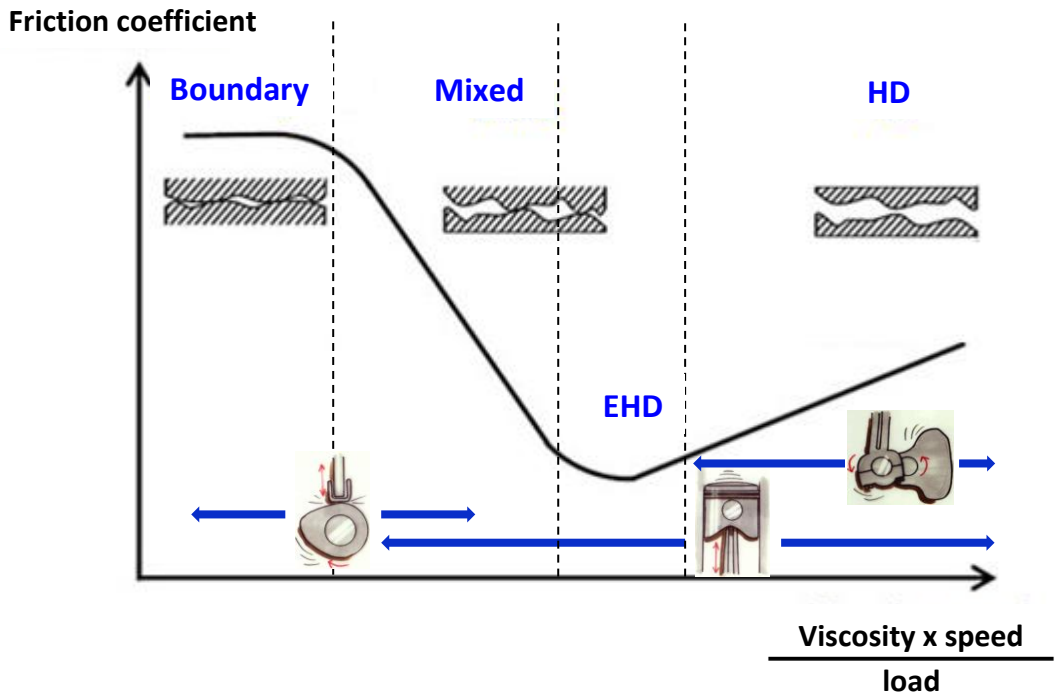


*Figure 19: Stribeck curve and engine parts for the different lubrication regimes*

The **elastohydrodynamic lubrication (EHL)** involves a thin film associated with elastic deformation of surfaces and large piezo-viscous effects. When the pressure generated in the fluid film is high enough, the surfaces are elastically deformed. These deformations have an important influence on the geometry of the lubricant film and their amplitude is generally larger than the film thickness. This regime is typical of non-conformal contacts that can be encountered in gears, rolling-element bearings [22] or also in human joints.

In the **mixed regime**, the film thickness approaches the roughness of the surfaces. The contributions of friction are both the hydrodynamic effects in the fluid and the interactions between asperities. Anti-wear, extreme pressure additives and friction improvers are essential in this regime.

Finally, when the contact is the most severe, the load is not bear by the fluid film anymore but by the direct contacts between surface asperities. This regime is called **boundary lubrication regime**. Under these conditions, the role of the lubricant is limited to dissipate heat and to introduce additives into the contact. The surfaces are generally damaged. The chemical interaction between friction additives and the surface materials predominates in this zone.

The lubrication regimes can be distinguished according to the value of the ratio $h_{min}/\sigma$ where $h_{min}$ is the minimal film thickness and $\sigma$ is the composite RMS (root mean square) roughness of a couple of solids (1 and 2) whose RMS roughness are $Rq_1$ and $Rq_2$ respectively [17] (cf. Table 1).

$$\sigma = \sqrt{Rq_1^2 + Rq_2^2} \tag{7}$$

| | |
|---|---|
| $h_{min}/\sigma \geq 2.5$ | Thick film in EHD lubrication |
| $2.5 \geq h_{min}/\sigma \geq 1.2$ | Mixed regime with a thick film trend |
| $1.2 \geq h_{min}/\sigma \geq 0.6$ | Mixed regime |
| $0.6 \geq h_{min}/\sigma \geq 0.35$ | Mixed regime with a boundary trend |
| $0.35 \geq h_{min}/\sigma$ | Boundary or limit lubrication |

*Table 1: Lubrication regimes in function of the $h_{min}/\sigma$ ratio*

Engine parts, as drawn on Figure 19, perform under different lubrication regimes. Traditional design philosophy assumes that the distribution - mainly composed of camshafts and cam-tappet elements - works in the boundary regime. However, recent advances show that the cams and followers rely upon the mixed and elastohydrodynamic modes of lubrication [50]. The piston-liner-segment operates from the HD regime to the mixed regime. Finally, the crankshaft and the rod bearings work in the HD regime to the EHL regime. Considering the variety of lubrication regimes in an engine, the lubricant composition must be complex to fulfill all its dedicated roles.

## II.1.2 Composition and role of engine lubricants

Engine lubricants are formulated from about 70-80% of base oil and 20-30% of chemical additives. Several base oils can be mixed in a single lubricant. Thus, lubricants are complex fluids performing many critical properties.

- Firstly, lubricants reduce energy losses due to friction and prevent wear of the contacting surfaces by separating the moving surfaces with a thin film.
- They play a strong role in the thermal equilibrium of engines. The calories generated by viscous heating or by mechanical friction between parts are evacuated through the lubricant to heat exchangers.
- The cooling property of lubricants helps to maintain an appropriate temperature in the engine which participates in the protection of surfaces against corrosion or at least, in the limitation of corrosion phenomena.
- Lubricants clean surfaces and remove contaminating species. Contaminants can be water, metal debris from wear, impurities resulting from corrosion, soot, dust, sludge… They can also come from the degradation and the ageing of the lubricant itself.
- Lubricants must contribute to a good sealing, especially for gas and liquids (water, fuel, cooling liquid…) in the cylinder block part.

Lubricants may also fulfill other roles like transferring energy to hydraulic circuits, absorbing shocks and reducing the noise due to vibrations. They can facilitate the start of mechanical parts at any temperature and ensure a good resistance to constraints like fire and aeration. All those properties aim at extending the lifetime of mechanical elements.

## II.1.3 Base oils

Most functions of the lubricant are insured by the base oil. Its role is to create a fluid layer to separate the sliding surfaces in order to lower the friction. It allows heat transfer and the evacuation of particles. The base stock must also maintain the additives in solution.

Base oils can be from mineral, synthetic or vegetable origins. Only the two first categories are used in actual automotive lubricants. Base oils coming from petroleum are widespread because of their performance, their availability and their competitive price. Synthetic base fluids are chosen if specific properties are sought because they are generally more expensive.

Base oils can be sorted into 5 groups according to the API (American Petroleum Institute) 1509 (API 2007) classification.

| | Group I | Group II | Group III | Group IV | Group V |
|---|---|---|---|---|---|
| **Saturates (% w/w)** | < 90 | ≥ 90 | ≥ 90 | PAO (PolyAlphaOlefin) | Esters, PAG (PolyAlkyleneGlycol) and everything else |
| **Sulfur (% w/w)** | > 0.03 | ≤ 0.03 | ≤ 0.03 | | |
| **Viscosity Index (VI)** | 80≤VI<120 | 80≤VI<120 | ≥ 120 | | |

*Table 2: API classification of base oils*

Saturates and sulfur mean saturated hydrocarbons and chemicals containing sulfur respectively. The notions described in Table 2 are explained just below.

Group I, II and III are mineral base oils and groups IV and V can be legally labeled "synthetic". The two following parts describe the mineral base oils in the one hand and the synthetic base oil in the other hand.

### *II.1.3.a Mineral base oils*

Mineral base oils result from a series of separating and refining processes of pure petroleum. Crude oil is a complex blend of different types of organic chemicals: hydrocarbons and non-hydrocarbons [27]. Hydrocarbons are in majority in a crude oil and include:

- **alkanes**, also called paraffins, are saturated linear hydrocarbons (n-paraffins) or branched-chain alkanes (iso-paraffins). The number of carbon atoms can be as high as 60 but is generally between 15 and 40 in mineral base oils. They represent 70 to 80% of the crude oil.
- **alkenes**, known as olefins, unsaturated molecules, are found in small proportions.
- **alicyclics**, also named naphthenes, have a saturated cyclic structure (5 and 6 carbon atom per cycle: cyclopentane and cyclohexane) and are often branched. They constitute 15-25% of the petroleum composition.
- **aromatics**, cyclic structures with conjugated double bonds, mainly based on the six-membered benzene ring. Only 5 to 10% of aromatics are present in crude oil. They are strongly toxic and mutagenic and are not welcome in base stocks.

The previous chemical families present in crude base oil exhibit many chemical and physical properties, summarized in Table 3.

The **pour point** is the lowest temperature at which an oil sample is able to flow by gravity alone. At this temperature, paraffins crystallize and wax crystals grow as the temperature declines. The lower the pour point, the higher the pumpability at cold temperatures.

The **Viscosity Index (VI)** represents the temperature dependence of viscosity. Its calculation is detailed in Appendix A. If the Viscosity Index is low, the viscosity depends steeply with temperature and reversely.

The **oxidation stability** is the property of a component to resist to the action of oxygen atoms at high temperature. Oxidation residues are not willing because they alter the original properties of the lubricant.

The s**olvency power** is essential for a base oil to solubilize chemical additives and even contaminants such as debris from wear or impurities resulting from corrosion to ensure cleanliness in the lubricant.

The **compatibility with elastomers** is important to avoid the damage of the elastomeric seals.

| | **Alkanes** | | **Alicyclics** | | **Aromatics** |
|---|---|---|---|---|---|
| **Other name** | n-paraffins | iso-paraffins | naphthenes | | |
| **Chemical structure** |  | 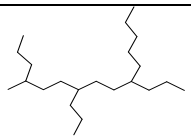 |  |  |  |
| **Number of carbon atoms** | up to 60 (generally between 15 and 40) | | 5 | 6 | 6 |
| **Proportion in crude oil (%)** | 70 to 80 | | 15 to 25 | | 5 to 10 |
| **Pour point (°C)** | -9 to -18 | | -20 to -45 | | variable |
| **Viscosity Index (VI)** | ≈100 | | $0 \leq VI < 60$ | | < 0 |
| **Oxidation stability** | high | | intermediate | | low |
| **Solvency power** | low | | high | | very high |
| **Compatibility with elastomers** | high | | intermediate | | low |

*Table 3: Comparison of chemical and physical properties of mineral oil components*

Non-hydrocarbon elements with ring structures or functional groups attached to a hydrocarbon structure are also part of the crude oil. Organosulfur compounds, molecules with nitrogen (heterocyclic compounds) and with oxygen (principally carboxylic acids), organometallics can also be found. Traces of phenols and furans may be present. Finally, there are very high molecular weight resins and asphaltenes which contain a variety of aromatic and heterocyclic structures. All these non-hydrocarbon elements represent less than 5% of the total composition of a base stock.

Chemical processes are necessary to separate the desired constituents from the others and obtain a base oil from a preferential API group. The traditional refining steps leading to base oil of group I (API) are:

- Distillations (atmospheric and vacuum): remove both the components of too low and too high boiling point.
- Solvent extraction, aromatics removal: leaves the oil high with a high rate of saturated hydrocarbons and improves the VI and the stability.
- De-waxing: removes wax, n-paraffins and controls low-temperature properties of the base oil.
- Finishing: removes traces of polar components and improves the color and stability of the base oil. After a catalytic hydrogenation, group II (API) base oils are obtained.

Further hydrotreatments involving chemical reactions are also used to enhance properties of the oil fractions and lead to base oils of group III (API). The base oil can be hydro-refined using hydrogen under high pressure. It can be treated by catalytic hydrocracking, replacing the solvent extraction, leading to a hydrocracked mineral base stock. Finally, the hydroisomerisation allows obtaining iso-paraffins from n-paraffins.

#### *II.1.3.b Synthetic base oils*

Synthetic lubricants have been available for many years. In the early 1930's synthetic hydrocarbon and ester technologies were simultaneously developed in Germany and the United States [27]. Synthetic base oils are parts of API groups IV and V. They have an elevated viscosity index (>120) and a high stability to oxidation but there are generally expensive. Among the mostly used, PolyAlphaOlefins (PAO), Poly-Internal Olefins (PIO), aliphatic diesters, polyolesters, phosphate ester, PolyAlkyleneGlycol (PAG), polybutenes, alkylated aromatics, etc. can be found. Other important synthetic lubricant materials are the silicones, borate esters, perfluoroethers and polyphenylene ethers but these have restricted applications due either to high cost or to performance limitations [27]. Several chemical syntheses are employed. For instance, the oligomerisation of α-olefins has been investigated for the production of polyalphaolefins (PAO). The most important method being free radical processes, Ziegler catalysis and cationic, Friedel-Crafts catalysis. Polyalkylene glycols (PAG) are produced by reacting compounds containing active hydrogen atoms, e.g. alcohols, water, with alkylene oxides, usually in the presence of a basic catalyst such as sodium or potassium hydroxides or tertiary amines. The commonly used alkylene oxides are ethylene oxide and propylene oxide. The others synthetic base oils are reached by different chemical synthesis like addition, polymerization, esterification, alkylation, etc.

### II.1.4 Additives

Additives are introduced in the formulation of engine lubricants, as required by specifications given by automotive makers, to strengthen the already-existing properties of the base oil or to add a specific one. Additives are generally supplied as a package in which there are several categories of chemicals that can be classified according to their efficiency. First, anti-wear and extreme pressure additives are considered. Then components acting on the frictional properties are described. Next, cleaning agents are detailed and finally, the rheology modifiers are depicted.

#### *II.1.4.a Anti-wear and extreme pressure*

One of the targets of oil makers is to specify a lubricant with a viscosity sufficient to generate hydrodynamic or elastohydrodynamic oil films that separate the engine's interacting surfaces, but not too high to induce excessive viscous drag loss. In practice, the various contact types in an engine, the incidence of operating conditions beyond the design range, and the pressure to improve efficiency by reducing oil viscosity lead to reduce oil film thickness below the optimum. Asperities on the interacting surfaces then start to interact with others high spots, initially through micro-elastohydrodynamic lubrication films and at the end, through direct surface contact, resulting in an increased friction and very likelihood in surface damage. Anti-wear and extreme pressure (EP) additives are added to lubricating oils to diminish wear and prevent seizure under such conditions corresponding to the mixed regime [51]. They are used to form a soft protection layer on metal surfaces which can be ripped off by friction and avoid welding phenomena [23]. The friction between the two solids initiates their action. Extreme pressure additives interfere when temperature and pressure are so high that anti-wear additives are not effective anymore. Generally, anti-wear additives

are designed to deposit surface films under normal operating conditions and thus, reduce the rate of continuous, moderate wear, whereas EP additives are expected to react rapidly with a surface under drastic distress and prevent more catastrophic failures such as scuffing and seizure [51]. Anti-wear additives can act in several ways. Some deposit multilayer films thick enough to supplement marginal hydrodynamic films and/or prevent direct asperity contact altogether. Some monolayer films reduce the local shear stress between contacting asperities and are preferentially removed instead of surface material. Others create chemical bonds with the surface and slowly modify surface asperity geometry by controlled surface material removal until the generation of the hydrodynamic film [51]. EP additives are designed to prevent metal-metal adhesion or welding when the degree of surface contact is such that the natural oxide films are removed and other surface-active species in the oil are not reactive enough to deposit a protective film. This is most likely to occur under conditions of high speed, high load, or high temperature operation. EP additives operate by reacting with the metal surface to form a metal compound such as iron sulfide. They act similarly to anti-wear additives, but their rate of reaction with the metal surface and therefore the rate of EP film formation are higher and the film itself is tougher [51].

Main compounds are synthesized from an alcohol or an alkylphenol with a pentasulfur phosphorus which leads to zinc salts like ZDDP, zinc dialkyldithiophosphates (Figure 20) or ZDTP, zinc dithiophosphates. In spite of their efficiency, their use is nowadays controversial because they contain sulfur and phosphorus. Interesting candidates to limit the quantity of sulfur are metallic dithiocarbamates. All these chemicals have also strong anti-oxidant properties.


*Figure 20: ZDDP chemical structure [51]*

### *II.1.4.b Friction improver*

Friction modifiers are added to complete the role of the previous additives. They aim at increasing fuel economy and limiting wear by reducing the friction coefficient in mixed and limit lubrication regimes. Solid lubricants are considered to be any solid material that reduces friction and mechanical interactions between surfaces in relative motion against the action of a high normal load. Solid lubricants offer alternatives to the lubricant formulator for situations where traditional liquid additives fall short on performance. An example is a high-temperature lubrication condition in which oxidation and decomposition of the liquid lubricant will certainly happen, resulting in lubrication failure [51]. Graphite, molybdenum disulfide ($MoS_2$), boron nitride, polytetrafluoroethylene (PTFE), fatty alcohols, fatty acids and fatty esters are typical friction modifiers. The two first species are widely used as solid lubricants. They intervene in the boundary regime of lubrication. These pigments are effective load-bearing lubricants additives due to their lamellar structure [51], as shown for the $MoS_2$ in Figure 21. Those additives are polar and adsorb on the metallic surfaces by chemisorption or physisorption. The molybdenum disulfide owes its properties to its crystalline structure made of parallel sheets. After adsorption, it acts by thermal and tribological decomposition.

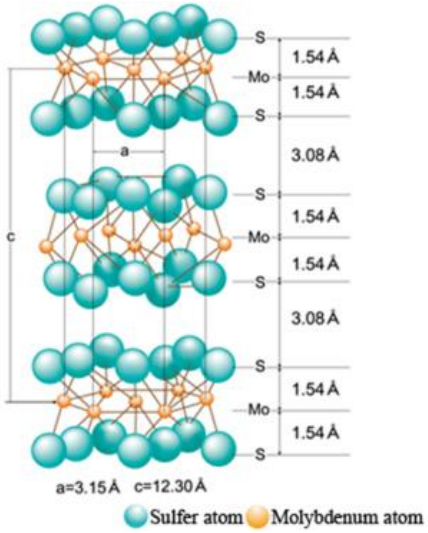


*Figure 21: Crystalline structure of the molybdenum disulfide ($MoS_2$)*

### *II.1.4.c Lubricant and surfaces cleaners*

While the engine is running, undesirable particles such as sludge, soot and other particles resulting from oxidation of the fuel or the lubricant are generated and the wear is increased. Thus, cleaner chemicals are needed. Detergents, dispersants, oxidation inhibitors are part of the general class of additives called "stabilizers" and "deposit control agents".

**Detergents**

Detergents are added to clean and neutralize the contaminants [23]. Detergents are metal salts of organic acids that frequently contain associated excess base. Calcium or magnesium sulfonates are generally used. The final products of combustion and lubricant decomposition include organic and inorganic acids, aldehydes, ketones and other oxygenated materials. The acids have the propensity to attack metal surfaces and cause corrosive wear. Detergents, especially basic detergents, contain reserve base that will neutralize the corrosive acids to form salts [51] (cf. Figure 22).

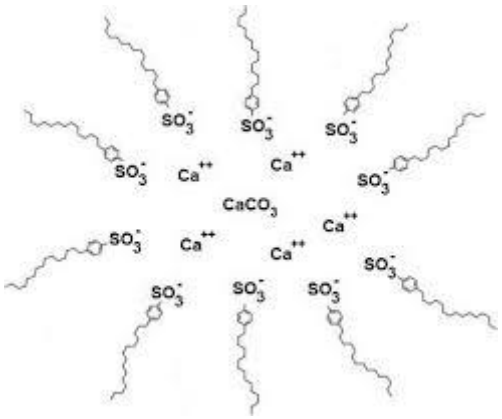


*Figure 22: Micelle of calcium carbonate and calcium sulfonate*

**Dispersants**

Dispersants solubilize contaminants and keep them in suspension in the lubricant to prevent agglomeration. The main ashless dispersants are: succinimides, succinic esters and alkylphenolamines. Physical bondings are created between the impurity and the polar head of the dispersant. The lipophilic chain insures the solubility. Micelles are formed around the sludge. Due to the large size of the hydrocarbon chain and its steric hindrance, contaminants cannot agglomerate anymore. The micelle structure of calcium sulfonates acts like a dispersant as well.

**Anti-oxidants**

Antioxidants can be divided into two categories. The one blocking the radical reactions: amines, sulfides and phenols and the one degrading products like peroxides, coming from oxidation reactions: zinc dialkyldithiophosphates, ZDDP or metallic dithiocarbamates.

**Anti-rust / anti-corrosion**

Corrosion comes from the reaction of acids on metal parts of the engine whereas rust results from the attack of water and oxygen on iron producing iron hydroxides. Anticorrosion or antirust additives must neutralize combustion acids and form a protection film adsorbed on the metal surfaces, preventing the oxygen to access the iron. Organo-metallic detergents are prime candidates. Alkenyl succinic acids act directly on surfaces.

**Anti-foam**

The lubricant is stirred while flowing in the engine, implying the formation of air bubbles and foam. This phenomenon is enhanced with the use of surfactants such as detergents and dispersants. An excessive foaming involves a loss of lubrication because the pumpability and the distribution of the lubricant in the different mechanical parts of the engine become more difficult. Incorporating air involves an increase of oxidation. Antifoam agents are principally polar polymers and have a surface tension lower than that of the oil: silicones such as polydimethylsiloxane (PDMS) or polyacrylates. They reduce foaming by decreasing the surface tension of the oil and by separating bubbles from the liquid phase. This causes the rupture of the air bubbles. Entrained air bubbles are agglomerated and the larger ones rise to the surface of the liquid. Since they are not soluble in the lubricant, they remain present but in small quantities [23].

### *II.1.4.d Rheology modifiers*

Rheology modifiers can be divided into two groups: those which facilitate the engine start (i.e., pour point depressants to improve the pumpability at cold temperatures) and those increasing the viscosity index (cf. Appendix A) of the lubricant.

**Pour Point Depressants (PPD)**

At low temperature, the presence of hydrocarbons in base oils implies the formation of crystals. The agglomeration of crystals thickens the lubricant and makes the flow of the fluid more difficult. Pour point depressants improve the ability of the lubricant to flow at low temperatures by modifying the crystallization of paraffins. Additives adsorb on the edges of the crystals and act as impurities stopping their growth. Thus, smaller crystals are formed which depresses the pour point by several tens of Celsius degrees below zero. Chosen chemicals are poly(alkylacrylates) such as poly(alkylmethacrylate) (PAMA) (Figure 23).

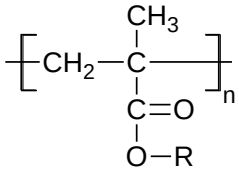


*Figure 23: Poly(alkylmethacrylate)*

**Viscosity Index Improvers (VII)**

Various key concepts are at stake to define the Viscosity Index Improvers (VII)**.** They must reduce the dependency of lubricant's viscosity on temperature and can be used in many different applications. The two main properties of the VII which need to be balanced for a specific lubricant application are thickening efficiency and shear stability. Moreover, fuel efficiency and durability, as well as improved performance can all be achieved through the selection of the proper VII [28]. Ideally, the lubricating film should not be too viscous at low temperatures which would involve important frictional energy losses and thick enough at high temperatures not to favor direct contacts between the moving surfaces and increase wear. Polymers are used to control the viscosity variation of the lubricants with temperature. Indeed, they act as thickeners at high temperature because strong forces are formed between the polymer and the solvent. When the temperature rises, the molecular agitation increases, the solubility of macromolecules is improved and the polymer coils swell. The viscous flow is then disturbed by the intermolecular friction between the solvent molecules and the polymer coils which involves a raise of viscosity. At lower temperatures, polymers contract and look like globules. The viscosity is low because polymer chains do not rub. Only weak interactions exist between the polymer chains and the solvent. The effect of viscosity modifiers in reducing temperature dependency for an engine oil is shown in Figure 24. The slope corresponding to the base oil is steeper than that of the polymer-thickened solution. The addition of a polymer diminishes the temperature dependence enabling a satisfying cold starting and easing the operation of the engine at high temperatures. At low temperatures, a fairly condensed polymer chain contributes less to the fluid viscosity whereas the polymer coil is more solvated be the base oil and uncoils (or swell) to impart viscosity to the base oil at higher temperatures. The higher the molecular weight, the greater the thickening for a given type of VI polymer [28].

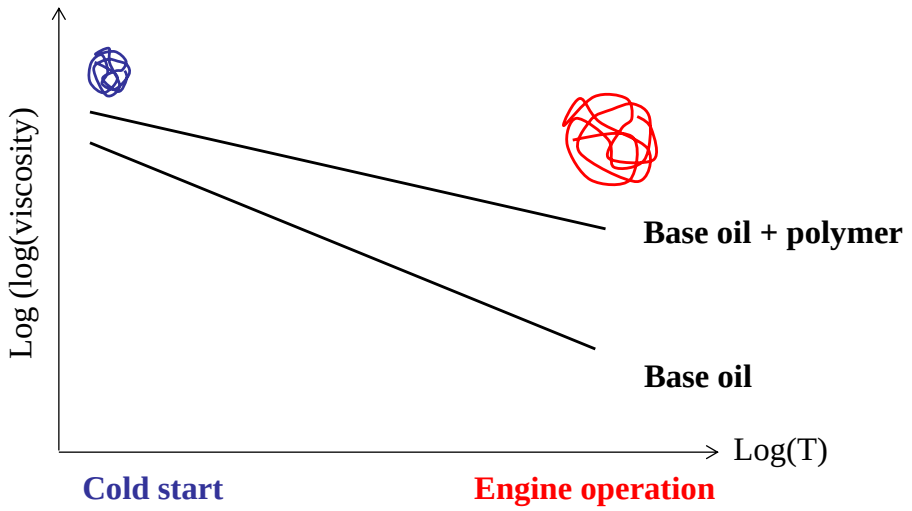


*Figure 24: Polymer coil expansion with temperature*

Polymers are used over a wide range of temperature. They are named “Viscosity Index Improvers (VII)” because the variation of viscosity in function of temperature is reduced and thus, the viscosity index is enhanced. Lubricants formulated with VII are called “multigrade” because they can be defined with both a low temperature grade and a high temperature grade. A grade is a number corresponding to a range of viscosities. It is determined according to standards. As required by the SAE (Society of Automotive Engineers) classification, in the denomination “10W-30”, “W” is used for “winter” and the number “10” represents the cold viscosity grade, “30” being the hot viscosity grade. The document SAE J300 defines the viscosity ranges related to grades for engine oils. In automotive applications, multigrade oils formulated with VII retain viscosity under high engine shear at high temperatures, while maintaining oil pumpability at low temperatures [28].

Several families of polymers are suitable to the desired properties [27]. Polymers structures are described in Figure 25.

- Polyesters like poly(alkylacrylates) and poly(alkylmethacrylate) (PAMA). The alkyl chains can count from 1 to 22 carbon atoms (the mean number is 12).
- Hydrocarbon polymers: poly(isobutenes) (PIB) and olefin copolymers (OCP), hydrogenated diene-styrene copolymers. The latter can contain either butadiene (PBSH) or isoprene (PISH) as the diene and can be either random, block or star-shaped polymers. A copolymer, also called heteropolymer, is a macromolecule resulting from the polymerization of at least two monomers (A and B) in opposition to a homopolymer for which only one monomeric species is used. The arrangement of the constitutional units of a macromolecule determines the type of copolymer. They can be classified into several groups: alternating, statistical, block or graft copolymers.
    - An alternating copolymer shows the monomeric units in a regular alternating sequence -A-B-A-B-A-B-A-B-A-B-A-B-A-B-.
    - A statistical copolymer consists in a random arrangement of the monomers -A-A-B-A-B-B-B-A-A-A-A-B-.
    - A block copolymer comprises two or more homopolymer subunits linked by covalent bonds -A-A-A-A-A-A-B-B-B-B-B-B-.
    - A graft copolymer is a special type of branched copolymer in which the side chains are structurally distinct from the main chain

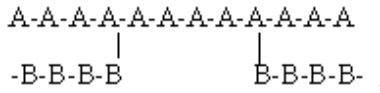


.

Three ways of manufacturing these classes of high molecular weight polymers can be distinguished. Polyalkylmethacrylates are obtained by free-radical initiation with peroxides on alkyl methacrylate monomers. VI modifiers for engine lubricants have a molecular weight $M_w$ between 250 000 and 750 000 g/mol. Olefin copolymers are manufactured by a copolymerization of ethylene and propylene, catalyzed by the Ziegler-Natta technique. The most common catalysts are aluminum alkyl halide with a soluble vanadium compound. The ethylene/propylene ratio is a key parameter for OCP. A compromise must be found between the thickening efficiency - insured by ethylene - and low-temperature solubility. If the polymer contains too much ethylene, the polymer crystallinity is increased and the solubility at low temperature is lowered. Their molecular weight $M_w$ can be in the range of 50 000 and 200 000 g/mol. Finally, hydrogenated diene-styrene copolymers are synthesized by anionic polymerization [27]. Block polymers are obtained from an anionic copolymerization of a diene like butadiene or isoprene (2-methyl-1,3-butadiene) with styrene (vinyl benzene), followed by a hydrogenation. Their molecular weight is between 75 000 and 200 000 g/mol. Star polymers are obtained by an anionic reaction between block copolymers diene/styrene/diene and the divinyl

benzene, followed by hydrogenation. Molecular weights of star polymers range between 300 000 and 700 000 g/mol [27].

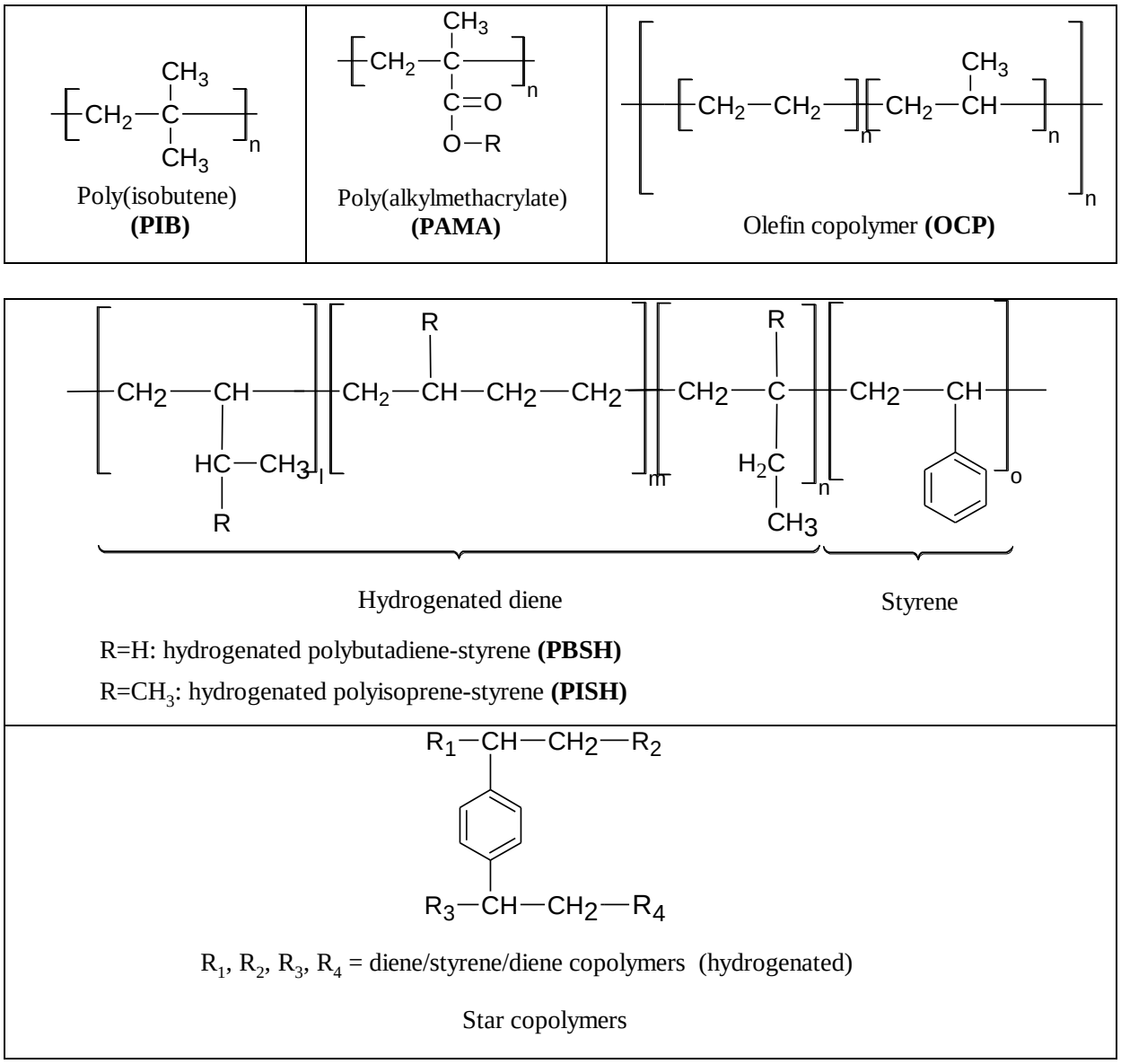


*Figure 25: Chemical structures of Viscosity Index Improvers*

The side chains, chemistry and geometry of the polymer play a major role in determining performance benefits like low-temperature fluidity or VI property. Using a variety of monomer combinations and processing techniques, one can produce numerous different types of polymer architectures such as linear, branched, star and comb polymers, each of which can have homopolymers, block, copolymers or random copolymers [28].

# *II.2 Rheology of lubricants*

Viscosity is one of the key physical properties of a lubricant and it is of main interest to study its rheological behavior. This part is dedicated to the rheology in general terms, to the rheological models classically used for lubrication and to the instruments designed to measure rheological properties.

## II.2.1 Generalities

Rheology refers to the study of the deformation and the flow of materials. The term comes from two Greek words: “rheo” meaning “flow” and “logos” meaning “communication” or “science”. The viscosity is the main physical notion studied in liquids. Viscosity measures the resistance of a gas, a liquid or a solid to deformation by shear stress. More specifically, the rheology of lubricants deals with the relationship between viscosity, shear rate or shear stress, temperature and pressure and their combined influences.

Considering a fluid trapped between two horizontal surfaces, one fixed and one moving horizontally at speed *u*, the flow is called “simple shear” and adjacent layers move parallel to each other with different speeds. Friction between fluid layers creates a resistant force in the opposite direction to the imposed motion. Therefore, an external force *F* is required to keep the top plate moving at constant speed (Figure 26).

$$F = \eta S \frac{du}{dy} \qquad (8)$$

where *S* is the surface between the fluid layers, *du/dy* the local shear rate, *h* the gap between the two solid surfaces and $\eta$ the dynamic viscosity.

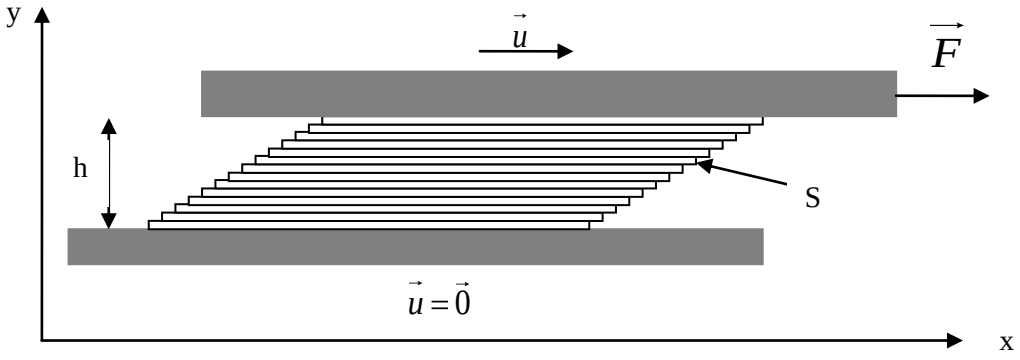


*Figure 26: Simple shear flow*

Newton wrote this expression as:

$$\tau = \eta \dot{\gamma} \qquad (9)$$

where $\tau$ *(=F/S)* is the shear stress and $\dot{\gamma}$ *(=du/dy)* the shear rate.

The kinematic viscosity $\upsilon$ is defined as:

$$\upsilon = \frac{\eta}{\rho} \qquad (10)$$

where $\rho$ is the mass density.

Newton considers that the shear stress is directly proportional to the shear rate with a slope equal to the viscosity of the fluid (see Equation (9)). Water, glycerine, mineral oils and solvents are typical Newtonian fluids. However, a lot of fluids do not follow to this law and the viscosity is not a constant. They are called "non-Newtonian" fluids (Figure 27).

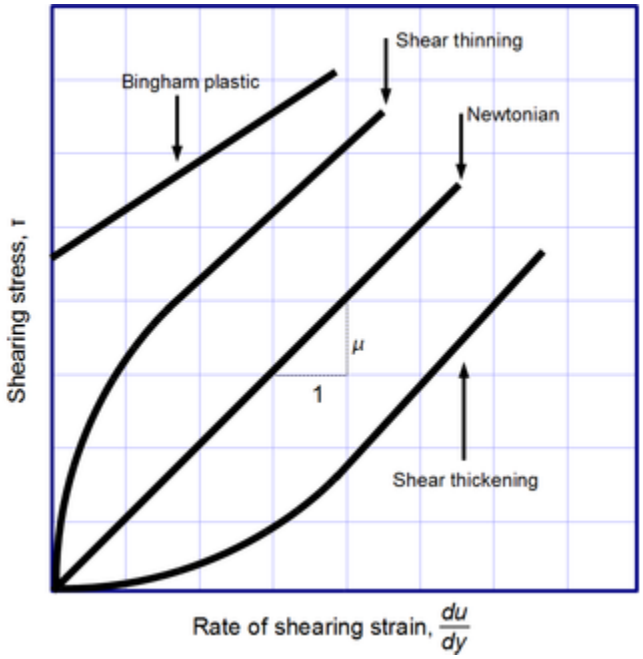


*Figure 27: Rheological response of different types of fluids*

Shear-thickening fluids display a viscosity increasing with the shear stress. The viscosity of shear-thinning liquids decreases in function of the shear stress. They can also be called "pseudo-plastic" fluids. Fluids named "Bingham plastics" behave as a solid at low shear stress and flow as a viscous fluid at shear stress higher than the yield stress. Other fluids can be classified in the category of Boltzmann fluids if their viscosity varies with time: thixotropic liquids become less and less viscous with time under a constant shear stress, such as paints or inks. For rheopectic (also named anti-thixotropic) fluids, the opposite phenomenon happens [52].

To complete the list, Maxwell viscoelastic fluids must be mentioned. The liquid is then considered having both an elastic response and a viscous behavior. The elastic behavior is governed by the Hooke law (the stress is directly proportional to the shear strain $\gamma$ by a factor *G*, the elastic shear modulus) and the viscous response, by the Newton equation.

Hooke law $$\tau = G\gamma \qquad (11)$$

According to Roland [53], "the relaxation time is a measure of the time scale for reorientation of the molecule or, in the case of polymers, correlated conformational transitions of a couple of

backbone bonds (local segmental dynamics)". It characterizes the time taken by a polymer coil to recover its initial state by releasing its stored energy after being stressed. Considering the Maxwell model as a first approximation, the relaxation time $\lambda$ is the ratio of the viscosity over the effective shear modulus *G*:

$$\lambda = \frac{\eta}{G} \qquad (12)$$

Lubricants are known to be shear-thinning fluids. Barnes *et al.* [8], Macosko [9] and Glass *et al.* [10] report that shear stress induces distortion and alignment of macromolecules. The amplitude of this mechanism depends on the molecular weight of the polymer and its conformation. If no - or low - shear stress is applied, the polymer coils remain in a steady initial state, the viscosity is stable and the latter is called the viscosity of the "first Newtonian plateau". The stretching of polymer chains in the flow leads to a viscosity drop. If the shear stress is not too high and the molecules are flexible, this phenomenon is temporary and the polymer chains come back to their previous shape at zero shear stress. If the shear stress is high enough and the strength of the polymer molecules is limited to a certain extent, the deformation can imply the degradation of the coils. Because of the rupture of some molecular chains, the viscosity decreases irreversibly and does not recover its initial value (Figure 28). In both cases, the viscosity reaches a steady value at high shear stress and this state is named the "second Newtonian plateau".

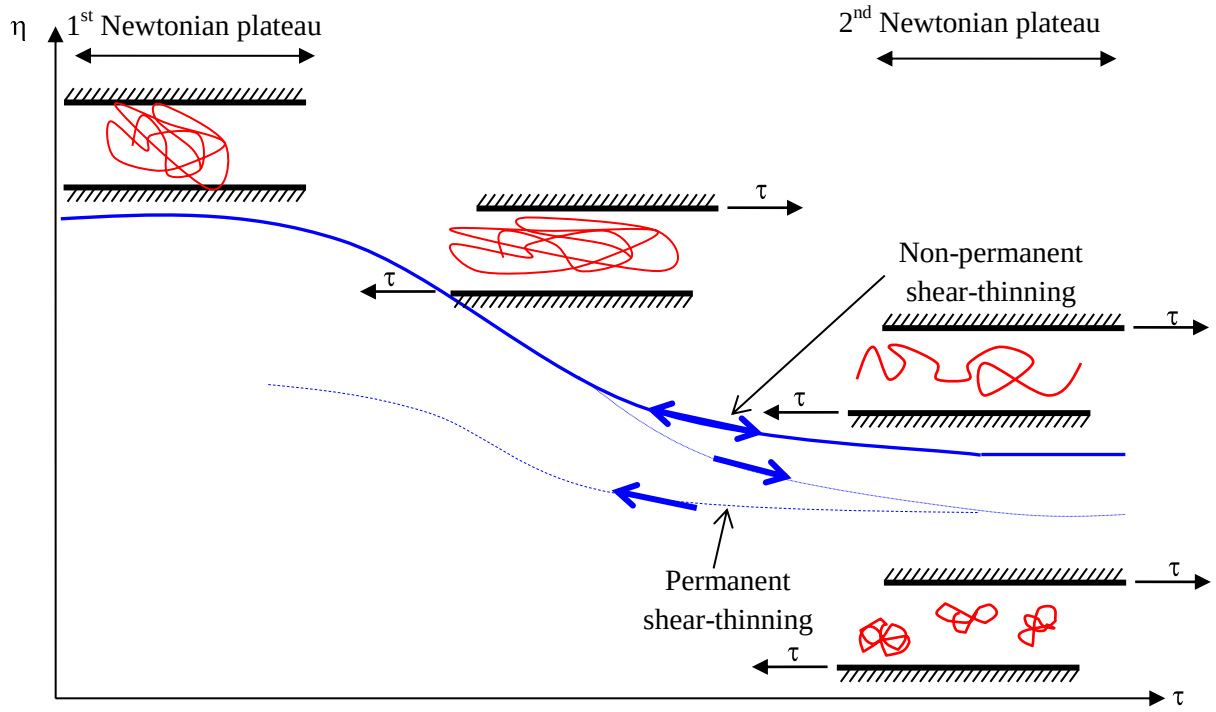


*Figure 28: Shear-thinning behavior of lubricants*

The viscosity of lubricants is highly dependent on shear stress, temperature and pressure. The following section describes some rheological models including the influence of all these parameters, individually and simultaneously.

## II.2.2 Rheological models for lubricants

Once a lubricant is rheologically characterized, it is of main importance to model its behavior in order to obtain accurate predictions of its viscosity in extended domains of temperature, pressure and shear stress comparable to the application conditions. This part is dedicated to the description of the most frequently used rheological equations for lubricating fluids at temperatures between -10 and 150 °C, pressures up to 800 MPa, shear rates going until $10^6$ $s^{-1}$ and for shear stresses up to 1 MPa. In the one hand, the temperature and the pressure dependencies on viscosity will be depicted and in the other hand, the relationships between viscosity and shear stress will be defined.

### *II.2.2.a Temperature and pressure influence*

#### *II.2.2.a.(i)* Temperature effect on viscosity

Many expressions of viscosity as a function of temperature have been proposed since 1840 by Poiseuille. Then, Slotte, Bingham, Batschinski, Groff, Walther and Mac Coull and many others tried to improve the relationship between viscosity and temperature [52]. Other developments came from Andrade [54] and Eyring [55] who applied the Arrhenius equation, based on the thermal activation theory for the transition of liquid molecules, to the viscosity of liquids:

Andrade
$$\eta_0(T) = \eta_\infty \exp\left(\frac{-E_a}{RT}\right) \qquad (13)$$

here, $\eta_0$ is the low shear viscosity, $\eta_\infty$ is the viscosity extrapolated to infinite temperature, $E_a$ the thermal activation energy, $R$ the gas constant and $T$, the temperature.

The Vogel, Tammann and Fulcher (VTF) [11] relationship introduces another constant:

VTF
$$\eta_0\ T\ = \eta_\infty \exp\left[\frac{D_F T_\infty}{T - T_\infty}\right] \qquad (14)$$

where $D_F$ is the fragility parameter, $\eta_\infty$ is the viscosity extrapolated to infinite temperature and $T_\infty$, the Vogel temperature at which the viscosity diverges.

An interesting modification of the VTF equation is the Williams, Landel and Ferry [56] (WLF) equation:

WLF
$$\eta_0\ T\ = \eta_g \exp\left[\ln\ 10\ \frac{C_1\ T - T_g}{C_2 +\ T - T_g}\right] \qquad (15)$$

where $T_g$ is the glass transition temperature at atmospheric pressure and taken as a reference state with the viscosity equal to $\eta_g$, the viscosity of the fluid at $T_g$. The glass transition temperature is the temperature above which a non-crystalline polymer material behaves rubbery or like a viscous fluid. Below the $T_g$, the polymer or the polymer solution looks like a brittle glass [57]. The parameters $C_1$ and $C_2$ are the universal WLF parameters. Williams *et al.* proposed limiting the use of this law for temperatures between $T_g$ and $T_g$+100 °C. This equation is an alternative to the thermal activation model based on the free volume theory. Doolittle [58] first introduced the free volume model:

Doolittle $$\eta_0 = A\exp\left[B\frac{v_o}{v_f}\right] \qquad (16)$$

with $A$ and $B$ are Doolittle constants depending on temperature, $v_f$ is the free volume available in the fluid for molecular transitions and $v_0$ is the occupied volume of closest packed liquid molecules ($v_f$=$v$-$v_o$ if $v$ is the total volume).

### *II.2.2.a.(ii)* Pressure influence on viscosity

In the Dowson and Higginson's book (1977) [59], the interest of inserting viscosity-pressure relationships in film thickness predictions has been fully described. Pioneer works, from the end of the 19th century and the first half of the 20th century, stressed the importance of using piezoviscous models because of the enhanced film thickness and load capacity. As a matter of fact, one of the fundamental features of elastohydrodynamic lubrication is that the viscosity of the lubricant increases significantly with pressure in the contact area. Many empirical correlations between viscosity and pressure were found and deeply detailed in [4]. Some of them were based on an exponential (Gatcombe, 1945; Sargent, 1983; Winer, 1984), others on a parabolic equation (Hersey and Lowdenslager, 1950) or on a power law (McEwen, 1952; Roelands, 1966) ([4], [60]). One of the most known relationships between viscosity and pressure is the empirical Barus [39] equation:

Barus $$\eta_0 \quad p \quad = \eta_{p=0} \ \exp \ \alpha p \qquad (17)$$

with $\alpha$ the piezoviscous coefficient. This equation supposes that the viscosity-pressure coefficient is constant but it is experimentally proven that it depends on temperature and pressure. Temperature and pressure must not be treated independently.

The viscosity-pressure dependence at constant temperature is estimated by the reciprocal asymptotic isoviscous pressure coefficient, $\alpha^*$. The relationship was proposed by Blok [61] in 1963.

$$\alpha^* = \frac{1}{\int_0^\infty \frac{\eta_{0(p=0)}}{\eta_0(p)}dp} \qquad (18)$$

This representative parameter can be introduced in EHD resolutions and can be calculated not only with all the others viscosity models but from experimental data

The exponential equation - actually, not always assigned to Barus - was often used in the analytical development proposed by Dowson and Higginson, derived from the Reynolds' equation, to obtain a correlation between pressure and viscosity. From Grubin (1949) to Chevalier (1996), those expressions have been used in the film thickness predictions in highly loaded contacts. As an illustration, all dimensionless film thickness relationships refer to the piezoviscous coefficient determined at the temperature of the contact inlet [60].

Finally, it was shown that none of the previous viscosity-pressure models are enough reliable for film thickness predictions [60]. First of all, they are empirical; then, equations do not fit over the entire temperature (> 150 °C) and pressure (> 500 MPa) domains. It is suggested that the deviations between the numerical EHD solutions and the experimental data come from the piezo-viscous models. We present in the next section, models considering both temperature and pressure influence on viscosity.

### *II.2.2.a.(iii)* Combined temperature and pressure dependences

Several models, based on the free volume concept, provide a good approach to evaluate the temperature and pressure dependence of viscosity with terms having a physical meaning. This part gives some equations and complementary models are described in [4] and in [13].

The Doolittle expression, written below, describes the dependence of viscosity on volume considerations. The occupied and free volumes are directly linked to pressure and temperature. The Tait equation of state accounts for these dependences:

Tait

$$\frac{V_{T,p}}{V_{T,p=0}} = 1 - \frac{1}{1+K_0'}\ln\left[1+\frac{p}{K_0}\ 1+K_0'\ \right] = \frac{\rho_{T,p=0}}{\rho_{T,p}}$$

$$\frac{V_{T,p=0}}{V_R} = \frac{\rho_R}{\rho_{T,p=0}} = 1 + a_V\ \ T - T_R \qquad (19)$$

$$K_0 = K_{00}\exp\ -\beta_K T$$

where $V_{(T,p)}$ is the total volume at $T$ and $p$, $V_{(T,p=0)}$ is the total volume at atmospheric pressure, $\rho_{(T,p)}$ is the density at pressure $p$, $\rho_{(T,p=0)}$ is the density at atmospheric pressure, $K_0$ is the isothermal bulk modulus at $p$=0, $K_{00}$ is $K_0$ at zero absolute temperature, $K_0'$ is the pressure rate of change of isothermal bulk modulus at $p$=0, $a_V$ is the thermal expansion defined for volume linear with temperature and $\beta_K$ is the temperature coefficient of $K_0$. The typical value of $K_{00}$ is 9 GPa and $\beta_K$ is usually close to $6.10^{-3}$ $K^{-1}$. $T_R$, $\rho_R$ and $V_R$ are the temperature, the density and the total volume at the reference state, respectively.

The use of a reference state leads to this modified Doolittle relationship:

Modified Doolittle

$$\eta_0(T,p) = \eta_R.\exp\left[BR_0\left(\frac{\frac{V_o}{V_{oR}}}{\frac{V_{T,p}}{V_R} - R_0\frac{V_o}{V_{oR}}} - \frac{1}{1-R_0}\right)\right] \qquad (20)$$

$$\frac{V_o}{V_{oR}} = 1 + \varepsilon\ \ T - T_R$$

where $B$ is the Doolittle parameter, $V_o$ is the occupied volume, $R_0$ is the occupied volume fraction ($V_o/V$) at the reference state and at atmospheric pressure and $\varepsilon$ is the occupied volume thermal expansion in the exponential term of Equation (13).
$V_{(T,p)}/V_R$ directly comes from the Tait equation (by multiplying the two first expressions in Equation (19)) and is replaced in the Doolittle formula. The parameters determined by least-mean square regression are $\eta_R$, $B$, $R_0$, $K_0'$, $K_{00}$ and $\beta_K$.

Another potential free volume model is the WLF expression modified by Yasutomi *et al.* [62] in 1984 to introduce the pressure dependence. This temperature-pressure-viscosity correlation is attractive for elastohydrodynamic lubrication analysis because it does not require an equation of state for the fluid.

WLF-Yasutomi

$$\eta_0(T,p) = \eta_g . \exp\left[ \ln(10) \frac{-C_1 (T - T_g(p)) F(p)}{C_2 + (T - T_g(p)) F(p)} \right] \qquad (21)$$
$$T_g(p) = T_g(0) + A_1 \ln(1 + A_2 p)$$
$$F(p) = 1 - B_1 . \ln(1 + B_2 . p)$$

where $T_g(p)$ is the glass transition temperature at pressure $p$, $\eta_g$ is the viscosity at the glass transition and $C_1$, $C_2$, $A_1$, $A_2$, $B_1$, $B_2$ are WLF numerical constants for each specific fluid. $F(p)$ is the dimensionless relative thermal expansion of the free volume and can also be defined as:

Relative thermal expansion of the free volume

$$F\ p = \frac{V \frac{dV_f}{dT}}{V_f \frac{dV}{dT}} \qquad (22)$$

Unlike Williams *et al.*, Yasutomi proposed to extend the application range of the temperature-pressure-viscosity relationship to temperatures up to $T_g$+300 °C, forsaking the universality of the parameters $C_1$ and $C_2$. This limit can vary depending on the nature of the fluid under study. Indeed, in case of oxidation or evaporation, this boundary is no longer valid. Moreover, this model is limited by phenomena of solidification at low temperature and at high pressure. Both conditions have to be examined to determine the limits of the model.

The original Yasutomi correlation suffers from the appearance of a zero in the function describing the pressure dependence of the relative free volume thermal expansivity. When the original correlation is employed, a fluid with a high inflection pressure lacks the inflection in the predicted pressure-viscosity behavior and a fluid with a low inflection pressure is predicted to have two inflections. A new function $F_m$ removes these concerns and provides improved precision without the need for an equation of state. The improved function gives a more faithful representation of viscosity at even low pressures [**12**] that contributes to a large extent in the $\alpha^*$ calculation.

Modified WLF-Yasutomi

$$\eta_0(T,p) = \eta_g . \exp\left[ \ln(10) \frac{-C_1 (T - T_g(p)) F_m(p)}{C_2 + (T - T_g(p)) F_m(p)} \right] \qquad (23)$$
$$T_g(p) = T_g(0) + A_1 \ln(1 + A_2 p)$$
$$F_m(p) = (1 + B_1 p)^{B_2}$$

The Roelands [**63**] empirical model describing viscosity in function of pressure deserves to be quoted because it was considered as the most reliable relationship during many years for temperatures up to 150 °C and pressures up to 300-500 MPa [**60**] but is not enough accurate for pressures above 500 MPa.

Roelands

$$\eta_0(T,p) = \eta_p \cdot \left(\frac{\eta_R}{\eta_p}\right)^{\left[\left(\frac{p_p - p}{p_p}\right)^Z \cdot \left(\frac{T_R - T_\infty}{T - T_\infty}\right)^S\right]} \quad (24)$$

where $\eta_P$ is the pole viscosity, located at the intersection of pressure-viscosity isotherms when extrapolated to negative pressures, occurring at the pole pressure $p_P$. $Z$ is the pressure-viscosity index and $S$ is the slope index. $\eta_R$ is the reference viscosity at the reference temperature $T_R$. $T_\infty$ is the divergence temperature. $\eta_P$, $p_P$ and $T_\infty$ are universal parameters equal to $6.31.10^{-5}$ Pa.s, -0.196 GPa and -135 °C respectively. Consequently, in this model only three parameters ($Z$, $S$ and $\eta_R$) are required.

### *II.2.2.b Shear stress dependence*

Shear stress, another important parameter which can have a strong influence on viscosity, is under study in this section. Empirical shear-thinning models will be detailed.

The power law (Otswald de Waele [13]) is a commonly used equation to evaluate the viscosity in function of the shear rate. It can also be expressed in function of the shear stress.

Power law

$$\eta(\dot{\gamma}) = \eta_0(\lambda\dot{\gamma})^{n-1} \quad (25)$$

$$\eta(\tau) = \eta_0\left(\frac{\tau}{\tau_c}\right)^{1-\frac{1}{n}} \quad (26)$$

where $\dot{\gamma}$ is the shear rate, $\tau$ the shear stress, $\eta_0$ the low shear stress viscosity depending on temperature and pressure (it should be written as $\eta_0(T, p)$), $n$ the power law exponent, $\lambda$ a characteristic time and $\tau_c$ a characteristic stress. Bair [13] explains that $\lambda$ can be associated to the relaxation time of the fluid and $\tau_c$ to $G$, the shear modulus.

With $\eta_0$ the Newtonian viscosity at low shear rate and $\eta_2$ the viscosity of the second Newtonian plateau, Cross [64] proposed:

Cross

$$\eta(\dot{\gamma}) = \eta_2 + \frac{\eta_0 - \eta_2}{1 + (\lambda\dot{\gamma})^{1-n}} \quad (27)$$

Ellis [65] modified this equation to obtain the dependence with the shear stress instead of the shear rate:

Ellis

$$\eta(\tau) = \eta_2 + \frac{\eta_0 - \eta_2}{1 + \left(\frac{\tau}{G}\right)^{\left(\frac{1}{n}-1\right)}} \quad (28)$$

Carreau suggested in 1972 another way to express the dependence of viscosity on shear rate [66]:

Carreau
$$\eta\ \dot{\gamma}\ = \eta_2\ + \frac{\eta_0 - \eta_2}{1 + \ \lambda\dot{\gamma}\ ^{\ 2}\ ^{\frac{1-n}{2}}} \tag{29}$$

In 1981, a modification of the Carreau equation was operated by Yasuda [14] to provide a better representation of the width of the transition between the zero-shear rate viscosity and the power-law regions:

Carreau-Yasuda
$$\eta\ \dot{\gamma}\ = \eta_2 + \frac{\eta_0 - \eta_2}{1 + \ \lambda\dot{\gamma}\ ^{\ a}\ ^{\frac{1-n}{a}}} \tag{30}$$

where $a$ is a parameter mainly impacting the slope of the shear-thinning behavior.

Later on, Bair *et al.* [67] changed Equation (29) to get a shear stress dependence of the viscosity:

$$\eta\ \tau\ = \eta_2 + \frac{\eta_0 - \eta_2}{\left(1 + \left(\frac{\tau}{G}\right)^2\right)^{\frac{\frac{1}{n}-1}{2}}} \tag{31}$$

Then, Bair wrote the generalized Carreau-Yasuda equation in function of shear stress [13]:

$$\eta\ \tau\ = \eta_2 + \frac{\eta_0 - \eta_2}{\left(1 + \left(\frac{\tau}{G}\right)^a\right)^{\frac{\frac{1}{n}-1}{a}}} \tag{32}$$

The modified version of the Carreau-Yasuda formula by Bair suits well for EHL solvers.

Since it is not so easy to reach experimentally the second Newtonian plateau under shear stress, the previous equations can be utilized with $\eta_2$ equals to zero. All the models presented in part II.2.2 fully describe the rheological behavior of fluids under severe conditions. The Newtonian viscosity at low shear rate $\eta_0$ can be determined from *T-p* expressions described in II.2.2.a.(iii) and then, inserted in shear-thinning relationships.

Complementary models can be found in [13] and [68].

The following part describes the instruments allowing the measurement of the viscosity in function of temperature, pressure and shear stress, necessary for the definition of the models.

## II.2.3 Rheometers

Rheometers are instruments measuring stress and deformation history of a material in response to applied forces. They measure the viscosity under shear stress or under extensional forces. In this work, many rheometers were used both at atmospheric pressure and at high pressure.

### *II.2.3.a Atmospheric pressure rheometers*

At atmospheric pressure, capillary viscometers measuring kinematic viscosity (KV) (see Appendix B-1 ), a High Temperature High Shear rate viscometer (HTHS) (Appendix B-2), an Ultra-Shear Viscometer (USV) (Appendix B-3) and a Cold Cranking Simulator (CCS) (Appendix B-4) are industrial standard tests used to verify and adjust the engine requirements.

Another device employed to measure the temperature dependence of the viscosity of polymer-thickened base oil solutions at atmospheric pressure is the Anton-Paar rotational rheometer (Physica MCR 301) (Figure 29).

*Figure 29: Picture of the Anton-Paar rheometer*

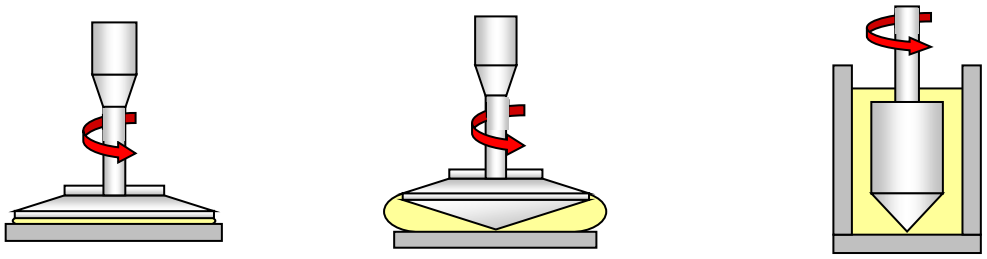

*Figure 30: Anton-Paar geometries (plate-plate; cone-plate, coaxial cylinders)*

Several geometries are commonly used: plate-plate, cone-plate and coaxial cylinders (Figure 30). Measurements were preferentially performed on the latter geometry. The viscosity is directly related to the dimensions of the cylinders.

$$\eta = \frac{M_t}{4\pi h_i \Omega}\left(\frac{1}{R_i^2} - \frac{1}{R_e^2}\right) \quad (33)$$

where $M_t$ is the torque to the inner cylinder, $h_i$ is the height of the inner cylinder, $\Omega$ is the angular speed, $R_i$ is the radius of the inner cylinder and $R_e$ is the radius of the outer cylinder. Two different cases have to be distinguished: either the torque of the inner cylinder is imposed or the angular speed is applied.

Temperature was varied from -10 to 150 °C, regulated by a Peltier system. Shear rate ranged from $10^{-2}$ $s^{-1}$ and 1000 $s^{-1}$ and is imposed by an electrically commutated motor. Shear stress changed from 0.01 to 100 Pa. The statistical uncertainty on the measurements was less than 2 %.

### *II.2.3.b Elevated pressure rheometers*

Two devices were used to study the viscosity under high pressure: a falling-body viscometer (HP-Visco) (Figure 31) and a Couette rheometer (Figure 32).

The first instrument is a falling-body viscometer and it measures the viscosity of fluids from atmospheric pressure up to 800 MPa. The pressure is applied by a pressurizing hand pump thanks to a hydraulic liquid and an intensifier. The resolution of the pressure transducer with digital display is 1 MPa and the accuracy on pressure is 1%. Temperature was varied from 40 °C to 150 °C, measured with a type K thermocouple (the accuracy of the temperature sample is considered to be ± 0.3 °C) and controlled by heated air flow forced through passages in the vessel. Three falling bodies were available to cover different viscosity domains and provide shear stresses, due to gravity, between 1.5 and 70 Pa. The statistical uncertainty on the viscosity was always below 4 %.

This viscometer was made by Dr. Scott Bair at Georgia Institute of Technology, Atlanta. A complete description of the principle of operation can be found in [13]. The experiment, perfected by Bridgman [69], consists in measuring the falling time of a stainless steel cylindrical sinker in a cylindrical cartridge containing the fluid under study. Several shapes of sinkers (cup, solid and hollow) were chosen to cover a wide window of viscosity. The position of the magnetic sinker is detected by an inductive LVDT (Linear Variable Differential Transformer) system and transcribed on an oscilloscope screen. From the falling time $t$ of a sinker required for a change of LVDT conditioned output of 100 mV, the density of the fluid $\rho$, that of the sinker $\rho_s$ and from a calibration constant $C$ (determined for standard liquids like octane [70] or diisodecylphtalate (DIDP), sample C [71]), the viscosity $\eta$ is calculated:

$$\eta = C.t.\frac{\rho_s - \rho}{\rho_s} \quad (34)$$

a)

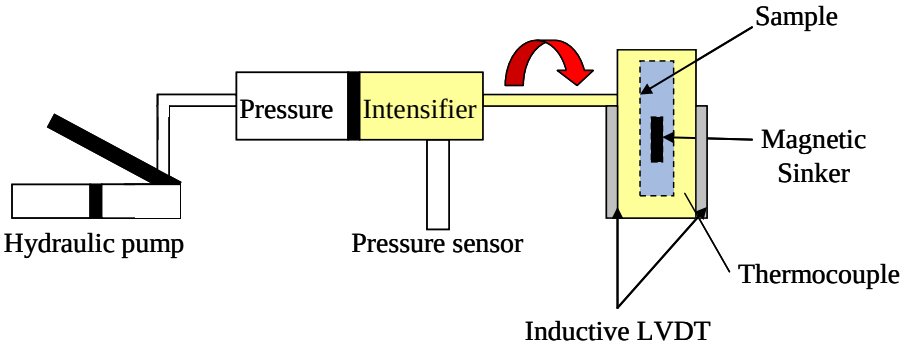


b)

*Figure 31: a) Picture b) Scheme of the high pressure falling-body viscometer (HP-visco)*

The second high pressure device is a Couette rheometer (Figure 32). It was specifically designed for this work by Dr. Scott Bair and was fully depicted in [72].

It allows exploring the shear stress influence (with an applied shear rate) on viscosity at pressures from 200 to 500 MPa. The pressure transducer with digital readout has a resolution of 1 MPa and an accuracy of 1%. No measurement can be run at atmospheric pressure because of the insufficient torque sensitivity and because of the possible occurrence of cavitation [73]. The pressure is applied through a solution of perfluorinated octane FC77 + 10% of Fomblin which is of much larger density and much lower viscosity than the sample, a pressurizing hand pump and an intensifier. Note that most of the lubricants are not soluble in this solution and thereby, the risk to mix with the sample is minimized.

Temperature is limited to 25°C and 40 °C. It is imposed by four copper cartridges surrounding the pressure vessel and measured with a type T thermocouple (the accuracy of the temperature sample is considered to be ± 0.1 °C).

The fluid under study is filled between the two cylinders. The inner cylinder is rotated by a stepper motor by means of a drive shaft. The outer cylinder is connected to strain gages measuring the torque. Four cylinder sets were used to cover an extended range of shear stresses (see appendix C-2). Their shearing gaps vary from 13.4 µm for the “low shear stress cylinder set” to 2.3 µm for the "extra shear stress cylinder set". The most used cylinder set was the “middle shear stress cylinder set” with a shearing gap of 5.1 µm resulting in a shear stress range from $10^3$ to $10^5$ Pa. Because of the small gaps, the high shear rates and the high viscosities, thermal softening can happen. To limit this phenomenon, high thermal conductivity copper or silver alloys were used for the cylinders and hard chrome was

chosen to coat the working surfaces. Details on materials, plating, dimensions of the cylinder sets, shear stress ranges, etc. are provided in Appendix C-1. The statistical uncertainty on the viscosity measurements was below 5 %.

a)

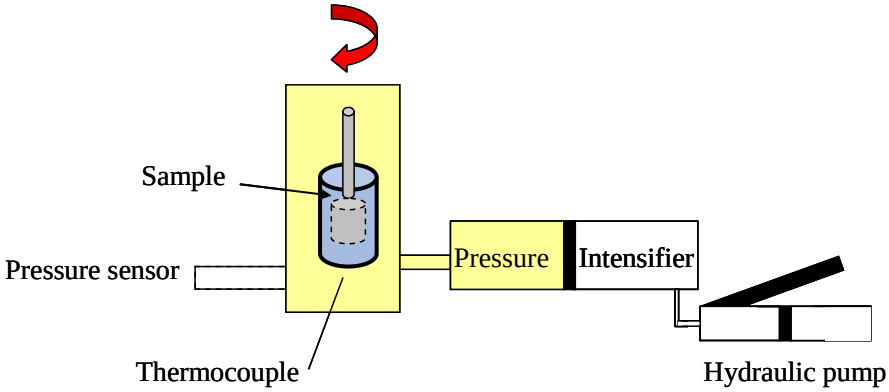


b)

*Figure 32: a) Picture b) Scheme of the high pressure Couette rheometer*

All the previously detailed test-rigs were used to characterize several solutions depicted in the last part of this chapter to measure the viscosity in function of temperature, pressure and shear stress. In order to understand the relationship between physico-chemistry of polymer solutions and rheology, some specific concepts have to be considered.

# *II.3 Physico-chemistry of polymers and polymer solutions*

This section explains some basic notions necessary to the understanding of phenomena described in the parts IV and V.

## II.3.1 Generalities

Among the characteristics of polymers, the molecular weight and the molecular weight distribution are of primary importance. Many properties of the polymer can be predicted if they are well known. There are two ways to determine the molecular weight of a polymer: the number-average molecular weight and the weight-average molecular weight [74].
The division of the total mass by the total number of monomers gives the number-average molecular weight $\overline{M_n}$.

$$\overline{M_n} = \sum_i n_i M_i = \frac{\sum_i N_i M_i}{\sum_i N_i} \qquad (35)$$

where $n_i$ is the mole fraction of polymers *i*, which molecular weight is $M_i$ and $N_i$ is the number of polymers *i*.

If the molecular weight of each species is weighted by its weight fraction, the weight-average molecular weight $\overline{M_w}$ is calculated.

$$\overline{M_w} = \sum_i w_i M_i = \frac{\sum_i N_i M_i^2}{\sum_i N_i M_i} \qquad (36)$$

The relationship between $\overline{M_n}$ and $\overline{M_w}$ depends on the molecular weight distribution. The ratio $\overline{M_w} / \overline{M_n}$ is called the polydispersity index (*PDI*). It is always superior or equal to one because $\overline{M_w}$ is always superior or equal to $\overline{M_n}$. It indicates the distribution of individual molecular masses of the macromolecules in a batch of polymers.

## II.3.2 Conformation and size

### *II.3.2.a Molecular architectures*

Polymers can take several structures drawn on Figure 33. They can be linear, branched, cross-linked, star or ladder-shaped [74]. In a linear polymer, each monomer is linked only to two others. If the chains grow from the main molecule skeleton at irregular intervals, the polymer is named branched. If the branches are short, the polymer is a comb. On the contrary, if the side chains are long, it is a long branched polymer. In the case of long chains connecting one to another, a three-dimensional structure is created. Polymer chains are linked to form a giant molecule network whose molecular weight is infinite. They are called thermosetting polymers. Because of their structure, they

cannot be dissolved in solvents and they cannot be melted by heat. Polymers can also look like a star if several (≥ 3) long chains are linked and cross at one point. This "point" can be one or more molecules constituting the "core" of the star shape. A ladder polymer is made of two parallel chains with regular crosslinks in between [74]. This list can be completed by brush polymers, ring polymers and coil-cycle-coil polymers.

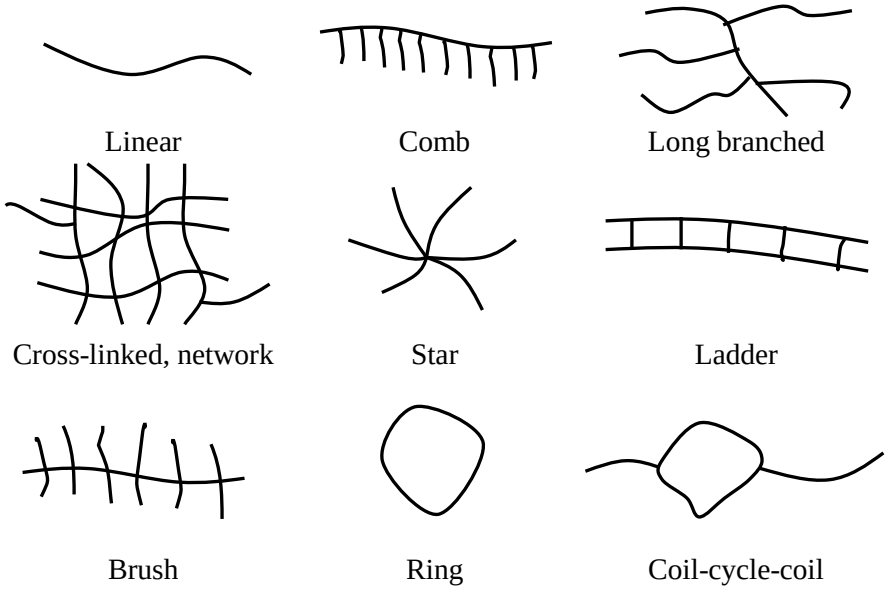


*Figure 33: Schematic representation of polymer conformations*

The size of macromolecules is an additional property interesting to study. The following section deals with the radius of gyration and the hydrodynamic radius of polymers.

### *II.3.2.b Radius of gyration and hydrodynamic radius*

The dimensions of polymer coils are often described in terms of the root mean square distance of a chain segment from the center of mass of the molecule [74]. The radius of gyration $R_g$ is a geometric and intrinsic definition of the size of a polymer coil. The following equation is given for unperturbed polymer molecules, in the absence of interactions with solvent or some imposed field. Further information on chain conformations under external actions can be found in [15]. A macromolecule can be identified with $i$ repeating units of mass $m_i$ located at distances $r_i$ from its center of mass: $R_g$ is calculated [75] as the root mean square (rms) distance of the polymer entities from its center of gravity.

$$\left\langle R_g^2 \right\rangle = \frac{\left\langle \sum_i m_i r_i^2 \right\rangle}{\sum_i m_i} \qquad (37)$$

The radius of gyration has the advantage that it also can be used to characterize the dimensions of branched and cyclic molecules. Moreover, properties of dilute polymer solutions that are dependent on the chain dimensions are controlled by the radius of gyration rather than the end-to-end root mean square distance [9], [74].

Flory [Flo53] specified three limit cases for the solubility of polymers in a solvent and determined three corresponding formulas for the radius of gyration.

He defined "good solvents" as solvents in which the attraction between polymer segments and solvent molecules is greater than intramolecular interactions in the polymer itself. In that case, the coils swell.

In "theta solvents", the attraction between polymer segments themselves is preferred from that with the solvent. There is a temperature, called theta temperature, at which a polymer solution behaves like an ideal solution: long-range interactions have no effect on the size of the macromolecules and the coils are in an unperturbed state. The chain size depends only on short range interactions that occur between neighboring atoms and groups [74] and that induce a contraction of the coils.

For a "bad solvent" - or poor solvent - the interaction between the coil and the solvent is negligible compared to the interaction inside the coil itself. The polymer bead totally collapses and the coils and the solvent are in two separate phases.

Flory [Flo53] proposed a way to calculate the radius of gyration $R_g$ from parameters such as $N$ and $l$, with $N$ the number of monomers ($N=M_w/m_0$ with $m_0$ the molecular mass of one monomer) and $l$ the mean monomer size.

The following scaling laws have to be taken with caution because they have been established for linear molecules and thus are neither so accurate nor rigorous for branched polymers. Actually, the equations only give an order of magnitude of the radius of gyration. Indeed, they should be multiplied by the square root of the characteristic ratio $C_\infty$ representing the flexibility of the molecule depending on its chemical nature. This quantity is not well known because of the complexity and the uncertainties of the molecular structures.

Bad solvent $$R_g \propto N^{0.33} l \qquad (38)$$

Theta solvent $$R_g \propto \frac{1}{\sqrt{7}} N^{0.5} l \qquad (39)$$

Good solvent $$R_g \propto \frac{1}{\sqrt{6}} N^{0.6} l \qquad (40)$$

The hydrodynamic radius $R_h$ represents the effective size of the polymer molecules moving in their environment (solvent, temperature, pressure…). The polymer coil is hypothetically represented by a hard sphere.

The relationship between the two dimensions of a polymer is:

Sphere $$R_g = 0.77 R_h \qquad (41)$$

Random coil $$R_g = 1.54 R_h \qquad (42)$$

## II.3.3 Concentration considerations

Concentration of polymers in solution is of main interest because it strongly influences the nature of the physical phenomena involved in the mixture. Consequently, it has a deep effect on the rheological behavior of the solution.

### *II.3.3.a Critical concentration*

The critical concentration $c^*$ is the limit between the dilute regime where the coils are totally separated from the semi-dilute regime in which the coils start to overlap and entangle, as shown on Figure 34. Obviously, the threshold is not sharp; there is a region of crossover between the different regimes [15].

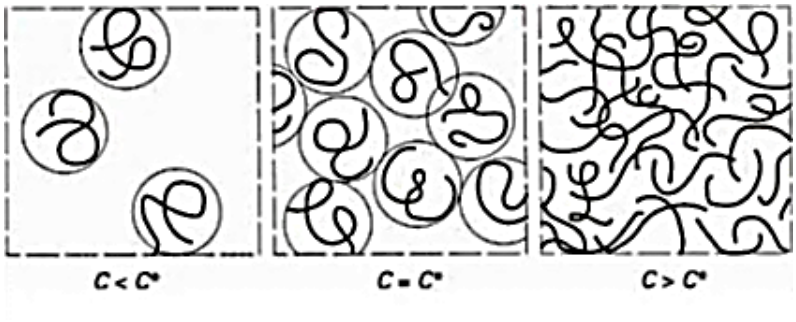


*Figure 34: Concentration regimes in polymer solutions (from left to right: dilute, onset of overlap and semi-dilute), [15]*

Several ways to calculate of the critical concentration exist, such as considering that $c^*$ is reached when the solution viscosity is roughly twice the solvent viscosity [76]. Alternatively, the critical concentration can be calculated from geometric considerations [77]:

$$c^* = \frac{M_w}{N_a \frac{4}{3}\pi R_g^3} \qquad (43)$$

where $M_w$ is the molecular weight of the polymer, $R_g$ is its radius of gyration and $N_a$ is the Avogadro number. Indeed, in the dilute regime, polymer molecules stay far from each other. Their size is significantly equal to the size of the isolated molecule. Considering that the polymer coil is a sphere, its volume equals:

$$V_{coil} = \frac{4}{3}\pi R_g^3 \qquad (44)$$

The concentration of one molecule is its mass ($M_w/Na$) divided by its volume. The critical concentration will be calculated for each polymer in the two extreme Flory cases for a polymer solubilized in a solvent (“theta solvent” and “good solvent” conditions, Equations (39) and (40)).

### *II.3.3.b Viscosity of dilute polymer solutions*

All the following equations aim at establishing relationships between viscosity and the hydrodynamic radius via physical or geometric parameters.

The Kirkwood approximation states that a dilute solution of polymers behaves hydrodynamically like a collection of impenetrable solid spheres of radius *R*. A calculation by Einstein suggested that the viscosity of the solution $\eta_{solution}$ has the form [15]:

$$\eta_{solution} = \eta_{solvent}(1+2.5\phi) \tag{45}$$

and

$$\phi = \frac{c}{M}\frac{4}{3}\pi R_{coil}^3 \tag{46}$$

where $\Phi$ is the volume fraction occupied by the spheres, *c* the concentration and *M* is the molecular mass of one molecule ($M=M_w/N_a$).

As described in part II.3.2.b, the radius of a randomly coiling macromolecule can be the root-mean-square end-to-end distance or we can choose the hydrodynamic radius $R_h$. The equation of the volume fraction becomes:

$$\phi = \frac{c}{M}\frac{4}{3}\pi R_h^3 \tag{47}$$

For given polymer, solvent, temperature, pressure and at zero shear stress, the intrinsic viscosity is defined as the specific hydrodynamic volume of the polymer at infinite dilution. It refers to the volume that one gram of a macromolecule would occupy in solution if it was totally isolated from the other coils [78]. Important formulas are listed below:

$$\eta = \lim_{c\to 0}\eta_{red} \tag{48}$$

$$\eta_{red} = \frac{\eta_{sp}}{c} = \frac{\eta_{solution}-\eta_{solvent}}{\eta_{solvent}c} \tag{49}$$

$$\eta_{sp} = \frac{\eta_{solution}-\eta_{solvent}}{\eta_{solvent}} \tag{50}$$

$$\eta_r = \frac{\eta_{solution}}{\eta_{solvent}} \tag{51}$$

where $[\eta]$, $\eta_{red}$, $\eta_{sp}$, $\eta_r$, $\eta_{solution}$ and $\eta_{solvent}$ denote respectively the intrinsic viscosity, the reduced viscosity, the specific viscosity, the relative viscosity, the viscosity of the solution and that of the solvent.

Several equations, specific to polymers, are mostly used for the determination of the intrinsic viscosity because of their easy use:

Huggins [79] $$\eta_{red} = \eta + k_H \eta^2 c \quad (52)$$

Kraemer [80] $$\ln(\eta_r) = c\,\eta - k_K \eta^2 c^2 \quad (53)$$

Martin [81] $$\ln(\eta_{red}) = \ln \eta + k_M c\,\eta \quad (54)$$

where $k_H$, $k_K$ and $k_M$ represent the Huggins, the Kraemer and the Martin constants respectively.

Combining the Einstein's equation (45) with the intrinsic viscosity formula (Equations (48) and (49)), the calculation of the hydrodynamic radius is direct:

$$R_h = \left( \frac{\eta M_w}{2.5 \frac{4}{3} \pi N_a} \right)^{1/3} \quad (55)$$

Derived from Equation (55), the Flory-Fox equation is commonly written as follows:

$$R_h = \frac{1}{\sqrt{6}} \left( \frac{\eta M_w}{\Phi_0} \right)^{1/3} \quad (56)$$

*With the universal Flory constant $\Phi_0 = 2.5.10^{23}\ mol^{-1}$*

As the Mark-Houwink-Sakurada relation suggests [9], the intrinsic viscosity is directly related to the molecular weight of the polymer:

$$\eta = KM^a \quad (57)$$

where *K* and *a* are empirical constants listed in [82]. *a* varies from 0.5 (in theta conditions) to 0.8 for different polymer-solvent combinations.

## II.3.4 Temperature considerations: LCST

According to IUPAC, the LCST (Lower Critical Solution Temperature) is the critical temperature above which the components of a polymer solution are no longer miscible: when the LCST is approached from below, the polymer molecules tend to collapse and their hydrodynamic radii decrease. For temperatures higher than the LCST, the polymer and the solvent separate into two distinct phases. This behavior is well-known for water-soluble polymers such as poly(N-

isopropylacrylamide) [83] or polyoxyethylene [84] but it can also occur for polymers in organic solvents [82]. The typical cloud-point diagram is drawn in Figure 35.

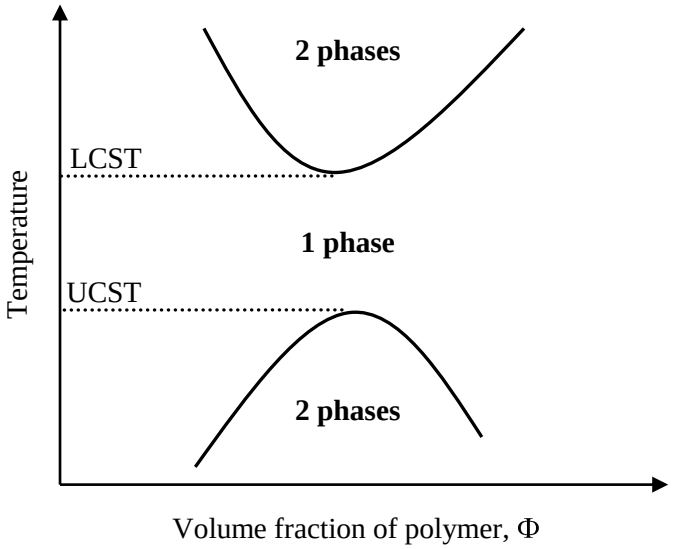


*Figure 35: Cloud-point diagram for a polymer solvent system*

There are several reasons why a LCST can be found in polymer solutions. As discussed in [85], two different cases have to be distinguished depending if the polymer and the solvent have the same polarity, or if one is polar and the other one non-polar.

In the first case, the separation of polymer/solvent systems into two phases as the temperature rises occurs because the thermal agitation prevents physical interactions. Hydrogen bonds typically break at 100 °C and dipole moments cannot align anymore, especially in polymers soluble in water.

In the second case, the thermal expansions of the polymer and the solvent are different. The solvent expands much more than the polymer, because the latter is restrained by its intramolecular and intermolecular bonds. Therefore, the number of solvent molecules that can be in interaction with any given monomer decreases as the temperature increases.

The influence of pressure has also to be considered in phase separation. Wolf [86] evidenced that pressure leads to changes in the demixing conditions for polymer solutions.

The UCST (Upper Critical Solution Temperature) is the critical temperature above which the components of a mixture are miscible in all proportions, according to IUPAC. Below this temperature, one phase of polymer coexist with another one of solvent. Polymer solutions can undergo demixing when cooling a homogeneous solution as well as when heating such a solution. The corresponding cloud-point curves display a maximum (UCST behavior) or a minimum (LCST behavior). For common polymer solutions, the LCST region is at higher temperature than the UCST region [82]. Polymer mixtures may exhibit a variety of coexistence behavior, including upper critical solution temperatures (UCSTs), lower critical solution temperatures (LSCTs), and a combination of both [87]. The temperature range between the UCST and LCST may be quite sensitive to changes in pressure or to component molecular weight.

# *II.4 Simplified lubricants*

As described in section "*II.1.4.d* Rheology modifiers", several types of polymers are currently used in engine lubricants to improve the viscosity of the base oil and to reduce the dependence of the lubricant on temperature.

In this investigation, mixtures of base oil and polymer were considered as simplified automotive lubricants. All materials were provided by Total and are property of Total. The base oil is a hydrocracked mineral base oil, from group III (API classification, cf. Table 2, p. 54). Three polymers with different conformation, chemistry and structure were chosen: a comb poly(alkylmethacrylate) (PAMA) (with comb branches made of $C_{16}$, $C_{12}$, $C_{14,}$ $C_{17,}$ $C_{13}$, $C_{15}$ in the decreasing percentage of the total side chains and with the presence of short chains such as $CH_3$ or $C_4$) which has a polar side due to the oxygen atoms in the ester group close to the backbone, a linear olefin copolymer (OCP) made of 40% in weight of ethylene and 60% in weight of propylene and a star-shaped poly(isoprene-styrene-hydrogenated) (PISH) on a styrene core. They were utilized as liquid polymers, previously diluted in another base oil (group III, API classification), chemically close to the hydrocracked mineral base oil. The final polymer concentration in the mineral base oil is 1.2% w/w, typical of automotive applications. A forth polymer - polyisobutylene (PIB) - was used for comparison purpose in the section dealing with LCST. It was fractionated from a BASF sample. Weight average molecular weights $M_w$ and polydispersity indexes (*PDI*) are detailed below.

| | **PAMA** | **OCP** | **PISH** | **PIB** |
|---|---|---|---|---|
| **Chemical formula** | 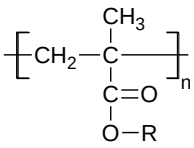 R=$C_{12}$ to $C_{17}$ Polar | 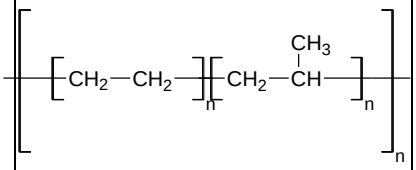 40% ethylene-60% propylene (in weight) | 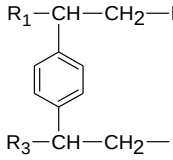 $R_1$,$R_2$,$R_3$,$R_4$= diene/styrene/diene copolymers (hydrogenated) | 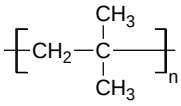 |
| **Molecular structure** |  |  | 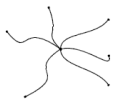 | |
| | Comb | Linear | Star | |
| **$M_w$ (g/mol)** | 400 000 | 88 420 | 413 500 | 62 300 |
| **PDI** | ≈ 2 | 1.6 | 1.1 | 1.4 |

*Table 4: Polymers characteristics*

Besides the neat base oil, the studied solutions were: the PAMA, the OCP, the PISH, a mixing of OCP and PISH (50/50, w/w) thickened solutions in the base oil, a solution of PIB in heptane and finally, a blend of PIB and cyclopentane. The concentration of all the polymer solutions was 1.2% w/w.

The case of fully formulated lubricants containing additives will be briefly discussed in section *IV.2*. Functionalizing additives as described in part II.1.4 were used: antiwear, extreme pressure, friction modifiers, detergents, dispersants, antioxidants, anticorrosion, anti-foam and pour point depressants. A package of additives (8.65 % in weight of the fully formulated solution) was mixed with the base oil, the PAMA and the OCP+PISH (50/50) solutions.

# III Rheological experiments and models

Establishing accurate rheological models for a polymer-thickened base oil at high temperature, high pressure and high shear stress is of primary importance to guide oil manufacturers in matching the Viscosity Index Improvers (VII) of the lubricant to the engine specifications.

One of the purposes of this research is to analyze the effect of temperature, pressure and shear stress over a wide window of operating conditions representative of the severe regimes in automotive engines. The present chapter is dedicated to both experimental measurement and modeling of the rheological behavior of dilute polymer-base oil solutions used for real automotive applications.

This chapter is divided into two parts: one dealing with the viscosity measurements and models at atmospheric pressure and another one outlining the rheological behavior of polymer solutions and their modeling at elevated pressure.

# *III.1 Rheological behavior at atmospheric pressure*

The temperature dependence of $\eta_0$, the low shear viscosity at atmospheric pressure, was obtained from measurements performed on the Anton-Paar rheometer. The evolution of the viscosity versus temperature is plotted on Figure 36 for the PAMA solution. The viscosity declines drastically as temperature increases. Indeed, as temperature rises, the volume of the solution increases (cf. Tait equation in part *II.2.2.a.(iii)*), mainly caused by the raise of the volume of the solvent. Therefore, the number of potential collisions between polymer coils drops, the transfer of momentum from one layer to another - occurring by molecular collisions - levels off and the viscosity collapses [16].

The results are fitted to the Vogel-Tamman and Fulcher (VTF) relationship [11] (Equation (14), p. 66) detailed in section *II.2.2.a* by the ordinary least mean square method. The relevance of the VTF model over the Arrhenius model was shown in [13] for a typical base oil and confirmed in Figure 36 for the studied base oil. Figure 36 also shows the temperature dependence of the viscosity for the PAMA solution. These curves justify the term “viscosity index improver (VII)” because the addition of polymer reduces the temperature dependence of the viscosity (at 40°C, the addition of PAMA involves a rise of viscosity of 13% compared to the base oil and at 150 °C, the viscosity of the PAMA solution is 40% higher than that of the base oil). Viscosity indexes are listed in Table 5 (p. 89): that of the base oil is 128 whereas that of polymer-thickened base oil mixtures is close to 170. The addition of polymers highly increases the viscosity index. OCP and PISH solutions behave similarly and the VTF equation fits the experimental data quite well for all the liquids.

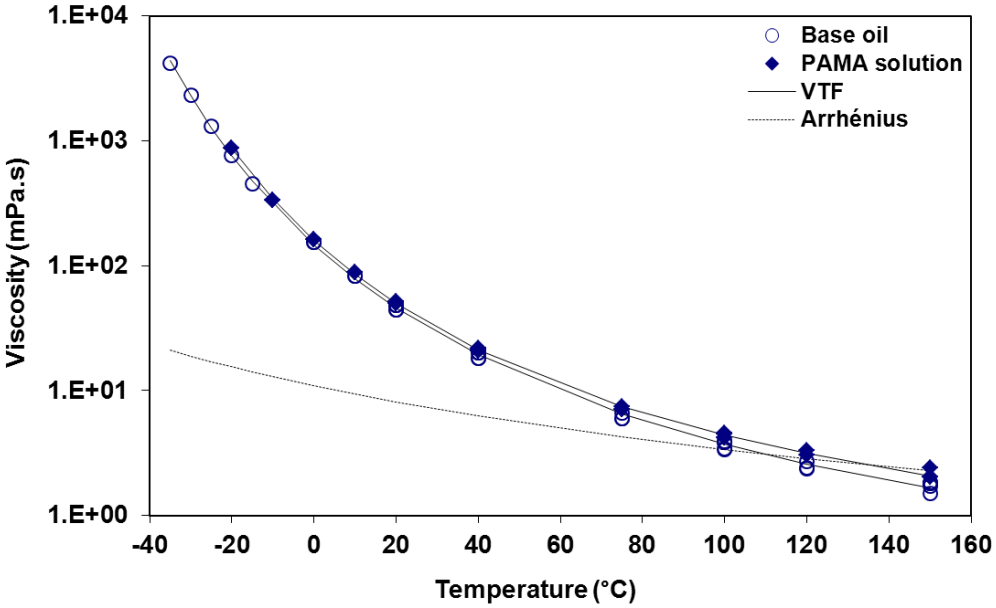


*Figure 36 : Viscosity of the base oil and the PAMA - thickened base oil at different temperatures fitted by the VTF equation. Viscosity of the base oil fitted by the Arrhenius equation*

Many standard tests - detailed in appendices B-1, B-2 and B-4 - are usually run on lubricants to match the rheological engine requirements. The viscosities are calculated from the kinematic viscosities (KV) at 40 and 100 °C thanks to Equation (10) (p. 64) and presented for the PAMA-thickened solution in Figure 37. The Anton-Paar rheometer (cf. *II.2.3.a*) data are added along with the high pressure falling body viscometer (HP-Visco) results at atmospheric pressure. Further data can be found in Appendix D.

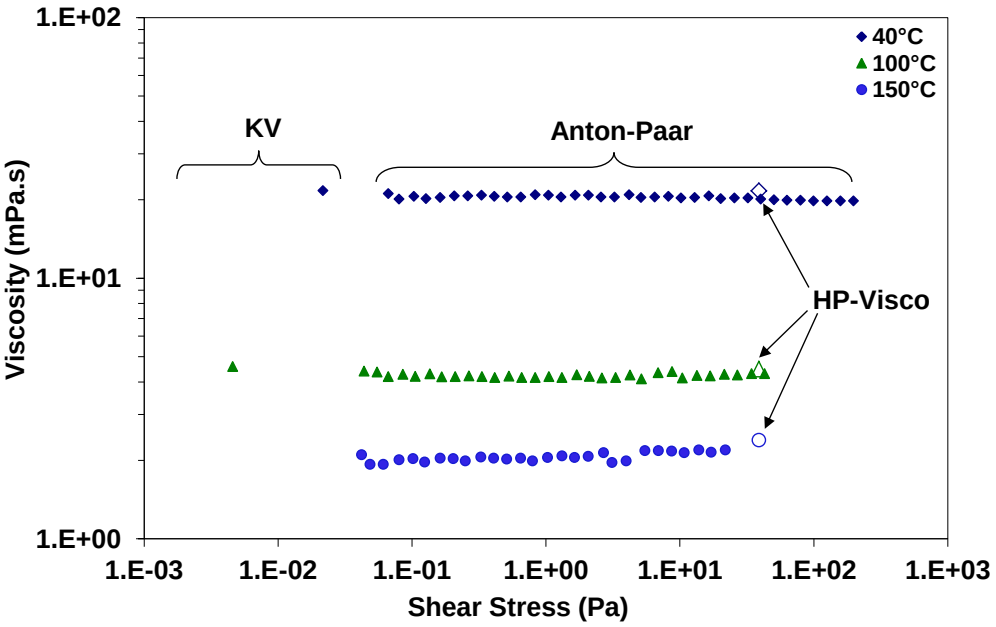


*Figure 37: Rheological behavior of the PAMA - thickened base oil at different temperatures and at atmospheric pressure*

The kinematic viscosities, the viscosity index, the HTHS data and the CCS results for the base oil and the polymer solutions are listed in Table 5.

| | **KV 40 (cSt)** | **KV 100 (cSt)** | **VI** | **HTHS (mPa.s)** | **CCS (mPa.s)** | | |
|---|---|---|---|---|---|---|---|
| ***T (°C)*** | *40* | *100* | | *150* | *-15* | *-25* | *-35* |
| **Base oil** | 24.3 | 4.9 | 128 | 1.7 | 4.5E+02 | 1.3E+03 | 4.2E+03 |
| **Base oil + PAMA** | 26.4 | 5.8 | 172 | 1.9 | 5.1E+02 | 1.4E+03 | 4.4E+03 |
| **Base oil + OCP** | 52.4 | 9.6 | 170 | 2.9 | 7.5E+02 | 1.8E+03 | |
| **Base oil + PISH** | 56.1 | 10.4 | 178 | 2.9 | 6.5E+02 | 1.5E+03 | 4.6E+03 |

*Table 5: Standard rheological data*

Noticeably, all the data evidence a good continuity between the different rheological devices. However, a range of missing data for shear stresses between $2.10^2$ Pa and $6.10^3$ Pa does not permit a good fitting of the results. The base oil displays a Newtonian behavior because its viscosity slightly declines by 1% which is comparable with the error on the measurements.

Even if the rheological study of lubricants offers interesting information at ambient pressure, it is necessary to investigate their behavior under severe conditions of pressure and at higher shear stress, representative of engine operation conditions, to obtain a full rheological characterization.

# *III.2 Rheological response at high pressure*

## III.2.1 Temperature and pressure effects at low shear stress

Series of tests were run on the high pressure falling-body viscometer (depicted in II.2.3.b) at different temperatures and pressures. The low shear viscosity $\eta_0$ of the base oil and the three polymer solutions versus pressure is shown in semi-log scales in Figure 38 to Figure 41 at five temperatures. Apparently, from atmospheric pressure to 800 MPa the viscosity increases drastically by 2 to 3 orders of magnitude. This can be explained by compressibility considerations: an increase of pressure generates a decrease of liquid volume (cf. Tait equation in part *II.2.2.a.(iii)*) and of free volume. This leads the solvent molecules to be closer to polymer molecules. If the fluid is in motion, the friction forces between the laminar layers of the fluid increase and, as a consequence, the viscosity rises.

The data were fitted to different models detailed in part II.2.2.a.(iii): Tait-Doolittle, WLF-Yasutomi, modified WLF-Yasutomi and Roelands. The relative root mean square (rms) error is the criteria used to compare the different curve-fittings (see Eq. (58)).

Relative root mean square error

$$\sqrt{\frac{\sum\left(\frac{\eta_{experiment}-\eta_{model}}{\eta_{experiment}}\right)^2}{N_{experiment}-N_{parameters}}} \quad (58)$$

Where $\eta_{experiment}$ is the experimental viscosity, $\eta_{model}$ is the viscosity calculated from the model, and $N_{parameters}$ is the number of parameters in the model. $N_{experiment}$ is the number of studied temperatures and pressures (which is close to 55) or the number of studied shear rates (close to 60) in the case of shear-thinning results. Table 6 compares the relative root mean square errors for different models for the base oil and the PAMA solution which is representative of the general trend for the other polymer solutions. The modified WLF-Yasutomi error is the lowest for all the solutions and thus, it is retained in this research.

| | **Base oil** | **Base oil+PAMA** | $N_{parameters}$ |
|---|---|---|---|
| **Tait-Doolittle** | 8.3% | 11.6% | 7 |
| **WLF-Yasutomi** | 5.1% | 8.0% | *6* |
| **Modified WLF-Yasutomi** | **2.6%** | **4.2%** | ***6*** |
| **Roelands** | 6.5% | 9.9% | *3* |

*Table 6: Relative root mean square error for four viscosity-temperature-pressure models and for two solutions*

The application of the modified WLF-Yasutomi model requires two steps. The first one is the determination of the glass transition temperature and the second is the fitting of the other parameters ($A_1$, $A_2$, $B_1$, $B_2$, $C_1$ and $C_2$).

Using the VTF equation and assuming that a viscosity of $\eta_g=10^{12}$ mPa.s or $\eta_g=10^{15}$ mPa.s indicates the glass transition at atmospheric pressure, which are typical viscosities for lubricants at the glass transition temperature [13], $T_g(0)$ values are deducted and reported in Table 7. The glass transition temperatures of polymer solutions are really close to that of the base oil because only a small amount of polymer is added and it does not influence very much the value of $T_g(0)$. The glass transition temperatures found here are of the same order of magnitude than that reported for mineral base oils at atmospheric pressure (about -85 °C in [62] and -75 °C in [88]).

Moreover, differential scanning calorimetry (DSC) (Appendix K-3) analyses on the pure polymers, the base oil and the polymer-thickened base oil solutions show consistent results. The measured $T_g(0)$ by DSC are listed in Table 7 as well. The $T_g(0)$ of the polymers are about 35 to 50 °C higher than that of the base oil and the polymers contribute for only 1.2% in weight in the solution. This explains why the glass transition temperatures of the polymer solutions, deducted from the VTF model, are slightly superior to that of the base oil.

The measured glass transition temperature of the base oil and the polymer solutions by DSC are close to the one deducted from the VTF model with $\eta_g=10^{12}$ mPa.s and even closer to the one with $\eta_g=10^{15}$ mPa.s. Therefore, the method of calculation of $T_g(0)$ from the VTF model appears to be quite accurate. Further calculations evidenced that an uncertainty of 5 °C on $T_g(0)$ - which is the difference between the measured (DSC) and modeled (VTF) $T_g(0)$ - implies a maximum change in viscosity of 2%.

| $T_g(0)$ (°C) | Base oil | Base oil+PAMA | Base oil+OCP | Base oil+PISH |
|---|---|---|---|---|
| ***VTF @ $\eta_g$=10$^{12}$ mPa.s*** | -86.8 | -81.2 | -83.0 | -83.7 |
| ***VTF @ $\eta_g$=10$^{15}$ mPa.s*** | -92.4 | -86.3 | -88.9 | -89.7 |
| **DSC on pure polymers** | | -36.1 | -48.7 | -48.4 |
| **DSC on solutions** | -91.9 | -90.5 | -89.5 | -89.7 |

*Table 7: Deducted or measured glass transition temperatures at atmospheric pressure $T_g(0)$ for the pure polymers or the polymer solutions*

The values of $T_g(0)$ are then used directly in the recently modified WLF-Yasutomi model (Equation (23), p. 69), [12] to determine the low shear stress viscosity $\eta_0$ in function of both temperature and pressure. All the remaining parameters ($A_1$, $A_2$, $B_1$, $B_2$, $C_1$ and $C_2$) are determined by least mean square regressions of the experimental data presented in Figure 38 to Figure 41. The viscosity values calculated from the modified WLF-Yasutomi parameters are directly plotted on the figures. The fitting procedure is constrained imposing realistic initial parameters. The parameter values obtained for the four different fluids are reported in Table 9 (p. 95). Equation (23) shows a fairly good fitting with experimental data.

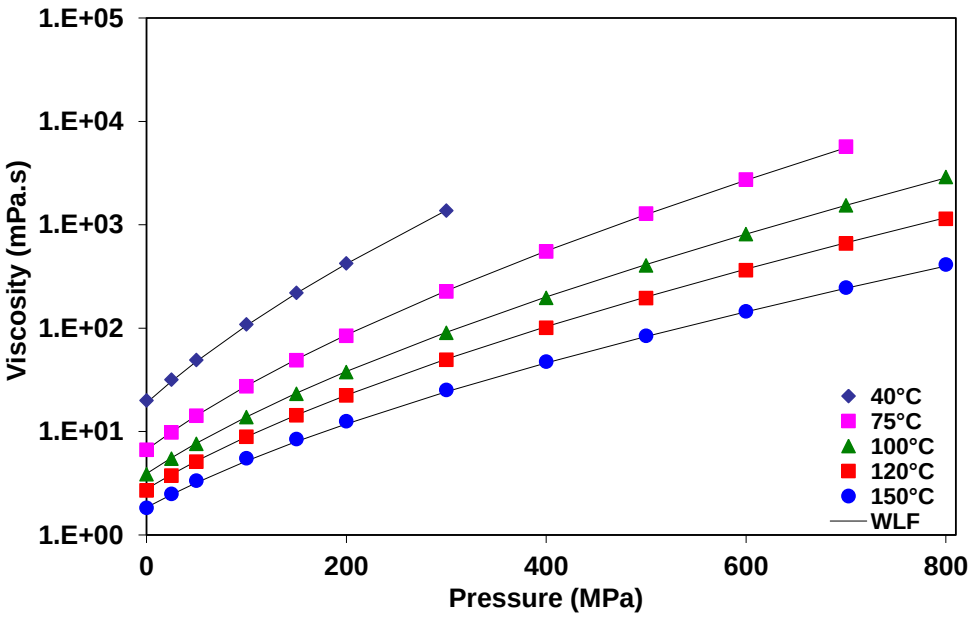


*Figure 38: Piezoviscous behavior of the base oil at different temperatures*

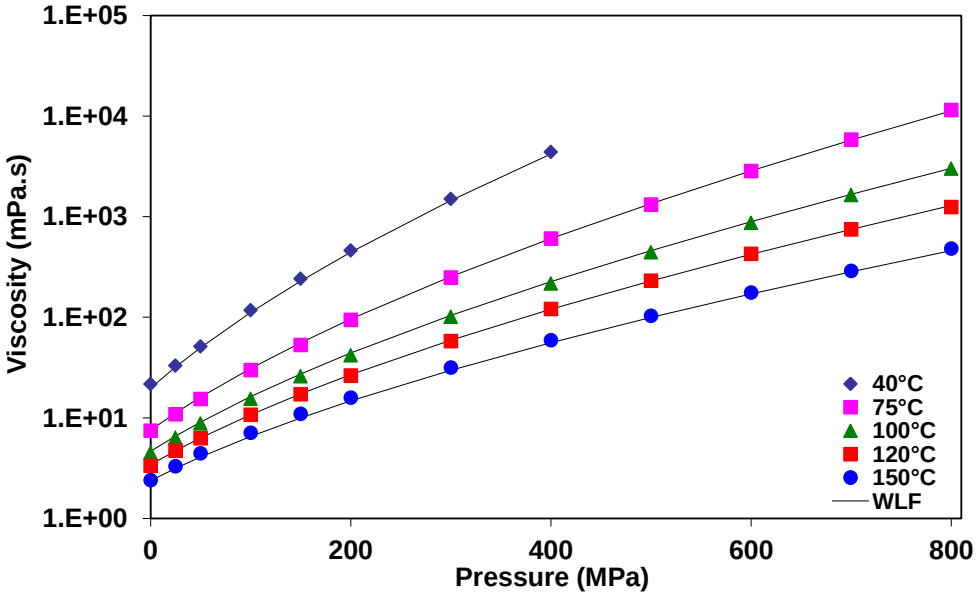


*Figure 39: Piezoviscous behavior of the PAMA-thickened base oil at different temperatures*

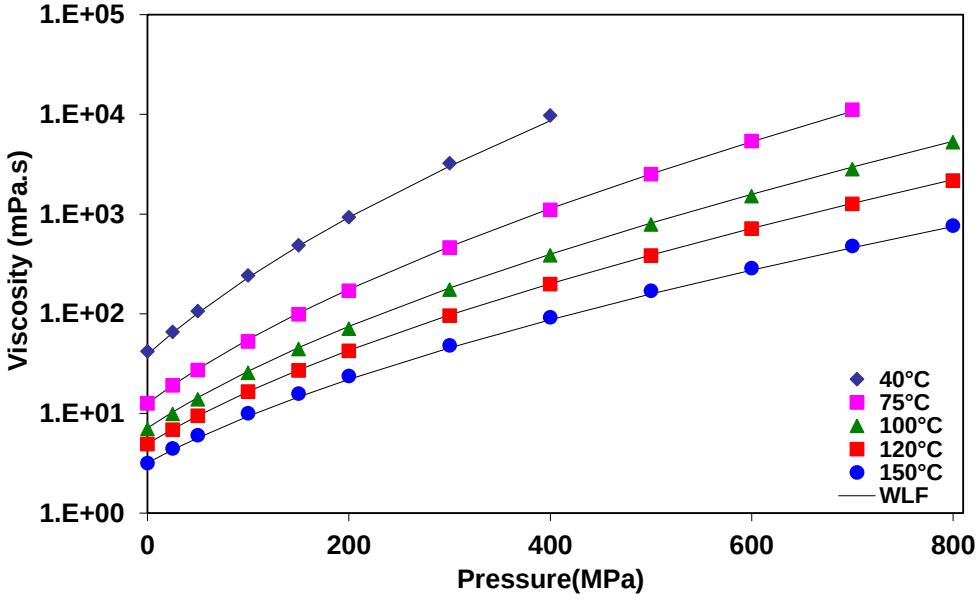


*Figure 40: Piezoviscous behavior of the OCP-thickened base oil at different temperatures*

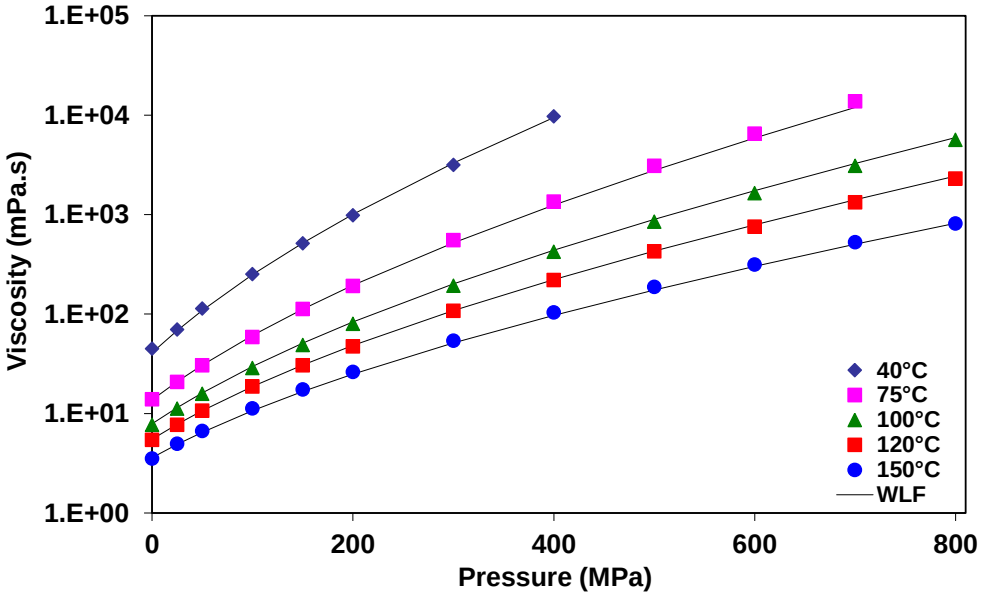


*Figure 41: Piezoviscous behavior of the PISH-thickened base oil at different temperatures*

Figure 42 compares the viscosity of the base oil and the polymer-thickened solutions over an extended range of pressure, at 100 °C. The addition of PISH in the base oil increases the viscosity of the base oil more than OCP and much more than the addition of PAMA. At atmospheric pressure and 100 °C, the PAMA, OCP and PISH solutions are respectively 16%, 81% and 100% more viscous than the base oil. At 800 MPa and 100 °C, the percentages are 3.6%, 81% and 94% respectively.

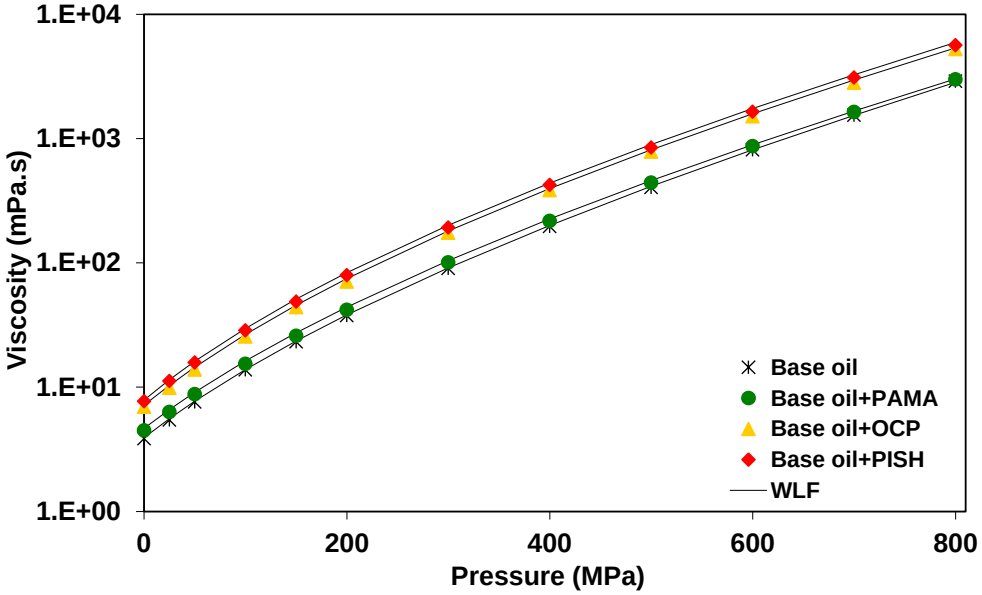


*Figure 42: Comparison of the piezoviscous behavior of the base oil and the polymer-thickened solutions at 100°C*

Table 8 compares the effect of the addition of 1.2% of polymer on the experimental viscosity of the base oil. The rates listed in the table are the relative viscosity between the polymer solutions and the base oil.

Clearly, at each temperature and pressure, the PAMA thickens the base oil less than the OCP and even less than the PISH.

At a given pressure, the raise of temperature increases the thickening rate in the PAMA solution. On the contrary, the thickening rate decreases for OCP and PISH.

At constant temperature, the relative viscosity of the PAMA solution decreases with pressure, whereas the one of the OCP and PISH solutions remains almost steady.

Visibly, once again, the PAMA behavior differs from the two other polymers.

| ***T* (°C)** | ***p* (MPa)** | $\frac{\eta_{PAMA}-\eta_{Base\,oil}}{\eta_{Base\,oil}}$ (%) | $\frac{\eta_{OCP}-\eta_{Base\,oil}}{\eta_{Base\,oil}}$ (%) | $\frac{\eta_{PISH}-\eta_{Base\,oil}}{\eta_{Base\,oil}}$ (%) |
|---|---|---|---|---|
| **40** | ***0.1*** | 8.0 | 109 | 124 |
| | ***300*** | 9.1 | 135 | 129.4 |
| | **-** | | | |
| **75** | ***0.1*** | 11.8 | 89.5 | 108.9 |
| | ***300*** | 9.7 | 103.6 | 143.7 |
| | ***700*** | 2.1 | 95.3 | 141.6 |
| **100** | ***0.1*** | 16.3 | 80.9 | 99.7 |
| | ***300*** | 11.8 | 93.3 | 113.1 |
| | ***800*** | 3.6 | 81.2 | 94.4 |
| **150** | ***0.1*** | 31.3 | 73.8 | 92.7 |
| | ***300*** | 24.9 | 90.1 | 112.7 |
| | ***800*** | 16.3 | 84.7 | 96.3 |

*Table 8: Effect of the addition of polymers on the thickening of the base oil at several temperatures and pressures*

The differences of thickening between the different polymers and the influence of temperature and pressure must be thoroughly analyzed. They may come from the nature of the polymers and the affinity between the polymer and the solvent. These observations will be explained in chapter IV with an investigation on the physico-chemical properties of macromolecules and in particular, on the conformation, the size and the solubility of the polymers in the base oil.

The viscosity-pressure dependence at constant temperature is estimated by the reciprocal asymptotic isoviscous pressure coefficient, $\alpha^*$ (Equation (18), p. 67). It is calculated at 40 °C and at 100 °C from the modified WLF-Yasutomi model (Equation (23), p. 69) and from raw data. The two values are really close (see Table 9).

| **Material** | **Base oil** | **Base oil+ PAMA** | **Base oil+ OCP** | **Base oil+ PISH** |
|---|---|---|---|---|
| $\eta_g$ / Pa.s | $10^{12}$ | $10^{12}$ | $10^{12}$ | $10^{12}$ |
| $T_g(0)$ / °C | -86.8 | -81.2 | -82.9 | -83.7 |
| $A_1$ / °C | 232.6 | 184.1 | 783.1 | 652.5 |
| $A_2$ / GPa$^{-1}$ | 0.178 | 0.197 | 0.0410 | 0.0563 |
| $C_1$ | 16.10 | 15.79 | 15.94 | 15.85 |
| $C_2$ / °C | 21.96 | 18.47 | 23.21 | 22.74 |
| $B_1$ / GPa$^{-1}$ | 7.60 | 8.19 | 7.62 | 8.3 |
| $B_2$ | -0.5258 | -0.5588 | -0.5280 | -0.5066 |
| Relative rms error on the viscosity | 2.6% | 4.2% | 4.3% | 4.9% |
| $\alpha^*(T=40°C)$ / $GPa^{-1}$ from Equation (23) | 16.8 | 16.9 | 17.4 | 17.7 |
| $\alpha^*(T=40°C)$ / $GPa^{-1}$ from experiments | 16.8 | 16.0 | 16.5 | 16.7 |
| $\alpha^*$ $T$=100°C / GPa$^{-1}$ from Equation (23) | 11.7 | 11.5 | 12.2 | 12.3 |
| $\alpha^*$ $T$=100°C / GPa$^{-1}$ from experiments | 12.0 | 11.5 | 12.0 | 12.2 |

*Table 9: Parameters of the Modified WLF-Yasutomi model, Equation (23)*

Figure 43 shows the master curves obtained from the viscosity-temperature-pressure equivalence suggested by Yasutomi *et al.* [62] for all the studied solutions. Isothermal curves of viscosity over pressure presented in Figure 38 to Figure 41 are plotted as the logarithm of viscosity over (T-Tg(p)).F(p). For one fluid, all the results overlap on a unique curve. Noticeably, the shapes of the master curves of all the solutions look similar. The curves can clearly be separated into two groups: on the one hand, the base oil and the PAMA blend and on the other hand, the OCP and the PISH solutions. The base oil curve is above the PAMA one and they cross each other at about 10 mPa.s. At specific combined conditions of temperature and pressure, the PAMA solution is less viscous than the base oil. The addition of PAMA decreases the viscosity of the base oil at high pressure and low temperature. On the contrary, the thickening action of the PAMA is efficient at high temperature and at low pressure. This is what one could expect from a Viscosity Index Improver. The

master curve of the OCP solution coincides almost exactly with that of the PISH-thickened base oil solution which shows that they have really close thermo and piezoviscous behaviors. These observations will be further explained in chapter IV.

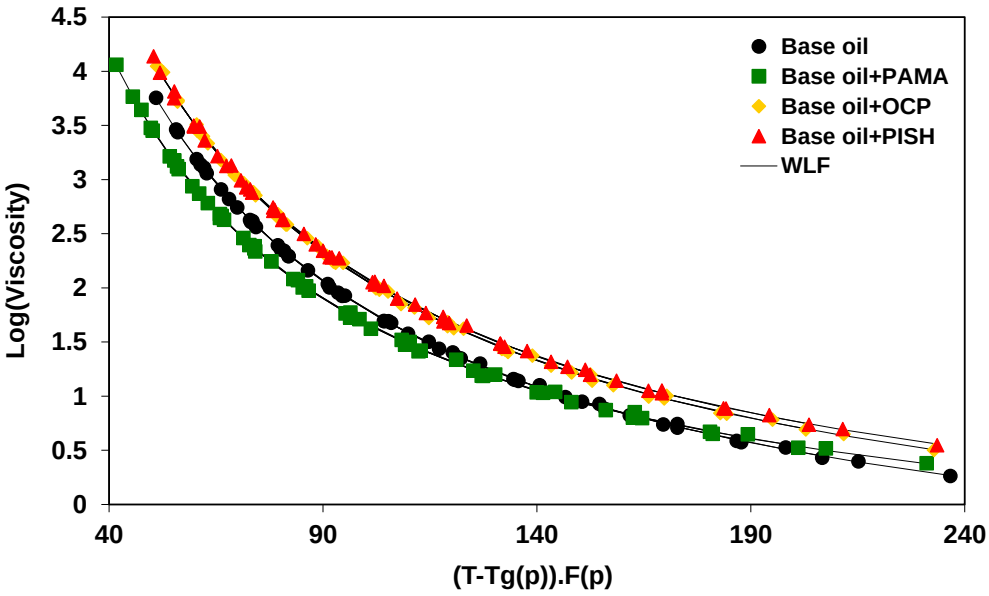


*Figure 43: Master curves of the base oil and the polymer solutions*

The third important parameter influencing the viscosity of lubricants, in addition to temperature and pressure, is the shear stress. The following section aims at modeling the shear-thinning behavior of polymer-thickened solutions from direct measurements at high shear stress and elevated pressure.

## III.2.2 Shear rate and shear stress influences

This section deals with the shear rate influence on viscosity at high pressure. The experimental data are shown along with their representation by shear-thinning models either with a first Newtonian plateau or with a first and a second Newtonian plateau.

Viscosity obtained from the pressurized Couette rheometer with the middle shear stress cylinder set, described in section II.2.3.b., is plotted in Figure 44 to Figure 47 versus shear stress for different conditions of temperature and pressure. It would have been interesting to explore the possibility of an onset of a second Newtonian plateau with the higher shear stress tool (shear stress was one decade higher and the gap was 3.5 µm) but, unfortunately, the data were not sufficiently reliable and did not exhibit a satisfying overlap with that of the middle shear stress tool. Consequently, it was wise to consider the data derived from the middle shear stress cylinders only.

Several models have been tested to fit the flow curves by ordinary least mean square regressions. The retained equation is the Carreau-Yasuda-like relationship (Equation (32), p. 71, with $\eta_2$=0 or $\eta_2$≠0) proposed and validated by Bair *et al.* [67, 89], as previously detailed in II.2.2.b. It was chosen because it displayed the best fitting, i.e. the lowest relative root mean square (rms) error on the viscosity. The extrapolation of the model from 0.01 to 700 kPa is plotted on Figure 44 to Figure 47. Fitting this equation to the experimental data yields the *G*, *a* and *n* values shown in Table 10 (p.

99). Even if the apparent shear modulus *G* should be temperature and pressure dependent, it was kept constant for the short range of temperature and pressure conditions studied here: 25.9 and 40.5 °C (written as 26 and 40 °C on Figure 44 to Figure 47) and from 200 to 400 MPa. The modeling was made using the low shear stress viscosities derived from the modified WLF-Yasutomi formula, described in part III.2.1, as non-variable initial parameters. An exception is conceded for the operating conditions 26 °C and 400 MPa, for which the viscosity is variable in the model. Indeed, at those conditions, the viscosity is so high that the high pressure falling-body viscometer should not give any response. The experimental data from the high pressure falling body viscometer (HP-Visco) are reported on the graphs (filled red squares), except for the condition 26 °C and 400 MPa.

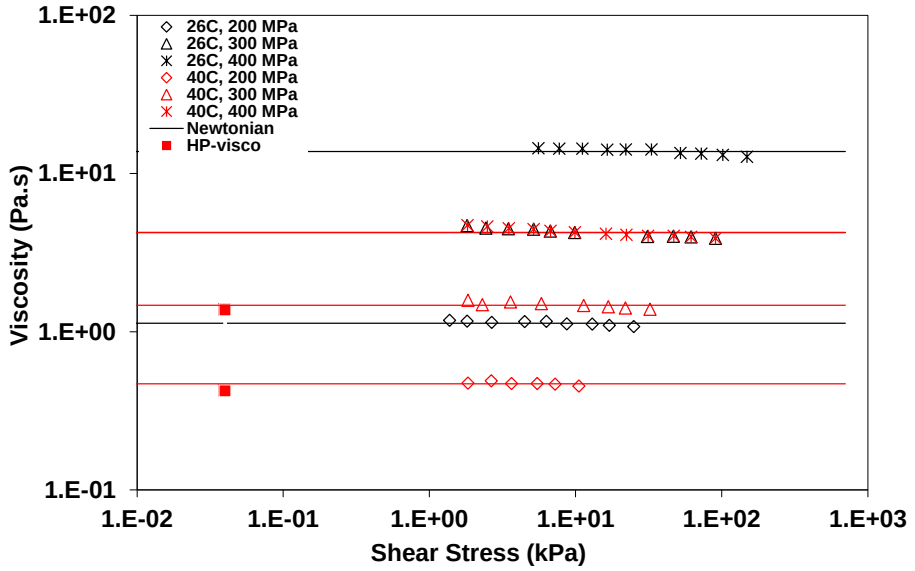


*Figure 44: Viscosity of the base oil versus shear stress at different temperatures and pressures*

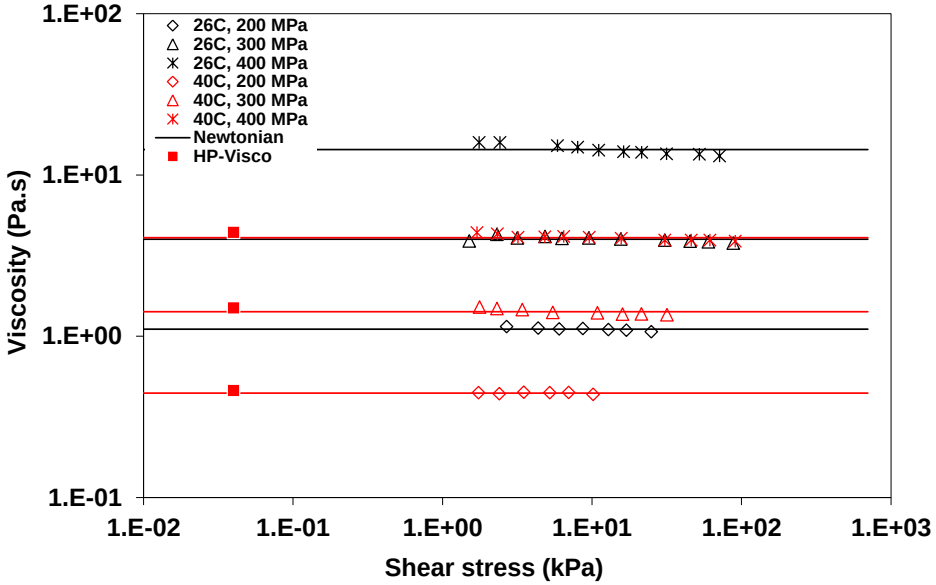


*Figure 45: Viscosity of the PAMA - thickened base oil versus shear stress at different temperatures and pressures*

The experimental viscosity data are constant in function of shear stress for the base oil and the PAMA solution. The model used for the two solutions is Newtonian. The experimental viscosities at

40 °C carried out from the high pressure falling body viscometer are in good agreement with the plateau value for the base oil and the PAMA solution.

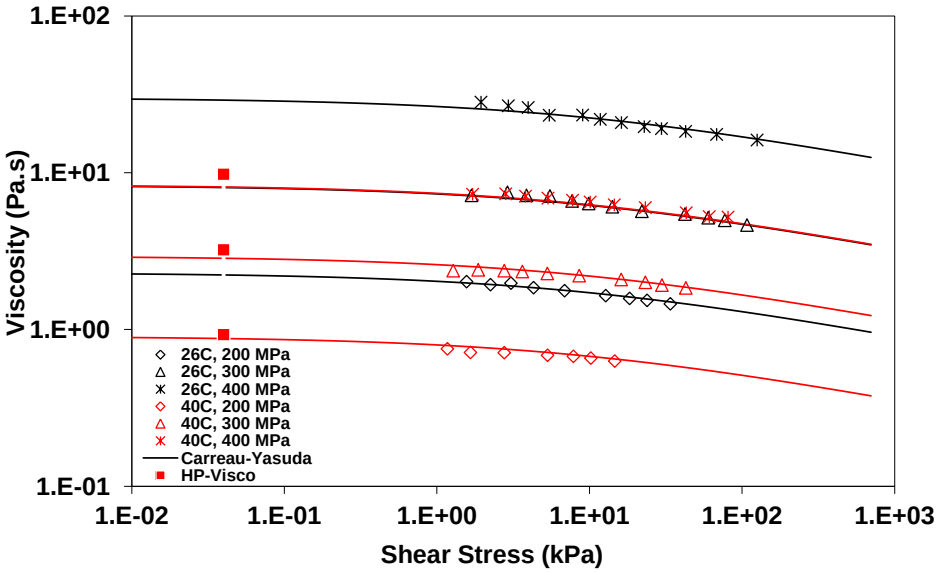


*Figure 46: Viscosity of the OCP - thickened base oil versus shear stress at different temperatures and pressures*

The OCP solution displays a shear-thinning behavior all along the experimental conditions explored with the high pressure Couette device. The first Newtonian plateau is estimated to correspond to the low shear stress viscosity value coming from the modified WLF-Yasutomi model. A little difference appears between the viscosities from the high pressure falling body viscometer (HP-Visco) and the first Newtonian plateau at 40 °C and 300 MPa and at 40°C and 400 MPa. These deviations may result from experimental uncertainties or from the approximation made on the modified WLF-Yasutomi modeling. They can slightly influence the modeling of the shear-thinning effects.

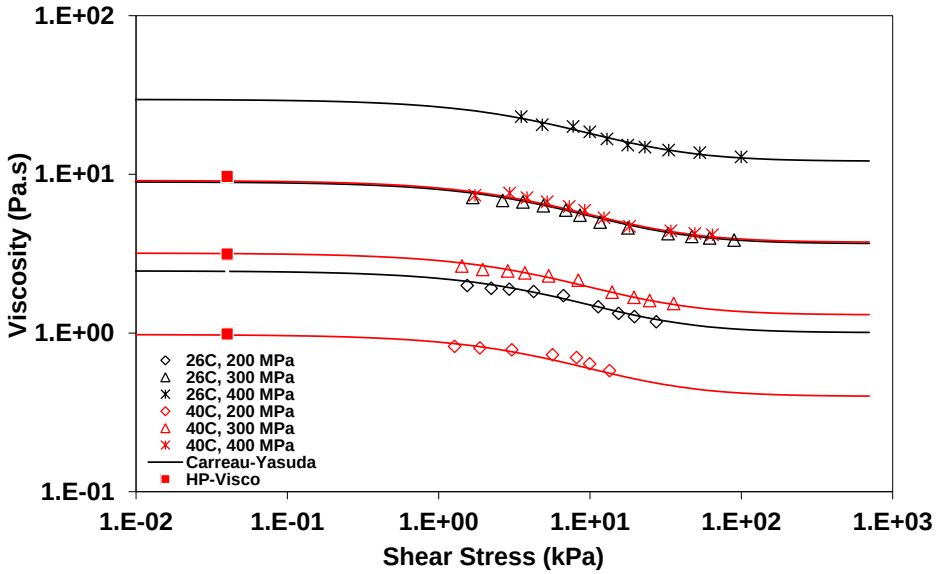


*Figure 47: Viscosity of the PISH - thickened base oil versus shear stress at different temperatures and pressures*

The PISH solution exhibits a large shear-thinning behavior. Here, the Carreau-Yasuda relationship was applied with a second Newtonian plateau. The fitting was applied on an additional

parameter which is the ratio between the second and the first Newtonian plateaus. The viscosities measured on the high pressure viscometer are strongly consistent with the first Newtonian plateau chosen for the PISH solution.

The values of the parameters of the Carreau-Yasuda-like equation (32) (p. 71) with or without a second Newtonian plateau are listed in the table below for the OCP and the PISH solutions.

| | **Base oil+OCP** | | **Base oil+PISH** |
|---|---|---|---|
| | $\eta_2=0$ | $\eta_2\neq0$ | $\eta_2\neq0$ |
| ***G (kPa)*** | 8.4 | 1.0 | 11 |
| ***n*** | 0.84 | 0.80 | 0.41 |
| ***a*** | 0.47 | 0.97 | 0.87 |
| $\frac{\eta_2}{\eta_{0(WLF)}}$ | - | 0.40 | 0.41 |
| **Relative rms error on the viscosity** | 4.2% | 4.7% | 4.0% |

*Table 10: Parameters of the Carreau-Yasuda model with or without a second Newtonian plateau, Equation (32)*

Visibly, the more the shear-thinning behavior is marked, the lower the power-law exponent *n* is.

Figure 48 compares the viscosities of the base oil and the polymer-thickened solutions in function of the shear stress at 40 °C and 400 MPa. The base oil and the PAMA solution have very close viscosities. At low shear stress, the viscosities of the OCP solution and the PISH solution are similar but that of the PISH solution is a little bit higher. At elevated shear stress, the viscosity of the OCP solution decreases and that of PISH diminishes more, crossing the flow curve of the OCP blend.

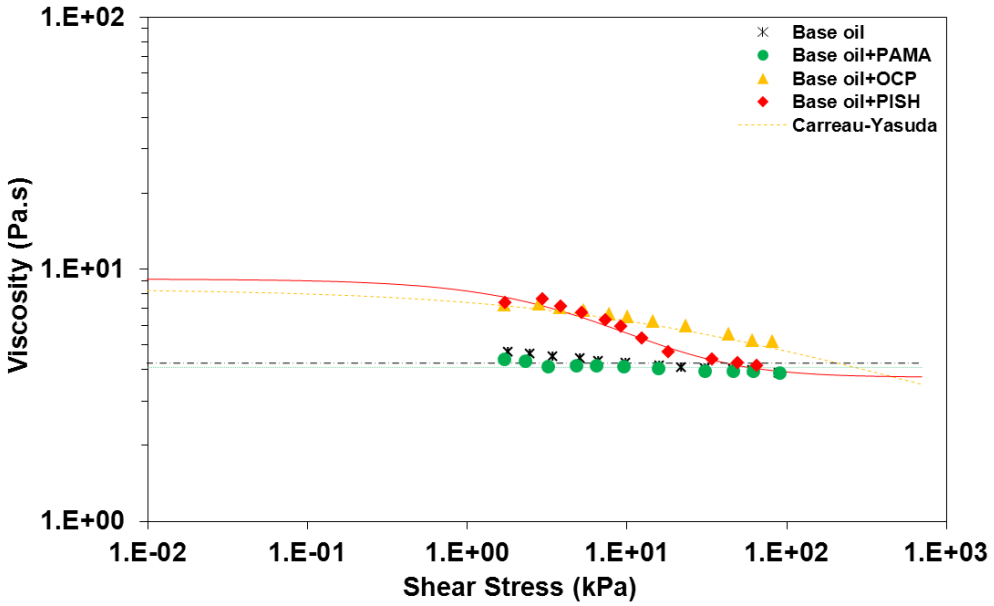


*Figure 48: Comparison of the rheological behavior of the base oil and the polymer-thickened solutions at 40 °C and 400 MPa*

Noticeably, shear-thinning is much more important for the OCP and PISH solutions (Figure 46, Figure 47 and Figure 48) than for the PAMA solution (Figure 45 and Figure 48). The viscosity decrease is between 20 and 45% for OCP and between 30 and 50% for PISH whereas the viscosity of the PAMA solution remains close to that of the base oil (Newtonian).

All the polymer solutions are expected to shear-thin as explained in II.2.1. The OCP and the PISH solutions answer the expectations whereas the PAMA solution shows a surprising Newtonian behavior.

The viscosity of the PAMA solution (mean viscosity is 4.1 Pa.s) is below or really close to the one of the base oil (mean viscosity is 4.2 Pa.s). For the OCP solution, the model crosses the base oil curve at 200 kPa. Moreover, the viscosity of the second Newtonian plateau for the PISH solution (3.7 Pa.s) is slightly below the viscosity of the base oil. The viscosity of the polymer solutions is not expected to be lower than that of the base oil since one of the properties of the polymers is to thicken the base oil solution.

Several hypotheses can be assumed. First of all, the uncertainties made on the experiments (below 5%) and on the models can be questioned. The measurements and the fitting could be improved by using a tool going to very high shear stress in order to more precisely know the second Newtonian plateau. Secondly, one may suppose that the base oil starts to shear-thin from 200 kPa. Finally, this deviation might come from some thermal softening of the solutions at high shear stress but we show that the Nahme-Griffith number is low.

Bair has outlined in [13] the use of the Nahme-Griffith number, *Na*, to give an estimate of the thermal softening influence due to viscous-heating.

$$Na = \frac{\beta \tau^2 h^2}{k\eta} \qquad (59)$$

where $\beta$ is the temperature-viscosity coefficient, $k$ is the liquid thermal conductivity and $h$ is the film thickness. The values of $\beta$ and $k$ are 0.1 $K^{-1}$ and 0.1 $W.m^{-1}.K^{-1}$ respectively.

The cylinder gap *h* was experimentally measured by calibration with a reference liquid (DIDP, sample C in [71]) and was found equal to 5.1 μm. In all the measurements reported in this work, the Nahme-Griffith number was low and well below 0.3 which decreases the possibility of heating by viscous friction [13]. Furthermore, the temperature rise of the working surfaces of the cylinders is minimized by shearing for a single revolution using very high thermal conductivity cylinders. The values of the Nahme-Griffith number mean that the drops in viscosity when the shear stress is increased, clearly visible in Figure 46 and Figure 47, are not related to temperature variations across the fluid film thickness.

Moreover, it is necessary to check the type of flow regime occurring in the high pressure Couette rheometer. The velocity of the inner cylinder can be high (up to 5 rad/s). Inertia effects could become important and might not be negligible. The Reynolds number *Re* is a dimensionless number characterizing the relative weight of inertia forces versus viscous forces and its value determines whether the flow takes place in a laminar or turbulent regime. Its expression is written as following:

$$\mathrm{Re} = \frac{\rho u L}{\eta} \qquad (60)$$

where $\rho$ and $\eta$ are respectively the density and the viscosity of the fluid, *u* is the velocity of the flow and *L* is the characteristic length of the flow (here, it is represented by the gap between the two cylinders).

In tribological applications, inertia effects are rare because the characteristic size is generally small and the viscosity is elevated, except for gas lubricated devices in which turbulent regime can occur [90] and the classic Reynolds equation is not applicable anymore. For an experiment conducted in the high pressure Couette rheometer, the condition for which the viscosity is the lowest is: 40 °C, 200 MPa. The viscosity of the PAMA-thickened base oil solution is 436 mPa.s and the density 907 kg/m$^3$. The characteristic length is 5.1 μm which is the gap of the "middle shear stress cylinder set" and the velocity is 3 rad/s. The radius of the inner cylinder is 6.3 mm. Thus, the Reynolds number can be estimated as:

$$\mathrm{Re} = \frac{907 \mathrm{x}\ \ 3 \mathrm{x} 6.3\,10^{-3}\ \ \mathrm{x} 5.1\,10^{-6}}{436\,10^{-3}} = 2\,10^{-4} \ll 2000 - 2500$$

The calculated Reynolds number for typical operating conditions in the high pressure rheometer is way below the critical Re for a turbulent flow (2000-2500). As a consequence, the flow under study corresponds to a laminar regime and inertia forces remain negligible.

On Figure 49, Figure 50 and Figure 51, the relative viscosity (the viscosity of the fluid divided by its viscosity at low shear stress, derived from the modified WLF-Yasutomi model) is plotted over the Weissenberg number [13]. This dimensionless number represents the ratio of the relaxation time of the fluid (considering the Maxwell model (cf. II.2.1 ), $\lambda = \eta_{0(WLF)}/G$, where $\eta_{0(WLF)}$ and *G* are derived from the modified WLF-Yasutomi and the Carreau-Yasuda models) over the characteristic time of the experiment ($1/\dot{\gamma}$):

$$W_i = \frac{\lambda}{\frac{1}{\dot{\gamma}}} = \frac{\eta_{0(WLF)}\dot{\gamma}}{G} \qquad (61)$$

If $W_i$ exceeds 1, the relaxation time of the fluid exceeds the time of the experiment leading to the occurrence of shear-thinning effects.

For each fluid, the normalization of the data presented on Figure 44 to Figure 47 leads all the viscosities at any conditions of temperature and pressure to overlap on a unique master curve. Only the master curves for solutions showing a shear-thinning behavior are plotted below.

The first master curve for the OCP solution is plotted using a Carreau-Yasuda model with a first Newtonian plateau only.

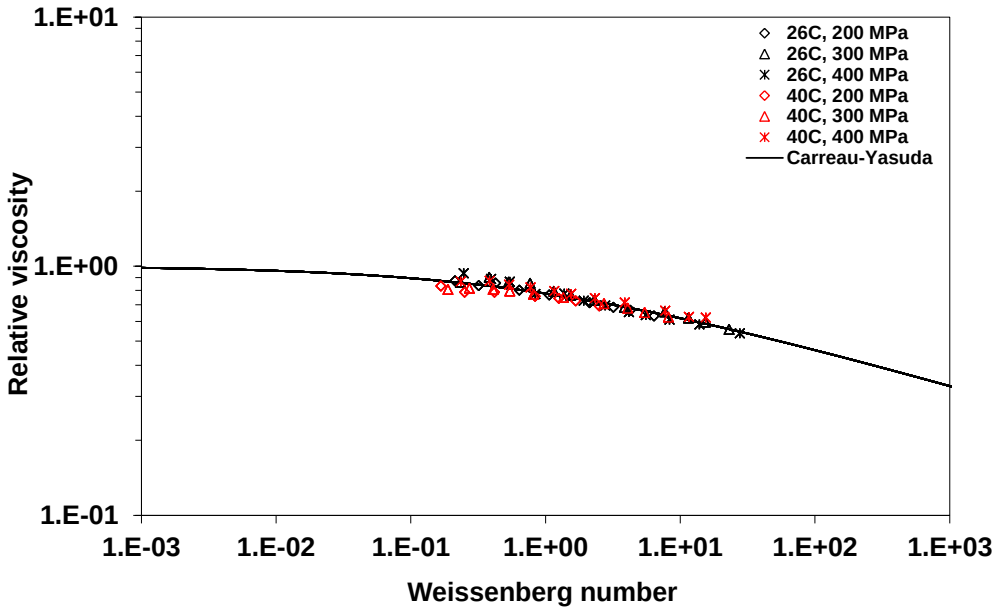


*Figure 49: Master curve of the rheological behavior of the OCP - thickened base oil. Model without a second Newtonian plateau ($\eta_2$=0)*

This modeling seems really consistent with the data for the OCP solution whose rheological parameters are listed in Table 10.

The flow master curves for the OCP and PISH solutions were fitted by the ordinary least mean square regression applied with the Carreau-Yasuda-like model (Equation (32), p. 71) with a second Newtonian plateau ($\eta_2 \neq 0$) and are plotted on Figure 50 and Figure 51. Fitting this model to the experimental data yields the $G$, $a$, $n$ values and the ratio $\eta_2/\eta_{0(WLF)}$ shown in Table 10 (p. 99). The apparent shear modulus $G$ and the ratio of the viscosity of the second Newtonian plateau $\eta_2$ and the low shear viscosity $\eta_{0(WLF)}$ derived from the modified WLF-Yasutomi model were set constant in the experimental range of temperature and pressure. An exception was conceded for the operating condition 26 °C and 400 MPa, for which the viscosity was a parameter in the model. Indeed, at this condition, the viscosity is so high that the high pressure falling-body viscometer cannot give any response.

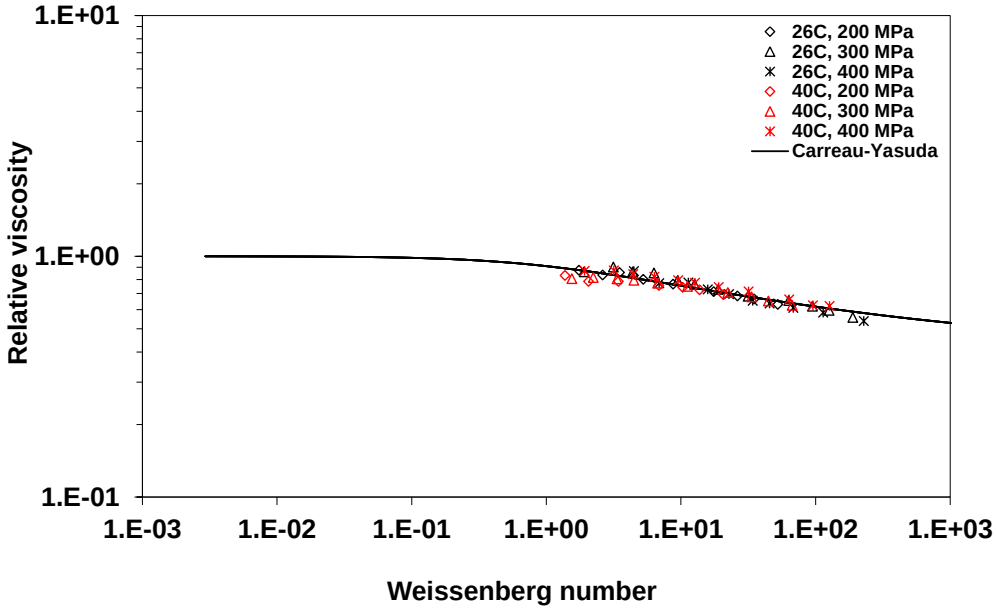


*Figure 50: Master curve of the rheological behavior of the OCP - thickened base oil. Model with a second Newtonian plateau ($\eta_2 \neq 0$)*

This model seems to be applicable to the OCP-thickened solution but one should extrapolate the graph to very high Weissenberg number to observe the second Newtonian plateau. The model with only one Newtonian plateau is thus more appropriate for the OCP blend.

However, the double Newtonian plateau expression looks relevant for the PISH solution for all the experimental conditions, see Figure 51 below.

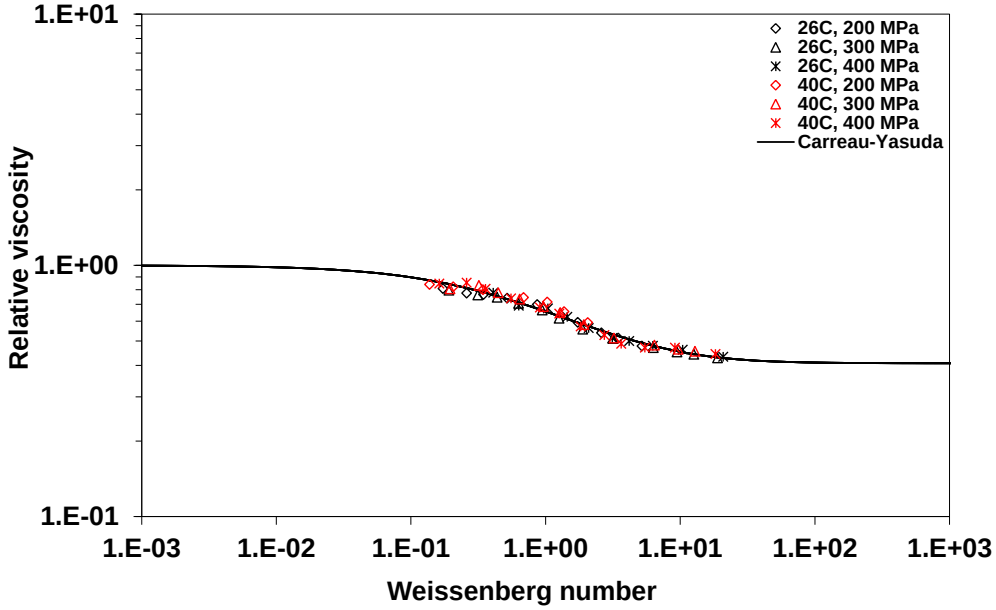


*Figure 51: Master curve of the rheological behavior of the PISH - thickened base oil. Model with a second Newtonian plateau ($\eta_2 \neq 0$)*

The choice of the rheological behavior is justified by the master curve shown on Figure 51. Indeed, when viscosity is plotted against the Weissenberg number, it becomes obvious that there is a second Newtonian plateau for the PISH solution.

## *III.3 Conclusion*

To conclude, firstly, the dependence of viscosity on temperature and pressure is fully and accurately characterized for all the fluids. Then, the shear dependence of their viscosity is studied and rheological models with one or two Newtonian plateaus are determined for all the polymer-thickened base oil solutions. A robust model with a second Newtonian plateau is fitted for the PISH solution. The notion of master curves was introduced to represent the viscosities at any conditions of temperature and pressure on a unique curve.

It was interesting to wonder how solutions would behave if they contained not only one polymer but two polymers. One of the multiple possibilities was studied: equal weights of OCP and PISH were added in the base oil. Not to overload this chapter, it was chosen to show the corresponding results in Appendix E. Its rheological behavior is really close to the one of the PISH solution with a viscosity drop of about 40% and a 2$^{nd}$ Newtonian plateau modelling.

For each fluid, it is now possible to predict precisely its rheological behavior in a contact knowing the temperature, the pressure and the shear stress. One of the goals can be to extrapolate these models to fluids with similar base oils and similar chemistry of polymers. It may orientate oil makers in the choice of the base oil and the polymers in function of the applications and the specifications asked by the car manufacturer.

Those models can easily be implemented in numerical models for the calculation of film thicknesses or friction coefficients for a point contact or for a full machinery. This will be explained in chapter V.

Finally, an unexpected behavior was underscored for the PAMA solution in this chapter. It is of main interest to understand the reasons why it did not show any shear-thinning response unlike the OCP and the PISH solutions. The principal goal of chapter IV is to explore the fundamentals of polymers and polymer solutions behavior in order to bring explanations on the relationship between the molecular mechanisms and the rheology.

# IV Bridging the gap between rheology and the molecular scale

In order to fully understand the rheological response of the base oil and the three polymer-thickened solutions, it is necessary to investigate the mechanisms occurring at the molecular scale. Furthermore, the relationship between the physico-chemistry of molecules and rheology is important to understand the observed behavior of PAMA which is not the expected shear-thinning trend regarding automotive lubricants ([8], [9] and [10]). This fourth chapter discusses the possible roles played by the concentration of polymers, the appended functional additives, the LCST and finally, by the conformation and the size of polymers in the mineral base oil. Many of the notions previously mentioned are related to the hydrodynamic radius of the macromolecules. Its influence on the rheological response of solutions is examined and different methodologies to determine it are compared. Many of the results detailed in this section were published in [91].

# *IV.1 Influence of concentration*

First of all, the percentage of polymer in the base oil can be questioned to explain the rheological behavior of the polymer-thickened base stock solutions. Indeed, if the concentration of the solution is above a certain threshold, the physical concepts that govern the flow involved are different from those below this concentration. As explained in II.3.3.a, above the critical concentration $c^*$, the polymers start to overlap and to entangle which can cause different flowing behaviors. De Gennes presents the physical properties of coils trapped in a network providing information on entanglement and reptation concepts [15]. If the concentration of the PAMA leads to one regime and the OCP and the PISH are in another, it could explain the difference on the evolution of viscosity over shear stress. Moreover, if there is not enough polymer, one can suppose that the shear-thinning behavior would be too low to be detectable. Nevertheless, the concentration of polymers used in the current work is typical for automotive lubricants and representative of recent applications.

Thus, it is important to determine the critical concentration and where the chosen concentration (1.2% w/w) is located for each polymer blend.

Here, a range of critical concentrations is approximated from Equation (43) (p. 79) together with the Flory Equations (39) and (40), assuming theta solvent or good solvent conditions. For linear polymers like OCP, the mean monomer size $l$ is equal to the sum of the C-C distances in the main polymer skeleton. For PAMA and PISH, $l$ is calculated from their densities. The mean monomer size, the number of monomers, the approximated radii of gyration and the critical concentrations (theta - good solvent) are listed in Table 11.

| | $l$ (nm) | $N$ | $R_g$ (nm) | | $c^*$ (%) | |
|---|---|---|---|---|---|---|
| | | | Theta solvent | Good solvent | Theta solvent | Good solvent |
| **PAMA** | 0.74 | 1418 | 10.6 | 23.5 | 16.5 | 1.5 |
| **OCP** | 0.31 | 2491 | 5.8 | 13.7 | 21.8 | 1.7 |
| **PISH** | 0.48 | 5907 | 13.9 | 35.9 | 7.4 | 0.4 |

*Table 11: Radii of gyration and critical concentrations of polymers*

The chosen concentration of polymers in this study (1.2% w/w) is lower than the critical concentrations, both for the theta and the good solvent conditions for the PAMA and the OCP. However, there is an exception for the PISH in the good solvent conditions. Its critical concentration appears low compared to 1.2% w/w, but a rather low solubility between PISH and the base oil was expected due to its steric hindrance with the long branches of the star. Thus, the good solvent assumption is not appropriate in the case of the PISH solution and its critical concentration should

actually be higher than 0.4%. To conclude, the chosen concentration for the study is below the calculated critical concentrations for the three polymer solutions. Consequently, this work concerns the dilute regime and the hypothesis of concentration to explain the differences in the rheological behaviors can be excluded.

Adding more PISH polymer while remaining below the $c^*$ to make the shear-thinning behavior more visible could be suggested but the limit with $c^*$ seems so close that the entangled regime could be rapidly reached. This suggestion is also rejected for OCP because OCP is supposed to be in good solvent conditions because they are both non-polar and 1.2% is close to 1.7%. Finally, the PAMA is presumably in bad solvent conditions because it is polar and the base oil is non-polar. Thus, its critical concentration might be 16.5% and it would be possible to add more polymer in order to notice a shear-thinning behavior. This eventuality was not considered for the sake of keeping equal conditions and because 1.2% is representative of the concentration of PAMA in an engine lubricant.

## *IV.2 The possible role of additives*

Secondly, the possible role of the lubricant additives (other than the VII) has to be analyzed because fully formulated lubricants are expected to show a shear-thinning behavior whereas the solution containing PAMA does not shear-thin. The absence of additives might be the origin of the non-shear-thinning behavior for the PAMA solution. Further experiments were run on the high pressure rheometer with the base oil and the polymer solutions containing a package of additives detailed in II.4. The flow curves of the base oil, the PAMA and the OCP+PISH solutions with functional additives are plotted on Figure 52, Figure 53 and Figure 54 and compared with the ones without additives (see chapter III and Appendix E).

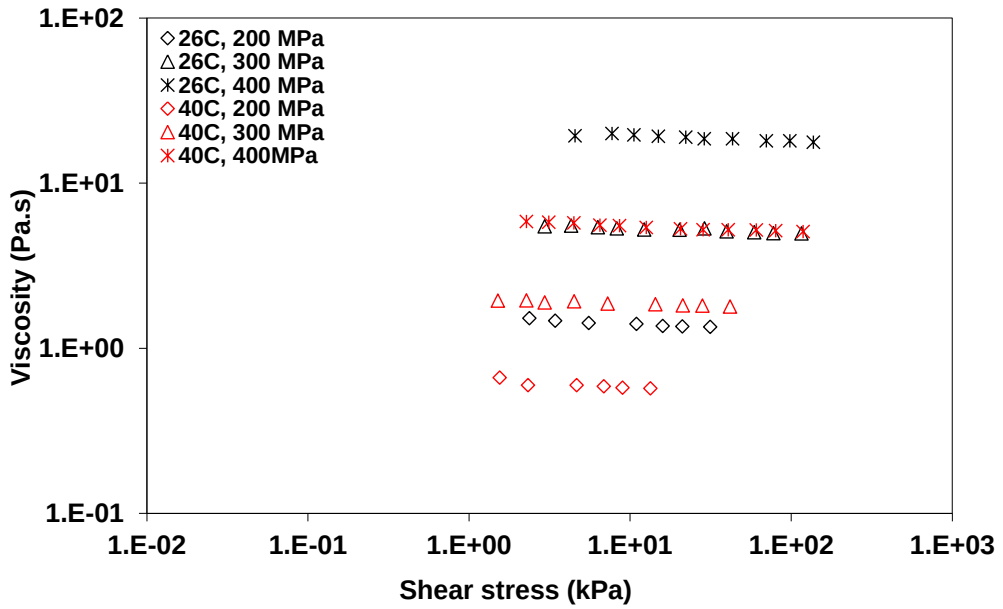


*Figure 52: Rheological behavior of the base oil **with functional additives** at several temperatures and pressures*

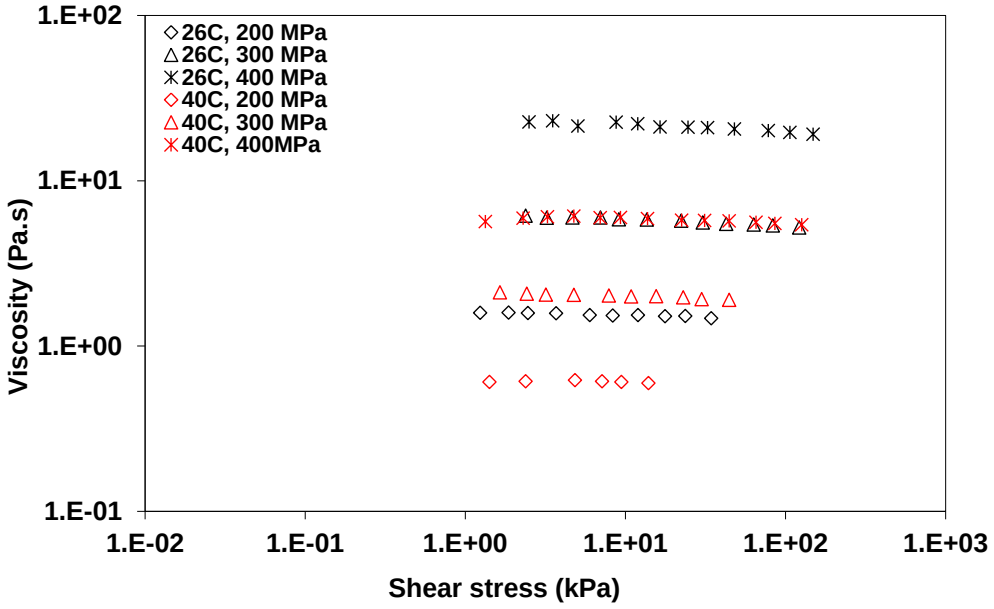


*Figure 53: Rheological behavior of the PAMA solution **with functional additives** at several temperatures and pressures*

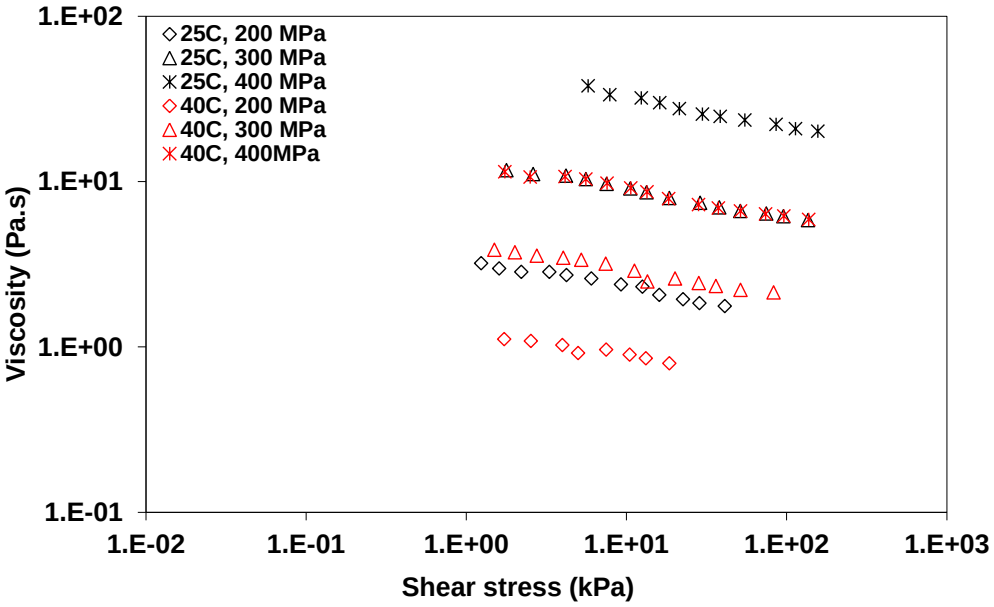


*Figure 54: Rheological behavior of the OCP+PISH (50/50) solution **with functional additives** at several temperatures and pressures*

On the one hand, the package of additives globally increases the viscosity of the polymer solution by a factor of 1.4. On the other hand, the additives do not affect the amplitude of the viscosity decrease as a function of shear stress. Indeed, with additives, the viscosity of the base oil decreases by 8 to 15%, the PAMA solution by 2 to 16% and the OCP+PISH solution by 30 to 50%. These percentages are really close to those detailed in part III.2.2 (from p. 96) and in Appendix E for solutions without additives. Therefore, in our case, no further shear-thinning effect is observed when adding a package of additives. The expected shear-thinning behavior of the marketed lubricants cannot be attributed to functionalizing additives but only to VI improvers.

# *IV.3 The potential effect of a LCST*

As explained in section II.3.4, close to the LCST or above it, the polymer coils collapse and they are no longer well soluble in the solvent. In that case, the polymer cannot fulfill its role of thickener of the base oil and the rheological properties might be altered. This is a possible cause of the unexpected behavior of the PAMA solution. Thus, it is of primary importance to check if the operating conditions in the high pressure rheometer lead to a temperature above the LCST and to a poor solubilization of the polymers in the base oil.

Due to the lack of data in the literature on the mixtures under consideration in this work, we have selected model systems whose LCST are known and which solvents are hydrocarbons, chemically close to the mineral base oil: polymer solutions of polyisobutylene (PIB) in heptane and cyclopentane. The PIB-cyclopentane system has a LCST around 70 °C and PIB-heptane close to 170°C [82] at the vapor pressure.

The four graphs in Figure 55 evidence the variations of the hydrodynamic radius $R_h$ of a PIB (described in Table 4) in heptane and in cyclopentane as a function of temperature and pressure. The $R_h$ data are deduced from measurements carried out with the high pressure falling body viscometer (shown in Figure 94, Appendix F, p. 162) and the application of the Einstein's law (Equations (45) and (47), p. 80). This method is presented in section IV.4.1.

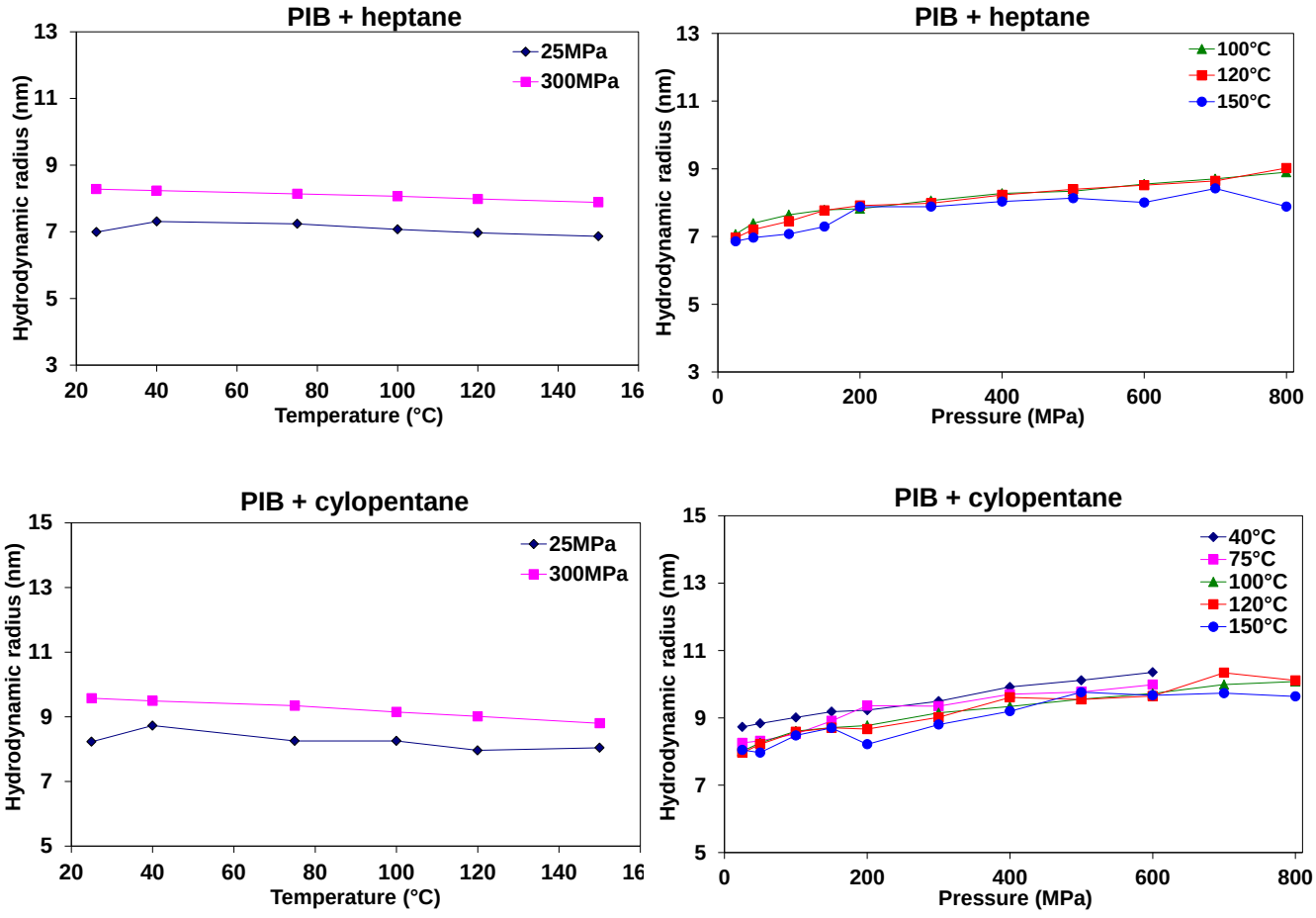


*Figure 55: Variation of the hydrodynamic radius as a function of temperature (left) and pressure (right) for PIB mixed in heptane (top line) and cyclopentane (bottom line)*

It is clear from these curves that the trends are similar for both solvents. In the case of PIB in cyclopentane, the LCST (70 °C) is within the experimental range; for PIB in heptane (170 °C) it is above the studied temperature conditions. In the case of PIB in cyclopentane, the hydrodynamic radius could have been modified - detectable by a sudden change of viscosity - around 70 °C, at least at the lowest pressure (i.e., 25 MPa). Furthermore the pressure might shift the LCST to higher temperatures ([92], [86]) but no clear evidence of a change in $R_h$ value is observed. As a consequence for this study, since no change or discontinuity is detected, it is concluded that the LCST can occur but it has no direct influence on the hydrodynamic radius, and thereby on the rheology for the two model fluids.

The hypothesis of LCST concerns the PAMA solution in particular because the behaviors of OCP and PISH were conform to the expected shear-thinning response. In order to check the occurrence of a LCST in the PAMA solution, we have performed turbidimetry measurements (cf. Appendix K-4) at atmospheric pressure and at 50 MPa. At the LCST, the solution should change abruptly from clear to completely cloudy due to the macroscopic phase separation. At atmospheric pressure no demixing was observed up to 250 °C in the PAMA solution. At 50 MPa, no phase separation was detected up to 200 °C. Since the pressure might shift the LCST to higher temperatures, this is further evidence that LCST considerations do not interfere in the rheological behavior of the PAMA solution in the studied temperature and pressure ranges. The LCST hypothesis can now be fairly excluded.

# *IV.4 Impact of conformation and size*

Last but not least, the chemistry of the polymers, their conformation, their molecular weight and their solubility need to be investigated to understand the rheological behaviors previously examined. The physical relevant notion which seems to be common to all these aspects is the hydrodynamic radius ($R_h$) of the polymer additives.

It is proposed to determine $R_h$ by extending the use of the Einstein's law [15] - usually applied at atmospheric pressure only - to very large pressures (up to 800 MPa). The results will be compared with data obtained from other methodologies at atmospheric pressure such as calculations from Flory equations, intrinsic viscosities and by direct measurements (size exclusion chromatography and dynamic light scattering). Finally, the different rheological behaviors will be explained regarding the microscopic (i.e., molecular) mechanisms - polymer conformation and polymer size - occurring in the polymer-thickened solutions.

## IV.4.1 Extension of the Einstein's law for the determination of the hydrodynamic radius at high pressure

One method has successfully been applied at various temperatures and at high pressure, using the Einstein's law [15]. The latter - detailed in part II.3.3.b - allows relating viscosity to the hydrodynamic radius. Two hypotheses are required for the calculation: the solutions are in the dilute regime and the polymers are considered as rigid spheres. Moreover, we consider that the notion of hydrodynamic volume remains valid at high pressure.

From the high pressure falling body viscometer measurements and Equations (45) and (47), the hydrodynamic radius of the three polymers is plotted versus temperature (Figure 56) and pressure (Figure 57). The uncertainty on the determination of the hydrodynamic radius through the Einstein's law is close to 5%. The deduced values of the hydrodynamic radii are really different from one polymer to another. They range between 7 and 14 nm, 10 and 12 nm and 17 and 20 nm in the full

experimental conditions window for PAMA, OCP and PISH respectively. The values are comparable for PAMA and OCP whereas they are larger for PISH.

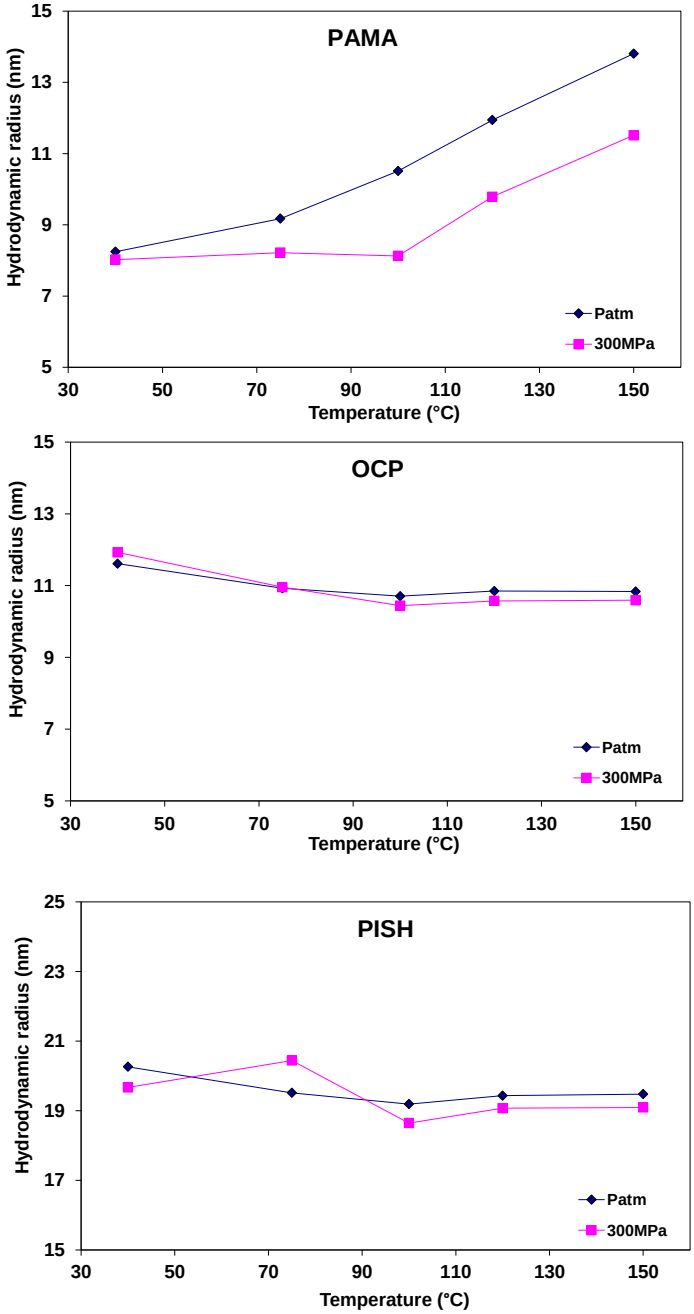


*Figure 56: Variation of the hydrodynamic radius (deduced from the Einstein's law) as a function of temperature for the 3 polymer base oil solutions (PAMA (top), OCP and PISH (bottom))*

In the case of PAMA, the hydrodynamic radius increases by 65 % at atmospheric pressure and by 40 % at 300 MPa in function of the temperature. Ver Strate and Struglinski showed in [10] that among all the typical polymer types used as commercial viscosity modifiers (detailed in II.1.4.d), only the methacrylates have positive variation of the mean square radius of gyration with temperature. As the temperature rises, the thermal agitation and the free volume of the solvent molecules increase. Thus, the interactions between the polymer coils and the solvent are enhanced and, as a consequence, the polymer chains swell. Moreover, some of the hydrogen and Van der Waals intramolecular bonds between the side chains of the comb can be broken at higher temperature which facilitates the swelling. The temperature acts on the solubility between the base oil and the polymer.

On the contrary, for OCP and PISH, $R_h$ remains almost steady (with a slight decrease) in function of temperature. The OCP is already in a quite good solvent because of its non-polarity in a non-polar mineral base oil (see IV.4.3.d), so the coils are already swelled. That is why temperature as almost no impact on its hydrodynamic radii. The $R_h$ of the PISH slightly diminishes very likely because of its steric hindrance. Indeed, the star branches are so close that they prevent the solvent molecules from penetrating inside the polymer coils which does not lead to their swelling. These observations are confirmed because according to [10], coil dimensions of the other polymers backbones (different from polymethacrylates) actually shrink as temperature increases ([93], [94]).

When it comes to the pressure influence, the hydrodynamic radius of PAMA drops by 30 to 45 % whereas for OCP and PISH, $R_h$ remains almost constant (with a small decrease). Thus, pressure variations do not significantly affect OCP and PISH polymer chain sizes.

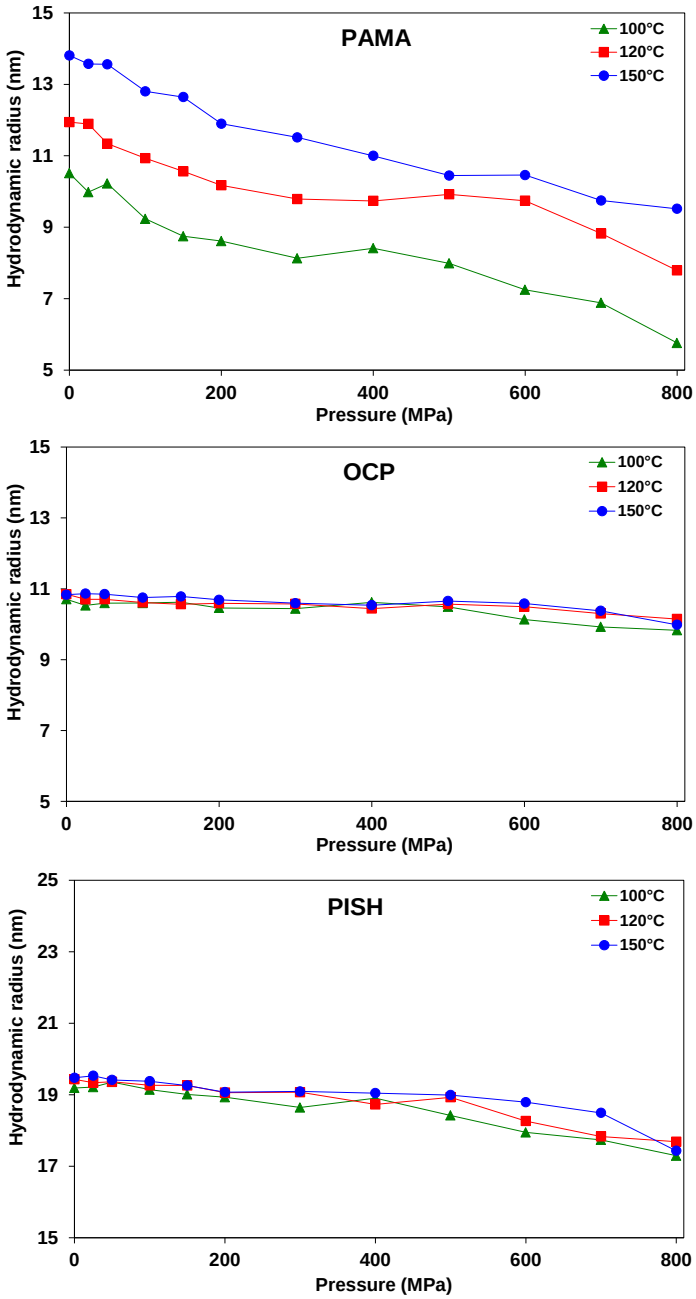


*Figure 57: Variation of the hydrodynamic radius (deduced from the Einstein's law) as a function of pressure for the 3 polymer base oil solutions (PAMA (top), OCP and PISH (bottom))*

The raise of pressure involves an increase of the density of the solvent, thus it is more difficult for the solute to be surrounded by solvent molecules which explains why the PAMA shrinks with pressure. The effect is even more obvious at temperatures above 100 °C when the coils are swelled. Once again, the pressure has an impact on the solubility between the base oil and the polymer coils by contracting the free volume of the solvent molecules. The pressure has almost no effect on the $R_h$ of OCP because the latter is in a good solvent state. Interactions between the polymers and the solvent are too numerous to be altered by pressure. The $R_h$ of PISH slightly decreases over pressure because the steric hindrance of the PISH is so important between the branches of the star that the polymer cannot collapse much.

Even if the deduced hydrodynamic radii of PAMA and OCP are of the same order of magnitude, two specific behaviors can clearly be discriminated: the $R_h$ of the PAMA is strongly affected by temperature and pressure variations while the ones of OCP and PISH undergo almost no fluctuation when the temperature and the pressure rise.

Considering the temperature and pressure effects on the hydrodynamic radius of polymers, it is necessary to take into account these evolutions in the calculation of the concentration and the critical concentration.

Indeed, if the temperature rises from 40 to 150 °C, the density decreases by about 8% for all the polymer solutions and thus, the concentration drops by 8%. At ambient temperature and at atmospheric pressure, the concentration of the different polymers in the base oil is 1.2%. With an increase of temperature, the concentration would become 1.1%. Moreover, the raise of temperature involves an increase of the hydrodynamic radius of PAMA by 40 to 65%. Since the critical concentration is inversely proportional to the hydrodynamic radius, $c^*$ would collapse by 40 to 65%, meaning that it would range between 5.8-9.9% (theta solvent) and 0.5-0.9% (good solvent) (cf. Table 11, p. 107). We have already explained that the PAMA is more likely to be in a theta solvent than in a good solvent because of polarity considerations and thereby, the concentration of the PAMA solution is still below the critical concentration. The critical concentrations of the OCP and the PISH are not changed because the temperature has almost no influence on their hydrodynamic radii and the concentration 1.1% is still below $c^*$.

In the one hand, if the pressure increases from 0.1 MPa to 800 MPa, the volume of the solution drops by about 25-30% and consequently, the density is enhanced by 25-30%. Therefore, the concentration rises by 25-30% and becomes close to 1.5-1.6%. In the other hand, the hydrodynamic radius of the PAMA decreases by 30 to 45% with pressure. Thus, the critical concentration increases by the same rate and is between 21.5-23.9% (theta solvent) and 2.0-2.2% (good solvent). As a consequence, the concentration of the polymer blend is still below the critical concentration. Since the hydrodynamic radii of OCP and PISH do not strongly vary in function of temperature and pressure, $c^*$ is not impacted and remains above the concentration of the polymer mixtures (cf. Table 11).

Considering temperature and pressure influences separately, the concentration of the solutions is always below the critical concentration and thus, the dilute regime is always respected. If the temperature and the pressure are simultaneously applied, their effects annihilate because they are contradictory and thereby, the polymer solutions still behave as dilute fluids.

The Einstein's method allowed the determination of the hydrodynamic radius of polymers in a solvent at high pressure. To certify its validity, it is necessary to compare it with other methods.

## IV.4.2 Determination of $R_h$ with other methods at atmospheric pressure

The following two parts illustrate two ways for determining the hydrodynamic radius at atmospheric pressure - from the intrinsic viscosity and from direct measurements - to confirm the results obtained from the previous methodology.

### *IV.4.2.a Intrinsic viscosity*

This part focuses on the intrinsic viscosity as a mean to reach the hydrodynamic radius. This method is commonly used for polymer solutions [9]. Definitions and equations are described in part II.3.2.b. Viscosity was measured on the Anton-Paar rheometer at several concentrations.

The usual manner to find the intrinsic viscosity - based on Equations (52), (53) and (54) (p. 81) - is to plot the reduced viscosity, the natural logarithm of the relative viscosity divided by the concentration or the natural logarithm of the reduced viscosity over concentration. Linear increasing curves are generally obtained and the intercepts are the intrinsic viscosity for the two first equations and its natural logarithm for the third one.

An unexpected response regarding Huggins [79], Kraemer [80] and Martin [81] is observed in Figure 58. The above Equations (52), (53) and (54) do not satisfactorily represent the experimental curves for the studied solutions. The same behavior occurs for PAMA and PISH. Indeed, the reduced viscosity increases dramatically upon dilution at very low concentration. When the concentration is divided by 100, the reduced viscosity in multiplied by more than 10 (at $c$=9.4 g/L, $\eta_{red}$ =0.13 L/g and at $c$=0.09 g/L, $\eta_{red}$ =1.79 L/g). Inspired by the work of Wolf [78] who had to face the same difficulties, the intrinsic viscosities were eventually calculated from the slope at the origin of the logarithm of the relative viscosity $\eta_r$ versus concentration (cf. Figure 59). Thanks to the intrinsic viscosity calculations, the hydrodynamic radii were deduced assuming a linear flexible chain molecule and using the Flory-Fox relationship (Equation (56), p. 81), derived from the Einstein's law. The results are reported in Table 12 and Table 13 (p. 117) for respectively the intrinsic viscosities and the hydrodynamic radii of polymer-thickened solutions at different temperatures.

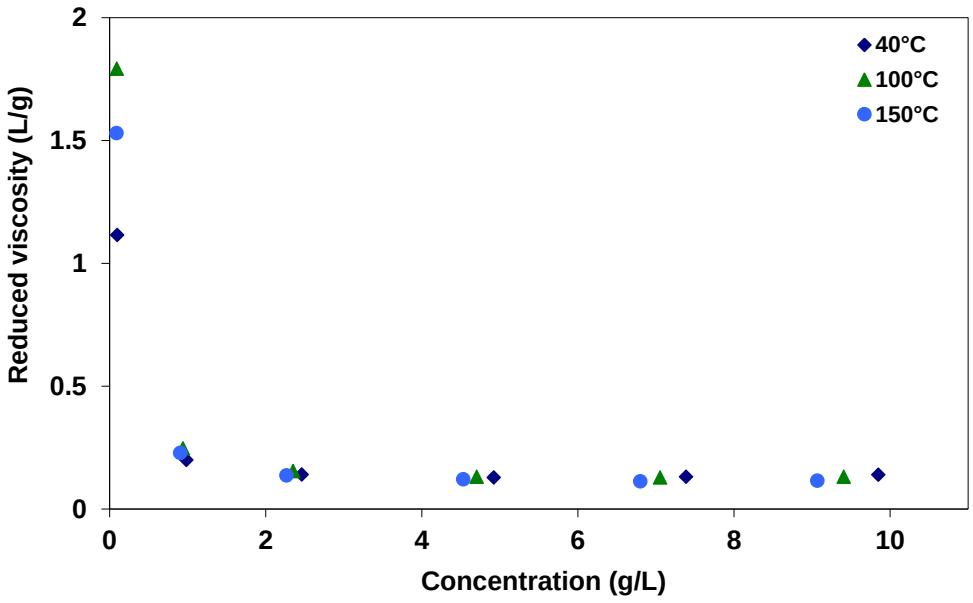


*Figure 58: Variation of the reduced viscosity of OCP versus polymer concentration*

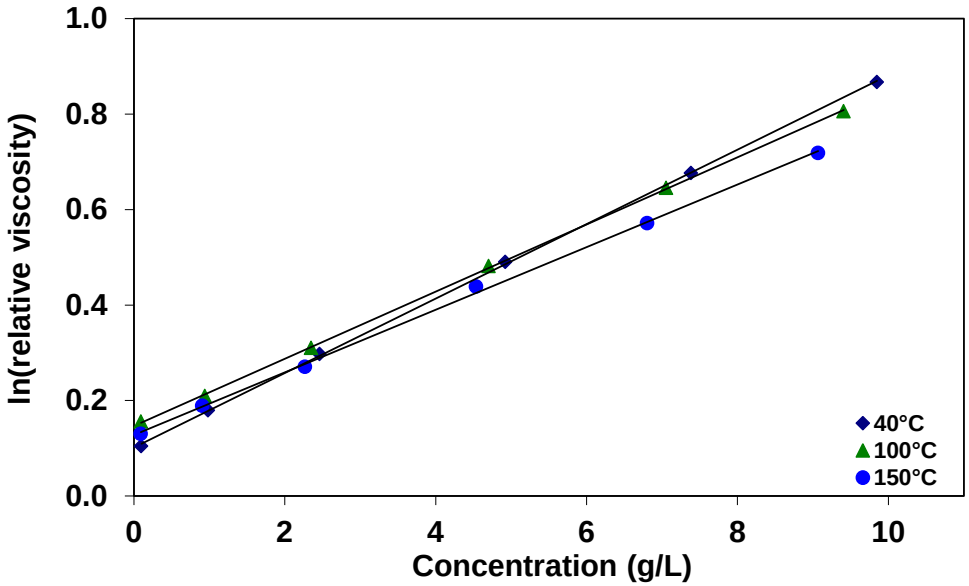


*Figure 59: Variation of ln(relative viscosity) of OCP versus polymer concentration*

| | [$\eta$] (L/g) | | |
|---|---|---|---|
| | **Base oil+PAMA** | **Base oil+OCP** | **Base oil+PISH** |
| **40 °C** | 8.30E-03 | 7.65E-02 | 8.29E-02 |
| **100 °C** | 1.68E-02 | 7.04E-02 | 8.38E-02 |
| **150 °C** | 2.93E-02 | 5.92E-02 | 6.70E-02 |

*Table 12: Intrinsic viscosities of polymer-thickened solutions at different temperatures*

Obviously, the intrinsic viscosities of the PAMA solution are lower than that of the OCP blending and the PISH-thickened base oil. The two latter exhibit really close intrinsic viscosities. Moreover, the intrinsic viscosity rises in function of temperature for the PAMA solution whereas it decreases for the two other blends. This is in good agreement with the observations on the hydrodynamic radius made in IV.4.1 since the intrinsic viscosity is proportional to $R_h$ (see Equation (56)).

### *IV.4.2.b Direct measurements of the hydrodynamic radius at atmospheric pressure*

Two direct methods were used at atmospheric pressure to confirm the values of the hydrodynamic radii derived from the Einstein's law.

Firstly, triple detection size exclusion chromatography (SEC) (Appendix K-1) was used to determine the average hydrodynamic radii of polymers in THF for OCP, PISH and PIB. However, PAMA adsorbed on the column surfaces, consequently, its hydrodynamic radius was not measurable by this method.

Secondly, the hydrodynamic radii of polymers in heptane were measured from the dynamic light scattering (DLS) facility (cf. Appendix K-2) except for PAMA because its refractive index increment (the dependence of the refractive index on concentration: *dn/dc*) was too low in heptane.

Table 13 summarizes all the calculations and measurements performed to find the hydrodynamic radius, at atmospheric pressure, of PAMA, OCP, PISH and PIB in mineral hydrocracked base oil, THF or heptane.

| | $R_h$ (nm) | PAMA | OCP | PISH | PIB* |
|---|---|---|---|---|---|
| Deducted | **Einstein law**<br>(in base oil, in heptane for PIB)<br>100 - 150 °C | 10.5 - 13.8 | 10.7 - 10.8 | 19.2 - 19.5 | 6.9 - 7.0<br>(At 25 MPa) |
| | **Intrinsic viscosity**<br>(in base oil)<br>40 - 150 °C | 9.7 - 14.7 | 12.3 - 11.3 | 21.1 - 19.6 | - |
| | **Flory** equations<br>($R_h$=$R_g$ / 0.77)<br>theta solvent<br>good solvent | <br><br>13.7<br>(30.6) | <br><br>7.5<br>17.8 | <br><br>18.1<br>(46.6) | <br><br>7.1<br>15.4 |
| Direct measurement | **Triple detection SEC**<br>(in THF)<br>20 °C | - | 14.5 | 21 | 9 |
| | **Dynamic light scattering**<br>(in heptane)<br>20 °C | - | 12.3* | 22.5* | 7 |

*Table 13: Hydrodynamic radii from different methodologies at atmospheric pressure*
** Solid polymer, not diluted beforehand*
*( ) good solvent hypothesis not validated a posteriori*

The calculated, deduced and measured hydrodynamic radii are really coherent. At ambient pressure the results given by the direct measurements techniques confirm the values deduced from the Einstein's law, meaning that the different methodologies are consistent. The method based on the Einstein's law is thus considered as validated. It is really attractive because experiments and data processing are rather rapid and simple: only one concentration is needed, it is usable under high pressure, for any type of molecules and solvents.

"Theoretical" Flory equations [95] provide another method to compare the hydrodynamic radii values. They give approximations of the radii of gyration for spheres (cf. Equation (41), p. 78). Values reported in Table 13 confirm those found by the other ways.

For PAMA, the deduced values of $R_h$ are close to the calculated ones in theta solvent conditions. This justifies the fact that theta solvent conditions are applicable and that the critical concentration for PAMA should be equal or close to 16.5% (cf. Table 11 in section IV.1, p. 107). This confirms that the actual concentration of 1.2% is far from the real critical concentration. The dilute regime hypothesis necessary for the use of the Einstein's law is thus verified. Secondly, the deduced and measured values of $R_h$ of OCP are between the calculated ones in the theta and good solvent conditions. This means that the critical concentration might be between 21.8 and 1.7%. Finally, for PISH, measured values of the hydrodynamic radius are closer to the values coming from the Flory equation for a theta solvent than to the values estimated from good solvent conditions. This confirms that the theta solvent conditions are justified for the calculation of the critical concentration. As a consequence for PISH, the critical concentration is more likely to equal 7.4 than 0.4%. To conclude,

the values of $R_h$ derived from all the different methods confirm the initial assumption of dilute regime in all the cases. Consequently, the use of the Einstein's law is justified.

The following chart summarizes the necessary steps to determine both the hydrodynamic radius and the relationship with the critical concentration and the solubility of the polymer in the extreme cases of theta and good solvent.

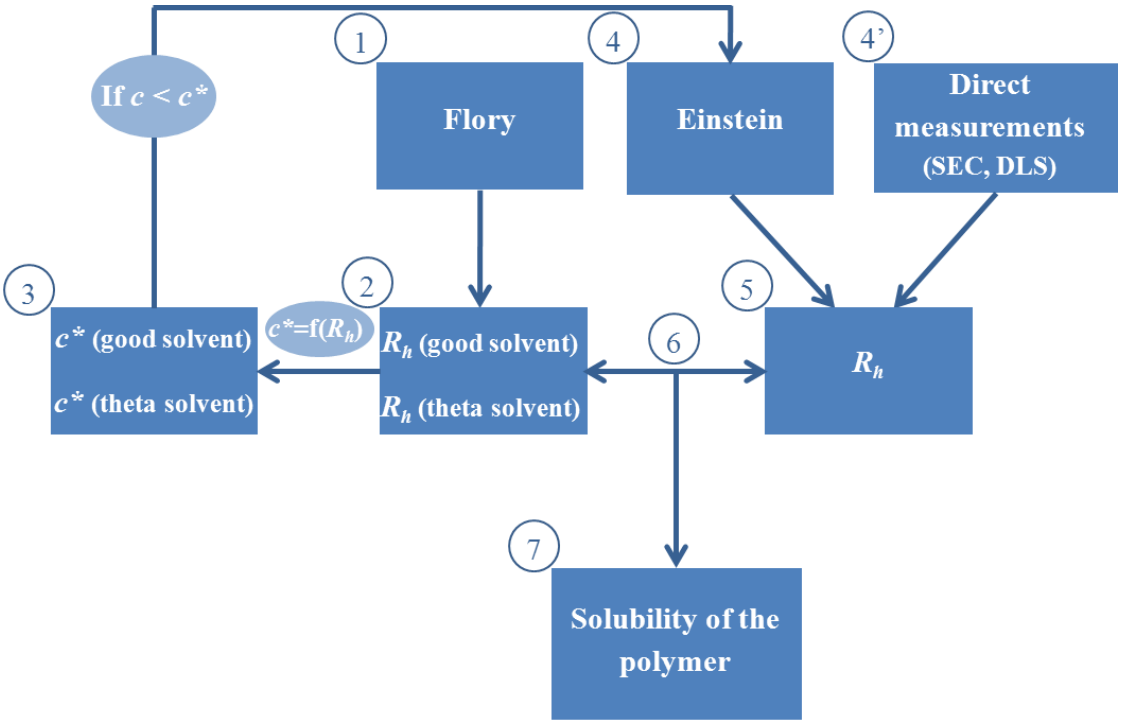


*Figure 60: Approach for the determination of the hydrodynamic radius and solubility*

The steps are described as follow:
1) Calculation of $R_h$ by the Flory equations
2) $c^*$ calculations
3) Comparison between $c$ and $c^*$
4&4') Deduction of $R_h$ (5) from high pressure viscosity and the Einstein law and direct measurements of $R_h$ (5) from SEC and DLS
6) Comparison between the various $R_h$ calculated from different methods
7) Conclusion on the solubility of the polymer

## IV.4.3 Discussion: relationship between the molecular properties and rheology

Molecular considerations in the dilute regime can now be taken into account to discuss the rheological results presented in section *III.2.2*.

### *IV.4.3.a Conformation effect*

The influence of conformation can be properly analyzed when the polymer sizes are comparable. Although PAMA and OCP have very different molecular weights (400 000 for PAMA and 88 420 for OCP), they have similar hydrodynamic radii. From 200 to 400 MPa, the hydrodynamic

radius of PAMA lies between 8 and 12 nm which is close to the radius of OCP ($R_h \approx 10$ nm). One observes no shear-thinning for the PAMA solution and a strong one for OCP. The major difference between PAMA and OCP is their conformation: the PAMA is comb and OCP is linear. As a consequence, PAMA presents intramolecular bonds (hydrogen and Van der Waals) between the branches of the comb and, therefore, the chain is less deformable than OCP: in other words, it is much more difficult to stretch PAMA molecules than OCP ones. Another explanation could be that the relaxation time of the PAMA would be inferior to the time of the measurement or that PAMA would relax more quickly than OCP (and PISH). Using Equation (12) at 40 °C and 400 MPa as a first approximation, its relaxation time is almost 100 times smaller than the ones of OCP and PISH.
In terms of rheology, as explained in II.2.1, if the polymer chain does not easily stretch, the viscosity will remain the same whereas if the polymer coil stretches, the viscosity of the solution will decrease. The latter phenomenon is called "shear-thinning". To conclude, for similar sizes of polymer coils, conformation plays a major role on the rheological response of the polymer base oil solutions.

#### *IV.4.3.b Size effect*

It is observed in our experiments that shear-thinning is stronger for PISH than for PAMA. Knowing that they have both conformations implying steric hindrance, this behavior can be explained by the fact that, for each temperature, the PISH hydrodynamic radius is larger (close to 20 nm) than that of PAMA (close to 10 nm). According to [10] and [96], shearing implies a drop of viscosity on larger molecules for comparable intramolecular bonds, and this is verified in this work.

#### *IV.4.3.c Competition between conformation and size effects*

Even if the star conformation is less deformable than the linear conformation, due to the intramolecular interactions between the branches of the star, shear-thinning is larger for PISH than for OCP. Indeed, the size of PISH is two times the one of OCP. We can conclude that the size effect prevails over conformation in this case.

#### *IV.4.3.d Solubility and swelling*

Furthermore, the explanation of the intramolecular interactions and of the steric hindrance of PAMA leading to a small hydrodynamic radius is emphasized by solubility and polarity considerations. Quoting Hansen [97], the best empirical rule for solubility problems is that "like dissolves like": it means that one solvent is more efficient when its solubility parameters are similar to the ones of the solute. To summarize, the Hansen parameters take into account polar and hydrogen bonding forces between the solvent and the solute. It is important to keep in mind that a polar solvent easily dissolves polar entities and a non-polar solvent dissolves non-polar chemicals. When the solubility is high, the affinity between entities is high as well, dipole-dipole interactions and hydrogen bonds are created and solvent molecules surround the solute and penetrate inside the polymer chains. As a consequence, the coils swell and the hydrodynamic radius gets larger. On the opposite, if the solubility is low, there is no good affinity between the solvent and the solute, no bonding exists and instead of being attracted, solvent molecules are repulsed. Thus, polymer chains tend to collapse, to take globule conformations and the hydrodynamic radius is small.

PAMA is polar and the mineral hydrocracked base oil is a non-polar hydrocarbon. There is no good affinity between the solvent and the polymer. The PAMA takes a globule conformation, in which intramolecular bonds are very strong. As said earlier, values in Table 13 (p. 117) confirm that PAMA behaves as if it was in a theta solvent because its hydrodynamic radius deduced from the viscosities is close to the one calculated with the Flory equation in a theta solvent condition.

# *IV.5 Conclusion*

In conclusion, this chapter has shown that there is a tight relationship between the rheology and the physico-chemistry of polymers. Different rheological behaviors have been highlighted according to the chemistry and conformation of the macromolecules. The low shear-thinning of the PAMA solution was unexpected and several reasons have been raised. We have shown that the usual concentration of polymer in an engine lubricant appears to be in a dilute regime which implies that polymer solutions can be compared using similar physico-chemical mechanisms, that functional additives have no influence on shear-thinning and that the absence of a viscosity drop in function of shear stress for PAMA is not related to the LCST of the solutions. All these previous hypotheses have been excluded.

The notion of hydrodynamic radius has been advanced to explain the different behaviors. First of all, different methods for determining this physical parameter have been detailed. The most straightforward one is based on the Einstein's law and allowed the determination of $R_h$ whatever the temperature and pressure conditions. For PAMA, $R_h$ rises with temperature and decreases with pressure. On the contrary, for OCP and PISH, temperature and pressure variations evidenced almost no influence on $R_h$. Other competing methods but limited to ambient conditions have shown a good agreement and have confirmed the results obtained from the one based on the Einstein law.

The effect of shear rate on hydrodynamic radii has been studied. At equal hydrodynamic radius, the linear polymer (OCP) is more easily stretched than the comb polymer (PAMA) because of the strong steric hindrance and intramolecular bondings of the latter. Moreover, even if the star polymer (PISH) is expected to be more difficult to stretch than the linear PAMA for the same reasons, the viscosity of the former decreases much more. In that case, the large hydrodynamic radius of the PISH polymer results in a stronger alignment effect than for OCP: the shear-thinning effect is thus more intense with PISH.

This section showed how the rheological behavior of polymer solutions, important to the automotive industry, can be rationalized on the basis of hydrodynamic size and molecular conformation (linear, comb or star) of polymer coils. The influence of $R_h$ seems to be dominant over conformation. However, for comparable $R_h$, conformation becomes a factor to be considered. Finally, this chapter emphasizes the successful use of the Einstein's law at high pressure to determine the hydrodynamic radius of polymer in solution which is helpful to explain their rheological behavior on a molecular basis.

# V From rheology towards tribology

An engine is a complex organ with tribological issues and overcoming the whole lubrication regimes. In hydrodynamic and elastohydrodynamic regimes, a full film separates the two sliding surfaces and the rheology of lubricants, in addition to compressibility, thermal properties etc., determine their performance. In part III, different rheological behaviors have been highlighted and it is of main interest to understand how they can control the tribological response under severe conditions, representative of those encountered in an engine.

The objective of this last chapter is to provide and analyze a complete tribological study of the polymer solutions. Film thicknesses and friction coefficients are measured and compared with both analytical and numerical models. This section also deals with the relationship between rheology and tribology. By extension (see chapter IV), it bridges the gap between tribology and physico-chemistry of polymers.

The operating conditions in an automotive engine are multiple and very drastic, leading to complex tribological behaviors. In order to represent them as accurately as possible, it is necessary to choose relevant experimental devices. Among the conditions found in an engine, we decided to simulate severe tribological conditions (0.5 GPa for the film thickness measurements, 1 and 1.5 GPa for the traction coefficient measurements) in test-rigs in which the experimental parameters are well controlled under steady state regime.

# *V.1 Film thickness*

This section describes the film thickness measurements run in specific operating conditions. The experimental data will be compared with analytical and numerical predictions. A qualitative analogy between rheology and tribology will be highlighted.

## V.1.1 Measurements and comparison with analytical models

The elastohydrodynamic regime was reproduced in the JEROTRIB test-rig whose picture, functioning scheme and full experimental ranges are described in Appendix G. The configuration adopted for the study is a ball-on-disc contact. Although it is not representative of all the geometries found in an engine, the lubrication mechanisms are respected. The functioning principle of the rolling/sliding tribometer is conform to the one described in [98]. Several improvements and facilities insure the control of supplementary parameters like the thermal boundary conditions, the absence of reactive materials regarding a possible interaction with some lubricant's components, etc. in addition to the classical EHD operating parameters (normal load, independent rolling and sliding velocities). The EHD contact is created between a mirror-polished 100C6 steel ball whose radius is 12.7 mm and a BK7 glass disc, coated on its underside with a 20 nm semi-reflective chromium layer. The ball and the disc were carefully polished leading to a composite RMS roughness close to 3 nm. The incident white light beams are perpendicular to the surface of the disc and the reflected ones are collected onto a 3CCD high resolution color camera through a microscope. The properties of the materials are reported in Table 14.

| | Material | *Rq* (nm) | *E* (GPa) | $\nu_p$ | $\rho$ (kg/m$^3$) | $c_m$ (J.kg$^{-1}$.K$^{-1}$) | *k* (W.m$^{-1}$.K$^{-1}$) |
|---|---|---|---|---|---|---|---|
| **Glass disc** | BK7 + 20 nm semi-reflective chromium layer | 1 | 81 | 0.208 | 2510 | 858 | 1.114 |
| **Steel ball** | 100C6 | 3 | 210 | 0.3 | 7850 | 470 | 46 |

*Table 14: Specimen materials and properties used in JEROTRIB*

The velocities of the ball and the disc are independently and precisely driven by two separate brushless motors. The contact between the two solids can be in pure rolling conditions if the slide-to-roll ratio (*SRR*) (see Equation (62), p. 124) is zero or in rolling-sliding conditions if *SRR* is different from zero. The bottom of the ball dips in a reservoir containing the lubricant, ensuring fully flooded conditions in the contact. The reservoir and the two shafts are thermally isolated and heated by an external thermal control system. A platinum temperature probe monitors the lubricant temperature in the test reservoir within ±0.1 °C. The normal load is applied on the ball spindle through a static force sensor.

$$SRR = \frac{\Delta U}{U_e} = 2\frac{U_{ball} - U_{disc}}{U_{ball} + U_{disc}} \qquad (62)$$

$$U_e = \frac{U_{ball} + U_{disc}}{2} \qquad (63)$$

Where $U_e$ is the mean entrainment speed, $U_{ball}$ is the speed of the ball and $U_{disc}$ is the disc velocity.

The measurement principle, developed by Molimard *et al.* [17], [18] and recently further detailed by Doki-Thonon [19], is based on white light optical interferometry (also called differential colorimetry). They improved the film thickness measurement facility and they perfected a reliable white light interferometry post-processing methodology.

The basic principle of monochromatic interferometry is shown in Figure 61. The incident light beam of intensity $I_0$ is partially transmitted through the glass disc and partly reflected, creating light beams of intensities $I_1$ to $I_n$. $n_0$ is the lubricant index of refraction and $\lambda_l$ is the incident light wavelength.

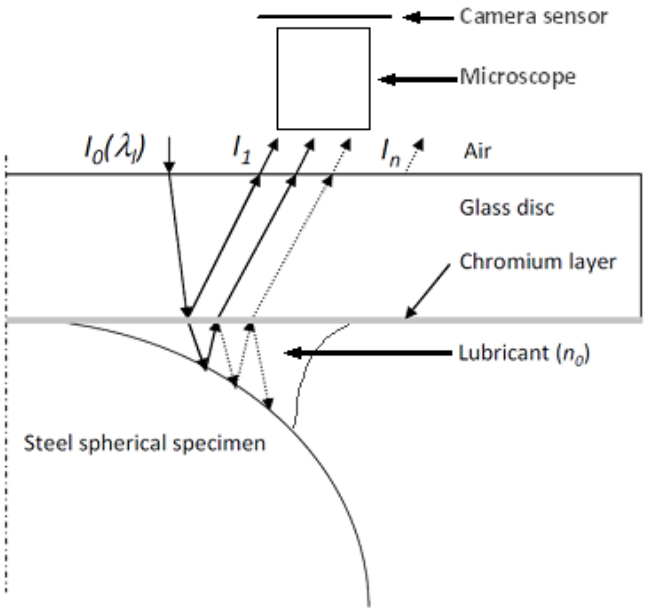


*Figure 61: Basic principle of monochromatic optical interferometry*

The distance between the ball and the disc - i.e., the film thickness of the fluid *h* - is directly linked to the values of intensities [19]. For a number of reflected and transmitted light beams (*n*) superior to 2, $I_n$ can be neglected and the intensity *I* captured by the detector is:

$$I = I_1 + I_2 + 2\sqrt{I_1 I_2}\cos\left(2\pi\left(\frac{2n_0 h}{\lambda_1} + \varphi_1\right)\right) \qquad (64)$$

where $\varphi_1$ is the phase shift due to reflection onto the steel spherical-end specimen. This phase shift depends on the quality and the thickness of the chromium layer and impact the contrast of pictures. Monochromatic interferometry shows limitations that can be overcome by the differential colorimetric techniques with a white light source. As explained in [19], the post-processing of white light interferometry pictures (see Figure 62) follows two steps. First of all, since no equation such as Equation (64) exist for the full white light spectrum, a calibration curve (see Appendix H, p. 164) is established from a static contact (the ball and the disc are stationary), giving the film thickness *h* as a function of the RGB intensity triplet, respectively the intensity of the Red, Green and Blue wavelengths, using the elasticity theory for a Hertz contact (Appendix I). The shape of the calibration curve shows that the precision of the measurements is lower for thicknesses under 100 nm. The second step is the evaluation of the film thicknesses at the center of the contact $h_c$ and at the side lobes area $h_{min}$ from a dynamic contact. The mean of the superior and the inferior $h_{min}$ is calculated. For this evaluation, a minimum of three pictures is analyzed and a mean of the film thicknesses is made by matching the measured intensities to the calibration curve. A correction on the central film thickness is applied because the pressure variations cause a density elevation and therefore, a change of the lubricant refractive index $n_0$ (see [19]). The refractive index $n(p)$ at the pressure *p* is corrected using the Lorentz-Lorenz formula [99]:

$$\frac{1}{\rho(p)}\cdot\frac{n(p)-1}{n(p)+2}=\frac{1}{\rho_0}\cdot\frac{n_0-1}{n_0+2} \qquad (65)$$

where $\rho(p)$is the mass density at the pressure $p$, $\rho_0$ the mass density at atmospheric pressure and $n_0$ is the index of refraction at atmospheric pressure.

For the sake of simplicity, the mass density at the pressure $p$ follows the Dowson-Higginson equation at a given temperature.

$$\rho(p)=\rho_0\frac{5.9.10^8+1.34p}{5.9.10^8+p} \qquad (66)$$

A change in the refractive index involves a modification of the optical path length and thereby, the film thickness must be adjusted with Equation (67):

$$h(p)=\frac{n_0}{n(p)}h_0 \qquad (67)$$

where $h(p)$ is the film thickness at the pressure $p$ and $h_0$ the film thickness at atmospheric pressure.

In the studied case, under a load of 27 N (which corresponds to a Hertzian pressure of about 500 MPa), the corrected central film thickness is lowered by 5.5% compared with the non-corrected value.

No pressure adjustment is applied on the minimal film thickness because it is determined in the side lobes region of the contact, thus, far from the center and the pressure is assumed to be close to the atmospheric pressure.

The image-processing is directly carried on a picture like the interferogram of Figure 62.

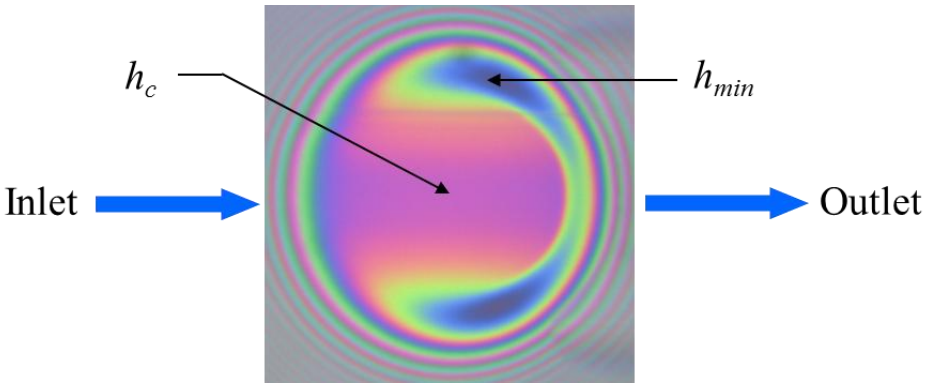


*Figure 62: White light interferogram (Base oil, 25 °C, 27 N, $U_e$=1.72 m/s, SRR=0)*

Many analytical solutions have been developed to model EHD contacts. Hamrock and Dowson [7], Moes *et al.* [20] and Chevalier [21] solved the EHD problem for circular contacts between two smooth solids in pure rolling, fully flooded, isothermal and steady state conditions, lubricated by a compressible, piezo-viscous and Newtonian fluid.

Hamrock and Dowson [7] used combinations of EHD parameters to define three dimensionless parameters allowing the complete description of a typical circular contact EHL problem. The load $W_{HD}$, the material properties $G_{HD}$ and the speed $U_{HD}$ parameters were defined as follows:

$$W_{HD} = \frac{W}{E_{eq} R_{ball}^{\ 2}}, \qquad G_{HD} = \alpha^{*} E_{eq} \qquad \text{and} \qquad U_{HD} = \frac{\eta_0 2U_e}{E_{eq} R_{ball}} \tag{68}$$

Where $W$ is the load, $E_{eq}$ the reduced Young elastic modulus of the contacting bodies (described in Appendix I), $R_{ball}$ the radius of the ball, $\alpha*$ the reciprocal asymptotic isoviscous pressure coefficient (Equation (18), p. 67) and $\eta_0$ the Newtonian viscosity at atmospheric pressure and at low shear stress.

The dimensionless film thickness $H_{HD}$ and the parameter $\varepsilon_{HD}$ are defined as:

$$H_{HD} = \frac{h}{R_{ball}} \qquad \text{and} \qquad \varepsilon_{HD} = 1.03\left(\frac{R_y}{R_x}\right)^{0.64} \tag{69}$$

$$H_{HD} = K_{HD} U_{HD}^{a_{HD}} W_{HD}^{b_{HD}} G_{HD}^{c_{HD}} \tag{70}$$

Where $K_{HD}$, $a_{HD}$, $b_{HD}$, $c_{HD}$ are given in Table 15.

| | $K_{HD}$ | $a_{HD}$ | $b_{HD}$ | $c_{HD}$ |
|---|---|---|---|---|
| $H_{HD}^{center}$ | $1.69\ \ 1-0.61e^{-0.73\varepsilon_{HD}}$ | 0.67 | -0.067 | 0.53 |
| $H_{HD}^{\min}$ | $2.27\ \ 1-e^{-0.68\varepsilon_{HD}}$ | 0.68 | -0.073 | 0.49 |

*Table 15: Hamrock-Dowson parameters [7]*

These equations are valid only when $R_x < R_y$.

Moes [100] have reduced the three dimensionless Hamrock-Dowson parameters to only two analytical parameters $M_{Moes}$ and $L_{Moes}$ to fully describe an EHD contact. The load parameter $M_{Moes}$ and the material properties parameter $L_{Moes}$ read:

$$M_{Moes} = \frac{W_{HD}}{U_{HD}^{\ 3/4}} \qquad \text{and} \qquad L_{Moes} = G_{HD}\ \ U_{HD}^{\ 1/4} \tag{71}$$

The Moes dimensionless film thickness is thus defined by:

$$H_{Moes} = \frac{h}{R_{ball}\sqrt{U_{HD}}} \tag{72}$$

The following mathematical formula describes the central film thickness:

$$H_{Moes}^{center} = \left[\ \ 1.70\, t\, M_{Moes}^{-1/9}\ L_{Moes}^{3/4}\ \ ^{r} + \ 1.96\, M_{Moes}^{-1/9}\ \ ^{r\ \ s/r} + \ 47.3\, M_{Moes}^{-2}\ \ ^{s}\ \right]^{1/s} \tag{73}$$

Where

$$r = \exp\left(1 - 6/L_{Moes}\right) + 8$$
$$s = 12 - 10\exp\left(-M_{Moes}^{-2}\right) \quad (74)$$
$$t = 1 - \exp\left(-0.9\, M_{Moes}^{1/6} / L_{Moes}^{1/6}\right)$$

According to [101], the minimal film thickness is calculated from the latter equation and the Chevalier table [21] as functions of the dimensionless parameters $M_{Moes}$ and $L_{Moes}$. The Moes-Venner and Chevalier predictions are valid for a wide range of $M_{Moes}$ and $L_{Moes}$ whereas the Hamrock-Dowson solutions are applicable for a much more reduced domain [101].

The experimental work presented in this manuscript aims at studying the tribological behavior for the different polymer-thickened base oil solutions and comparing them firstly with analytical solutions. The following figures show the evolution of the central and minimal film thicknesses in function of the mean entrainment speed $U_e$, in pure rolling conditions (*SRR*=0). Analytical predictions are added on the same graphs to provide visual comparison. In black line, the Hamrock-Dowson solution is plotted for $h_c$ and in red line, the Moes Chevalier predictions are plotted for $h_{min}$. The Hamrock-Dowson minimal film thickness and the Moes central film thickness are not plotted because of a lack of accuracy of these analytical predictions [101].

The experimental conditions applied for the film thickness measurements are listed in Table 16.

| | |
|---|---|
| **Load *W* (N)** | 27 |
| **Hertz pressure $p_H$ (GPa)** (see Appendix I) | 0.497 |
| ***SRR*** | 0 |
| **Temperature (°C)** | 25, 75 |

*Table 16: Experimental conditions for film thickness measurements*

The following log-log graphs show both the evolution of the experimental central and minimal film thicknesses versus the mean entrainment speed and the analytical predictions at 25 °C and 75 °C.

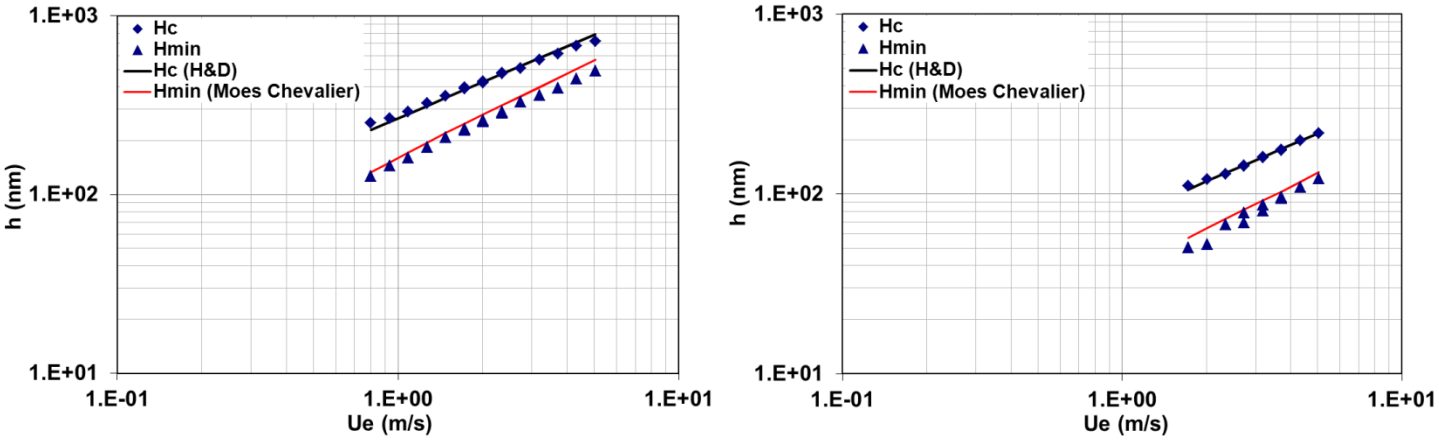


*Figure 63: Experimental and analytical central and minimal film thicknesses of the base oil at 25°C (left) and 75 °C (right)*

At 25 °C and 75 °C, the minimal and central film thicknesses of the base oil fairly follow the evolution of the analytical values in function of the entrainment speed. One of the specific assumptions for the use of these analytical models is that the fluid is Newtonian. Thereby, the base oil can be truly considered Newtonian.

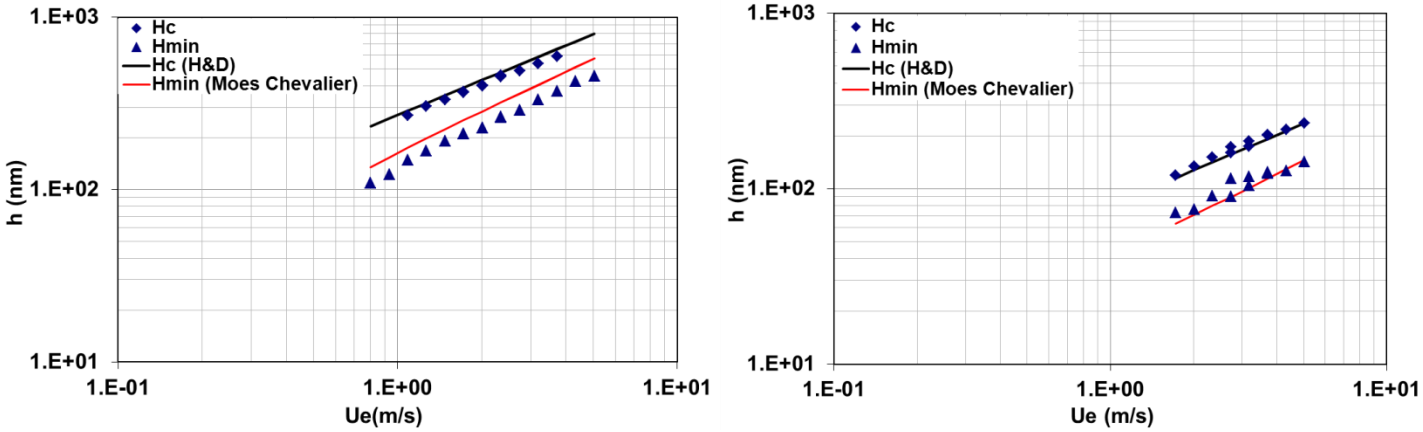


*Figure 64: Experimental and analytical central and minimal film thicknesses of the PAMA solution at 25°C (left) and 75 °C (right)*

At 25 °C the PAMA-thickened base oil film thicknesses are close to the analytical predictions but there is still a small deviation of around 10%. At 75°C, the experimental film thicknesses fairly follow the analytical estimations. The PAMA solution can thus be considered as Newtonian.

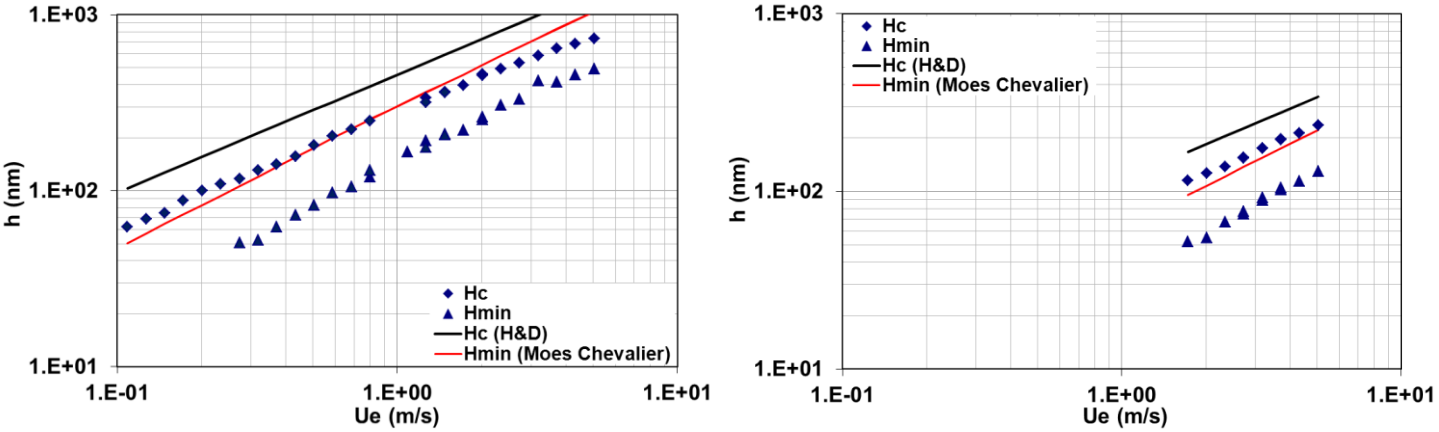


*Figure 65: Experimental and analytical central and minimal film thicknesses of the OCP solution at 25°C (left) and 75 °C (right)*

At 25 °C and 75 °C, the film thicknesses of the OCP solution deviate from the analytical models by 30 to 40%, but keeping a slope close to the predictions. This is typical of a non-Newtonian behavior [101]. The shear-thinning behavior mainly occurs in the convergent of the contact where the polymers are severely sheared by the intense recirculation of the fluid. At 25 °C the slope of $h_c$ is 0.67 from 0.1 to 0.8 m/s and above, it decreases down to 0.57. This might be attributed to the occurrence of thermal effects. Cheng [102] proposed a formula to calculate a thermal factor and Jubault *et al.* [103] evidenced a yield value below which lubricants properties are modified by shear-heating: when the film thickness reduction coefficient is below 0.96. The latter takes values equal to or lower than 0.96 from 1.1 m/s which proves that the lubricant flow cannot be considered as isothermal anymore. The thermal coefficient reaches values below 0.96 for entrainment speeds above 2 m/s if we consider the actual value of the viscosity at the inlet of the contact (see Table 18).

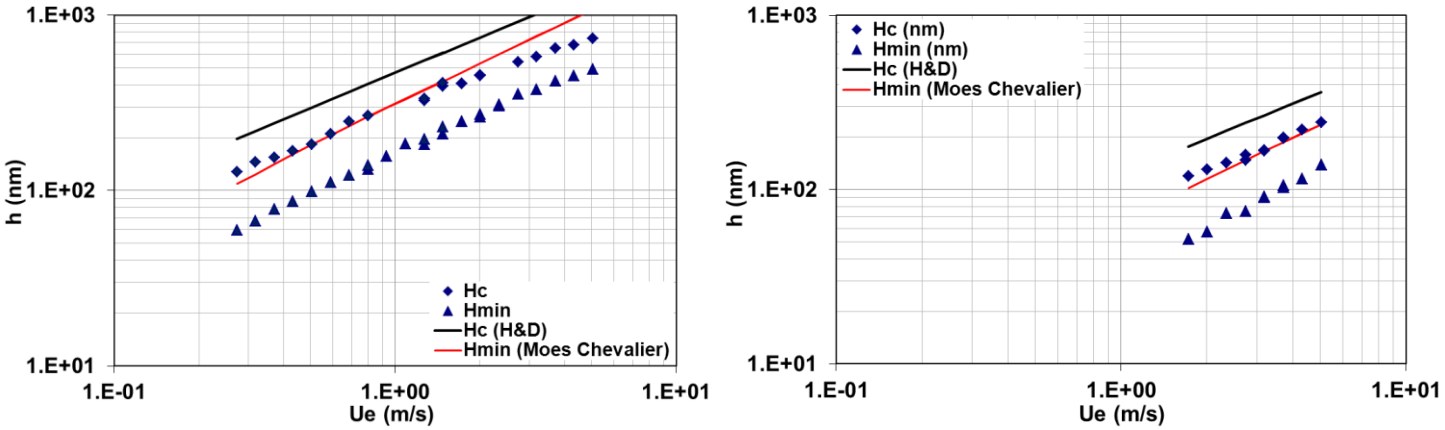


*Figure 66: Experimental and analytical central and minimal film thicknesses of the PISH solution at 25°C (left) and 75 °C (right)*

At 25 °C and 75 °C, the PISH-thickened solution shows film thicknesses deviated by 30 to 50% from the analytical predictions but remaining parallel to the predicted film thicknesses. Once more, the shear-thinning effect can explain this deviation. At 25 °C, the $h_c$ slope is 0.67 from 0.3 m/s to 1.5 m/s and lowers to 0.56 at higher speeds. The Cheng [102] film thickness reduction coefficient is lower than 0.96 beyond 1.5 m/s which justifies the change in slope for the film thicknesses graphs in function of speed. Considering the real viscosity at high shear rate deducted from the Hamrock-Dowson predictions (see Table 18), the thermal Cheng coefficient is below 0.96 from 2.3 m/s.

Power regressions have been carried out for all the experimental curves of $h_c$ in function of the mean entrainment speed at 25 °C and 75 °C but they are not shown in the graphs for the sake of clarity. The power exponents (i.e., the slopes in log-log plots) and the pre-factors (corresponding to $\log K_{HD} W_{HD}^{b_{HD}} G_{HD}^{c_{HD}}$ ) are listed in Table 17 for $h_c$. In order to provide a reasonable comparison, one should verify that the pre-factors are close, which means that only the parameter $U_{HD}$ is compared.

In the Hamrock-Dowson formula (Equation (70), p. 127), isothermal conditions and a Newtonian fluid are assumed. The speed exponent corresponds to $a_{HD}$ which is equal to 0.67 for $h_c$. If it is slightly different, it might be because the hypotheses of the analytical models cannot be applied or because of the experimental uncertainties. If the dissimilarity is more obvious, thermal effects may occur.

| | Temperature (°C) | $U_e$ (m/s) | Power exponent $a_{HD}$ | Pre-factor | Correlation coefficient |
|---|---|---|---|---|---|
| **Base oil** | 25 | 0.8 - 5 | 0.59 | 282.8 | 0.998 |
| | 75 | 1.7 - 5 | 0.64 | 76.7 | 1.00 |
| **Base oil + PAMA** | 25 | 0.8 - 5 | 0.64 | 259.26 | 0.997 |
| | 75 | 1.7 - 5 | 0.63 | 86.8 | 0.983 |
| **Base oil + OCP** | 25 | 0.1 - 0.8 | 0.67 | 282.3 | 0.997 |
| | | 1.3 - 5 | 0.57 | 297.6 | 0.994 |
| | 75 | 1.7 - 5 | 0.69 | 78.3 | 0.997 |
| **Base oil + PISH** | 25 | 0.3 - 1.5 | 0.67 | 303.1 | 0.991 |
| | | 1.5 - 5 | 0.56 | 301.2 | 0.989 |
| | 75 | 1.7 - 5 | 0.68 | 79.7 | 0.977 |

*Table 17: Power law parameters for the log-log plots of $h_c$*

For all the studied solutions, the Hamrock-Dowson power exponent $a_{HD}$ is close to 0.67 except for the OCP and PISH solutions at 25 °C and high entrainment speed which are equal to 0.57 and 0.56 respectively. This might be an evidence of thermal effects.

The real viscosity in the contact inlet was calculated from the experimental $h_c$ and the Hamrock-Dowson analytical equation at 4.3 m/s at 25 and 75 °C and compared with the low shear stress viscosity predicted by the modified WLF-Yasutomi model.

| | **Temperature (°C)** | **$\eta_{inlet}$ (Pa.s) H&D** | **$\eta_0$ (Pa.s) WLF** | **$\frac{\eta_{0\,WLF} - \eta_{H\&D}}{\eta_{WLF}} x100$ (%)** |
|---|---|---|---|---|
| **Base oil** | 25 | $3.3\ 10^{-2}$ | $3.5\ 10^{-2}$ | < 15 |
| | 75 | $7.2\ 10^{-3}$ | $6.7\ 10^{-3}$ | < 15 |
| **Base oil + PAMA** | 25 | $3.0\ 10^{-2}$ | $3.5\ 10^{-2}$ | < 15 |
| | 75 | $7.8\ 10^{-3}$ | $7.6\ 10^{-3}$ | < 15 |
| **Base oil + OCP** | 25 | $3.2\ 10^{-2}$ | $7.6\ 10^{-2}$ | 57.9 |
| | 75 | $7.3\ 10^{-3}$ | $1.3\ 10^{-2}$ | 42.5 |
| **Base oil + PISH** | 25 | $3.1\ 10^{-2}$ | $7.8\ 10^{-2}$ | 60.2 |
| | 75 | $7.6\ 10^{-3}$ | $1.4\ 10^{-2}$ | 44.7 |

*Table 18: Comparison between the viscosity in the contact inlet calculated from the Hamrock-Dowson correlations and the low shear stress viscosity from the modified WLF-Yasutomi model*

For the base oil and the PAMA solution, at 25 and 75 °C, the viscosity deducted from Hamrock-Dowson is close to the one predicted by the modified WLF-Yasutomi model which confirms that the two solutions are Newtonian. On the contrary, the viscosity coming from the Hamrock-Dowson equation is lower by 40 to 60% than the modified WLF-Yasutomi viscosity for the OCP and the PISH solutions which evidences once again their non-Newtonian behavior. At 25 °C, for the OCP and the PISH solutions, thermal effects may occur which can also be a cause of the drop of viscosity. At 25 °C and 4.3 m/s, the shear stress is close to $2\ 10^5$ Pa and at 75 °C and 4.3 m/s, it is nearby $1.5\ 10^5$ Pa for all the solutions.

All the presented curves confirm that the lubricant film linearly thickens while the entrainment speed increases in a logarithm scale, as predicted by the analytical formulas of Hamrock-Dowson *et al.*. Nevertheless, for some fluids, the experimental film thicknesses deviate from the analytical predictions. The latter do not precisely predict neither the central film thickness nor the minimal film thickness - which is critical - in case the lubricant is non-Newtonian and if thermal effects arise. We evidenced that the drop in film thickness was close to 10%, 30-40% and 30-50% for the PAMA, the OCP and the PISH solutions respectively. According to the results of chapter III, the decrease of viscosity in the range of the studied operating conditions reaches 3-11%, 20-45% and 30-50% for the PAMA, the OCP and the PISH solutions respectively. One can notice that the decline of film thickness is of the same order of magnitude as the drop of the viscosity. This observation must be taken with caution. Indeed, in the Hamrock-Dowson equation, the viscosity interferes in the speed parameter $U_{HD}$ with the exponent 0.67 and the piezo-viscous coefficient in the materials parameter $G_{HD}$ to the power of 0.53.

The previous curves show that the lowest value of the minimal film thickness (at 75 °C and for the base oil) is about 50 nm. According to Table 1 (p. 53), Table 14 (p. 124) and knowing that the

composite RMS roughness of the ball and the disc is close to 3 nm, the $h_{min}/\sigma$ ratio is higher than 5. Consequently, the fluid film is considered thick and the contact occurs in EHL regime.

In order to corroborate with the specific trends observed so far, a numerical model in which the nature of the fluid, through its rheology and thermal effects are considered, was utilized. Moreover, we used film thickness measurements to deduce behaviors but a more rigorous approach would be to use a numerical model fed with data independent from film thickness experiments. The goals of the following part are to show that it is possible to accurately predict film thicknesses comparable with the experimental ones and to establish the analogy between rheology and tribology.

## V.1.2 Comparison with numerical models

First of all, this part will give a brief overview of the numerical model used in the study. Then, the experimental and the modeled film thicknesses will be compared while revealing the importance of the rheological behavior to predict the tribological response and investigating the influence of thermal effects.

The model developed by Habchi [22] and Doki-Thonon [19] is based on a finite element approach and solves elastohydrodynamic lubrication issues. One of the purposes of this model is to solve it for stationary, three dimensional, non-Newtonian and thermal EHD circular contact problems. Figure 67 schematically summarizes the properties of the two solids (1 and 2) and the lubricant in a rolling-sliding contact. As the target is to compute the EHD problem in the experimental conditions defined of the JEROTRIB device, solid 1 represents the flat glass disc and solid 2 is the steel sphere. The applied load is $W$, $E$ is the Young modulus (subscript 1 or 2 corresponding to solid 1 or 2 respectively), $\nu_1$ and $\nu_2$ are the Poisson's coefficients for solid 1 and 2, $R_x$ and $R_y$ are the curvature radii in the $x$-direction and $y$-direction respectively. The lubricant features, already detailed, are the density and the viscosity, depending on temperature, pressure and/or shear stress.

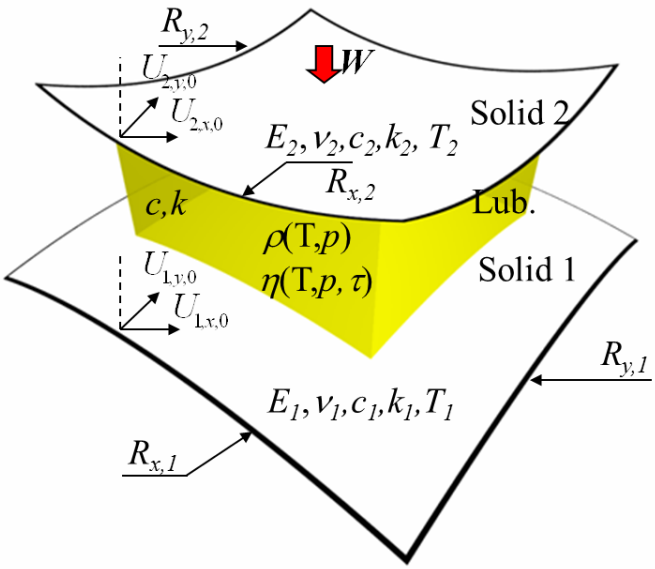


*Figure 67: Scheme of a lubricated rolling-sliding contact*

The lubricant trapped and compressed under high loads between the two solids undergoes severe conditions. Its viscosity steeply increases and the bodies deform elastically according to the EHD theory. This deformation is superior to the film thickness.

Some keys will be given to understand the general principle of the non-Newtonian Thermal ElastoHydroDynamic (TEHD) contact resolution, without pretending to be exhaustive. For further details, we advise the interested reader to refer to the PhD theses of Habchi [22] and Doki-Thonon [19].

The complete computation is based on the simultaneous resolution of strongly coupled equations, among which we find the generalized Reynolds equation, considering also the compressibility and the piezo-viscosity of the lubricant, to determine the pressure field on the contact surface. An important boundary condition is the pressure outside the contact area equals to the atmospheric pressure. Moreover, the linear elasticity equations are introduced to define the vertical deformation on an equivalent body (with an equivalent Young modulus and an equivalent Poisson's coefficient) as defined by Habchi [22]. The displacement of the solids control the film thickness expression for a circular contact in which the gap between the two solids in the center of the contact in the non-deformed state is found. A load equilibrium equation ensures the conservation of the applied normal load.

Additional equations are implemented to model the heat transfers. No heat is supposed to be created in the two solids whereas the generation of heat in the lubricant is caused by two phenomena: on the one hand, the compression of the lubricant at the inlet of the contact and its expansion at the outlet of the contact and, on the other hand, the shearing of the fluid. The created heat in the lubricant is transported and evacuated by convection and conduction through solid 1, solid 2 and in the fluid. Concerning the boundary conditions on temperature, the temperature is set constant to the initial temperature used in the experiment on solid surfaces far from the contact (≈ 2 mm), all along the computing. The lateral surfaces of the two solids and the lubricant are also set to the initial temperature when the velocity vector is pointing towards the contact center; otherwise, a free-flux condition is set. At the interfaces between the lubricant and the solids, continuity of fluxes is applied.

The model was computed using the materials' properties (detailed in Table 14, p. 124) and the experimental conditions (described in Table 16, p. 128) for the base oil and the polymer solutions. Isothermal cases were first solved. The following figures show the comparison between the experimental and numerical film thicknesses in function of the entrainment speed under pure rolling condition. The experimental minimal film thicknesses plotted in the graphs are the average of the ones determined in the upper part and the lower part of the horse-shoe shaped constriction. The model was run with the modified WLF-Yasutomi correlation (Equation (23), p. 69) for the temperature-pressure-viscosity dependence and the Tait equation (Equation (19), p. 68) for the compressibility whose parameters are presented in Table 19.

| | |
|---|---|
| **$a_v$ ($K^{-1}$)** | $7.922\ 10^{-4}$ |
| **$K_0$'** | 11 |
| **$K_{00}$ (GPa)** | 9 |
| **$\beta_K$ ($K^{-1}$)** | $6.18\ 10^{-3}$ |

| | **$\rho$ at 15 °C (kg/m$^3$)** |
|---|---|
| **Base oil** | 837.2 |
| **Base oil + PAMA** | 839.0 |
| **Base oil + OCP** | 837.7 |
| **Base oil + PISH** | 836.8 |

*Table 19: Tait parameters (left) and densities at 15°C and at atmospheric pressure (right)*

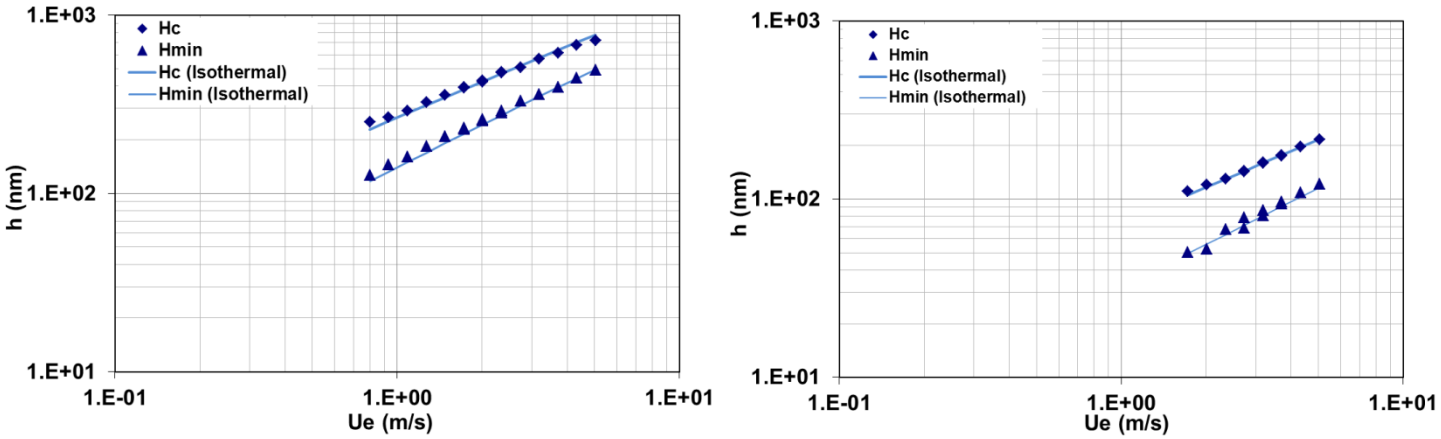


*Figure 68: Experimental and numerical **(isothermal, Newtonian)** central and minimal film thicknesses of the base oil at 25°C (left) and 75 °C (right)*

In Figure 68, the numerical model was computed considering a Newtonian fluid. The numerical results are in good agreement with the experimental data which confirms the first conclusions drawn with the analytical models, i.e. the base oil behaves as a Newtonian liquid under the operating conditions explored here.

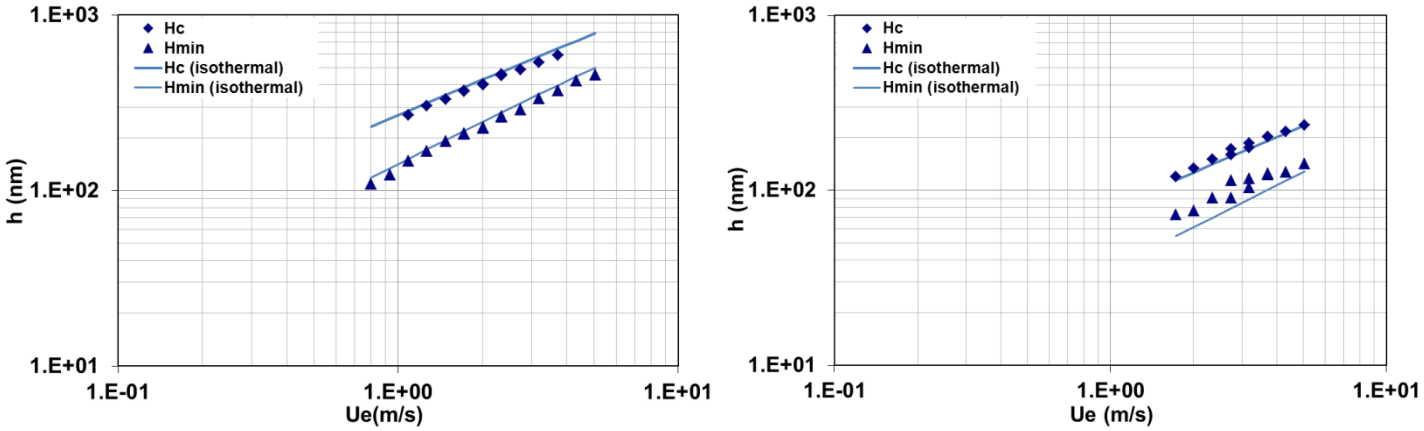


*Figure 69: Experimental and numerical **(isothermal, Newtonian)** central and minimal film thicknesses of the PAMA solution at 25°C (left) and 75 °C (right)*

The PAMA solution was considered as Newtonian in the isothermal numerical predictions. The latter are realistic because they show a fairly good agreement with the experimental film thicknesses at 25 °C and 75 °C which evidences once again the Newtonian behavior of the PAMA solution highlighted in part III.

In chapter IV, several hypotheses have been raised to explain the unexpected Newtonian behavior of the PAMA solution, as shown at 25 and 40 °C in the high pressure Couette rheometer and at 25 and 75 °C in the tribometer. Another idea can be that the shear-thinning behavior of the PAMA blend starts at higher temperatures, assuming the break of the intramolecular bonds at a critical temperature. The central film thickness was measured at 100 °C and compared with the numerical solution under isothermal conditions, considering a Newtonian fluid and plotted on Figure 70. The experimental data are in agreement with the numerical model from 3 m/s and they show a small

deviation (lower than 30 nm) below 3 m/s. Since, the precision of the measurements decreases when the thickness is lower than 100 nm because of the shape of the calibration curve (see Appendix H, p. 164), the data can still be considered to coincide with the numerical Newtonian model. As a consequence, there is no evidence of shear-thinning behavior for the PAMA solution for temperatures up to 100 °C.

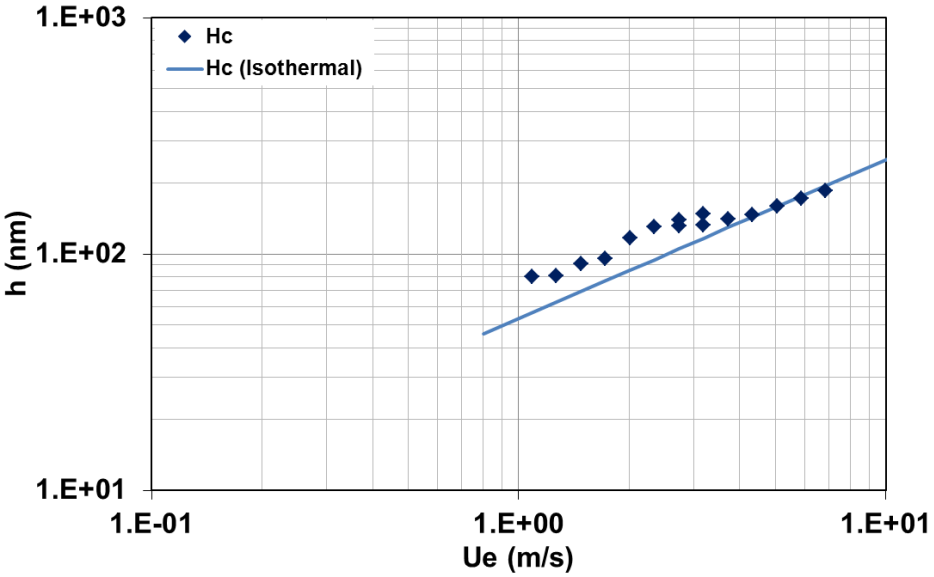


*Figure 70: Experimental and numerical **(isothermal, Newtonian)** central film thickness of the PAMA solution at 100 °C*

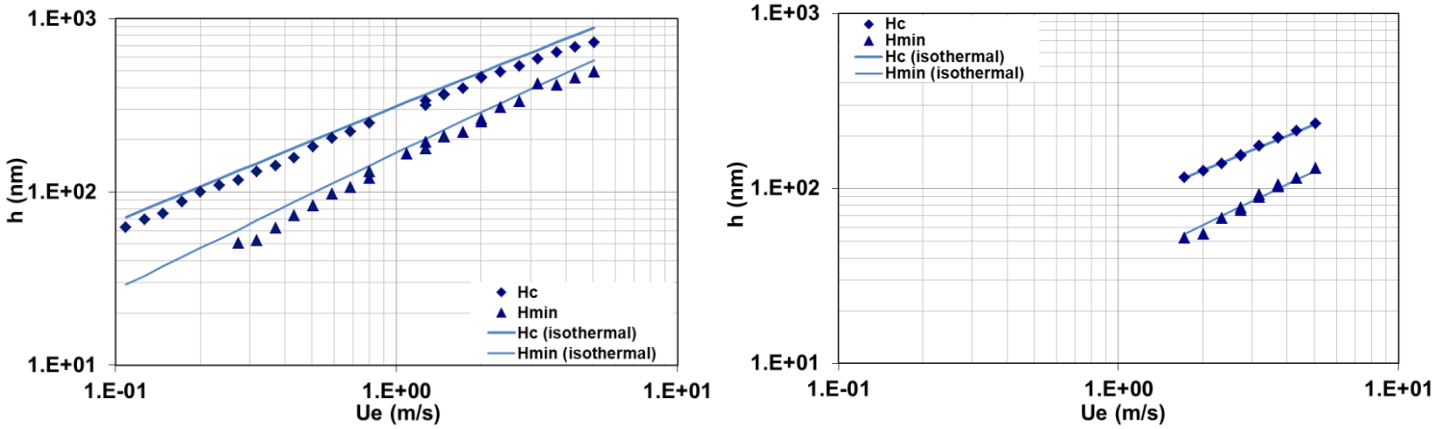


*Figure 71: Experimental and numerical **(isothermal, non-Newtonian)** central and minimal film thicknesses of the OCP solution at 25°C (left) and 75 °C (right)*

The parameters of the Carreau-Yasuda equation with a second Newtonian plateau were picked in Table 10 (p. 99) to compute the isothermal numerical model for the OCP solution. The numerical curves are really consistent with the experimental graphs at 25 and 75 °C (Figure 71) which corroborate with the conclusions of the comparison with the analytical solutions and with the rheological behavior described in chapter III. The film thickness is determined by the conditions at the inlet of the contact ($\dot{\gamma} \approx 10^6$ s$^{-1}$; $\tau \approx 10^4$ Pa) where the lubricant recirculation is the main cause of the intense shearing. The simulations slightly overestimate the film thickness which supposes that the modelled viscosity is overvalued. The second Newtonian plateau might be lower.

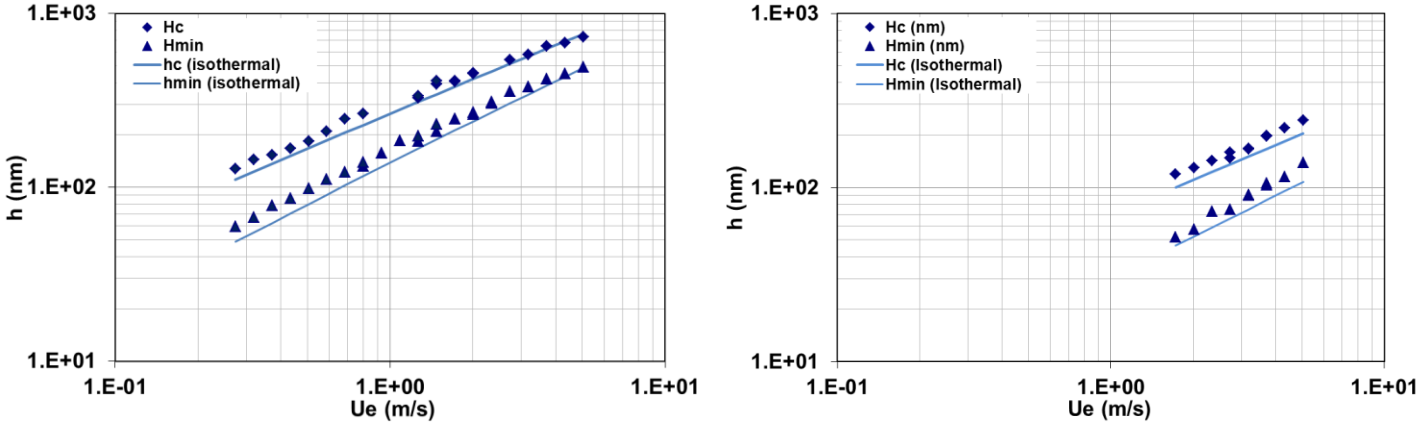


*Figure 72: Experimental and numerical **(isothermal, non-Newtonian)** central and minimal film thicknesses of the PISH solution at 25°C (left) and 75 °C (right)*

Finally, when it comes to the PISH solution, the parameters of the Carreau-Yasuda equation were also taken from Table 10 (p. 99) for the isothermal numerical solutions. At 25 °C and 75 °C, the experimental film thicknesses are well predicted by the numerical model in Figure 72. The assumption made in section V.1.1 with the analytical models saying that the PISH solution behaves as a non-Newtonian fluid is confirmed by these curves. The rheological models established in part III and used in the computing give a good agreement with the predicted film thicknesses. They are essential for relevant predictions of the film thicknesses. The predictions are lightly below the experimental data which means that the viscosity used in the simulations is likely underestimated.

In the two last figures, we showed that the numerical models accurately predict film thickness if we consider a non-Newtonian behavior. We can wonder what the graphs would be if we have considered a Newtonian liquid. The following figures illustrate the comparison between the Newtonian and the non-Newtonian film thickness predictions at 25 °C in isothermal conditions for the OCP and the PISH solutions.

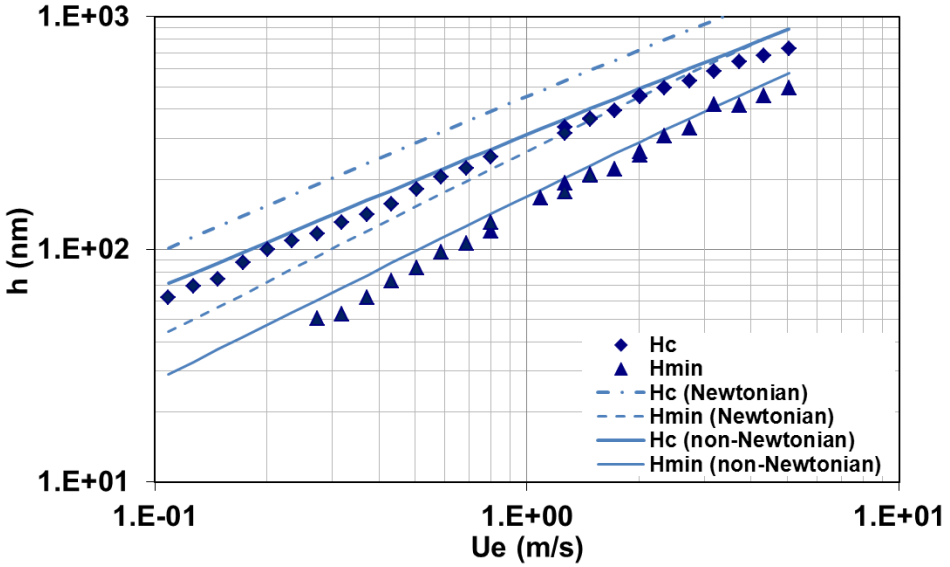


*Figure 73: Experimental and numerical **(isothermal, Newtonian and non-Newtonian)** central and minimal film thicknesses of the OCP solution at 25°C*

Using a non-Newtonian equation for the lubricant leads to film thicknesses lowered by 40% than if they were computed with a Newtonian behavior (Figure 73). The predicted film thicknesses with the non-Newtonian response are consistent with the experimental data. Moreover, 40% corresponds to the deemed difference between the analytical correlations and the experimental film thicknesses detailed in V.1.1.

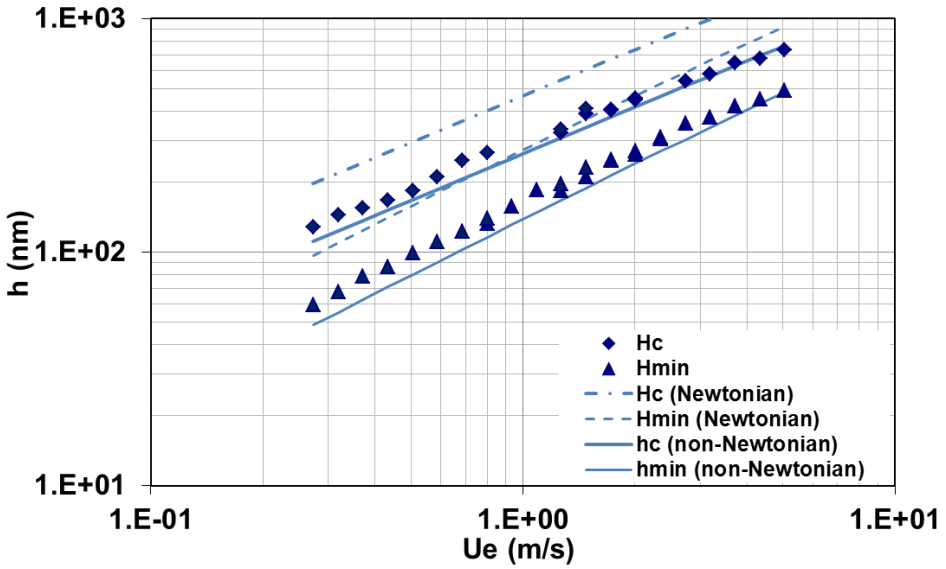


*Figure 74: Experimental and numerical **(isothermal, Newtonian and non-Newtonian)** central and minimal film thicknesses of the PISH solution at 25°C*

Central and minimal film thicknesses deduced from a non-Newtonian correlation differ by 40 to 50% from the one obtained with the Newtonian resolution for the PISH solution (Figure 74). The predictions with the non-Newtonian formula are really robust since they stick to the experimental data. The difference between the analytical models and the experimental data was also close to 40%.

As shown for the OCP and PISH solutions, the non-Newtonian predictions are way more reliable than the Newtonian ones. Consequently, it is of first importance to establish accurate rheological features for a lubricant to forecast its tribological behavior.

The film thickness decrease between the Newtonian and the non-Newtonian behavior are close to the ones determined between the analytical predictions and the experimental data. Again, we proved that there is a strong relationship between the rheological responses investigated in chapter III and explained in section V.1.1, and the decline of the film thicknesses. Obviously, there is a strong relationship between rheology and tribology. As demonstrated in chapter IV, the rheology is linked to the physico-chemistry of lubricants. By extension, the tribology is directly influenced by the molecular nature and the associated properties of the polymers and of the base oil. Thus, these deductions are useful for the selection of additives by formulators.

In order to study the eventuality of thermal phenomena, we chose two extreme cases: the base oil whose viscosity is the lowest (see Figure 75) compared to the other studied blends, and the PISH solution which is the most viscous solution at low shear stress (see Figure 76). The models were computed at 25 °C because at this temperature thermal effects are more likely to appear. The specific

heat capacity $c_m$ and the thermal conductivity $k$ were equal to 2210 $J.kg^{-1}.K^{-1}$ and 0.134 $W.m^{-1}.K^{-1}$ respectively, for both the base oil and the PISH solution.

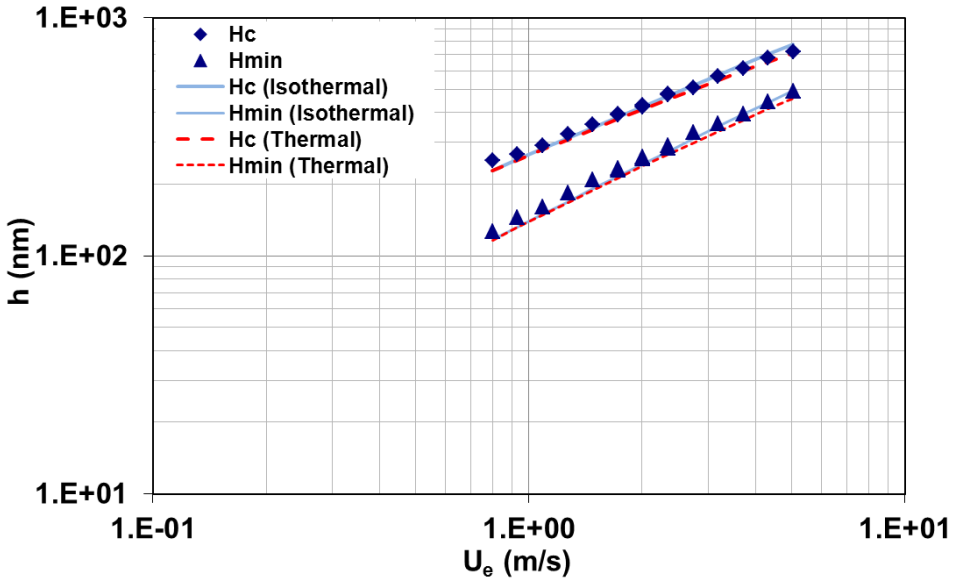


*Figure 75: Experimental and numerical **(isothermal and thermal, Newtonian)** central and minimal film thicknesses of the base oil at 25°C*

For the base oil, the Newtonian response was used in the numerical model. At 25 °C, there is a slight gap between the computed curves (isothermal and thermal) from 3 m/s (Figure 75). The maximum deviation between both simulations is close to 8% (≈ 65 nm) at 5 m/s. Consequently, in those conditions, there are no important thermal effects.

Actually, at high entrainment speed, high *SRR* or even at high load, the numerical model might not exactly represent the experiments, especially in terms of boundary conditions, which could be at the origin of the difference between the experimental data and the model.

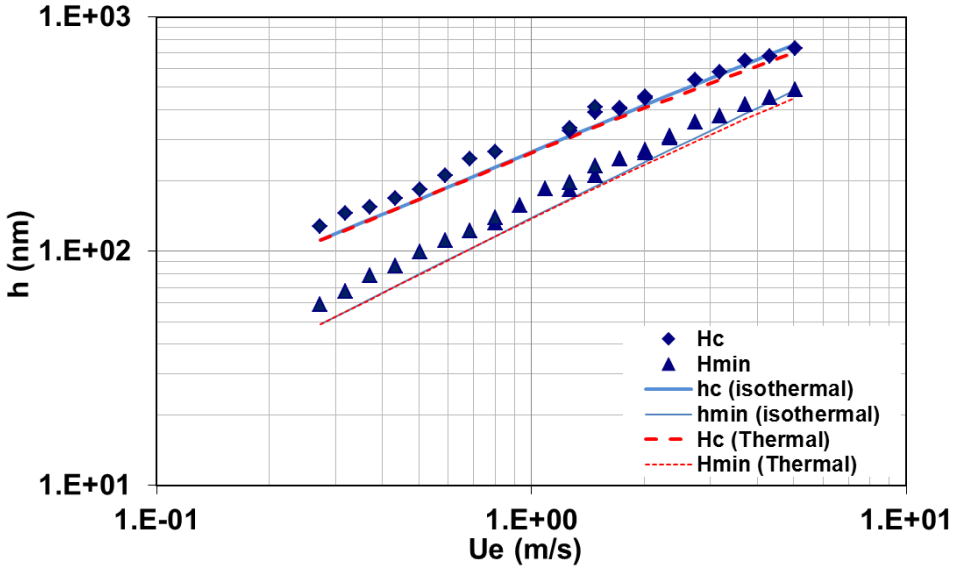


*Figure 76: Experimental and numerical **(isothermal and thermal, non-Newtonian)** central and minimal film thicknesses of the PISH solution oil at 25°C*

The non-Newtonian behavior was taken into account to predict film thickness. At 25 °C, the thermal model starts to deviate from the isothermal curves from entrainment speeds larger than 2 m/s, as evaluated by the calculation of the Cheng thermal coefficient. The maximum dissimilarity is about 7% (≈ 60 nm) at 5 m/s which is quite low. Consequently, we can consider that thermal effects occur for the PISH solution above 3 m/s but they remain weak compared to the shear-thinning influence. By extension, since the two other solutions are less viscous than the PISH solution, we can suppose that low thermal phenomena take place as well. These observations corroborate with the power exponents listed in Table 17 at 25 °C and at high entrainment speeds (0.57 and 0.56 for the OCP and the PISH solutions respectively).

To conclude, powerful numerical models showed strong agreement with experimental film thicknesses. Then, the importance of the rheological behavior in the accuracy of these resolutions was stressed. Finally, the absence of large thermal effects in the studied operating conditions was underlined. Now the film thicknesses - from tests to predictions - were fully studied, the investigation of traction coefficients is the next step to complete the tribological study.

## *V.2 Friction coefficient*

The traction coefficient is another important parameter to investigate when it comes to the full tribological performance of a system.

Measurements were still performed on the JEROTRIB test-rig (see Appendix G), equipped with three dimensional sensors. The experimental operating conditions are listed in Table 20.

| | |
|---|---|
| **Load *W* (N)** | 64, 210 |
| **Hertz pressure $p_H$ (GPa)** (see Appendix I) | 1, 1.5 |
| **$U_e$ (m/s)** | 0.8, 2.5, 5 |
| **Temperature (°C)** | 25, 75 |

*Table 20: Experimental conditions on JEROTRIB for traction coefficient measurement*

Traction coefficients in function of positive and negative *SRR* are plotted on Figure 77 for the OCP solution at 25 °C at different loads and entrainment speeds.

One can notice that the curves are almost symmetric for positive and negative *SRR*. The traction coefficient rises drastically in the region close to pure-rolling conditions (*SRR*=0) and tends to stabilize at higher slide-to-roll ratios.

At constant speed, the traction coefficient is more important for the higher load. Indeed, the increase of pressure involves the rise of the viscosity of the fluid and consequently, the internal frictions grow and the traction coefficient as well. At 2.5 m/s and 210 N, the friction coefficient slightly decreases as *SRR* increases. This effect is still present for 0.8 m/s and 210 N and for 2.5 m/s and 65 N but less visible. Again, this might be attributed to the elevated raise of viscosity implying viscous heating at large *SRR* which lowers the viscosity and thereby, the friction coefficient.

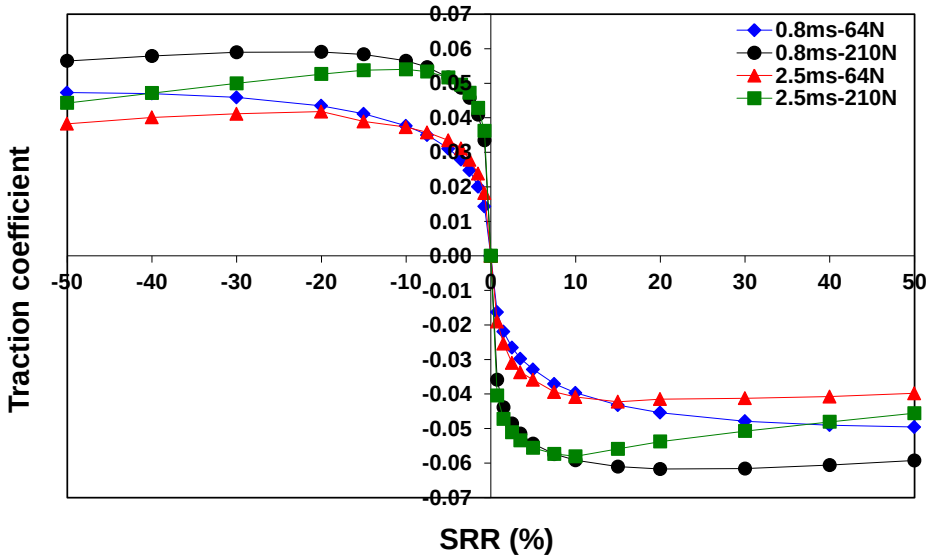


*Figure 77: Traction coefficient versus SRR for the OCP solution at 25 °C*

The following graphs compare the traction coefficients of the base oil and the three polymer solutions at two temperatures (Figure 78 and Figure 79), two loads (Figure 79 and Figure 80) and two entrainment speeds (Figure 80 and Figure 81).

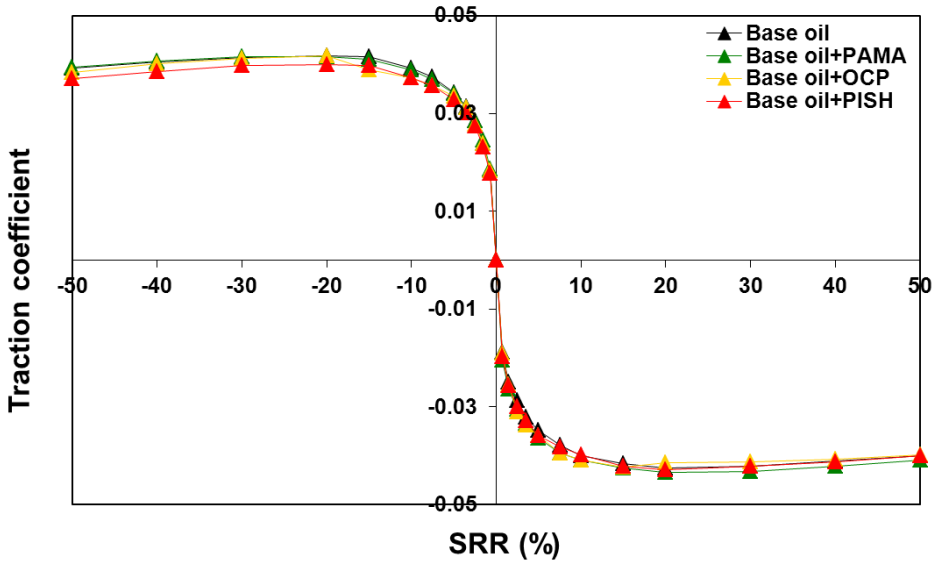


*Figure 78: Traction coefficients for all fluids at 25 °C, 2.5 m/s and 64 N (1 GPa)*

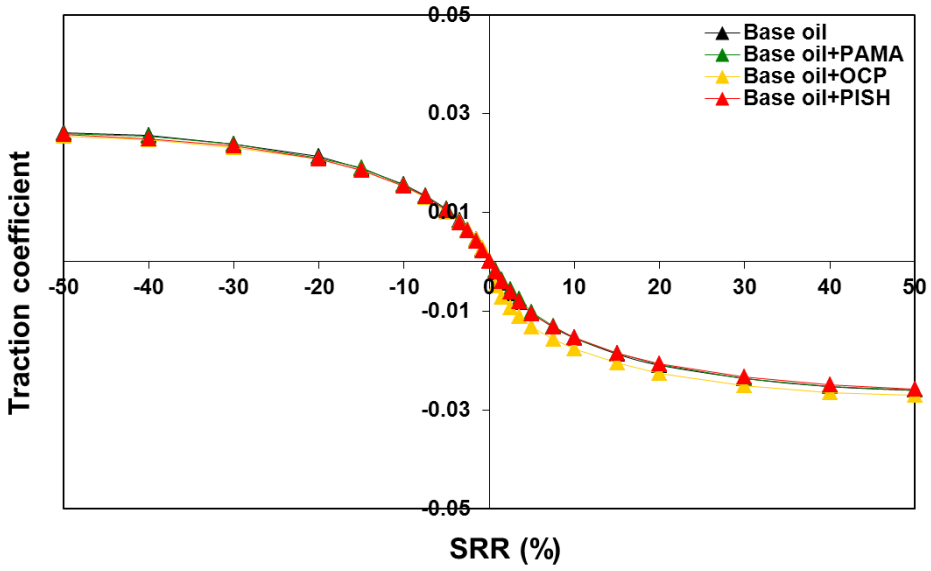


*Figure 79: Traction coefficients for all fluids at 75 °C, 2.5 m/s and 64 N (1 GPa)*

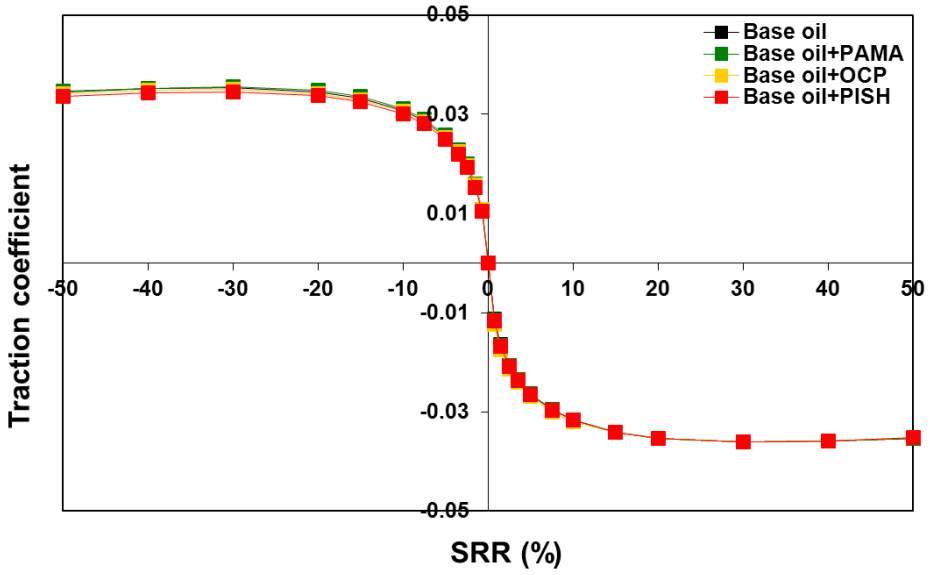


*Figure 80: Traction coefficients for all fluids at 75 °C, 2.5 m/s and 210 N (1.5 GPa)*

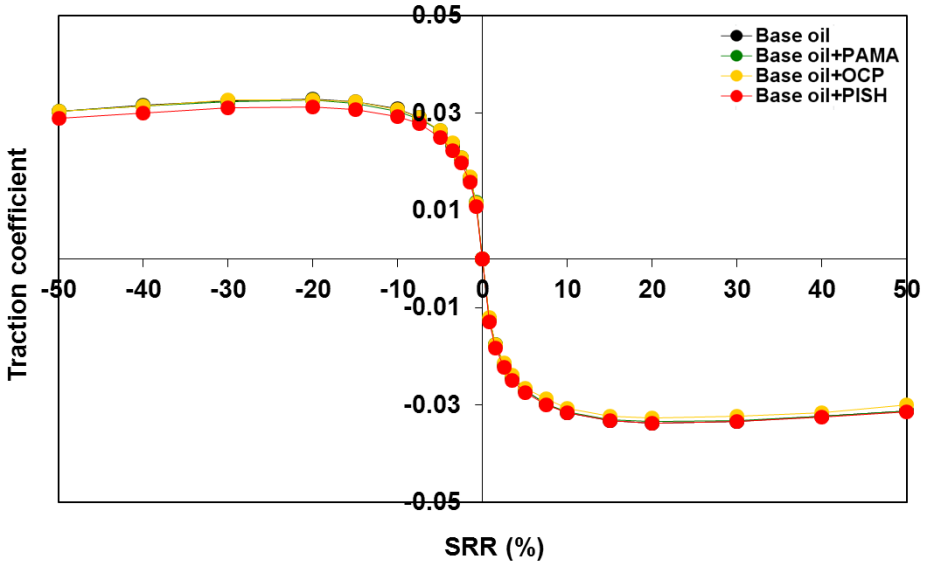


*Figure 81: Traction coefficients for all fluids at 75 °C, 5 m/s and 210 N (1.5 GPa)*

It is noticeable that the base oil and the three polymer-thickened solutions behave similarly at both temperatures, 2.5 and 5 m/s and 64 and 210 N. Other experimental conditions detailed in Table 20 (p. 139) have been tested and the traction curves do not show clear discrimination between the four lubricants. Therefore, it is difficult to draw conclusions on the role played by polymers on the friction coefficient but one can conclude that friction is mainly governed by the base oil. However, it is important to precise that given the different rheological behavior of polymer solutions, the resulting film thickness in the contact is different for each fluid.

Moreover, the results have been compared with those obtained with the Mini-Traction-Machine MTM in Appendix J.

To conclude, no significant trend was found to discriminate the four lubricants by their traction coefficient performance. It does not seem to be a relevant parameter to compare the tribological influence of those polymers under these operating conditions.

Numerical models were computed to calculate the friction coefficients in the studied operating conditions but they did not show a good agreement with the experiments, even with the consideration of non-Newtonian and thermal effects. The parameters that fully describe the traction coefficient are not entirely controlled when the shear stress is too high. In particular, the limiting shear stress needs to be better known to reach a closer fitting.

# *V.3 Conclusion*

In this chapter, the tribological behavior of the base oil and the polymer-thickened solutions in an EHD circular rolling-sliding contact was deeply studied. Both film thickness and traction coefficient were measured.

Film thickness predictions were compared to classical analytical models and numerical models under pure rolling conditions. The comparisons evidenced a deviation compared to the Newtonian behavior for two polymer-solutions. Indeed, the Newtonian predictions overestimate the real film

thicknesses which reveal the importance of using adequate rheological models in film thickness calculations. Modified WLF-Yasutomi and Carreau-Yasuda (with a second Newtonian plateau) equations were incorporated in the numerical resolution - based on the generalized Reynolds' equation - along with the Tait formula for the density variations. The rheology is, thereby, sharply influencing the tribology. As showed in chapter IV, the rheology is strongly correlated to the physico-chemistry of the base oil and the polymers. By extension, the tribology is linked to the molecular properties of the lubricants. This conclusion is of main interest for formulators because they can select the chemicals of the lubricants in function of the desired tribological performance.

Moreover, we investigated the possible occurrence of thermal effects. In the frame of the experimental operating conditions, no significant shear heating was evidenced.

Then, friction coefficients were provided under variable *SRR*, temperatures, loads and entrainment speeds for the base oil and all the three solutions. Surprisingly, no clear discrimination was found between the different fluids.

# Summary and conclusion

This thesis aimed at understanding the roles and functions played by the Viscosity Index Improvers in the formulation of engine lubricants. A multi-scale overview was adopted: from physico-chemistry to tribology through rheology.

First of all, the initial literature review on the impact of friction on the environment made us aware of the importance to study lubrication. Due to the legislative pressures on the limitation of greenhouse gases rejections and due to the willing to live on a healthier planet, the investigation on lubricants has become of first interest. Actually, the rheological study of lubricants is essential to control the friction losses in an automotive engine. One of the general industrial motivations is that the formulation process should be optimized which leads to savings of time and money for the formulator. If the relationship between physico-chemistry, rheology and tribology is well established, the process can be improved by avoiding the systematic full-scale engine tests. The main objective of the study was to compare the rheological and the tribological responses of a hydrocracked mineral base oil and several polymer-thickened solutions with different natures of polymers.

The use of complex formulation for a lubricant is necessary to overcome the various degradations undergone in the different parts of the engine and to maintain a high performance level. In chapter II, the composition and the role of engine lubricants were extensively described. Notions of friction, lubrication and particularly lubrication regimes were introduced. The rheology of lubricants was presented. The classical models of the dependence of viscosity on temperature, pressure and shear stress were depicted. In order to perform measurements, several instruments were used: a rheometer with coaxial cylinders, other standard devices operated at ambient pressure, a high pressure falling-body viscometer and a high pressure Couette rheometer. Finally, generalities on the physico-chemistry of polymers and polymer solutions were explained. Conformation, hydrodynamic radius, radius of gyration, critical concentration and temperature-solubility considerations were described in order to provide elements necessary for the discussion of chapter IV.

In part III, in order to get a deeper knowledge of the rheology of lubricants under engine operating conditions, powerful models were combined to estimate the viscosity of solutions at chosen temperatures, pressures and shear stress. A VTF model was used to fit the temperature dependence of viscosity and provide the glass transition temperature at atmospheric pressure. A modified WLF-Yasutomi equation served to model the temperature-pressure-viscosity response up to 800 MPa which was implemented in the Carreau-Yasuda (with one or two plateaus) formula, reliable for the shear stress dependence of viscosity. All the previous models exhibited strong agreement with the experimental data for the base oil and the polymer solutions. The characterizations showed close responses in function of temperature and pressure for all the solutions. Nevertheless, different shear-thinning behaviors were pointed out. Indeed, the base oil and the PAMA solution behaved as Newtonian fluids whereas the OCP and the PISH solutions were non-Newtonian. The observed rheology of the PAMA solution was unexpected according to its common use in fuel-economy

lubricants. Thus, we wondered why this polymer did not show shear-thinning response at high pressure, which leads to the chapter IV, where some clues are given.

Chapter IV evidenced the strong connection between rheology and the physico-chemistry of the lubricants' components. The different rheological behaviors identified in the previous chapter were mirrored with the characteristics of polymers such as concentration, composition, conformation, hydrodynamic radius, elasticity and solubility in the base oil.

Several hypotheses were explored to explain the unexpected Newtonian behavior of the PAMA solution. The chosen concentration of polymers was the same for all the solutions, representative of the concentration found in the engine lubricants. It did not imply interactions between the polymer coils. Moreover, the presence of additives did not lead to an increase of the shear-thinning behavior. Finally, the Lower Critical Solution Temperature (LCST) was not in cause in the studied operating conditions.

The core of this part focused on the hydrodynamic radius and its determination at high pressure. One originality of the thesis came from the deduction of the hydrodynamic radius from viscosity measurements at pressures up to 800 MPa with the use of the Einstein's law.

The PAMA behaved differently than the two other polymers. Its hydrodynamic radius increases in function of temperature and decreases in function of pressure whereas temperature and pressure have almost no effect on the $R_h$ of OCP and PISH. These observations were explained in terms of solubility and steric hindrance.

In addition to the influence of temperature and pressure on $R_h$, the relationship between the shear stress and the physico-chemistry has been investigated. Comparing PAMA and OCP, at equal $R_h$ (≈10 nm), and different conformation (comb and linear), the conformation governs. The comb conformation is less stretchable than the linear conformation due to its intramolecular attractive interactions (Van der Waals). Considering the PAMA (8-12 nm) and the PISH (20 nm), for which conformations imply strong intramolecular bondings and different sizes, the size dominates in the shear-thinning response. For different conformations and different sizes, the size prevails over the conformation. Indeed, the PISH solution is more shear-thinned than the OCP solution. Furthermore, the PAMA does not stretch because it is less deformable than the two others or because the relaxation time is lower than the time of the experiment and the shear-thinning behavior is not visible.

Finally, this section showed that the knowledge of the nature and properties of polymers can bring many clues in the prediction of the rheological response. This analysis may be helpful for the formulators and can orientate the oil makers to find new improvement directions for fuel-economy lubricants.

The last chapter represented the ultimate step of this work. Once the physico-chemistry and the rheology were studied, this part shed light on the tribological response of an EHD circular rolling-sliding contact. First of all, film thickness was measured by white light colorimetric optical interferometry. Film thickness increases dramatically with the entrainment speed for all the studied solutions. Analytical models such as Hamrock-Dowson, Moes and Chevalier, were compared with the experiments. Good agreement was shown for the base oil and the PAMA solution which are Newtonian whereas a gap between the analytical predictions and the experimental results was found for the OCP and the PISH solutions. The more the shear-thinning behavior is, the larger the deviation. The film thicknesses decreased by 40 to 50% compared to the isothermal Newtonian behavior. These results were confirmed by full numerical simulations based on the generalized Reynolds' equation and on the lubricant properties correlations. Modified WLF-Yasutomi and Carreau-Yasuda equations for

the rheological behavior and the Tait formula for the density variations were introduced in the model to fully describe the response of the lubricant under high pressure and elevated shear stress. Since the Newtonian predictions overestimated the real film thicknesses for OCP and PISH solutions, it was of primary interest to introduce the actual lubricants' behavior in the model in order to provide accurate predictions. We obtained a good agreement between the measurements and the numerical solutions using rheological models independently established. Moreover, it was numerically proven that thermal effects have no large influence on film thickness, in the frame of the experimental operating conditions studied in this work.

The traction coefficients were measured under variable slide-to-roll ratio. The curves for different experimental conditions and several fluids overlapped. Thus, even if the comparison did not occur for iso-film thickness, the effect of the polymer on the friction coefficient was really insignificant under our specific conditions.

Finally, chapter IV proved the strong relationship between physico-chemistry and rheology. Chapter V evidenced that rheology is deeply correlated to tribology. By extrapolation, one can deduce that tribology is linked to the physico-chemistry of lubricants. The selection of chemicals by formulators is oriented by the understanding of those coupled relationships.

The insights into the relationship between the molecular scale and the rheology give interesting clues to find the optimal formulation of engine lubricants.

An ideal automotive lubricant is expected to be viscous enough to provide the surfaces separation, to carry a viscosity index improver, to shear-thin and to maintain these properties at very high temperatures and pressures.

The polymer should show a large variation in size when the temperature rises, meaning that the polymer should not be too soluble in the base oil at low temperature. It should have a high molecular weight and a high extensibility (with weak or few intramolecular bonds).

When it comes to the base oil, its compressibility should not be too elevated to keep the solubility of the polymer independent from the pressure. The base oil should not be a too good solvent for the polymer at low temperature. A good compromise could be to mix two preferential solvents.

Obviously, for a fair comparison, the comparisons should be performed at iso-viscosity but considering the previous requirements, this comb-like PAMA seems to be the best candidate. Indeed, at low temperature, it is at the limit of the solubility and its swelling with temperature is satisfying. Thus, the viscosity index improver property is verified. We showed in the PhD that the PAMA solution does not show any shear-thinning behavior which is contrary to its extensive use as a fuel economy lubricant. Further experiments should be run at high temperature and low pressure when the hydrodynamic radius is the highest and the intramolecular bondings are the weakest to understand the role played by the PAMA. Knowing that the PAMA behaves as a polar (ester groups)/apolar (alkyl chains) copolymer, its properties can be adjusted through the length of the alkyl side chains by adapting its solubility in the base oil and by settling the intramolecular bonds.

# Recommendations for future work

In spite of the extensive work accomplished during the study, in terms of physico-chemistry, rheology and tribology, both experimentally and numerically, there are still several fields to be investigated and complementary questions to be answered. This section is an overview of the possible directions to consider in order to go deeper into the understanding of structure-properties-performance relationships of viscosity index improvers (VII) in engine lubricants under realistic operating conditions.

First of all, one of the important parameter of this research is the concentration of the polymer in the solution. We chose a single typical concentration of the industrialized engine lubricants which appeared to be in the dilute regime (1.2%). One can wonder what would happen with a slightly higher concentration, still in the dilute regime, or way higher, up to the entangled regime and even in the concentrated regime. Would the lubricant properties be improved with a higher VII's concentration?

Moreover, the choice not to include functional additives in the polymer-thickened solutions was made for the sake of simplicity and to provide a better understanding of the individual molecular mechanisms involved. Even if the effect of the package of additives on the viscosity was briefly examined in chapter IV and showed that the shear-thinning behavior was not more impacted by its presence, it still deserves to be thoroughly analyzed.

The investigation of the degradation and ageing of lubricants after several cycles could be studied in the high pressure rheometer or tribometers such as the JEROTRIB or MTM test-rigs to represent the realistic conditions in an engine. Permanent shear-thinning would then be considered.

Then, it is obvious that the analysis on the relationship between the molecular scale and the rheology must be carried further with the use of other polymers with different chemistries, molecular weights, conformations, etc. and with other base oils such as a polar one for instance. If the explanations advanced in chapter IV were still true, in a polar base stock, the PAMA should be in a better solvent and its coils should expand more than in the non-polar base oil. The PAMA solution would be expected to shear-thin more than the two other polymer solutions. Indeed, the OCP and PISH solutions would be in a worse solvent, they would collapse and thus, the effect of shear would be less visible. Furthermore, mixing several polymers, which is industrially commonly done, is also an interesting way to consider molecular mechanisms influencing the rheology. One case was illustrated with the mixture of OCP and PISH in the base oil, as shown in Appendix E.

In chapter IV, the notion of relaxation time was proposed to explain that the PAMA would recover its initial state quicker than the two other polymers under shear stress. This parameter can directly be approached by means of dynamic rheology, by measuring the elastic modulus (or storage modulus $G'$) and the viscous modulus (or loss modulus $G''$). The link between physico-chemistry and rheology would take its full meaning by this determination.

Comparing the results with molecular dynamics simulations would also be of highly interest for the understanding of molecular mechanisms. Reasonable size of molecules should be considered in order to limit the time of calculations.

Chapter V revealed the interest of knowing the equation of the density under high pressure to provide powerful numerical models and accurate film thicknesses predictions in an EHD rolling-sliding circular contact. The use of the Tait formula could be improved by the experimental determination of the exact density variations for each single lubricant.

Finally, numerical modelling of the traction coefficient is limited when the shear stress is too high. The experimental characterization of the limiting shear stress would be interesting to precisely predict the friction coefficients in a contact.

# Appendices

## Appendix A Viscosity Index

The viscosity index (VI) is an arbitrary value quantifying the dependence of viscosity with temperature. If this index is high, the viscosity shows little variations with temperature. The Society of Automotive Engineers (SAE) defined this index in the ASTM standard D2270 [104] and its formula is:

$$VI = 100\frac{L-U}{L-H} \qquad (75)$$

Where L is the kinematic viscosity at 40°C of an oil of 0 viscosity index having the same kinematic viscosity at 100°C as the oil whose viscosity index is to be calculated, H is the kinematic viscosity at 40°C of an oil of 100 viscosity index having the same kinematic viscosity at 100°C as the oil whose viscosity index is to be calculated and U is the kinematic viscosity at 40°C of the oil whose viscosity index is to be calculated.

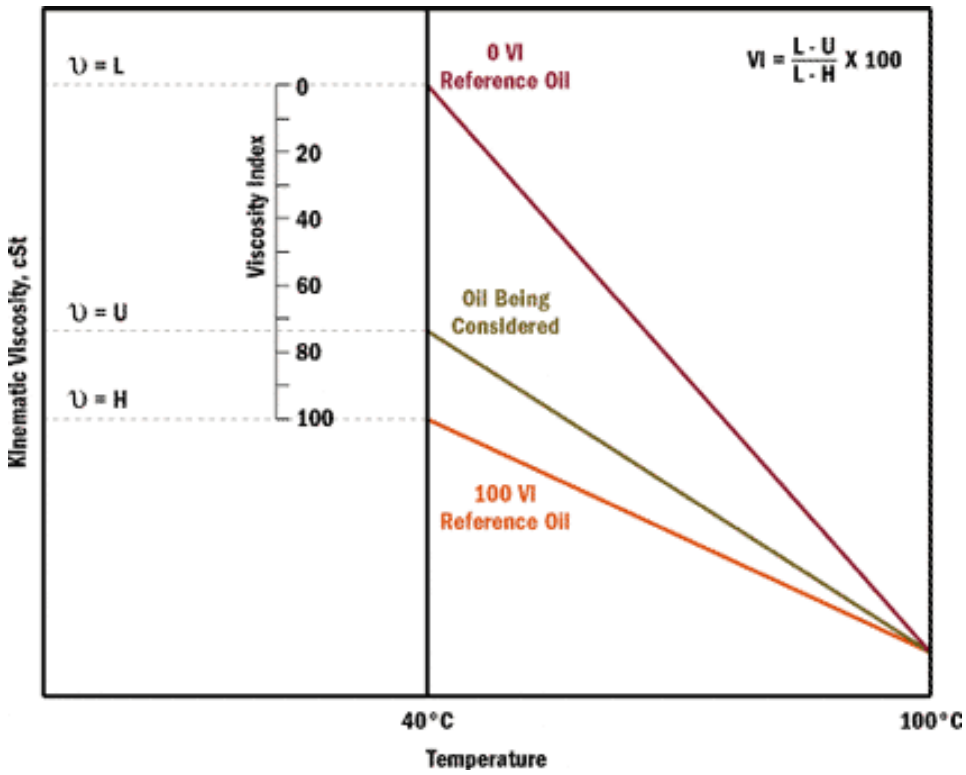


*Figure 82: Viscosity index determination*

# Appendix B Industrial standardized rheometers

## B-1 Capillary viscometer

The capillary viscometer employed is of Ostwald type from Cannon-Fenske (*Figure 83*). The kinematic viscosity (KV) is deduced - according to the ASTM standard D445 [105] - from the automatic measurement of the flow time, under the effect of gravity, of a volume $V_c$ of liquid through the capillary, at 40 °C and 100 °C.

The Poiseuille equation shows this relationship:

$$\nu = K_c t_c \quad (76)$$

$$K_c = \frac{\pi R_c^{\,4} g}{8 V_c} \quad (77)$$

Where $K_c$ is the calibration constant, $t_c$ is the flow time of the liquid, $R_c$ is the radius of the capillary and g the gravitational constant.

*Figure 83: Cannon-Fenske capillary viscometer*

## B-2 High Temperature High Shear rate viscometer HTHS

The HTHS (High Temperature High Shear rate) test (Figure 84), from Ravenfield, leads to the measure of the dynamic viscosity of fluids at 150 °C and at an elevated shear rate ($10^6$ $s^{-1}$), according to the ASTM standard D4741 [106]. The viscosity is determined by the measure of the resistant torque imposed by the liquid located between a conic rotor and a thermostatic conic stator.

*Figure 84: Picture of the Ravenfield HTHS viscometer*

This data is part of the engine specifications because it shows whether the viscosity of the lubricant is sufficient for the operation of the hydrodynamic bearings and to keep an appropriate film thickness in the piston-liner-segment and the distribution zones.

## B-3 Ultra-Shear Viscometer (USV)

The Ultra-Shear Viscometer (USV) (Figure 85) from PCS Instruments [107], is an automatic Couette viscometer with a shearing gap of approximately 1 μm and shear rates between $10^6$ and $10^7$ $s^{-1}$ (equivalent to shear stresses from 4 kPa to 20 kPa). Measures are run at 100 and 150°C.

*Figure 85: Picture of the USV from PCS Instruments*

This rheometer is equipped (Figure 86) with an engine driving speeds greater than 20000 rotations per minute. An electromagnetic clutch engages the rotor during a short time (close to 30 ms) to try to overcome the heating problem due to shearing. The torque is measured by a piezoelectric force sensor connected to the stator. The rotor and the stator are in tungsten carbide (K=90 W/mK, Cp=260 J/kg.K). The regulation of temperature occurs thanks to a Peltier system. A platinum thermocouple is located in the stator and another is at the bottom of the test chamber.

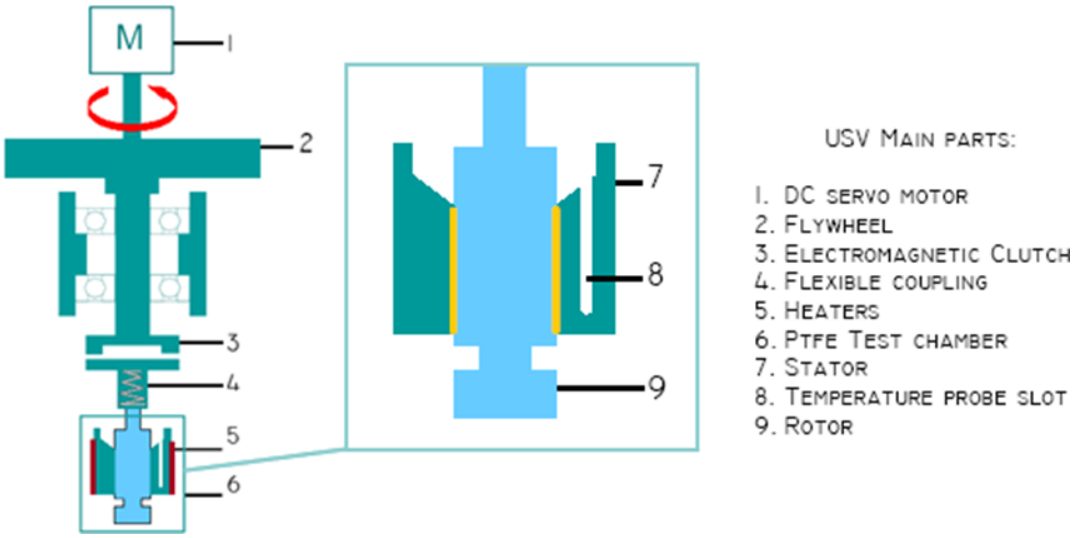


*Figure 86: Schematic view of the USV*

## B-4 Cold Cranking Simulator (CCS)

The CCS (Cold Cranking Simulator) (Figure 87), from Cannon, measures the dynamic viscosity of liquids under high shear stress ($5.10^4$ and $10^5$ Pa) and high shear rates ($10^4$ and $10^5$ $s^{-1}$) at temperatures from -5 to -35°C, according to the ASTM standard D5293 [108].

This method simulates the shear of the oil in the crankshaft bearings during the cold cranking phase. The device consists in a DC electric motor driving a rotor which rotates in a thermostated stator.


*Figure 87: Picture of the Cannon CCS*

# Appendix C Characteristics of non-conventional rheometers

## C-1 Characteristics of the cylinder sets of the high pressure Couette rheometer

| | | Designation | Low Stress | Middle stress | High Stress | Extra Stress |
|---|---|---|---|---|---|---|
| | | Material | Brass 360 | AL60 | W72Cu28 | W72Cu28 |
| | | Plating | None | None | Cu | Cu |
| Cylinder Sets | Dimensions / mm | Diameter | 13.48 | 12.65 | 12.65 | 3.96 |
| | | Length | 22.0 | 9.68 | 2.41 | 1.83 |
| | | h / µm | 13.4 | 5.1 | 3.5 | 2.3 |
| | | Piloted | No | No | Yes | Yes |
| | Pictures | |  |  |  |  |
| Drive Shaft | Dimensions / mm | Length | Special spring shaft | 24.5 | 24.4 | Special 0.69 in long |
| | Pictures | |  |  |  |  |
| | Shear Stress /kPa | Min | 0.4 | 2 | 20 | 150 |
| | | Max | 70 | 250 | 1000 | 3500 |
| | Gain | | 200X10 | 20X10 | 20X10 | 20X10 |

*Table 21: Characteristics of the cylinder sets of the high pressure Couette rheometer*

## C-2 Shear stress ranges of several rheometers

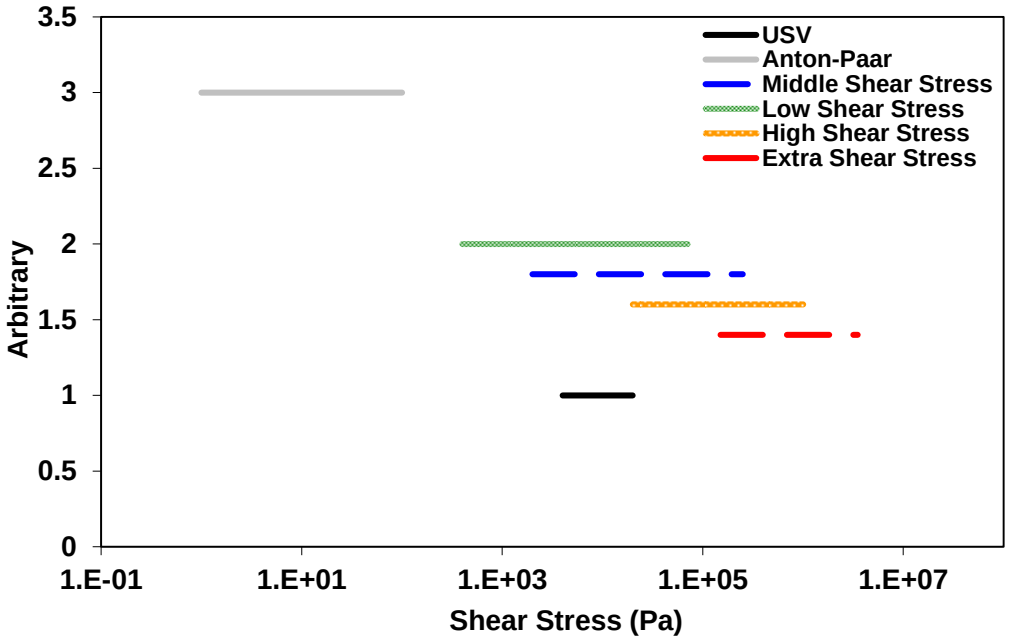


*Figure 88: Shear stress ranges of several rheometers*

# Appendix D Complementary data from standard tests on the PAMA solution

Many standard tests - detailed in appendices B-1, B-2 and B-4 - are usually run on lubricants to match with the rheological engine requirements. The results of those tests are presented for the PAMA-thickened solution (Figure 89) with USV (cf. Appendix B-3) and Anton-Paar rheometer (cf. *II.2.3.a*) data added. Moreover, the high pressure falling body viscometer (HP-Visco) data are reported as well.

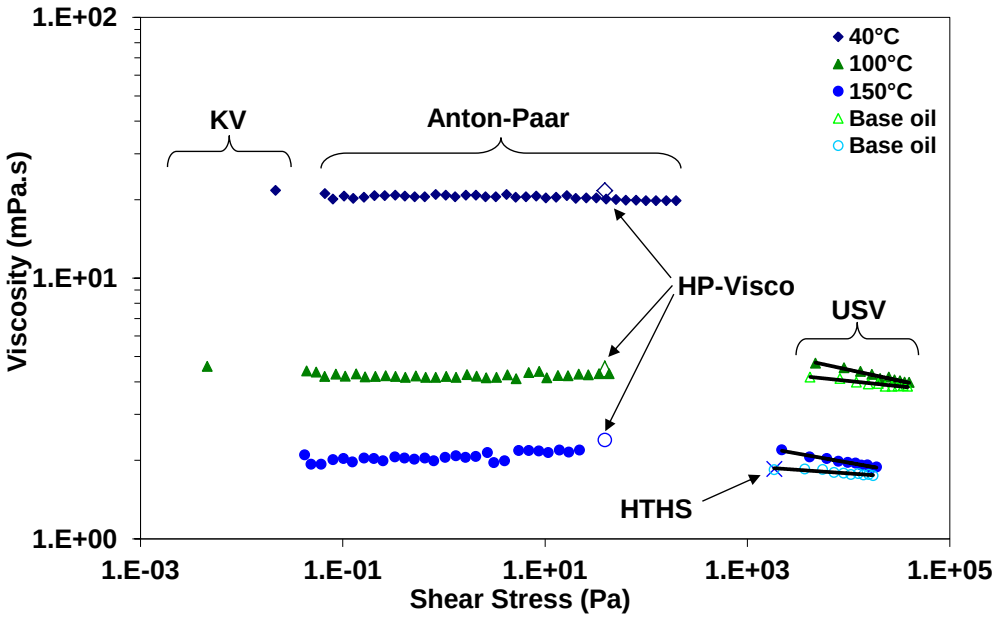


*Figure 89: Rheological behavior of the PAMA - thickened base oil at different temperatures*

The viscosity of the PAMA solution decreases by 5% at 100 °C and 8% at 150 °C. The power law exponent (Equation (26), p. 70), detailed in II.2.2.b, is equal to 0.96 for the base oil and 0.92 for the PAMA solution at both temperatures. The power-law exponents are really close. As a consequence, the base oil and the PAMA solution behave as Newtonian fluids.

# Appendix E Complementary data on the OCP+PISH solution

It is of main interest to study the behavior of lubricants made of a combination of several polymers because it is the usual practice in the real engine lubricants. In this appendix, additional information on the rheology and the models of the OCP+PISH-thickened base oil is given. This part is complementary to the chapter III. First of all, standard rheological data will be listed; then, the piezoviscous behavior will be studied before investigating the influence of the shear rate on the viscosity of this ternary blend.

## E-1 Standard rheological data

Figure 90 and Table 22 provide the data carried out on the standard tests, described in appendices B-1, B-2 and B-4. The results of those tests are presented along with the USV (cf. Appendix B-3) and Anton-Paar rheometer (cf. *II.2.3.a*) data on Figure 90. The high pressure falling body viscometer (HP-Visco) data are reported as well.

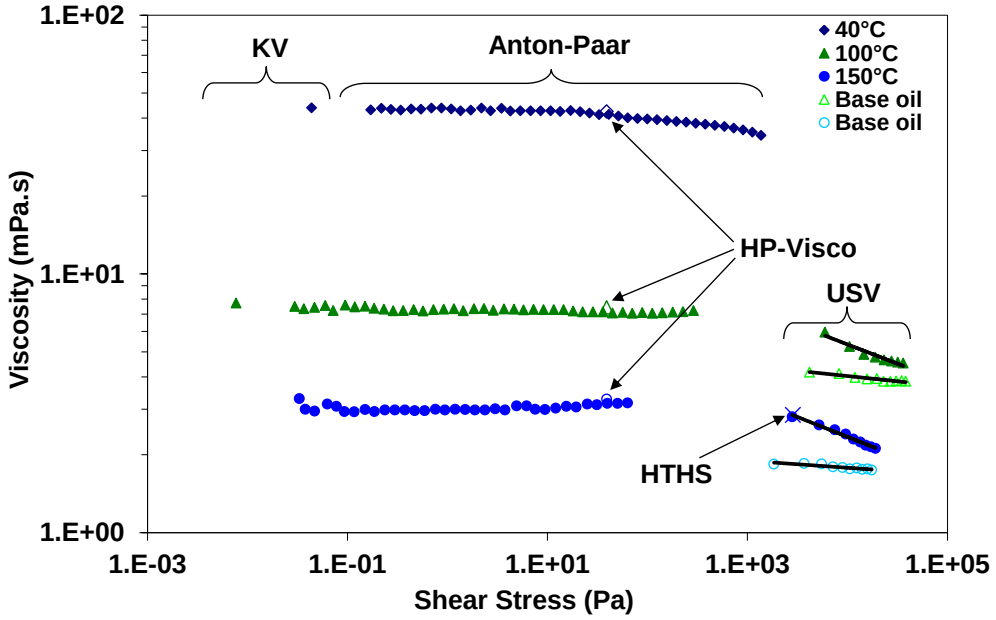


*Figure 90: Rheological behavior of the OCP+PISH - thickened base oil at different temperatures*

The viscosity the OCP+PISH solution drops by 30% at 100 °C and 40% at 150 °C. The power law exponent (Equation (26), p. 70), detailed in II.2.2.b, is equal to 0.96 for the base oil and 0.87 for the OCP+PISH solution. The lower the power law exponent, the stronger the shear-thinning behavior. Thus, the OCP+PISH solution shear-thins more than the base oil.

| | **KV 40 (cSt)** | **KV 100 (cSt)** | **VI** | **HTHS (mPa.s)** | **CCS (mPa.s)** | | |
|---|---|---|---|---|---|---|---|
| ***T (°C)*** | *40* | *100* | | *150* | *-15* | *-25* | *-35* |
| **Base oil + OCP+PISH (50/50)** | 53.3 | 9.8 | 172 | 2.9 | 7.8E+02 | 1.6E+03 | 5.2E+03 |

*Table 22: Standard rheological data for the OCP+PISH solution*

These experiments show that the rheological behavior of this blend is close to the one of the OCP solution and of the PISH solution.

## E-2 Piezoviscous behavior

When it comes to the pressure dependence, the viscosity is plotted on Figure 91 for five isotherms from 40 °C to 150 °C and from atmospheric pressure to 800 MPa. The modified WLF-Yasutomi (Equation (23), p. 69) correlation fits quite well with the experimental data. Table 23 lists the parameters of the model and the reciprocal asymptotic isoviscous pressure coefficients (Equation (18), p. 67) at 40 °C and 100 °C.

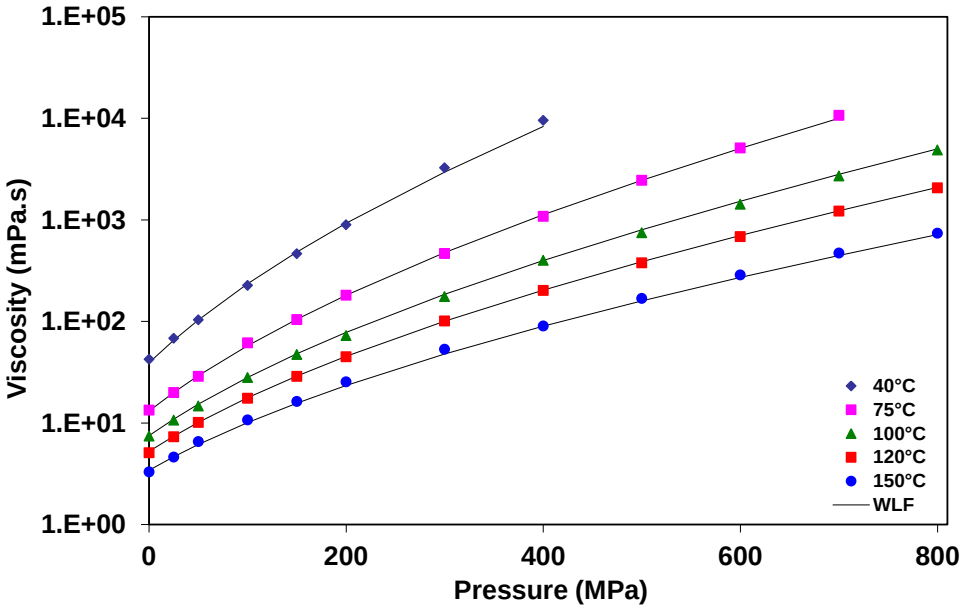


*Figure 91: Piezoviscous behavior of the OCP+PISH-thickened base oil at different temperatures*

| **Material** | **Base oil+ OCP+PISH (50/50)** |
|---|---|
| $\eta_g$ / Pa.s | $10^{12}$ |
| $T_g(0)$ / °C | -84.0 |
| $A_1$ / °C | 505.5 |
| $A_2$ / GPa$^{-1}$ | 0.0678 |
| $C_1$ | 15.88 |
| $C_2$ / °C | 22.86 |
| $B_1$ / GPa$^{-1}$ | 8.4 |
| $B_2$ | -0.5032 |
| Relative rms error on the viscosity | 4.8% |
| $\alpha^*(T=40°C)$ / $GPa^{-1}$ from Equation (23) | 17.5 |
| $\alpha^*(T=40°C)$ / $GPa^{-1}$ from experimental data | 16.5 |

| | |
|---|---|
| $\alpha^*$ $T$=100°C / GPa$^{-1}$ from Equation (23) | 12.2 |
| $\alpha^*$ $T$=100°C / GPa$^{-1}$ from experimental data | 12.1 |

*Table 23: Parameters of the Modified WLF-Yasutomi model for the OCP+PISH solution, Equation (23)*

The parameters of this piezoviscous model are truly close to the one of the OCP solution and the PISH solution.

## E-3 Shear-thinning response at high pressure

Figure 92 shows the viscosity in function of shear stress at various temperatures and pressures for the OCP+PISH solution. The Carreau-Yasuda model with a second Newtonian plateau (Equation (32), p. 71) is fitted to the values and the viscosities coming from the high pressure viscometer at 40 °C are reported.

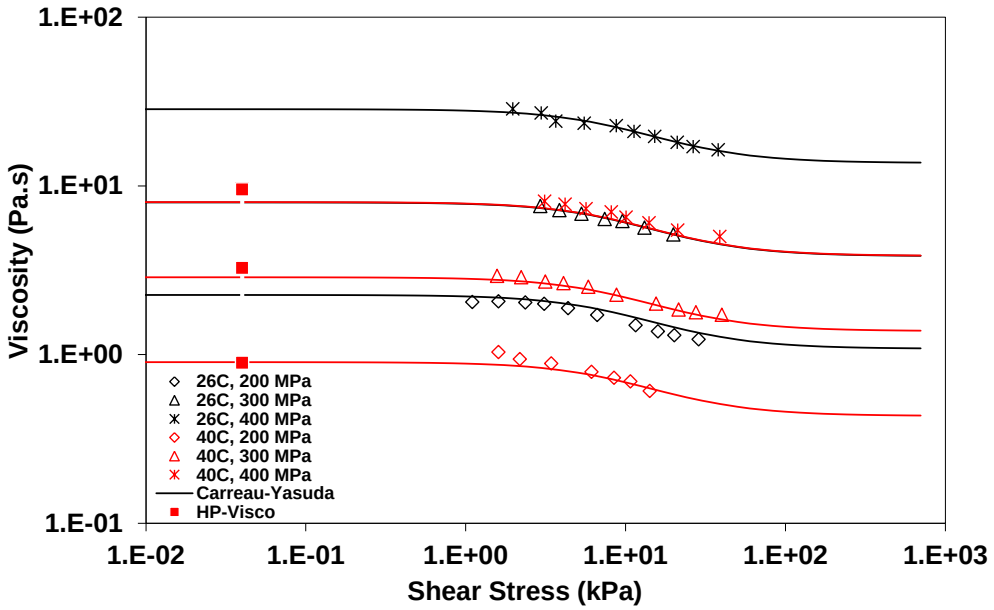


*Figure 92: Rheological behavior of the OCP+PISH - thickened base oil at different temperatures and pressures*

The OCP+PISH solution exhibits a strong shear-thinning behavior (the viscosity decreases by about 40%). The first Newtonian plateau is estimated to be the low shear stress value of viscosity coming from the modified WLF-Yasutomi model. A little difference between the viscosities from the high pressure falling body viscometer (HP-Visco) and the first Newtonian plateau at 40 °C and 300 MPa and at 40°C and 400 MPa. These discards might come from the error made on the modified WLF-Yasutomi modeling. They can slightly influence the amplitude of the modeled shear-thinning effects. From 100 kPa, the second Newtonian plateau is slightly below (5%) the modeled viscosity of the base oil for all the studied conditions. One can assume it is due to the uncertainties on measurements, on modeling or on thermal softening, even if the Nahme-Griffith number is low.

The parameters of the Carreau-Yasuda relationship are listed in Table 24.

| | **Base oil+ OCP+PISH (50/50)** |
|---|---|
| | $\eta_2 \neq 0$ |
| ***G (kPa)*** | 10.5 |
| ***n*** | 0.44 |
| ***a*** | 1.3 |
| $\frac{\eta_2}{\eta_{0(WLF)}}$ | 0.48 |
| **Relative rms error on the viscosity** | 6.4% |

*Table 24: Parameters of the Carreau-Yasuda model with a second Newtonian plateau for the OCP+PISH solution, Equation (32)*

The relative viscosity (the viscosity of the fluid divided by its viscosity at low shear stress, derived from the modified WLF-Yasutomi model) is plotted over the Weissenberg number in Figure 93. Its rheological behavior is really close to the one of the PISH solution. Like the PISH fluid, the double plateau modelling is justified as shown in the following master curve.

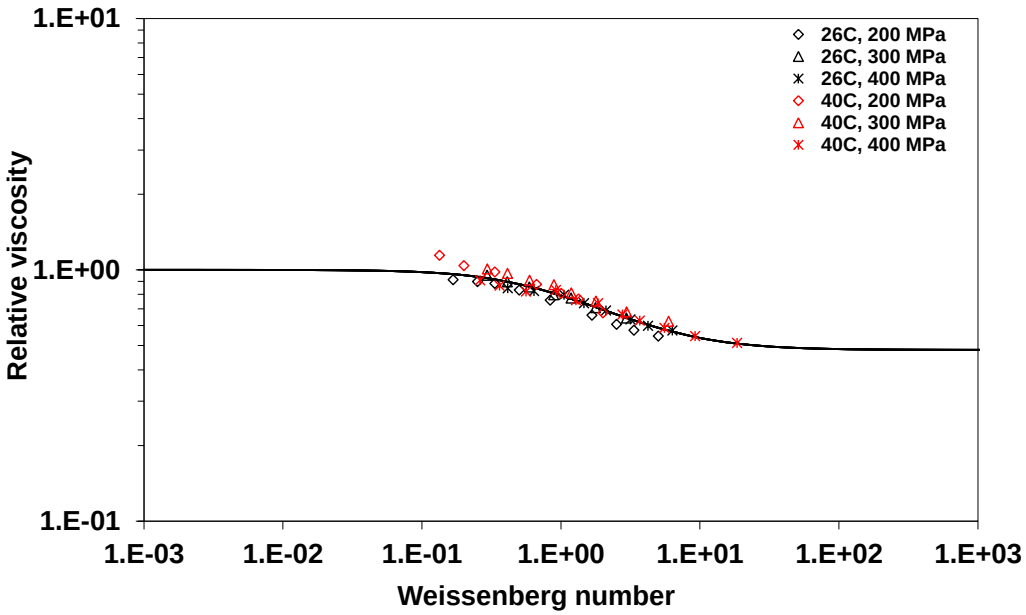


*Figure 93: Master curve of the rheological behavior of the OCP+PISH - thickened base oil. Model with a second Newtonian plateau ($\eta_2 \neq 0$)*

# Appendix F Piezoviscous behavior of PIB blends

In part IV.3, the viscosities of heptane, cyclopentane, and solutions of both solvents mixed with PIB (1.2% in weight) are used to deduce the hydrodynamic radius of the PIB and to understand the influence of the LCST on the values of $R_h$. The experimental data measured at high pressure with the falling body viscometer are reported in Figure 94.

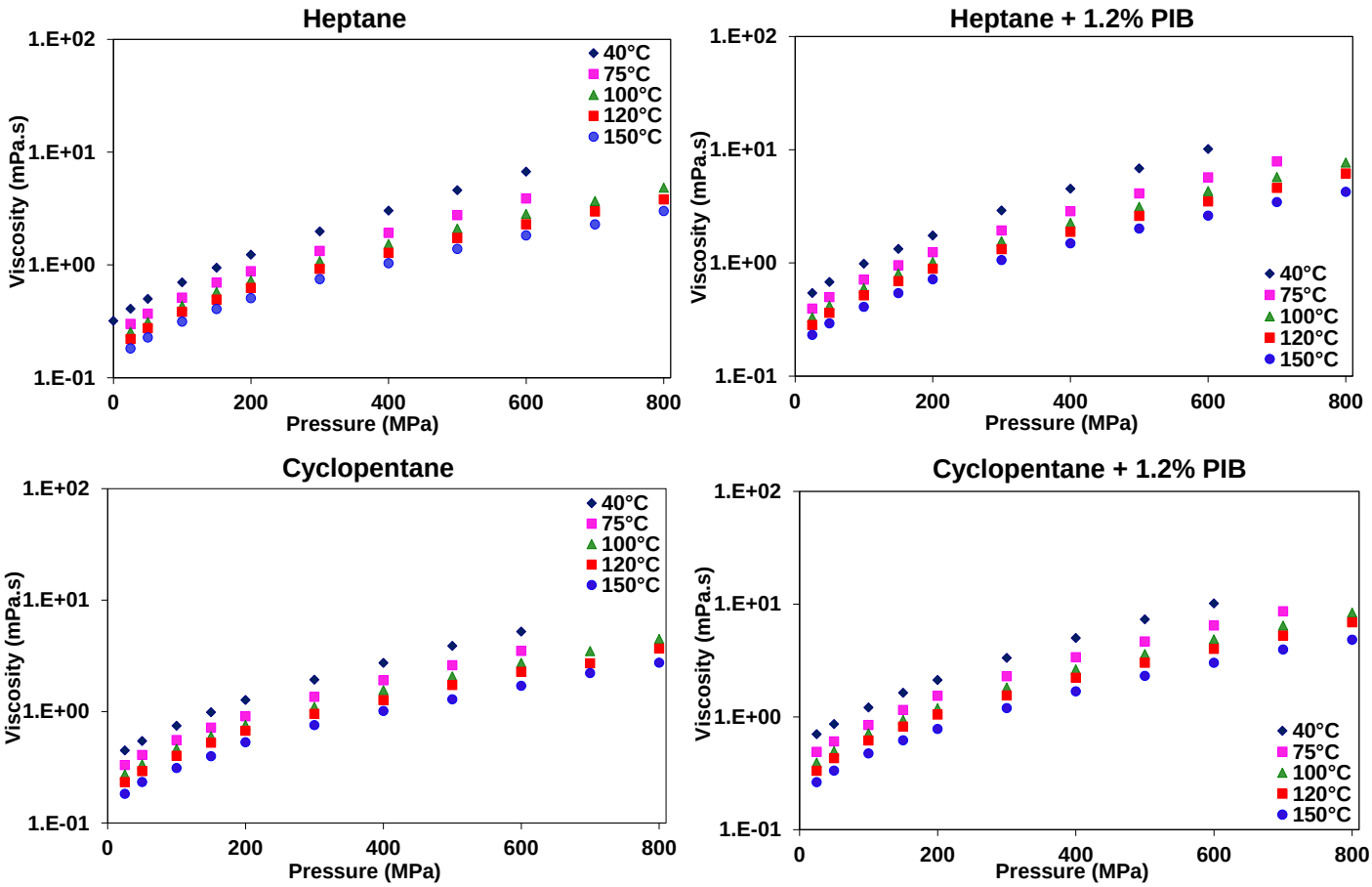


*Figure 94: Piezoviscous behaviors of heptane, cyclopentane, and solutions of both solvents mixed with PIB (1.2% in weight)*

At 40 °C and 600 MPa, the addition of PIB in heptane and in cyclopentane increases the viscosity by 52% and 95% respectively whilst at 150 °C and 25 MPa, the viscosity is raised by 28% and 44%.

# Appendix G JEROTRIB

The JEROTRIB device was developed at LaMCoS (INSA-Lyon) by Molimard [17]. It is a ball-on-disc rolling/sliding tribometer. Both film thicknesses and traction coefficients are outputs of this test-rig, using optical interferometry and multi-directional sensors respectively. The full operating ranges are the following:

- Maximum normaerrl load: 300 N
- Film thickness down to a few nm
- Entrainment speed: 1 cm/s to 6 m/s
- Adjustable sliding (*SRR*=0-100%)
- Imposed temperature: 0-120 °C
- Smooth (arithmetic average $R_a$< 5 nm) or real surfaces
- Materials of the ball/disc: steel/steel, steel/glass or steel/sapphire
- Lubricant confined with passive materials

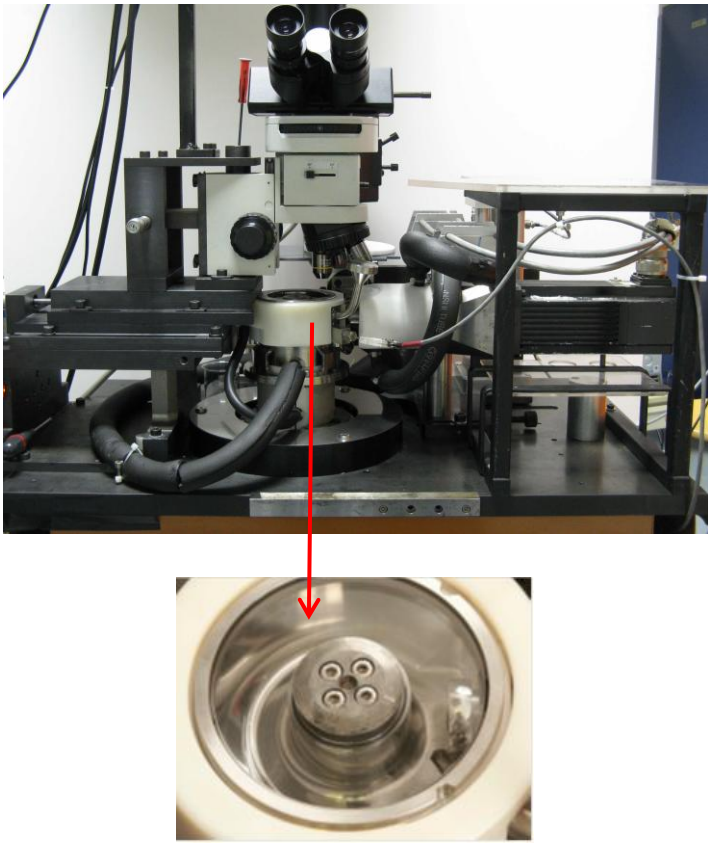

a)

b)

*Figure 95: a) Picture of the JEROTRIB test-rig*
*b) Zoom on the ball-on-disc part*

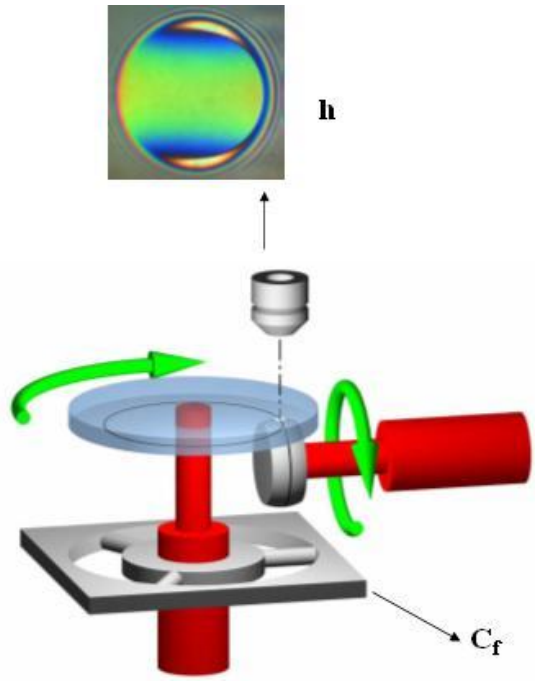


*Figure 96: Scheme of the JEROTRIB functioning*

# Appendix H Calibration curve

The RGB (Red, Green, Blue) intensity triplet is plotted over the film thickness. The following graph is called the "calibration curve".

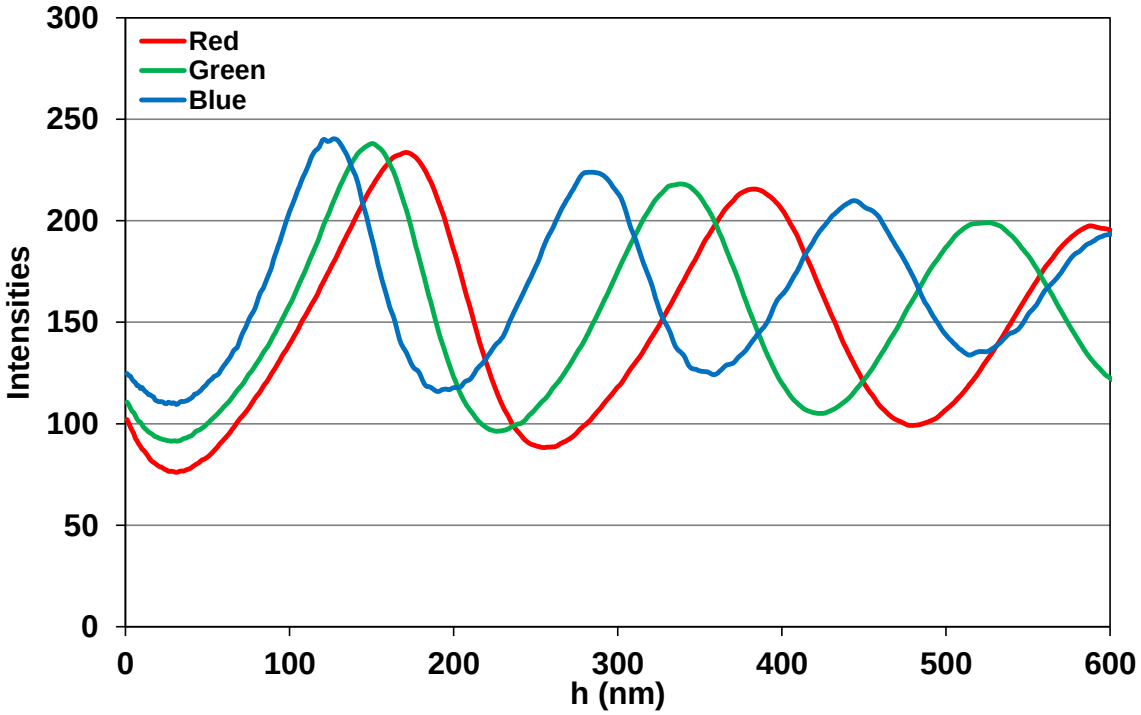


*Figure 97: Calibration curve used for the interferogram on Figure 62 (Base oil, 25 °C, 27 N, $U_e$=1.72 m/s, SRR=0)*

# Appendix I The Hertz theory

The Hertz [109] theory evaluates the deformation of semi-infinite elastic bodies under dry contact conditions, their pressure profile and their geometry. The surfaces of the two solids are locally spherical and their curvature radii are respectively $R_1$ and $R_2$. It is supposed that there is no adherence in the contact. The following parameters are dimensionless and coming from the Hertz theory.

For a circular contact, the Hertzian pressure profile is:

$$p\ x,y\ = \begin{cases} p_H \sqrt{1-\left(\frac{x}{a_H}\right)^2-\left(\frac{y}{a_H}\right)^2} & \text{if } \sqrt{x^2+y^2} \le a_H \\ 0 & \text{otherwise} \end{cases} \qquad (78)$$

Where $p_H$ is the maximum Hertzian pressure:

$$p_H = \frac{3W}{2\pi a_H^2} \qquad (79)$$

$a_H$ is the radius of the contact circle:

$$a_H = \sqrt[3]{\frac{3WR_{eq}}{2E_{eq}}} \qquad (80)$$

$W$ is the external applied load, $R_{eq}$ the reduced radius of curvature and $E_{eq}$ is the reduced Young elastic modulus of the contacting bodies defined as:

$$R_{eq} = \frac{1}{\frac{1}{R_1}+\frac{1}{R_2}} \qquad (81)$$

$$E_{eq} = \frac{2}{\frac{1-\upsilon_1^2}{E_1}+\frac{1-\upsilon_2^2}{E_2}} \qquad (82)$$

where $E_1$, $\nu_1$ *and* $E_2$, $\nu_2$ are the material properties (Young's moduli and Poisson's coefficients) of the solids 1 and 2 respectively.

Equation (83) gives the deformed shape of a sphere against a flat surface:

$$h(r) = \frac{r^2}{2R_{ball}} - \frac{a^2}{R_{ball}} + \frac{1}{\pi R_{ball}}\left[ 2a^2 - r^2 \ \arcsin\left(\frac{a}{r}\right) + r^2\left(\frac{a}{r}\right)\sqrt{1-\left(\frac{a}{r}\right)^2} \right] \quad for\ r \ge a \qquad (83)$$

where $R_{ball}$ is the radius of curvature of the ball and $r$ is the distance from the contact center.

# Appendix J Mini-Traction Machine (MTM)

The Mini-Traction Machine (MTM) is dedicated to the measurement of traction coefficients. In the standard configuration the test specimens are a 19.05mm (3/4 inch) 100C6 steel ball and a 46 mm diameter steel disc (arithmetic average roughness *Ra*= 0.01 µm*)*. The ball is loaded against the face of the disc and the ball and disc are driven independently to create a mixed rolling/sliding contact for a fixed duration. The ball is changed after each test and about 100 mL of sample is used. The frictional force between the ball and disc is measured by a force transducer. Additional sensors measure the applied load, the lubricant temperature and (optionally) the electrical contact resistance between the specimens and the relative wear between them [110]. Optional accessories such as the microscope and the RGB color camera (parts of the 3D Spacer Layer Imaging Method (SLIM)) help in the acquisition of scanned images of the rubbing surface of the ball. A post-processing can determine the average thickness of a possible reactional film. The test device is depicted in Figure 98.

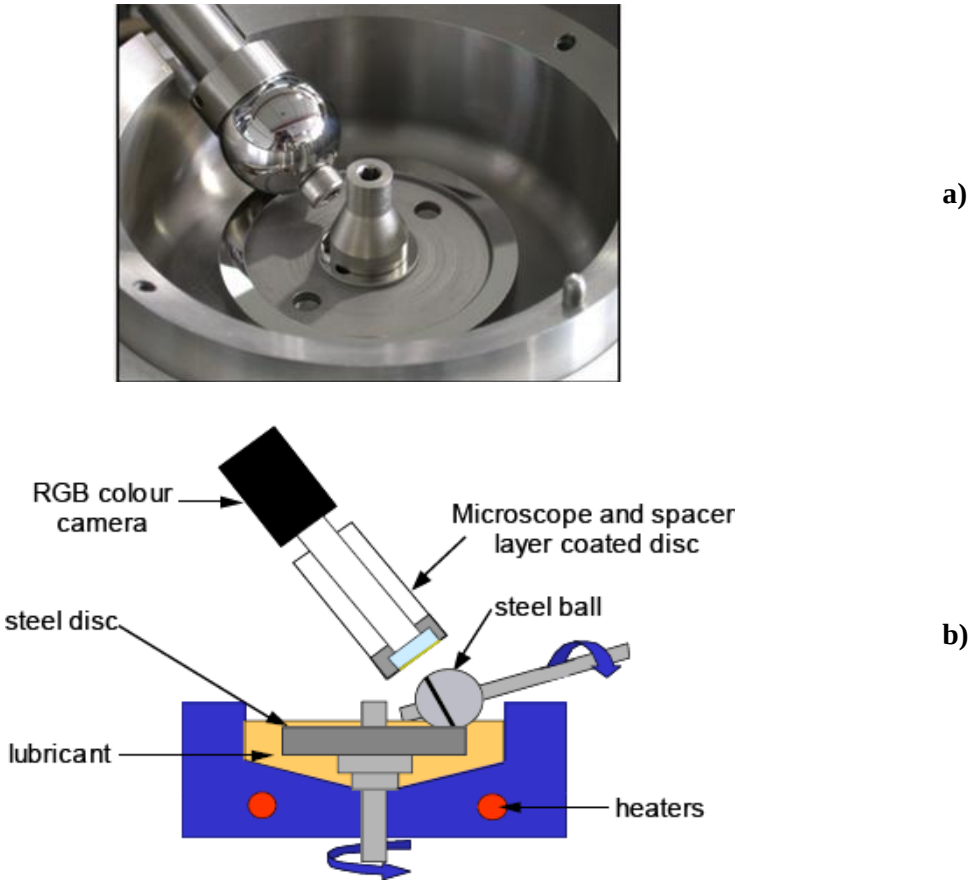


*Figure 98: a) Picture of the ball/disc parts in the MTM*
*b) Scheme of the principle of the MTM*

Traction coefficients obtained from the JEROTRIB test-rig are added on the two following graphs.

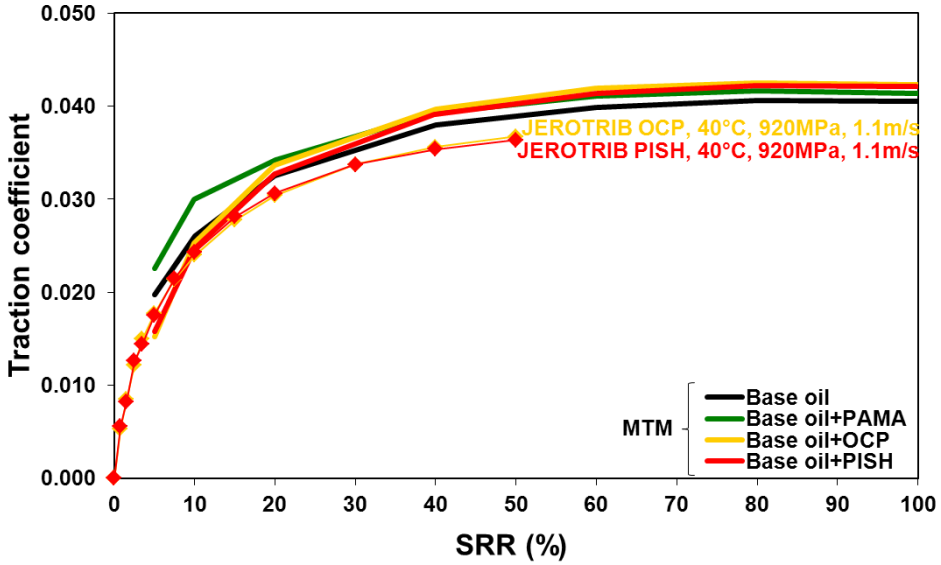


*Figure 99: Traction coefficients for all the solutions at 40 °C, 1 m/s and 920 MPa*

At 40 °C, the traction coefficients over the *SRR* are not clearly differentiated between the solutions. This conclusion must be taken with caution because the comparisons are not at iso-conditions. Indeed, as the viscosity changes, the film thickness changes. The reported values carried on the JEROTRIB instrument are close to the one coming from the Mini-Traction Machine. There is a little discard which may come from the fundamental differences of operation between the two devices. Indeed, in JEROTRIB, the whole components (the ball, the disc, the spindles, the lubricant, etc.) are confined below the disc in a thermo-regulated vessel whereas in the MTM, the ball is above the disc and the tools are outdoors. In the second case, one can imagine that the temperature regulation is more difficult and less accurate. Moreover, the speeds are not exactly equal: in JEROTRIB, it is 1.1 m/s against 1 m/s for the MTM.

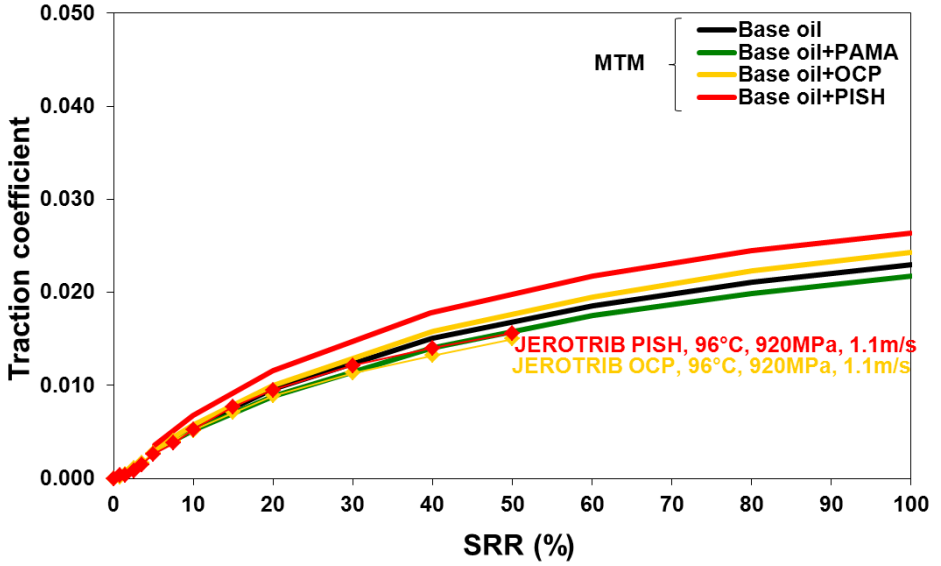


*Figure 100: Traction coefficients for all the solutions at 100 °C, 1 m/s and 920 MPa*

At 100 °C, it seems that the curves are differentiated for the solutions. However, the y-axis scale is small and considering the uncertainties in the measurements, again, one cannot deduce any discrimination between the blends. Globally, there is quite a good agreement between the two devices considering the possible uncertainties.

# Appendix K Analytical tools

## K-1 Size Exclusion Chromatography (SEC)

The Size Exclusion Chromatography (SEC) analyses were performed on a Prominence HPLC system from Shimadzu equipped with a flow refractive index (RI) detector (RID10A from Shimadzu) and a miniDAWN TREOS static light scattering (LS) detector from Wyatt, operating at three scattering angles 49°, 90°, 131° and at a wavelength of 658 nm. The samples were analyzed in THF at room temperature using a flow rate of 1 $mL.min^{-1}$. All polymers were injected at a concentration of ~ 1 $mg.mL^{-1}$ in THF after filtration through a 0.2 µm pore-size membrane. Separation was performed with a guard column and two Agilent PL columns (one mixed D column and one uniform 50 $\dot{A}$) (both 5 µm, 300 x 7.5 mm). The average molecular weights ($M_n$ and $M_w$) and the polydispersity indexes PDI were derived both from the RI signal and from the LS signal using the adequate value of the specific refractive index increment $dn_0/dc$ for each polymer. The latter was measured for OCP (0.075), PISH (0.110), PIB (0.115) and was taken from literature [12][13][15] for PAMA (0.088). The average hydrodynamic radius was derived from both static LS and viscometry.

## K-2 Dynamic light scattering

The Dynamic light scattering measurements were run on a Compact Goniometer System (ALV-CGS3) operating with a vertically polarized laser with wavelength 632 nm (Neon-Helium). It allowed the determination of $R_h$ for OCP and PISH in heptane at ambient temperature. Their concentrations were between 0.2 and 1.25 % (w/w) and angles between 20 and 140 °. For polyisobutylene (PIB) in heptane, the apparent hydrodynamic radius was measured at a concentration of 5 g/L (0.7 %) and angles between 30 and 150 °. Solutions were filtered through a 0.1 µm pore-size membrane.

## K-3 Differential Scanning Calorimetry (DSC)

The Differential Scanning Calorimetry (DSC) is a thermoanalytical method which allows the measure of heat exchanges. Thus, it is possible to determine specific temperatures such as the crystallization temperature or the melting point and particularly, the glass transition temperature $T_g$. Both the sample (with a well-defined heat capacity) and the reference are maintained at nearly the same temperature throughout the experiment. The heat flow rate useful to keep the sample at the imposed temperature is measured.

Measurements were carried out with a DSC NETZSCH (model 204 F1) on polymer solutions. The temperature ramp was as follow: isotherm at 25 °C during 5 minutes, decrease of temperature to -80 °C at 1 °C/min, decrease to -120 °C at 10 °C/min, isotherm at -120°C during 5 minutes, rise of T to 50 °C at 10 °C/min. The determination of the glass transition temperature occurs during the heating phase.

## K-4 LCST measurement - cloud point

The Lower Critical Solution Temperature (LCST) was measured at WEE-Solve (Auf der Burg 6, D-55130 Mainz, Germany) by Dr. J. Eckelt. The equipment consists in a thermostatic pressure cell with two windows on the opposite sides. The pressure was kept constant and the pressurized cell was electronically heated with an accuracy of 0.5°C. The experimental setup is depicted in Figure 101 (a). The onset of the phase separation upon heating was detected by means of the naked eye through the opposed windows. The initially clear solution was expected to become cloudy if the phase separation takes place (formation of droplets scattering the light). The Part b) of Figure 101 shows what a solution looks like below (left) and above the LCST (right). The example of the solution of hydroxypropylcellulose (2.9% w/w) in water was taken because its LCST is well known and is quite low (LCST: between 45 and 58 °C [82]).

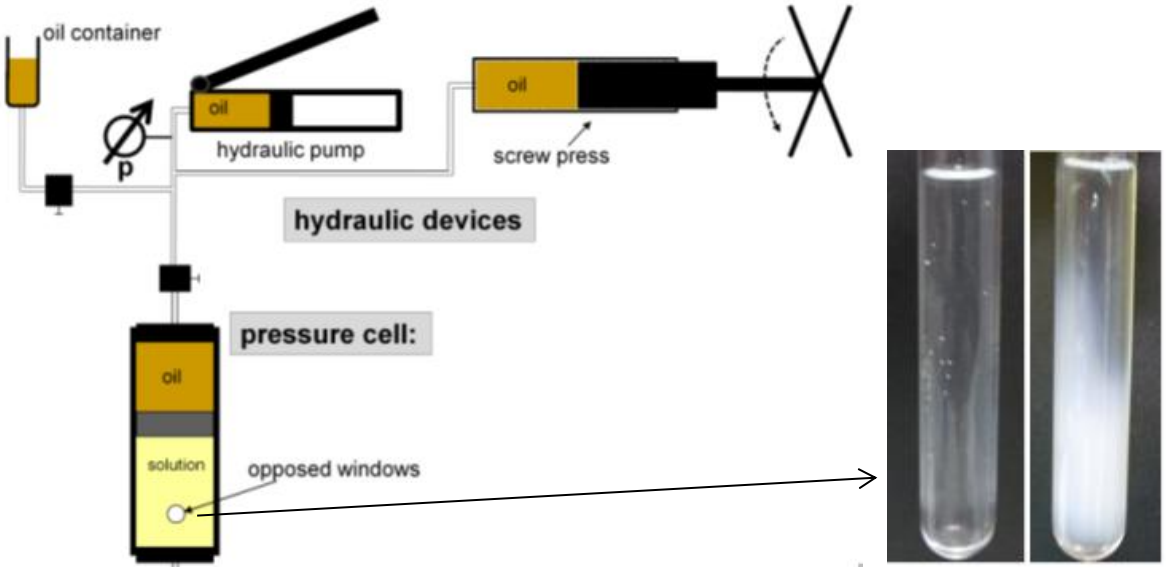


a) b)

*Figure 101: a) Experimental set up for the LCST determination b) an example of the cloud of a solution of hydroxypropylcellulose (2.9% w/w) in water*

# Publications

The work presented in this document has lead so far to several international journal papers and has been presented in different conferences listed below in chronological order.

## Journal papers:

- S. Bair, **C. Mary**, N. Bouscharain, and P. Vergne. An improved Yasutomi correlation for viscosity at high pressure. *Proceedings of the Institution of Mechanical Engineers, Part J: Journal of Engineering Tribology*, 227(9):1056–1060, 2013

- **C. Mary**, D. Philippon, L. Lafarge, D. Laurent, F. Rondelez, S. Bair, and P. Vergne. New insight into the relationship between molecular effects and the rheological behavior of polymer-thickened lubricants under high pressure. *Tribology Letters*, 52(3):357–369, 2013.

## Conferences:

- **C. Mary**, D. Philippon, S. Bair, O. Lerasle, F. Jarnias, and P. Vergne. New insight into the relationship between molecular effects and the rheological behaviour of polymer-thickened lubricants. In *39th Leeds-Lyon Symposium on Tribology "Great Challenges in Tribology"*, Leeds, UK, September 2012.

- **C. Mary**, D. Philippon, D. Laurent, S. Bair, and P. Vergne. A rheological study of Viscosity Index Improvers (VII) in a base oil under severe conditions. In *World Tribology Congress*, Torino, Italy, 2013.

# References


[1] R. I. Taylor. Tribology and energy efficiency: from molecules to lubricated contacts to complete machines. *The Royal Society of Chemistry*, 156:1–22, 2012.

[2] P. Andersson K. Holmberg and A. Erdemir. Global energy consumption due to friction in passenger cars. *Tribology International*, 47:221–234, 2012.

[3] M. I. De Barros Bouchet, J. M. Martin, T. Le Mogne, and B. Vacher. Boundary lubrication mechanisms of carbon coatings by MoDTC and ZDDP additives. *Tribology International*, 38(3):257–264, 2005.

[4] D. Berthe and P. Vergne. High pressure rheology for high pressure lubrication: A review. *Journal of Rheology*, 34(8):1387–1414, 1990.

[5] H. A. Spikes. Sixty years of EHL. *Lubrication Science*, 18(4):265–291, 2006.

[6] P. M. Lugt and G. E. Morales-Espejel. A review of elastohydrodynamic lubrication theory. *Tribology Transactions*, 54:470–496, 2011.

[7] B. J. Hamrock and D. Dowson. Isothermal elastohydrodynamic lubrication of point contacts: Part III-fully flooded results. *J. of Lubrication Tech.*, 99(2):264–275, 1977.

[8] H. A. Barnes, J. F. Hutton, and K. Walters. *An Introduction to Rheology*. Elsevier Science B.V., 1989.

[9] C. W. Macosko. *Rheology Principles, Measurements and Applications*. Wiley-VCH, N.Y., 1994.

[10] J. E. Glass, D. N. Schulz, and C. F. Zukoski. *Polymers as Rheology Modifiers*. ACS, Washington DC, 1991.

[11] C. A. Angell. Formation of glasses from liquids and biopolymers. *Science*, 276:1924–1935, 1995.

[12] S. Bair, C. Mary, N. Bouscharain, and P. Vergne. An improved Yasutomi correlation for viscosity at high pressure. *Proceedings of the Institution of Mechanical Engineers, Part J: Journal of Engineering Tribology*, 227(9):1056–1060, 2013.

[13] S. Bair. *High-pressure rheology for quantitative elastohydrodynamics*. Elsevier Science B.V., 2007.

[14] K. Yasuda, R.C. Armstrong, and R.E. Cohen. Shear flow properties of concentrated solutions of linear and star branched polystyrenes. *Rheologica Acta*, 20(2):163–178, 1981.

[15] P.-G. De Gennes. *Scaling Concepts in Polymer Physics*. Cornell University Press, Ithaca, N.Y., 1979.

[16] J. Briant, J. Denis, and G. Parc. *Rheological Properties of Lubricants*. Institut français du pétrole publications, 1989.

[17] J. Molimard. *Etude expérimentale du régime de lubrification en film mince-application aux fluides de laminage*. PhD thesis, INSA de Lyon, 1999.

[18] M. Hartl, I. Krupka, R. Poliscuk, M. Liska, J. Molimard, M. Querry, and P. Vergne. Thin film colorimetric interferometry. *Tribology Transactions*, 44(2):270–276, 2001.

[19] T. Doki-Thonon. *Thermal effects in elastohydrodynamic spinning circular contacts*. PhD thesis, INSA de Lyon, July 2012.

[20] G. Nijenbanning, C.H. Venner, and H. Moes. Film thickness in elastohydrodynamically lubricated elliptic contacts. *Wear*, 176(2):217 – 229, 1994.

[21] F. Chevalier. *Modélisation des conditions d'alimentation dans les contacts élastohydrodynamiques ponctuels*. n° 96 ISAL0124, Institut National des Sciences Appliquées, Lyon, 1996.

[22] W. Habchi. *A full-system finite element approach to elastohydrodynamic lubrication problems : application to ultra-low-viscosity fluids*. PhD thesis, INSA de Lyon, 2008.

[23] J. M. Georges. *Frottement, usure et lubrification: La tribologie ou science des surfaces*. Collection Sciences et techniques de l'ingénieur. Eyrolles, 2000.

[24] D. Dowson. *History of Tribology*. Professional Engineering Publications, 2nd edition, 1998.

[25] G. Amontons. *De la résistance causée dans les machines*. Mémoires de l'Académie Royale, 1706.

[26] C. A. Coulomb. *Théorie des machines simples, et ayant égard au frottement de leurs parties, et à la roideur des cordages*. 1781.

[27] R. M. Mortier, M. F. Fox, and S. T. Orszulik. *Chemistry and Technology of Lubricants*. Springer Science, 2010.

[28] N. Canter. Viscosity index improvers. *Tribology & Lubrication Technology STLE*, 67(9):10–22, September 2011.

[29] G.-A. Hirn. Etudes sur les principaux phénomenes que présentent les frottements médiats, et sur les diverses manieres de déterminer la valeur mécanique des matieres employées au graissage des machines. *Bulletin de la Société Industrielle de Mulhouse*, 26, 1854.

[30] B. Tower. First report on friction experiments (friction of lubricated bearings). *Proc. Instn. Mech. Engrs*, 35(1):29–35, 1884.

[31] N. P. Petrov. Friction in machine and effect of the lubricant (in russian). *Inzh. Zh., St-Peterburg*, 1:71–140, 1883.

[32] O. Reynolds. On the theory of lubrication and its application to Mr. Beauchamp Tower's experiments, including an experimental determination of the viscosity of olive oil. *Proceedings of the Royal Society of London*, 40(242-245):191–203, 1886.

[33] H. M. Martin. Lubrication of gear teeth. *Engineering (London)*, 102:119–121, 1916.

[34] L. Gümbel. Uber geschmierte arbeitsräder (on the lubrication of gears). *Z. Ges. Turbinenwiesen*, 13:357, 1916.

[35] A. Meldahl. Contribution to theory of lubrication of gears and of stressing of lubricated flanks of gear teeth. *Brown Boveri Review*, 28(11):374–382, 1941.

[36] A. von Mohrenstein-Ertel. Die berechnung der hydrodynamischen schmierung gekrummter oberflachen unter hoher belastung und relativbewegung. *Fortschrittsberichte VDI*, 115 Lang, O.R., and Oster, P. (Eds.), VDI Verlag: Dusseldorf. First Published in 1945 in Russian under the name A. M. Ertel, 1949.

[37] A. N. Grubin. Investigation of the contact of machine components. *Central Scientific Research Institute for Technology and Mechanical Engineering: Moscow, DSIR translation*, 337, 1949.

[38] A. Cameron. Righting a 40-year-old wrong; A. M. Ertel–the true author of Grubin's EHL solution. *Tribology International*, 18(2):92, 1985.

[39] C. Barus. Isothermals, isopiestics and isometrics relative to viscosity. *Am. J. of Sience*, 45:87–96, 1893.

[40] R. Gohar and A. Cameron. Optical measurement of oil film thickness under elasto-hydrodynamic lubrication. *Nature*, 200:458–459, 1963.

[41] A. Cameron and R. Gohar. Theoretical and experimental studies of the oil film in lubricated point contact. *Proceedings of the Royal Society of London A*, 291:520–536, 1966.

[42] C. A. Foord, W. C. Hammann, and A. Cameron. Evaluation of lubricants using optical elasto-hydrodynamics. *ASLE Transactions*, 11:31–43, 1968.

[43] G. J. Johnston, R. Wayte, and H. A. Spikes. The measurement and study of very thin lubricant films in concentrated contacts. *Tribology Transactions*, 34:187–194, 1991.

[44] A. I. Petrusevich. Fundamental conclusions from the contact hydrodynamic theory of lubrication. *Izvestiya Akademii Nauk SSSR (OTN)*, 3(2):209–223, 1951.

[45] D. Dowson and G. R. Higginson. A numerical solution to the elasto-hydrodynamic problem. *Journal of Mechanical Engineering Science*, 1(1):6–15, 1959.

[46] B. J. Hamrock and D. Dowson. Isothermal elastohydrodynamic lubrication of point contacts, part I, theoretical formulation. *Journal of Tribology*, 98:223–229, 1976.

[47] A. A. Lubrecht, W. E. ten Napel, and R. Bosma. Multigrid, an alternative method of solution for two-dimensional elastohydrodynamically lubricated point contact calculations. *Journal of Tribology*, 109:437–443, 1987.

[48] C. H. Venner. *Multilevel Solution of the EHL Line and Point Contact Problems*. PhD thesis, University of Twente, Enschede, The Netherlands, 1991.

[49] W. Habchi, P. Vergne, S. Bair, O. Andersson, D. Eyheramendy, and G. E. Morales-Espejel. Influence of pressure and temperature dependence of thermal properties of a lubricant on the behaviour of circular TEHD contacts. *Tribology International*, 43(10):1842 – 1850, 2010.

[50] S. C. Tung and M. L. McMillan. Automotive tribology overview of current advances and challenges for the future. *Tribology International*, 37(7):517 – 536, 2004.

[51] L. R. Rudnick. *Lubricant Additives: Chemistry and Applications*. Chemical Industries. 2009.

[52] J. Briant, J. Denis, and G. Parc. *Propriétés rhéologiques des lubrifiants*. Publications de l'Institut Français du Pétrole, 1985.

[53] C. M. Roland. Characteristic relaxation times and their invariance to thermodynamic conditions. *Soft Matter*, 4(12):2316–2322, 2008.

[54] E. N. da Costa Andrade. The viscosity of liquids. *Nature*, 125:309–310, 1930.

[55] H. Eyring. Viscosity, plasticity, and diffusion as examples of absolute reaction rates. *The Journal of Chemical Physics*, 4(4):283–291, 1936.

[56] R. F. Landel M. L. Williams and J. D. Ferry. The temperature dependence of relaxation mechanisms in amorphous polymers and other glass-forming liquids. *Journal of the American Chemical Society*, 77(14):3701–3707, 1955.

[57] R. M. Overney, C. Buenviaje, R. Luginbuhl, and F. Dinelli. Glass and structural transitions measured at polymer surfaces on the nanoscale. *Journal of Thermal Analysis and Calorimetry*, 59(1-2):205–225, 2000.

[58] A. K. Doolittle. Studies in newtonian flow. II. the dependence of the viscosity of liquids on free-space. *Journal of Applied Physics*, 22(12):1471–1475, 1951.

[59] D. Dowson and G. R. Higginson. *Elastohydrodynamic lubrication*. Oxford, 1977.

[60] P. Vergne. *Comportement rhéologique des lubrifiants et lubrification: approches expérimentales*. HdR, INSA de Lyon, 2002.

[61] H. Blok. Inverse problems in hydrodynamic lubrication and design directives for lubricated flexible surfaces. *Proc. Int. Symp. on Lubrication and Wear, Houston, McCutchan Pub. Corp., Berkeley*, pages 1–151, 1963.

[62] S. Yasutomi, S. Bair, and W. O. Winer. An application of a free volume model to lubricant rheology. I: dependence of viscosity on temperature and pressure. II: Variation in viscosity of binary blended lubricants. *ASME Journal of Tribology*, 106:291–312, 1984.

[63] C. J. A. Roelands, J. C. Vlugter, and H. I. Waterman. The viscosity-temperature-pressure relationship of lubricating oils and its correlation with chemical constitution. *Journal of Basic Engineering*, 85(4):601–607, 1963.

[64] M. M. Cross. Rheology of non-newtonian fluids: A new flow equation for pseudoplastic systems. *Journal of Colloid Science*, pages 417–437, 1965.

[65] D.M. Meter and R. B. Bird. Tube flow of non-newtonian polymer solutions: Part I. laminar flow and rheological models. *AIChE Journal*, 10(6):878–881, 1964.

[66] P. J. Carreau. Rheological equations from molecular network theories. *Transactions of the Society of Rheology*, 16(1):99–127, 1972.

[67] S. Bair and M. Khonsari. An EHD inlet zone analysis incorporating the second newtonian. *Journal of Tribology*, 118(2):341–343, 1996.

[68] R. I. Tanner. *Engineering rheology*. Oxford University Press New York, 1988.

[69] P. W. Bridgman. The effect of pressure on the viscosity of forty-three pure liquids. *Proc. Amer. Acad.*, 61:57–99, 1926.

[70] D. R. Caudwell, J. P. M. Trusler, V. Vesovic, and W. A. Wakeham. Viscosity and density of five hydrocarbon liquids at pressures up to 200 MPa and temperatures up to 473 K. *J. Chem. Eng. Data*, 54:359–366, 2009.

[71] K. Harris and S. Bair. Temperature and pressure dependence of the viscosity of diisodecyl phthalate at temperatures between (0 and 100) °C and at pressures to 1 GPa. *J. Chem. Eng. Data*, 52:272–278, 2007.

[72] S. Bair. Measurements of real non-newtonian response for liquid lubricants under moderate pressures. *Proceedings of the Institution of Mechanical Engineers, Part J: Journal of Engineering Tribology*, 215(3):223–233, 2001.

[73] S. Bair, P. A. Kottke, and W. O. Winer. Cavitation in creeping shear flows. *American Institute of Chemical Engineers AIChE J*, 51:2150–2170, 2005.

[74] M. Chanda. *Introduction to Polymer Science and Chemistry: A Problem Solving Guide*. CRC Press, 2006.

[75] Y. Gnanou and M. Fontanille. *Organic And Physical Chemistry of Polymers*. 2008.

[76] R. H. Colby. Structure and linear viscoelasticity of flexible polymer solutions: comparison of polyelectrolyte and neutral polymer solutions. *Rheologica Acta*, 49(5):425–442, 2010.

[77] G. Jannink J. Des Cloizeaux. *Les polymeres en solution: leur modélisation et leur structure*. 1987.

[78] B. A. Wolf. Polyelectrolytes revisited: Reliable determination of intrinsic viscosities. *Macromolecular Rapid Communications*, 28(2):164–170, 2007.

[79] M. L. Huggins. The viscosity of dilute solutions of long-chain molecules. IV. dependence on concentration. *Journal of the American Chemical Society*, 64(11):2716–2718, 1942.

[80] E. O. Kraemer. Molecular weights of celluloses and cellulose derivates. *Industrial & Engineering Chemistry*, 30(10):1200–1203, 1938.

[81] A. F. Martin. Cellulose and cellulose derivatives. In *Memphis Meeting of the American Chemical Society*, page 966, 1942.

[82] J. Brandrup, E. H. Immergut, and C. Wohlfarth. *Handbook of Chemistry and Physics - Upper Critical (UCST) And Lower Critical (LCST) Solution Temperatures of Binary Polymer Solutions*, volume 88th edition. CRC, 2007-2008.

[83] C. Boutris, E. G. Chatzi, and C. Kiparissides. Characterization of the LCST behaviour of aqueous poly(n-isopropylacrylamide) solutions by thermal and cloud point techniques. *Polymer*, 38(10):2567 – 2570, 1997.

[84] H. Fujimatsu, S. Ogasawara, and S. Kuroiwa. Lower critical solution temperature (LCST) and theta temperature of aqueous solutions of nonionic surface active agents of various polyoxyethylene chain lengths. *Colloid & Polymer Science*, 266:594–600, 1988.

[85] J.M.G. Cowie and V. Arrighi. *Polymers: Chemistry and Physics of Modern Materials*, volume 50. Taylor & Francis, Contemporary Physics, 2009.

[86] B. A. Wolf. Improvement of polymer solubility: Influence of shear and of pressure. *Pure & Appl. Chem*, 69(5):929–933, 1997.

[87] E. A. Clark and J. E. G. Lipson. LCST and UCST behavior in polymer solutions and blends. *Polymer*, 53(2):536 – 545, 2012.

[88] ASME pressure–viscosity report. *American Society of Mechanical Engineers*, I & II, 1953.

[89] S. Bair, P. Vergne, and M. Querry. A unified shear-thinning treatment of both film thickness and traction in EHD. *Tribology Letters*, 18(2):145–152, February 2005.

[90] J. Frene, M. Arghir, and V. Constantinescu. Combined thin-film and Navier–Stokes analysis in high Reynolds number lubrication. *Tribology International*, 39(8):734–747, 2006.

[91] C. Mary, D. Philippon, L. Lafarge, D. Laurent, F. Rondelez, S. Bair, and P. Vergne. New insight into the relationship between molecular effects and the rheological behavior of polymer-thickened lubricants under high pressure. *Tribology Letters*, 52(3):357–369, 2013.

[92] L. Zeman and D. Patterson. Pressure effects in polymer solution phase equilibriums. II. systems showing upper and low critical solution temperatures. *The Journal of Physical Chemistry*, 76(8):1214–1219, 1972.

[93] Y. Iwama M. Kamada K. Kurata, M. Tsunashima. *Polymer Handbook*. John Wiley, NY, 1975.

[94] J. E. Mark. *Rubber Chem. Tech*, 46:593–618, 1973.

[95] P. J. Flory. *Principles of Polymer Chemistry*. Cornell University Press, Ithaca, N.Y., 1953.

[96] D. Petera and M. Muthukumar. Brownian dynamics simulation of bead–rod chains under shear with hydrodynamic interaction. *The Journal of Chemical Physics*, 111(16):7614–7623, 1999.

[97] C. M. Hansen. *The three dimensional solubility parameter and solvent diffusion coefficient: Their importance in surface coating formulation*. Copenhagen Danish Technical Press, 1967.

[98] F. J. Westlake and A. Cameron. Optical elastohydrodynamic fluid testing. *ASLE Transactions*, 15(2):81–95, 1972.

[99] M. Born and E. Wolf. *Principles of Optics: Electromagnetic Theory of Propagation, Interference and Diffraction of Light*. Cambridge University Press, 1999.

[100] H. Moes. Communication in proceedings of the symposium on elastohydrodynamic lubrication, London. *Proc. Instn. Mech. Engrs*, 180:244–245, 1965.

[101] J.-P. Chaomleffel, G. Dalmaz, and P. Vergne. Experimental results and analytical film thickness predictions in EHD rolling point contacts. *Tribology International*, 40:1543–1552, 2007.

[102] H. S. Cheng. A refined solution to the thermal elastohydrodynamic lubrication of rolling and sliding cylinders. *ASLE Transactions*, 8:397–410, 1965.

[103] I. Jubault, J. L. Mansot, P. Vergne, A. A. Lubrecht, and J. Molimard. *Proc. 29th Leeds-Lyon symp. on Tribology, Leeds, D. Dowson et al. (Editors) Elsevier 2003*, pages 663–673, 2002.

[104] ASTM D2270 - calculating viscosity index from kinematic viscosity at 40 and 100°C.

[105] ASTM D445 - standard test method for kinematic viscosity of transparent and opaque liquids (and calculation of dynamic viscosity).

[106] ASTM D4741 - measuring viscosity at high temperature and high shear rate by tapered-plug viscometer.

[107] PCS Instruments. *Ultra Shear Viscometer (USV)*. Available at: http://www.pcs-instruments.com/usv/usv.shtml, Accessed 20 September 2013.

[108] ASTM D5293 - apparent viscosity of engine oils and base stocks between -5 and -35°C using cold-cranking simulator.

[109] H. Hertz. Uber die berührung fester elastischer körper. *J. reine und angew. Math.*, 92:156–171, 1881.

[110] PCS Instruments. *Mini-Traction Machine (MTM)*. Available at: http://www.pcs-instruments.com/mtm/mtm.shtml, Accessed 20 September 2013.

FOLIO ADMINISTRATIF

THESE SOUTENUE DEVANT L'INSTITUT NATIONAL DES SCIENCES APPLIQUEES DE LYON

NOM : MARY DATE de SOUTENANCE : 03/02/2014
(avec précision du nom de jeune fille, le cas échéant)
Prénoms : Charlotte

TITRE: Physico-chemistry, high pressure rheology and film-forming capacity of polymer-base oil solutions in EHL

NATURE : Doctorat Numéro d'ordre : 2014ISAL0013

Ecole doctorale : MEGA

Spécialité : Mécanique

RESUME:
The development of high value-added lubricants overcoming more and more drastic operating conditions, fuel-efficient and providing excellent performance during a long time remains a huge challenge for oil makers. This thesis is dedicated to the study of the role and the actions of Viscosity Index Improvers (VII) in engine lubricants.
The first objective targeted in this work is the characterization of the rheological behaviors and the modeling of viscosity in function of realistic conditions of temperature, pressure and shear stress for polymer-thickened base oil solutions without functional additives. Several polymers (PAMA, OCP and PISH) with different molecular weights and conformations (comb, linear and star) are used with a concentration of 1.2% (w/w) in a hydrocracked mineral base oil. The originality of the thesis lies in the use of non-commercial rheometers under high pressure (up to 800 MPa).
A second challenge is the understanding of the relationship between the rheological response of simplified engine lubricants and the mechanisms occurring at the molecular scale by exploring the notions of conformation, solubility and hydrodynamic radius by the extension of the Einstein's law at high pressure.
Finally, the study focuses on the link between rheology and tribology and by extrapolation, between the chemical composition of the lubricant and tribology. The film thickness is measured and compared with the Hamrock-Dowson analytical predictions and with the numerical simulations based on the generalized Reynolds' equation including the rheological models. Both experimental and numerical data are in good agreement.

MOTS-CLES: rheology, non-Newtonian behavior, elastohydrodynamic lubrication, hydrodynamic radius, polymer, lubricant, rheological models, pressure, tribology

Laboratoire(s) de recherche : LaMCoS

Directeur de thèse: Philippe VERGNE

Président de jury : Philippe CASSAGNAU

Composition du jury :

| | | |
|---|---|---|
| Président | P. Cassagnau | Professeur (Université Claude Bernard Lyon 1) |
| Rapporteur | M. Priest | Professeur (University of Leeds, U.K.) |
| Rapporteur | J.-F. Tassin | Professeur (Université du Maine) |
| Directeur | P. Vergne | Directeur de recherche (CNRS) (INSA de Lyon) |
| Co-directeur | D. Philippon | Maître de conférence (INSA de Lyon) |
| Invité | S. Bair | Docteur (Georgia Institute of Technology, U.S.A.) |
| Invité | D. Laurent | Ingénieur de recherche (Total, Solaize) |
| Invité | F. Rondelez | Directeur de recherche émérite (CNRS, Institut Curie) |